THE
BENDIX
CORPORATION

GUIDANCE SYSTEMS
DIVISION
DENVER OPERATIONS

Prepared by:

The Guidance and Control Group
The Bendix Corporation

FLOATED PALLET DEFINITION STUDY

FINAL REPORT

APRIL 1975

VOLUME II
SUSPENDED
PALLET POINTING
PERFORMANCE STUDY

Approved by:

S. Calvin Rybak
Program Manager

O. Taylor
Technical Manager

M. Brown
Manager,
Denver Operations

PREPARED FOR:

GEORGE C. MARSHALL
SPACE FLIGHT CENTER
HUNTSVILLE, ALABAMA

NASA CONTRACT NO.
NAS8-30889

FOREWORD

This final report is submitted in accordance with the requirements of NASA-GSFC, Contract No. NAS8-30889. The report includes:

Volume I - Evaluation of Alternate Telescope Pointing Schemes

Volume II - Suspended Pallet Pointing Performance Study

Volume III - Retention/Suspension Systems, Pallet Common Module Configuration Study

CONTENTS

		Page
Foreword		ii
Contents		iii
1.	INTRODUCTION	1-1
1.1	General	1-1
1.2	Study Objectives	1-1
1.3	Relationship to Other Efforts	1-2
1.4	Method of Approach and Principal Assumptions	1-3
1.5	Basic Study Output and Significant Results	1-3
1.6	Study Limitations	1-4
1.7	Suggested Additional Effort	1-4
2.	SUMMARY	2-1
3.	VEHICLE DESCRIPTION	3-1
3.1	Space Shuttle System Description	3-1
3.2.1	Orbiter	3-1
3.2.2	Pallet	3-7
3.3	CMG Control System	3-7
3.4	Coordinate System Definition	3-7
3.4.1	Inertial Pointing System (X_I, Y_I, Z_I)	3-10
3.4.2	Orbiter System (X_S, Y_S, Z_S)	3-10
3.4.3	Pallet System (X_P, Y_P, Z_P)	3-10
3.4.4	P'-System	3-10
3.4.5	CMG System	3-11
4.	MISSION REQUIREMENTS	4-1
4.1	Vehicle Orbit	4-1
4.2	Vehicle Attitudes	4-1
4.3	Vehicle Maneuver Guidelines	4-2
4.4	Pallet Pointing Requirements	4-2
4.5	Pallet Control Loop Requirements	4-2
5.	CMG SYSTEM REQUIREMENTS	5-1
5.1	Orbiter/Pallet Mass Properties	5-1
5.2	Torque and Momentum Requirements	5-2
5.2.1	X Axis Perpendicular to the Orbital Plane (XPOP)	5-3
5.2.2	X Axis in the Orbital Plane (XIOP)	5-8
5.2.3	Maneuvering Requirements	5-16
5.3	Summary of Torque and Momentum Requirements	5-19

CONTENTS (Continued)

		Page
6.	CMG CONFIGURATION STUDY	6-1
6.1	CMG Types and Type Selection	6-1
6.2	Survey of Double Gimbal CMGs	6-4
6.3	CMG Cluster Definitions	6-4
6.4	CMG Actuator Recommendations	6-4
6.5	CMG Cluster Configuration	6-8
6.6	CMG Control Law	6-8
7.	CONTROL MOMENT GYRO (CMG) MODEL	7-1
7.1	Compliances	7-1
7.2	Shockmount	7-1
7.3	CMG Friction	7-1
7.4	Coordinate Systems	7-4
7.4.1	Wheel Coordinate System (W-space)	7-4
7.4.2	Inner Gimbal Coordinate System (A-space)	7-6
7.4.3	Outer Gimbal Coordinate System (C-space)	7-6
7.4.4	Base Coordinate System (B-space)	7-6
7.4.5	Shockmount Coordinate System (P'-space)	7-7
7.5	CMG Dynamics	7-7
7.5.1	Inner Gimbal/Rotor Compliance (γ) Dynamics	7-7
7.5.2	Inner Gimbal Dynamics	7-10
7.5.3	Outer Gimbal Dynamics	7-10
7.5.4	CMG Base Dynamics	7-13
7.5.5	Shockmount Dynamics	7-17
7.6	CMG/Shockmount Dynamic Model	7-17
7.7	CMG Frequency Response	7-21
8.	CMG-PALLET CONTROL LOOP STUDIES	8-1
8.1	Vehicle Control Law	8-1
8.2	CMG-Pallet Control Loop	8-2
8.3	Analysis With Ideal CMG	8-4
8.3.1	Determination of Rate and Position Gains	8-4
8.3.2	Determination of Position Integral Gain	8-7
8.4	CMG Characteristics	8-9
8.5	Loop Stability Investigation	8-12
8.6	Compensation Analysis	8-12
8.6.1	Combined CMG/Compensator System	8-14
8.6.2	Combined System With Integral Gain	8-18
8.7	Pointing Error Estimation	8-19
9.	VEHICLE DYNAMIC MODEL	9-1
9.1	Resolution of CMG Control Torques	9-1
9.2	Derivation of the Detailed Dynamics	9-2

CONTENTS (Continued)

		Page
9.2.1	Suspension System Dynamics.	9-2
9.2.2	Orbiter Rotational Dynamics	9-8
9.2.3	Pallet Rotational Dynamics.	9-9
9.2.4	Translational Dynamics.	9-9
9.2.5	Summary of the Detailed Dynamics.	9-11
9.3	Simplified Vehicle Dynamics	9-12
10.	COMPUTER STUDY.	10-1
10.1	Hybrid Simulation Details	10-1
10.1.1	CMG Models.	10-1
10.1.2	Vehicle Dynamics Model.	10-2
10.2	CMG Frequency Response.	10-2
10.3	Simulation Study Outline.	10-2
10.4	Pointing Performance Study Results.	10-4
10.4.1	CMG Friction Study.	10-4
10.4.2	Vehicle Disturbance	10-5
10.4.3	Crew Motion Disturbances.	10-5
10.5	Summary	10-5
11.	CONCLUSIONS	11-1
12.	NOTES	12-1
12.1	References.	12-1
12.2	Abbreviations	12-1
12.3	Symbols	12-2
12.4	Transformations	12-7

Figure

2-1	Logical Flow of the Pointing Performance Evaluation.	2-2
3-1	Space Shuttle Flight System	3-2
3-2	Orbiter/Pallet Configuration.	3-3
3-3	Orbiter Related to the Inertial Coordinate System.	3-5
3-4	Coordinate System Location.	3-6
3-5	Pallet System	3-9
5-1	XPOP Attitude Geometry.	5-4
5-2	XPOP Torque Histories - One Orbit	5-7
5-3	XPOP Momentum History With Vehicle Axis Pointing.	5-9
5-4	XIOP Attitude Geometry.	5-10
5-5	XIOP Momentum History for One Orbit, $\beta=-\pi/4$ . . .	5-14

CONTENTS (Continued)

		Page
6-1	Types of Control Moment Gyroscopes.	6-2
6-2	Related In-Line CMG Cluster Configuration	6-9
6-3	Relation of CMG Output Axes to Pallet Axes. . . .	6-11
7-1	Coordinate Frame Relationship With No Deflections	7-5
7-2	Inner Gimbal/Rotor Compliance (γ) Dynamics. . . .	7-9
7-3	Z Axis Dynamics of the CMG Base	7-15
7-4	Block Diagram of Base Dynamics for X and Y Axes.	7-18
7-5	Generation of Shockmount Torques.	7-19
7-6	CMG Rate Loop	7-20
8-1	CMG-Pallet Linearized Control Loop.	8-3
8-2	Root Locus of the Ideal Loop With $K_{PI}=0$	8-6
8-3	Closed Loop Response for K_{PI}/K_P of 0 and 2 With Ideal CMG.	8-11
8-4	Bode Diagram of Open Loop Rate Plus Position Control Law With Second-Order CMG	8-13
8-5	Bode Diagram of Open Loop Rate Plus Position Control Loop With Compensated CMG	8-15
8-6	Roof Locus Diagram of Rate Plus Position Control Loop, CMG, and Compensator.	8-16
8-7	Root Locus of Compensated CMG With Rate, Position and Integral Control Law	8-20
9-1	Geometry of One Suspension Point With No Deflections	9-3
9-2	Geometry of One Suspension Point With a General Deflection.	9-5
9-3	Suspension Point Identification - Four Point System.	9-13
9-4	Vehicle Dynamics Block Diagram (2 sheets)	9-18
10-1	Floated Pallet Pointing Performance Study, Hybrid Computer Model	10-11
10-2	Shockmounted Six-Mass CMG Dynamic Model	10-12
10-3	Floated Pallet Pointing Performance Study, Vehicle Dynamics.	10-13
10-4	Floated Pallet CMG Frequency Response to Inner Gimbal Rate Command	10-14
10-5	Floated Pallet CMG Frequency Response to Outer Gimbal Rate Command	10-15
10-6	No Torque Disturbance, 1/2 Hz System, Zero Gimbal Angles	10-16
10-7	Step Torque Disturbance, 1/2 Hz System, Zero Gimbal Angles	10-17

CONTENTS (Continued)

		Page
10-8	Crew Motion Torque Disturbance Case I, 1/2 Hz System, Zero Gimbal Angles	10-18
10-9	Crew Motion Torque Disturbance Case II, 1/2 Hz System, Zero Gimbal Angles	10-19
10-10	Crew Motion Torque Disturbance Case III, 1/2 Hz System, Zero Gimbal Angles	10-20
10-11	No Torque Disturbance, 1/2 Hz System, 45 deg Gimbal Angles.	10-21
10-12	Step Torque Disturbance, 1/2 Hz System, 45 deg Gimbal Angles.	10-22
10-13	Crew Motion Torque Disturbance Case I, 1/2 Hz System, 45 deg Gimbal Angles	10-23
10-14	Crew Motion Torque Disturbance Case II, 1/2 Hz System, 45 deg Gimbal Angles	10-24
10-15	Crew Motion Torque Disturbance Case III, 1/2 Hz System, 45 deg Gimbal Angles	10-25
10-16	No Torque Disturbance, 1 Hz System, Zero Gimbal Angles.	10-26
10-17	Step Torque Disturbance, 1 Hz System, Zero Gimbal Angles.	10-27
10-18	Crew Motion Torque Disturbance Case I, 1 Hz System, Zero Gimbal Angles	10-28
10-19	Crew Motion Torque Disturbance Case II, 1 Hz System, Zero Gimbal Angles	10-29
10-20	Crew Motion Torque Disturbance Case III, 1 Hz System, Zero Gimbal Angles	10-30
10-21	No Torque Disturbance, 1 Hz System, 45 deg Gimbal Angles.	10-31
10-22	Step Torque Disturbance, 1 Hz System, 45 deg Gimbal Angles.	10-32
10-23	Crew Motion Torque Disturbance Case I, 1 Hz System, 45 deg Gimbal Angles	10-33
10-24	Crew Motion Torque Disturbance Case II, 1 Hz System, 45 deg Gimbal Angles	10-34
10-25	Crew Motion Torque Disturbance Case III, 1 Hz System, 45 deg Gimbal Angles	10-35
10-26	No Torque Disturbance, 2 Hz System, Zero Gimbal Angles.	10-36
10-27	Step Torque Disturbance, 2 Hz System, Zero Gimbal Angles.	10-37
10-28	Crew Motion Torque Disturbance Case I, 2 Hz System, Zero Gimbal Angles	10-38
10-29	Crew Motion Torque Disturbance Case II, 2 Hz System, Zero Gimbal Angles	10-39

CONTENTS (Continued)

		Page
10-30	Crew Motion Torque Disturbance Case III, 2 Hz System, Zero Gimbal Angles	10-40
10-31	No Torque Disturbance, 2 Hz System, Zero Inner Gimbal Angles and 45 deg Outer Gimbal Angles	10-41
10-32	Step Torque Disturbance, 2 Hz System, Zero Inner Gimbal Angles and 45 deg Outer Gimbal Angles	10-42
10-33	Crew Motion Torque Disturbance Case I, 2 Hz System, Zero Inner Gimbal Angles and 45 deg Outer Gimbal Angles	10-43
10-34	Crew Motion Torque Disturbance Case II, 2 Hz System, Zero Inner Gimbal Angles and 45 deg Outer Gimbal Angles	10-44
10-35	Crew Motion Torque Disturbance Case III, 2 Hz System, Zero Inner Gimbal Angles and 45 deg Outer Gimbal Angles	10-45
10-36	No Torque Disturbance, 45 Hz System, Zero Gimbal Angles	10-46
10-37	Step Torque Disturbance, 4 Hz System, Zero Gimbal Angles	10-47
10-38	Crew Motion Torque Disturbance Case I, 4 Hz System, Zero Gimbal Angles.	10-48
10-39	Crew Motion Torque Disturbance Case II, 4 Hz System, Zero Gimbal Angles.	10-49
10-40	Crew Motion Torque Disturbance Case III, 4 Hz System, Zero Gimbal Angles	10-50
10-41	No Torque Disturbance, 1 Hz System, Zero Gimbal Angles, Half CMG Friction.	10-51
10-42	No Torque Disturbance, 1 Hz System, Zero Gimbal Angles, Double CMG Friction.	10-52
10-43	No Torque Disturbance, 2 Hz System, Zero Gimbal Angles, Half CMG Friction.	10-53
10-44	No Torque Disturbance, 2 Hz System, Zero Gimbal Angles, Double CMG Friction.	10-54
10-45	No Torque Disturbance, 4 Hz System, Zero Gimbal Angles, Half CMG Friction.	10-55
10-46	No Torque Disturbance, 4 Hz System, Zero Gimbal Angles, Double CMG Friction.	10-56
10-47	Unloaded Limit Cycle Peak Value Versus System Bandwidth (Zero Gimbal Angles)	10-57
10-48	Unloaded Limit Cycle X-Axis Peak Value Versus CMG Friction Level (Zero Gimbal Angles).	10-58

CONTENTS (Concluded)

		Page
10-49	Torque Disturbance Required to Eliminate Limit Cycle Versus System Bandwidth (Zero Gimbal Angles)	10-59
10-50	Crew Motion Disturbance Peak Value Versus System Bandwidth (Zero Gimbal Angles)	10-60

Table

3-1	Orbiter/Pallet Vehicle Mass Properties	3-4
3-2	Orbiter Mass Properties	3-8
3-3	Pallet Mass Properties	3-8
5-1	Summary of Torque and Momentum Requirements	5-20
6-1	Candidate Double Gimbal CMG Actuators	6-5
6-2	Candidate Actuator Clusters	6-6
8-1	Closed Loop Gain at $\omega=4\pi$ for Various K_{PI}/K_R (Ideal CMG)	8-10
8-2	Factors of the Closed Loop Transfer for Various K_{PI}/K_R (Ideal CMG)	8-10
10-1	Floated Pallet Pointing Performance Study CMG Parameters (2 sheets)	10-6
10-2	Floated Pallet Pointing Performance Study Vehicle Parameters	10-8
10-3	Floated Pallet Pointing Performance Study Vehicle Control Law Gains	10-9
10-4	Floated Pallet Hybrid Simulation Study Results	10-10

1. INTRODUCTION

1.1 General - With the maturation of the space shuttle concept of a reusable launch vehicle for earth orbital missions, two divergent modes of operation have been defined. One mode involves the use of the shuttle as a logistics vehicle placing free flying experiment packages in orbit and replacing, repairing or servicing existing packages. In addition it will perform a crucial role as a manned experiment base, remaining in earth orbit from 7 to 30 days performing various experiments with equipment mounted in the payload bay.

Current assessments of the experiments proposed for operation in low earth orbit in conjunction with a manned vehicle indicate that nearly 45 percent of the payloads require pointing accuracy greater than that afforded by the orbiter capability using the Reaction Control System (RCS) and 39 percent have requirements exceeding the capabilities of the orbiter under the direct control of Control Moment Gyroscopes (CMGs). One concept under study to meet these higher accuracy pointing requirements is to mount the experiment packages to a pallet structure which in turn is attached to the orbiter through a suspension system which isolates the pallet from the disturbances arising in the orbiter which occur during periods of instrument operation.

The study described in this report involves the definition and evaluation of a floated pallet control system utilizing CMG actuators attached to the pallet and controlling it directly, affecting and affected by the orbiter only through the suspension system.

1.2 Study Objectives - The objectives of the suspended pallet pointing performance study were the following:

a. Selection of a CMG actuator and definition of a system configuration that best satisfies the overall mission requirements.

b. Development of a detailed nonlinear model of the selected CMG for analog computer analysis of the actuator characteristics.

c. Definition of a vehicle control law translating vehicle disturbance effects into a correcting torque command and a CMG control law to generate appropriate gimbal rate commands to generate the commanded torque.

d. Development of a model of the rigid body dynamics of the pallet and orbiter connected through the suspension system.

e. Integration of all models into a hybrid simulation to be used in the evaluation of the pointing performance realizable by the CMG-pallet-suspension-orbiter system.

All of the above objectives were met during the course of the study.

1.3 Relationship to Other Efforts - The Bendix Corporation was critically involved with the Skylab program from its inception, performing studies in the areas of communications, mission operations, experiment integration, stabilization and control, human factors, and test and reliability. Bendix also furnished the double gimbal CMGs, double gimballed star tracker and the experiment pointing electronics assembly (EPEA) which formed a critical part of the total Skylab attitude and pointing control system (APCS) in addition to the C&D console used to operate and command virtually all systems aboard Skylab. During the course of the Skylab program detailed studies were made into the behavior of CMG systems and the software required to satisfactorily control and manage such a system. Valuable experience and insight into the behavior and idiosyncracies of CMG systems was gained over the seven years that these studies were performed, and was directly applicable to the performance of the present study.

Data generated during the course of the Research and Applications Module (RAM) study (May 1971-June 1972) in which Bendix was a prime participant, provided valuable input to the present study in the area of proposed experiment payloads for the shuttle vehicle and the requirements placed upon that vehicle due to those payloads. In addition the experience gained in the analysis and design of candidate CMG control systems for RAM applications is directly applicable to the present study.

The Astronomy Sortie Mission (ASM) Definition study (December 1971-March 1973) in which Bendix was a prime participant, also provided valuable inputs to the present study in the area of shuttle vehicle requirements due to proposed astronomy experimentation and in the design of possible attitude control systems which included reaction control, CMG, and experiment isolation systems that could be used to meet these requirements.

A "Study to Define Logic Associated With CMGs to Maneuver and Stabilize an Orbiting Vehicle" was performed by Bendix (July 1972-September 1973) defining a CMG system capable of controlling the orbiter and developing the software required to manage and control the system. The experience gained in the performance of this study was directly applicable to the present study, particularly in the areas of CMG system selection and CMG control software.

The experience gained during the performance of the preceeding programs formed the technological base for the present study from which the preliminary determination of the floated pallet control system was derived.

1.4 Method of Approach and Principal Assumptions - The approach followed in this study throughout was to make use of applicable results and expertise obtained in previous programs. A primary consideration in the selection of the CMG actuator was the availability of developed hardware in order to obtain a cost effective system. Required software was derived from existing software packages and consisted only of items required to support the pointing performance evaluation.

Evaluation of the pointing accuracy was accomplished through the use of a hybrid computer. The use of the hybrid machine was indicated primarily because of the selection of a digital CMG control law but also because it enabled the simulation of the primary A/D and D/A interfaces between the dynamics of the vehicles and actuators and the flight control system allowing some evaluation of the effects of quantization in the performance evaluation.

The orbiter as defined in mid-1974 along with pallet designs of the latter part of 1974 were the vehicles for which the control system was defined. Both the orbiter and pallet were modeled as rigid bodies. For the purposes of this study such items as sensor noise, frequency characteristics, biases and drifts were neglected.

1.5 Basic Study Output and Significant Results - The results and conclusions of the pointing performance study are listed below:

a. The CMG system is sized to allow continuous pointing for one orbit under the worst case XIOP gravity gradient momentum accumulations.

b. The CMG system selected consisted of four double gimbal CMGs of the type used on the Skylab ATM, modified to allow unlimited gimbal freedom.

c. The vehicle control law used is a rate plus position plus position integral formulation. The CMG control law used is an optimal pseudo-inverse law giving decoupled vehicle control while minimizing CMG gimbal rates.

d. A comprehensive model of the CMG actuator including internal compliances, friction levels, dead zones and servo nonlinearities was developed to evaluate actual characteristics of the actuator.

1.6 Study Limitations - This study was geared to the determination of a bound on the pointing accuracy of the floated pallet concept using a CMG control system. Although the pointing stability achievable by the CMG system selected has been determined, the pointing performance that could ultimately be obtained would require a more comprehensive simulation for its determination. This simulation could include vehicle flexibility, CMG vibration characteristics, and adequate representation of disturbances of all types. A more accurate determination of the pointing stability achievable by the CMG system is desirable since it would have a very strong effect on the type and complexity of the required experiment integration equipment and pointing devices. This in turn can appreciably effect the overall cost of the shuttle experiment program.

Although trade studies were performed to select a candidate CMG system configuration from several alternatives, they did not constitute a major portion of the study and hence were top level in nature. When the design of an actual CMG system for the pallet is contemplated, considerably more effort would be required in trading various candidate CMG system configurations in order to determine the optimum configuration that would meet overall pallet/orbiter requirements in a cost effective manner. Mass characteristics should be updated to reflect the present configurations. Additionally the latest experiment payloads slated to fly in a sortie mode should be examined in order to better ascertain and update the requirements placed upon the vehicle by these experiments.

Finally, software required to implement the vehicle control system was not considered beyond the point of specifying basic control laws. Software required to accomplish momentum management in particular should be considered in the selection of a CMG actuator cluster based on detailed mission requirements, since the momentum storage capability essentially determines the number of actuators. By using knowledge of vehicle attitudes together with biasing of the actuator momentum states, the possibility exists of accomplishing some missions with fewer actuators than specified here, allowing a corresponding increase in payload weight.

1.7 Suggested Additional Effort - The following additional investigations affecting the floated pallet control system are suggested:

a. Review the instruments and payload experiment combinations which are candidates for the floated pallet to revise and update mission requirements as they affect the total control loop.

b. Investigation of the pointing accuracy realizable when flexible body dynamics, CMG vibration propagation and non-ideal sensors are included in the analysis. This would affect the design and specification of instrument pointing devices independent of the primary control loop.

c. Define candidate CMG control system configurations including sensors that could meet pallet mission requirements. Perform indepth trade studies between the various CMG control system configurations in order to determine the optimum CMG configuration that will meet overall mission requirements in a cost effective manner. These studies should include detailed hardware trade-offs with respect to size, weight, power consumption, reliability and cost as well as the impact various CMG configurations have on software complexity and overall software cost. In addition candidate types of control logic (e.g., CMG gimbal rate control laws, singularity avoidance laws, etc.) required to satisfactorily manage the CMG control system should be evaluated from the standpoint of software complexity and required computer capacity for implementation as well as overall performance. These software trades will be of key significance in determining whether a dedicated computer or the central orbiter computer would be used to drive the chosen CMG system configuration.

2. SUMMARY

The floated pallet definition study consisted of three related but separate studies. The first was an evaluation of alternate pointing systems for orbiter experimental instrumentation, the results of which are presented in volume I of this final report. The second was the pallet pointing performance study treated in this volume II. The third was a hardware conceptual design study including pallet suspension and retention systems, experiment erection, CMG mounting, etc., with results presented in volume III of this report. Figure 2-1 is a diagram of the logical flow of activity during the performance of the pointing performance study.

The basic requirements under which this study was performed are shown as block 0 on the diagram. The contract statement of work defines all tasks and schedules. Input data for the study included baseline shuttle data, particularly payload interface information required for pallet mounting and mass properties. Pallet data included mass properties, structural and dimensional data and typical experiment layouts. The mission requirements applicable to this study included orbital parameters, vehicle attitudes and typical experimental constraints. The pointing requirements included stated pointing accuracies, stability rates and associated parameters, control loop characteristics desired and some typical disturbance profiles under which control loop operation was to be investigated. This material is discussed in sections 3 and 4 of this volume.

The pointing performance study was initiated with block 1, the CMG Selection Trade Studies. The basic mission requirements and vehicle mass properties were translated into CMG system requirements such as torque levels, momentum storage, redundancy and actuator bandwidths needed to meet the overall study requirements with results given in section 5. Next, the industry was surveyed for available or nearly available CMG actuators which could meet the cluster requirements. The candidate CMGs were traded with respect to size, weight, power, and cost on an actuator and cluster basis with both single and double gimbal actuators considered. From this survey, the CMG actuator and cluster configuration to be used throughout the study were defined. This portion of the study is detailed in section 6 of this volume.

In parallel with the hardware studies presented in volume III a control system study was performed and shown as blocks 2, 3, and 4. Initially a complex nonlinear CMG actuator model including internal compliances, frictional characteristics, deadbands, and shock-mount characteristics was derived and programmed for analog simulation in order to evaluate the actuator characteristics, in particular

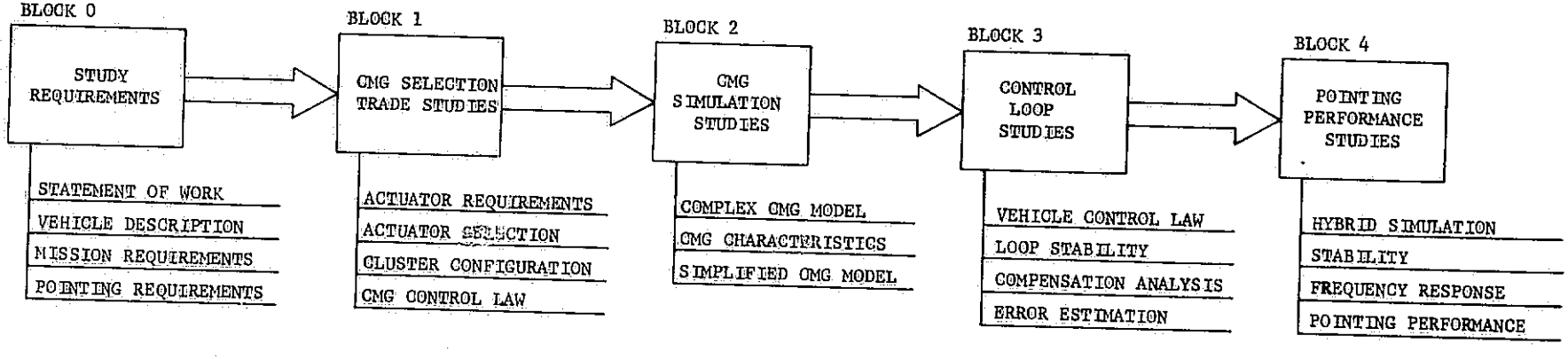

Figure 2-1. Logical Flow of the Pointing Performance Evaluation

the frequency response. At the same time the model was simplified as far as possible while retaining all significant nonlinearities. This material is given in section 7. The control loop studies represented by block 2 are presented as section 8 of this report and included analytic studies to determine single axis loop stability, provisional gain selections, compensation analysis and determination, and linear error analysis. The actual pointing performance study of block 3 was initiated with the definition of a three axis hybrid simulation model assuming rigid body dynamics for the shuttle and pallet, the pallet suspension characteristics, the nonlinear shockmounted CMG models derived earlier and the various control laws and compensations as outlined in section 8. Using this model, the pointing performance that could be achieved with the selected CMG actuators was studied, including response to short period (man-motion) and long period (gravity gradient) disturbance profiles with emphasis on the amplitude of limit cycles incurred, the conditions of their occurence and their variations as a function of CMG parameter variation. The results of the pointing performance study are shown and discussed in section 10 of this volume.

3. VEHICLE DESCRIPTION

3.1 Space Shuttle System Description - There are three main components which comprise the Space Shuttle Flight System; the orbiter, an external tank containing the ascent propellants to be used by the orbiter main engines, and two Solid Rocket Boosters (SRBs). The Space Shuttle Flight System is shown in figure 3-1. The SRBs and the orbiter main engines fire in parallel, providing thrust for lift-off. The SRBs are jettisoned when the fuel is exhausted, and the orbiter main engines continue firing until the vehicle reaches the desired suborbital conditions where the external tank is jettisoned. At this time the Orbital Maneuvering Subsystem (OMS) is fired to place the orbiter in the desired orbit.

The orbiter portion shown in figure 3-1 is a reusable vehicle which delivers and retrieves payloads, conducts orbital operations, and returns to a land base in a manner similar to that of an aircraft. Typical orbital missions are designed to operate for a duration of up to 7 days, however, orbiter design will not preclude mission of up to 30 days being accomplished.

3.2 Orbiter/Pallet System - Payloads are carried by the orbiter in the payload bay (figure 3-1). The payload used for this study is a floated pallet which is connected to the orbiter through vibration isolators. Both the pallet and orbiter segments are considered to be rigid bodies. Figure 3-2 is an overall view of the orbiter/pallet combined configuration.

Each isolator suspension point is assumed to exhibit linear compliance, viscous damping and friction along each axis with no rotational effects or cross-coupling. The design goal of the suspension is to have uncoupled rotational and translational isolation with equal natural frequencies.

Mass properties of the orbiter/pallet configuration are given in table 3-1. All center-of-mass locations are given referenced to the Inertial (I) coordinate system, which has its origin located at the nose of the external tank. Figure 3-3 shows the location of the orbiter with respect to the I coordinate system. As shown, the centerline of the payload bay is 400 inches above the inertial axis. Figure 3-4 shows the relationship of all coordinate systems to the Inertial (I) system.

3.2.1 Orbiter - Once the orbiter has reached the desired orbit, attitude control is maintained by the Reaction Control System (RCS) or by some control mechanism which has been placed in the payload bay. Through use of the RCS system, the orbiter is capable of

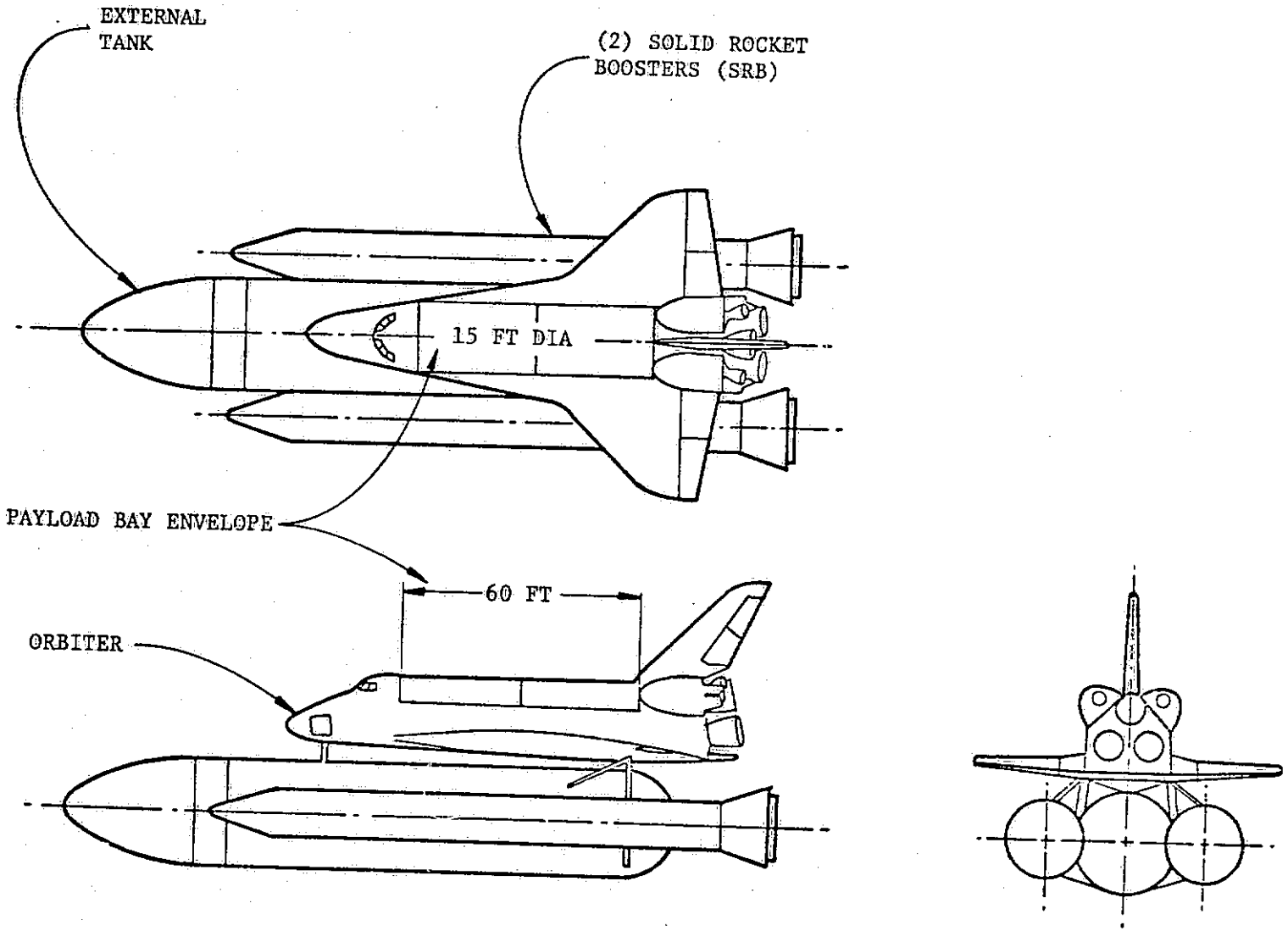

Figure 3-1. Space Shuttle Flight System

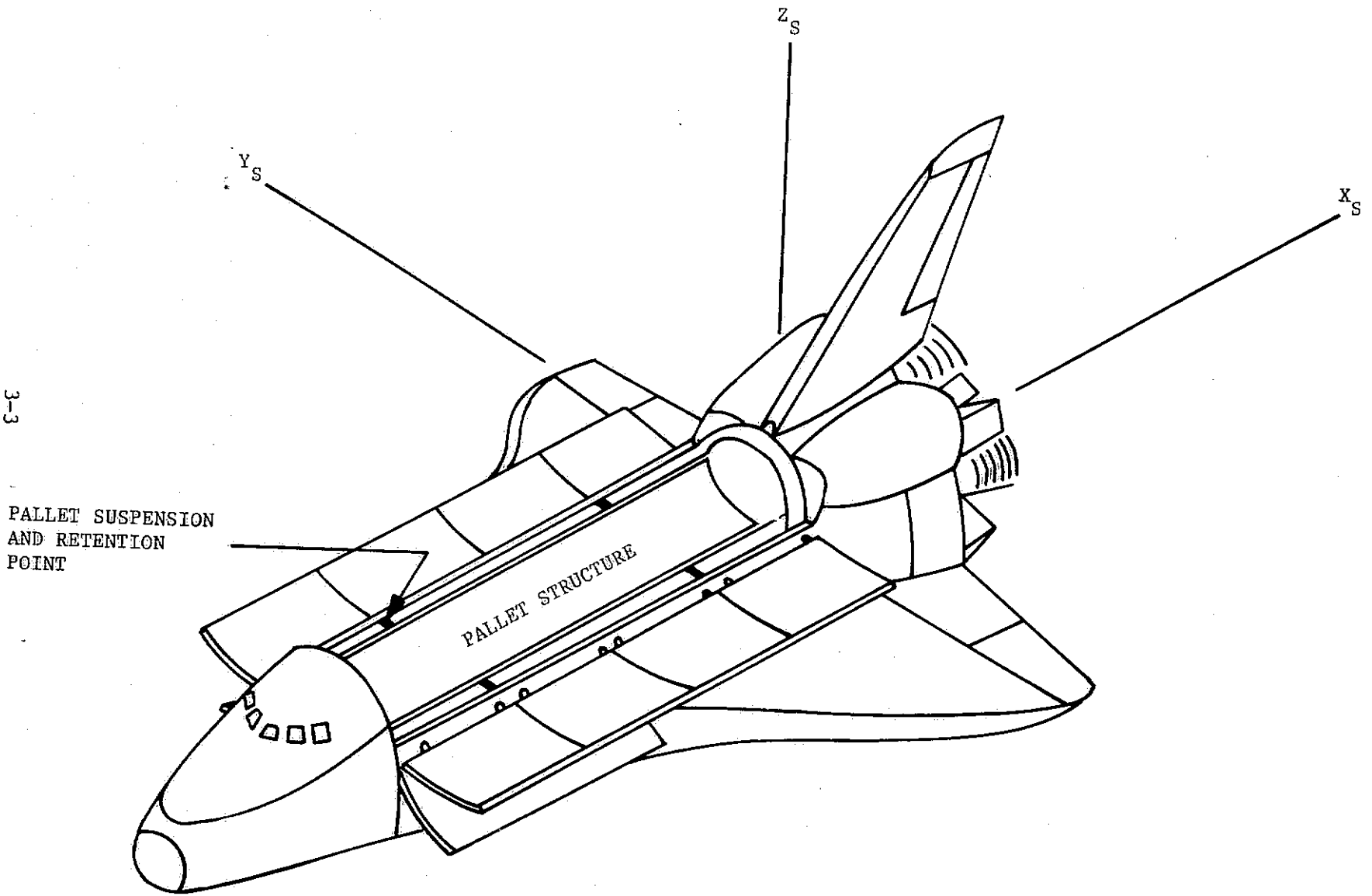

Figure 3-2. Orbiter/Pallet Configuration

Table 3-1. Orbiter/Pallet Vehicle Mass Properties

Mass = 82,394 kg	
Center-of-Mass wrt I Coordinate System $(27.97, 0.0027, 9.54)^T$ meters	
I_{xx}=1,010,359 kg-m^2	I_{xy}=-9,490.8 kg-m^2
I_{yy}=7,400,759 kg-m^2	I_{xz}=266,419 kg-m^2
I_{zz}=7,614,979 kg-m^2	I_{yz}=-3,118 kg-m^2
$\Delta I_x \triangleq I_{zz} - I_{yy}$=214,220 kg-m^2	
$\Delta I_y \triangleq I_{xx} - I_{zz}$=-6,604,620 kg-m^2	
$\Delta I_z \triangleq I_{yy} - I_{xx}$=6,390,400 kg-m^2	

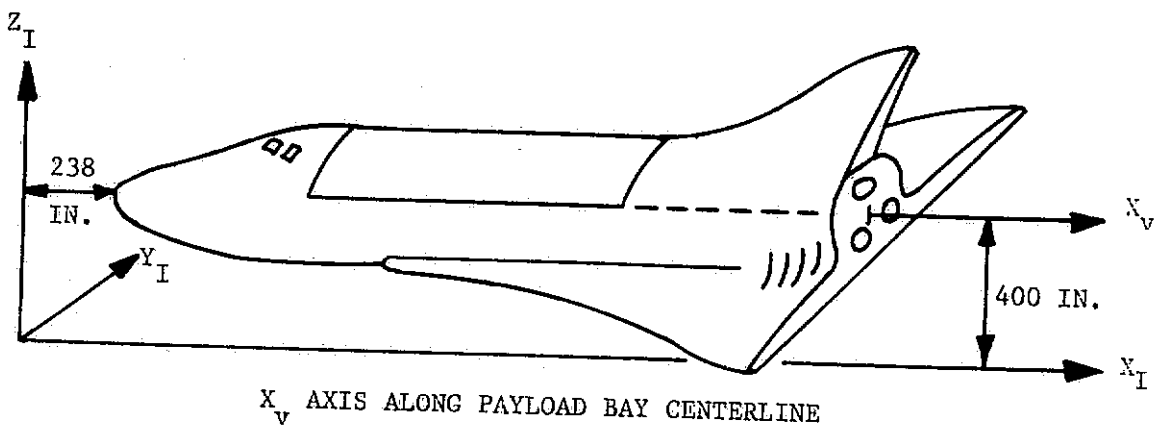

Figure 3-3. Orbiter Related to the Inertial Coordinate System

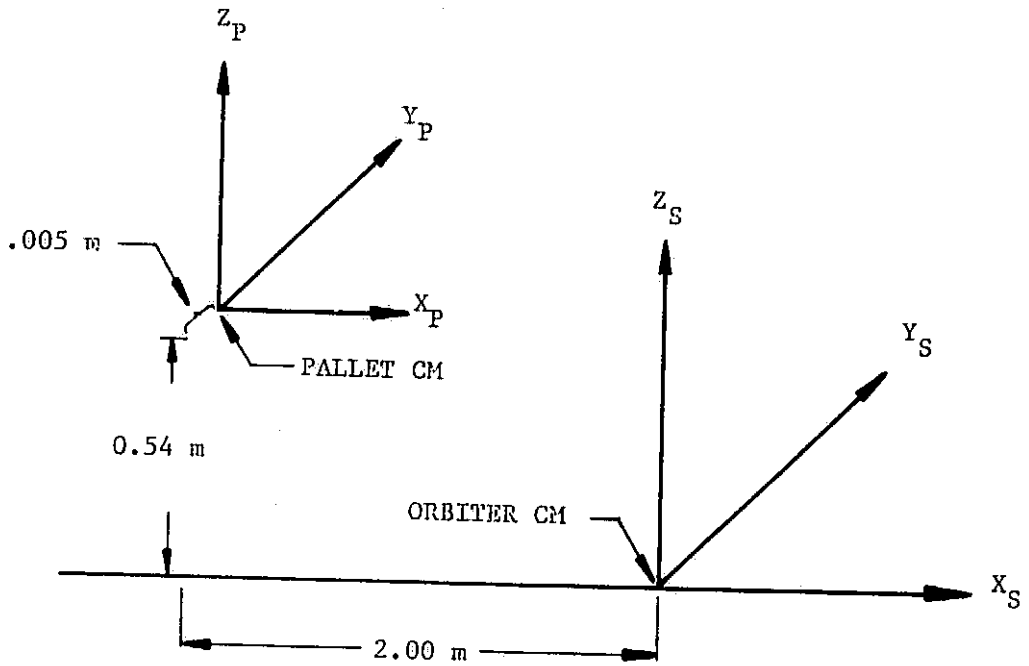

LOCATION OF PALLET CM wrt ORBITER CM

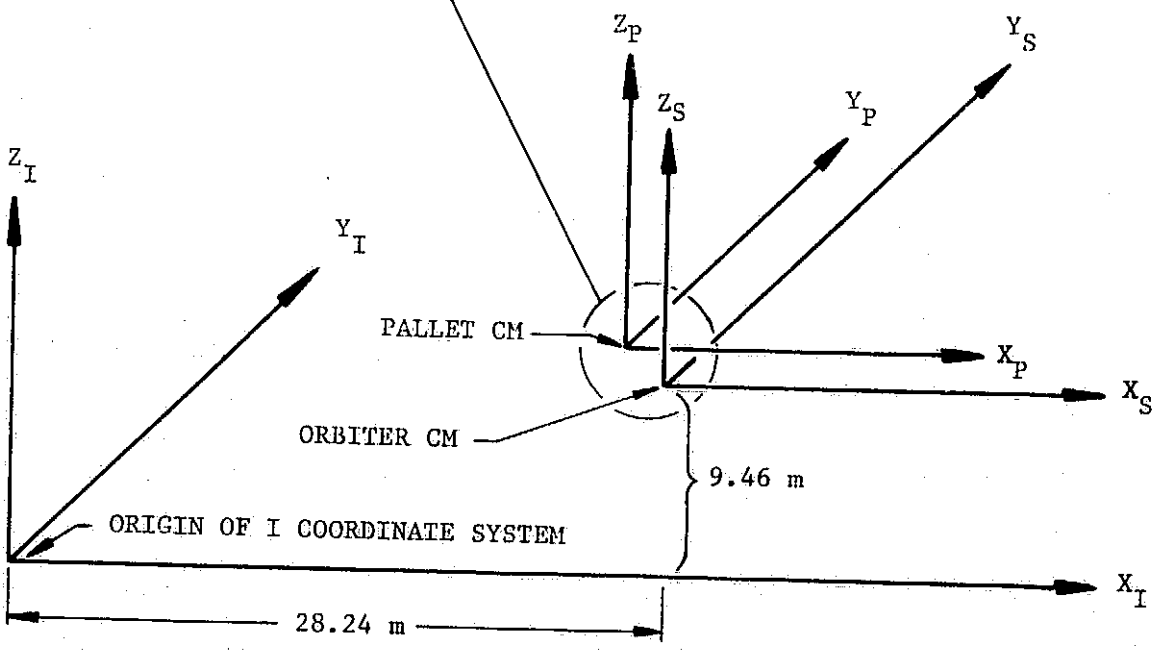

LOCATION OF ORBITER CM wrt I SYSTEM

Figure 3-4. Coordinate System Location

achieving and maintaining any attitude to a certain degree of accuracy. If more accurate pointing is required for a particular payload, then pointing capability must be included within the payload, this being the case for this particular study. The method chosen to increase pointing capability for the present study is to control the pointing of the pallet via use of the CMG cluster.

Mass properties for the orbiter are defined about the orbiter (S) coordinate system and are given in table 3-2. Figure 3-4 shows the orbiter center-of-mass location with respect to the I system.

3.2.2 Pallet - Experiment equipment will be mounted on the pallet. When performing experiments, it is undesirable to allow disturbances caused by orbiter RCS firings. Therefore, the pallet will be controlled by the CMG cluster which provides pallet pointing to within one sec. Since the orbiter will also be controlled by the CMGs via the isolators, the RCS deadband should not be exceeded and no firings should occur.

The pallet will consist of mechanically coupled segments and the pallet attached to the orbiter through the isolators. There will be a separate retention system which will support the pallet during launch. Once in orbit, the retention system will be disengaged and the pallet will float on the isolators.

Figure 3-5 is a pictorial diagram of the pallet. A detailed description of the pallet along with a detailed analysis of suspension systems is given in volume III of this final report.

Mass properties for the pallet are defined in table 3-3 with respect to the P system and the location of the pallet center-of-mass is shown in figure 3-4.

3.3 CMG Control System - The CMGs are required to provide the pointing control of the pallet and to absorb the momentum buildup due to GG torque. The CMGs are mounted on the pallet through isolators which provide a bandpass of 20 Hz with damping of 0.15. The purpose of these isolators is to prevent high frequency disturbances generated by the CMGs from reaching the pallet. Volume III gives a detailed discussion of the CMG mounting system, while the CMG control system is discussed in other sections of this document.

3.4 Coordinate System Definition - All vehicle coordinate systems are defined nominally with the X axis directed to the rear of the orbiter, the Z axis pointing out of the payload bay and the Y axis completing the right-handed system.

Table 3-2. Orbiter Mass Properties

Mass = 71,419 kg	
Center-of-Mass wrt I Coordinate System $(28.24, 0.005, 9.46)^T$ meters	
J_{xxs}=985,683 kg-m^2	J_{xys}=-8,135 kg-m^2
J_{yys}=7,219,756 kg-m^2	J_{xzs}=256,250 kg-m^2
J_{zzs}=7,386,523 kg-m^2	J_{yzs}=-4,067 kg-m^2

Table 3-3. Pallet Mass Properties

Mass = 10,975 kg	
Center-of-Mass wrt I Coordinate System $(26.22, 0.01, 10.05)^T$ meters	
J_{xxp}=21,293 kg-m^2	J_{xyp}=-991 kg-m^2
J_{yyp}=138,821 kg-m^2	J_{xzp}=-1,231 kg-m^2
J_{zzp}=135,426 kg-m^2	J_{yzp}=903 kg-m^2

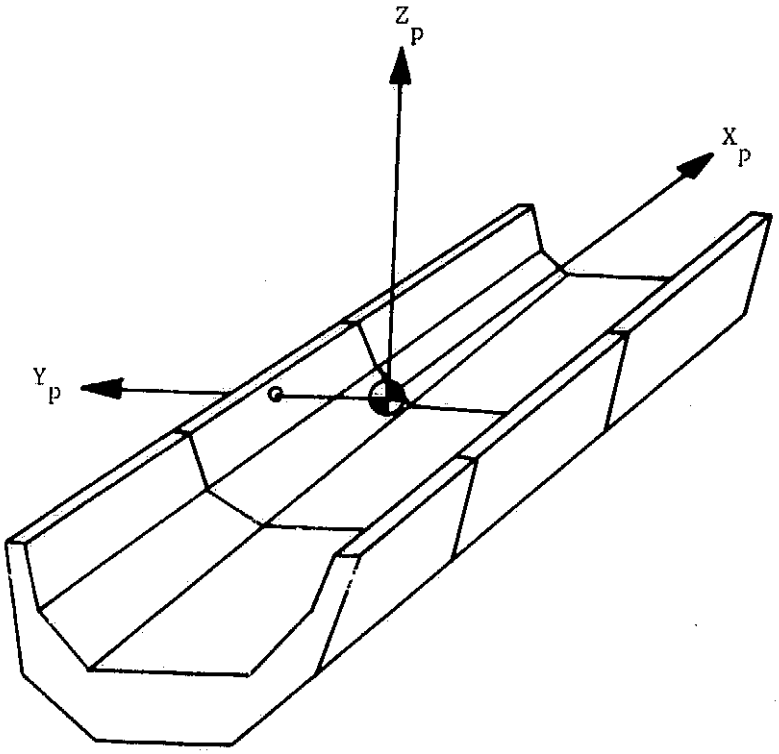

Figure 3-5. Pallet System

3.4.1 Inertial Pointing System (X_I, Y_I, Z_I) - This system is based on the physical system by which all shuttle components are defined. The origin of this coordinate system is fixed at the nose of the disposable boost tank. All coordinate systems used in this study are referenced to this system either directly or indirectly. It is used in this study to define the inertially held attitude. The X_I axis is 10.16 m (400 in.) below the shuttle payload bay centerline (figure 3-3) and the I system origin is 6.045 m (238 in.) ahead of the orbiter nose.

3.4.2 Orbiter System (X_S, Y_S, Z_S) - This system origin is located at the orbiter center-of-mass. The origin of the system is translated from the origin of the inertial system by the vector $\vec{\rho}_S$. Equation 3-1 gives the rotational transformation from the I coordinate system to the S coordinate system through the angle $\vec{\theta}_S$.

$$[{}_S T_I] = \begin{bmatrix} 1 & \theta_{Sz} & -\theta_{Sy} \\ -\theta_{Sz} & 1 & \theta_{Sx} \\ \theta_{Sy} & -\theta_{Sx} & 1 \end{bmatrix} \tag{3-1}$$

3.4.3 Pallet System (X_P, Y_P, Z_P) - The origin of the pallet coordinate system is located at the center-of-mass of the pallet. The pallet system is translated from the I coordinate system by the vector $\vec{\rho}_P$. The transformation from the I to the P coordinate system is given by equation 3-2 through the angle $\vec{\theta}_P$.

$$[{}_P T_I] = \begin{bmatrix} 1 & \theta_{Pz} & -\theta_{Py} \\ -\theta_{Pz} & 1 & \theta_{Px} \\ \theta_{Py} & -\theta_{Px} & 1 \end{bmatrix} \tag{3-2}$$

3.4.4 P'-System - Since the CMGs will not be aligned with one another, and the torque output from the CMG/shockmount is defined along the CMG base coordinate system, a set of transformations is required to relate the individual torque outputs to the pallet (P) coordinate system. A P' coordinate system is defined to make the necessary transformations. Each of the P' systems is centered at the center-of-mass of one of the CMGs. The relationship between the pallet (P) and P' system is discussed further in section 6.

3.4.5 CMG System - Identical CMGs are used in the cluster. The derivation of the CMG model is given in detail in section 7. All coordinate systems associated with the CMG are defined in section 7 and the torque output from the CMG/shockmount system is defined in the P' coordinate system.

4. MISSION REQUIREMENTS

In this section typical floated pallet mission requirements are defined that influence the conceptual design of the CMG attitude control system. These requirements are utilized in succeeding sections of this report to size and configure the CMG actuator cluster and to accomplish the preliminary design of the control system. The data discussed in this section is based in part on requirements of the dedicated solar sortie and the combined astronomy missions projected for the floated pallet concept. The balance of the information is baseline data extracted from the contract statement of work and sources related to the statement of work.

4.1 Vehicle Orbit - For the purposes of this study a circular orbit of 500 km (270 n.mi.) will be used. The orientation of the orbit in space does not impact this study in any way.

4.2 Vehicle Attitudes - Both sortie mission payloads considered for the floated pallet require inertial or nearly inertial attitudes which allow individual instruments to be directed toward stellar targets or toward the sun. The vehicle attitudes considered for this study are: 1) an inertial attitude with the composite vehicle X axis perpendicular to the orbital plane (XPOP) and 2) an inertial attitude with the X axis constrained to lie in the orbital plane (XIOP).

The astronomy and solar physics payloads can be pointed and stabilized using either of the above attitudes. These two inertial attitudes impact with the designs of the CMG attitude control and experiment pointing systems in different ways. For an inertial XPOP attitude, the vehicle's Y and Z axes are constrained to the orbital plane thus reducing the spacecraft's rotational degrees-of-freedom from three to one. The vehicle can be rotated about only the X axis. In order to permit a hemispherical experiment coverage capability at least one wide angle gimbal must be added to the experimental instrument to provide the second degree-of-freedom required.

For an inertial XIOP attitude, the vehicle's X axis is constrained to the orbital plane thus reducing the vehicle's rotational degrees-of-freedom from three to two. The vehicle can be rotated about the X axis and an axis normal to the orbital plane. Because the vehicle still has two rotational degrees-of-freedom, the experiment package can be pointed anywhere in the celestial sphere hardmounted to the spacecraft, i.e., no wide angle gimbal is required. The cost of this additional rotational degree-of-

freedom for an XIOP attitude is a large increase in the CMG momentum storage requirement per orbit over that required by an XPOP attitude. This increase momentum storage requirement significantly impacts the size of the CMG control system; it can be directly related to additional CMGs required and more frequent CMG momentum desaturation "dumps." Depending on the experiment payload and its pointing and stabilization requirements, one of these two inertial attitudes may be required or exhibit certain characteristics that are particularly attractive for a specific mission or class of missions.

4.3 Vehicle Maneuver Guidelines - For the purpose of this study it has been specified that the CMG control system will not be required for any gross vehicle maneuvers. Larger angle maneuvers will be accomplished (if required) by the orbiter reaction control system. Small angle maneuvers required for momentum desaturation will, however, be performed with CMG system.

4.4 Pallet Pointing Requirements - The floated pallet under the control of the CMG system should provide a pointing accuracy of 1 sec. Since all instruments will be pointed along the pallet Z axis or at some specified orientation with respect to that axis, the pallet pointing will be evaluated by considering the rotational displacement of the Z axis with respect to an arbitrary inertial direction. The pointing error for any instrument offset from the Z axis can be derived from the Z axis pointing error.

4.5 Pallet Control Loop Requirements - The design goal for the pallet control loop is a system with a -3 db bandwidth of 2 Hz. The pallet loop consists of ideal sensors, the vehicle and CMG control laws, the CMG actuator cluster and of course the pallet dynamics.

5. CMG SYSTEM REQUIREMENTS

CMG torque and momentum storage requirements are defined for two shuttle pointing orientations, i.e., vehicle X axis perpendicular to the orbital plane (XPOP) and vehicle X axis in the orbital plane (XIOP). These requirements are based on the appropriate gravity gradient disturbances with consideration given to the effects of aerodynamics, internal motion, and venting disturbance torques. Consideration is also given to the effects of vehicle positioning misalignments, principal axis misalignments, and gravity gradient desaturation maneuvering on the torque and momentum requirements.

5.1 Orbiter/Pallet Mass Properties - The orbiter and pallet mass properties to be used in this study are summarized in tables 3-2 and 3-3 of this volume. The mass properties are defined with respect to axis systems shown in figure 3-4. Using the basic mass properties of the two components, the center of mass of the shuttle/pallet combination can be determined, then the inertia tensor of the combination can be computed. The mass properties of the composite vehicle are given in table 3-1.

Since the products of inertia are small compared to the moments of inertia about the vehicle axis, the misalignment of the principal axes can be estimated quite closely by assuming that the principal axis inertia tensor has the same values as the main diagonal of the vehicle axis inertia tensor and further assuming that a small angle rotation $\vec{\varepsilon}_p=(\varepsilon_{xp},\varepsilon_{yp},\varepsilon_{zp})^T$ about the vehicle axes will define the transformation from vehicle to principal axis coordinates.

$$[{}_pT_v]=\begin{bmatrix} 1 & \varepsilon_{zp} & -\varepsilon_{yp} \\ -\varepsilon_{zp} & 1 & \varepsilon_{xp} \\ \varepsilon_{yp} & -\varepsilon_{xp} & 1 \end{bmatrix}$$

Then, the inertia tensor in vehicle coordinates $[J_v]$ can be written as:

$$[J_v]=[{}_vT_p]\,\mathrm{diag}\{I_{xx},I_{yy},I_{zz}\}[{}_pT_v]$$

Performing the similarity transformation of the above and solving for the components of $\vec{\varepsilon}_p$ then gives:

$$\varepsilon_{xp} = -\frac{I_{yz}}{\Delta I_x} = 0.014557 \text{ rad} = 0.834° \tag{5-1}$$

$$\varepsilon_{yp} = -\frac{I_{xz}}{\Delta I_y} = 0.040338 \text{ rad} = 2.31° \tag{5-2}$$

$$\varepsilon_{zp} = -\frac{I_{xy}}{\Delta I_z} = 0.001485 \text{ rad} = 0.0851° \tag{5-3}$$

The composite vehicle mass properties to be used in the CMG sizing can be taken directly from table 3-1 and equations 5-1, 5-2, and 5-3, and it should be stressed that the angles of these equations are defined as rotations about the vehicle axes.

5.2 Torque and Momentum Requirements - The disturbances acting on the vehicle which can be considered in the CMG sizing include gravity gradient, aerodynamic, internal motion, and vehicle venting torques. For the purposes of this report vehicle venting will not be considered due to lack of definition. In addition, it should be noted that analyses of the Skylab missions indicate that typical venting disturbances do not significantly affect the CMG torque requirements and are rarely a problem in momentum storage (reference 1). Prior studies of shuttle systems (reference 2) indicate that peak aerodynamic torques are an order of magnitude smaller than the peak gravity gradient torques for XIOP attitudes and of a similar magnitude for XPOP attitudes. Aerodynamic effects will thus be approximated by the appropriate factors applied to the gravity gradient torques for each attitude. Short period internal mass motion disturbances will not affect the cluster sizing, although they are considered in detail as they affect vehicle pointing in subsequent analyses.

The gravity gradient torque acting on a vehicle is given by:

$$\vec{T}_{gg} = 3\omega_o^2 \begin{bmatrix} a_y a_z \Delta I_x \\ a_x a_z \Delta I_y \\ a_x a_y \Delta I_z \end{bmatrix} \tag{5-4}$$

Where the a_i, $i=x,y,z$ are the components of the unit vector along the local vertical resolved into vehicle coordinates, the ΔI_i are defined in table 3-1, and the products of inertia are ignored. This is equivalent to stating the sizing will be performed in the principal axis system. The basic sizing will be accomplished with this assumption, then the effects of angular offsets with respect to the basic attitudes will be developed to investigate the effect of principal axis misalignments and pointing offsets. In all cases the circular orbit of 500 km will be used, for which the orbital rate is:

$$\omega_o = 1.107 \times 10^{-3} \text{ rad/sec} \tag{5-5}$$

Another significant contribution to torque and momentum storage requirements is vehicle maneuvering. Although any gross vehicle maneuvers will be accomplished without the use of the CMG system, these maneuvers will be examined as to their effect on torque and momentum requirements. A minimum desaturation period of one-third orbit will be considered with a small angle desaturation scheme assumed.

5.2.1 <u>X Axis Perpendicular to the Orbital Plane (XPOP)</u> - The XPOP orientation is advantageous in the sense of minimizing torque levels and accumulated momentum, however, to achieve full pointing capability the experimental payload must have a wide angle degree of freedom about one of the axes constrained to the orbital plane.

Referring to figure 5-1, it can be seen that for XPOP, the components of the unit vector along the local vertical are:

$$\hat{r} = \begin{bmatrix} a_x \\ a_y \\ a_z \end{bmatrix} = \begin{bmatrix} 0 \\ \cos\omega_o t \\ \sin\omega_o t \end{bmatrix} \tag{5-6}$$

The corresponding gravity gradient torque is obtained from equations 5-4 and 5-6 as:

$$\vec{T}_{gg} = \frac{3}{2}\,\omega_o^2 \begin{bmatrix} \Delta I_x \sin 2\omega_o t \\ 0 \\ 0 \end{bmatrix} \tag{5-7}$$

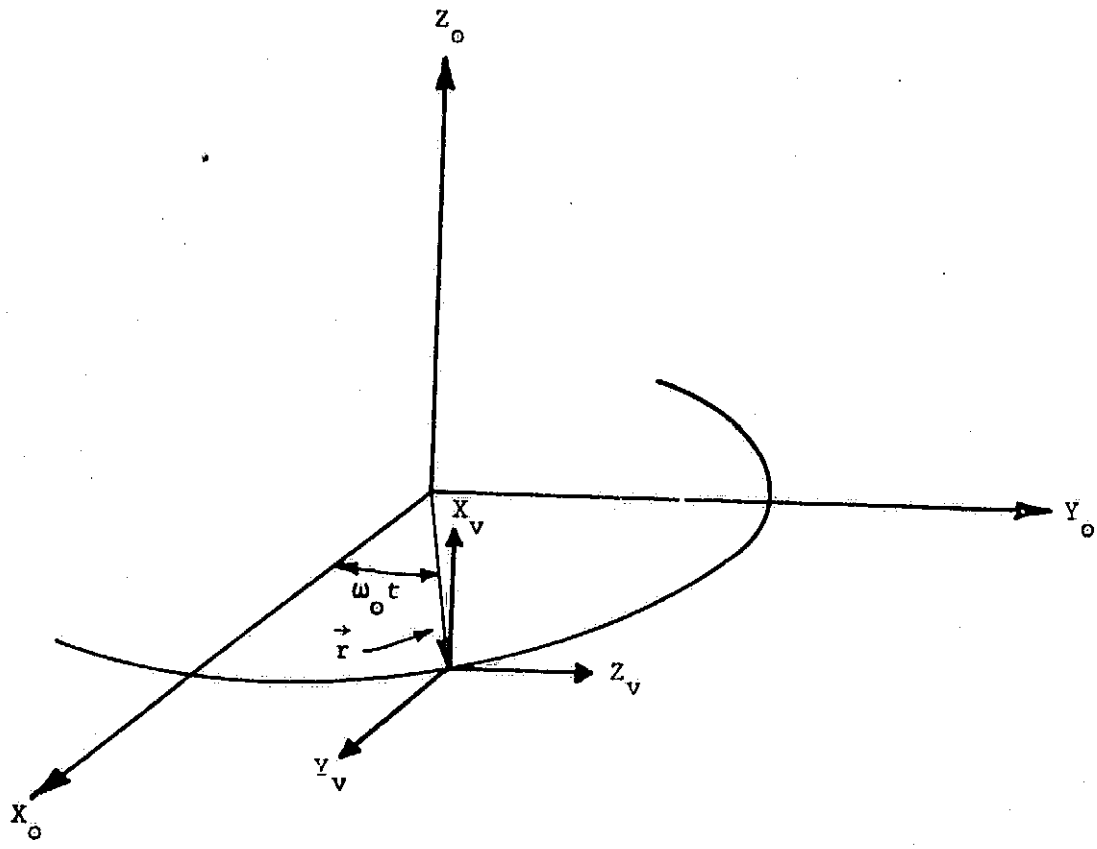

Figure 5-1. XPOP Attitude Geometry

From equation 5-7 it is evident that the peak gravity gradient torque occurs for $\sin 2\omega_o t = \pm 1$, i.e, $\omega_o t = n\pi/4$, n=1,3,5,7. Substituting the numerical values for ω_o and ΔI_x gives the values of peak torques as ± 0.4 n-m at these points for the ideal XPOP attitude. The momentum accumulation as a function of time is the time integral of equation 5-7:

$$\vec{H}_{gg} = \frac{3}{4}\omega_o \begin{bmatrix} \Delta I_x(1-\cos 2\omega_o t) \\ 0 \\ 0 \end{bmatrix} \qquad (5\text{-}8)$$

Examination of eaution 5-8 shows that the momentum accumulation as a function of time is cyclic and therefore bounded, thus ideally no desaturation would be required. The peak momentum accumulation occurs for $\cos 2\omega_o t = -1$, $\omega_o t = \pi/2$ or $3\pi/2$ at which point the magnitude of the accumulation is 355 n-m-sec.

The effect of offsets of the vehicle from the ideal attitude can be determined by defining a small rotation ε_i about each vehicle axis. The components of the unit vector along the local vertical become:

$$\hat{r}_o = \begin{bmatrix} 1 & \varepsilon_z & -\varepsilon_y \\ -\varepsilon_z & 1 & \varepsilon_x \\ \varepsilon_y & -\varepsilon_x & 1 \end{bmatrix} \begin{bmatrix} a_x \\ a_y \\ a_z \end{bmatrix} = \begin{bmatrix} \varepsilon_z \cos\omega_o t - \varepsilon_y \sin\omega_o t \\ \cos\omega_o t + \varepsilon_x \sin\omega_o t \\ \sin\omega_o t - \varepsilon_x \cos\omega_o t \end{bmatrix} \qquad (5\text{-}9)$$

The gravity gradient torque including the offset rotations is thus:

$$\vec{T}^{\,0}_{gg} = \vec{T}_{gg} - 3\omega_o^2 \varepsilon_x \begin{bmatrix} \Delta I_x \cos 2\omega_o t \\ 0 \\ 0 \end{bmatrix} - \frac{3}{2}\omega_o^2 \varepsilon_y \begin{bmatrix} 0 \\ (1-\cos 2\omega_o t)\Delta I_y \\ \Delta I_z \sin 2\omega_o t \end{bmatrix}$$

$$+ \frac{3}{2}\omega_o^2 \varepsilon_z \begin{bmatrix} 0 \\ \Delta I_y \sin 2\omega_o t \\ (1+\cos 2\omega_o t)\Delta I_z \end{bmatrix} \qquad (5\text{-}10)$$

For rotations ε_x there is no effect on the torque magnitude, merely a shift of the values in the orbit by the angle ε_x as can be seen from figure 5-1 and verified from equation 5-10 with $\varepsilon_y=\varepsilon_z=0$. For Y offsets ($\varepsilon_x=\varepsilon_z=0$) the peak torques increase from the ideal values and shift in pairs from the quarter orbit points toward $\omega_o t=\pi/2$ and $3\pi/2$. Figure 5-2 shows the torque magnitude history for one orbit for the ideal attitude and for $\varepsilon_y=1°$, 2°, and 3°. For $\varepsilon_y=1°$ the torque peaks occur at 53.6°, 126.4°, 233.6°, and 306.4° with a magnitude of 0.5 n-m. For 2° and 3° the torque peaks have coalesced at 90° and 270° with magnitudes of 0.85 n-m and 1.27 n-m, respectively. For Z offsets the results are similar with the peaks moving toward the $n\pi$ points of the orbit. For $\varepsilon_z=1°$ the peaks occur at 36.1°, 143.9°, 216.1°, and 323.9° with a magnitude of .5 n-m and for 2° and 3° the peaks occur at 0°, 180°, and 360° with magnitudes of 0.83 n-m and 1.24 n-m, respectively.

The momentum accumulation can be found by taking the time integral of equation 5-10:

$$\vec{H}_{gg}^{\,0}=\vec{H}_{gg}-\frac{3}{2}\omega_o\varepsilon_x\begin{bmatrix}\Delta I_x\sin 2\omega_o t\\ 0\\ 0\end{bmatrix}-\frac{3}{4}\omega_o\varepsilon_y\begin{bmatrix}0\\ \Delta I_y(2\omega_o t-\sin 2\omega_o t)\\ \Delta I_z(1-\cos 2\omega_o t)\end{bmatrix}+\frac{3}{4}\omega_o\varepsilon_z\begin{bmatrix}0\\ \Delta I_y(1-\cos 2\omega_o t)\\ \Delta I_z(2\omega_o t+\cos 2\omega_o t)\end{bmatrix} \quad (5\text{-}11)$$

For X offsets, the momentum remains cyclic and bounded with the same magnitude as the ideal case with the momentum values shifted ε_x in the orbit. For Y and Z offsets, however, a secular component of momentum appears which dominates the cyclic momentum for a 1° offset about either axis. Although the momentum peaks at $\omega_o t=\pi/2$ and $3\pi/2$ for the ideal attitude, the addition of a Y or Z offset of 1° or greater shows only local maxima or an inflection point moving from these positions toward $\omega_o t=\pi$ with the peak momentum occurring at $\omega_o t=2\pi$ with this value representing the net

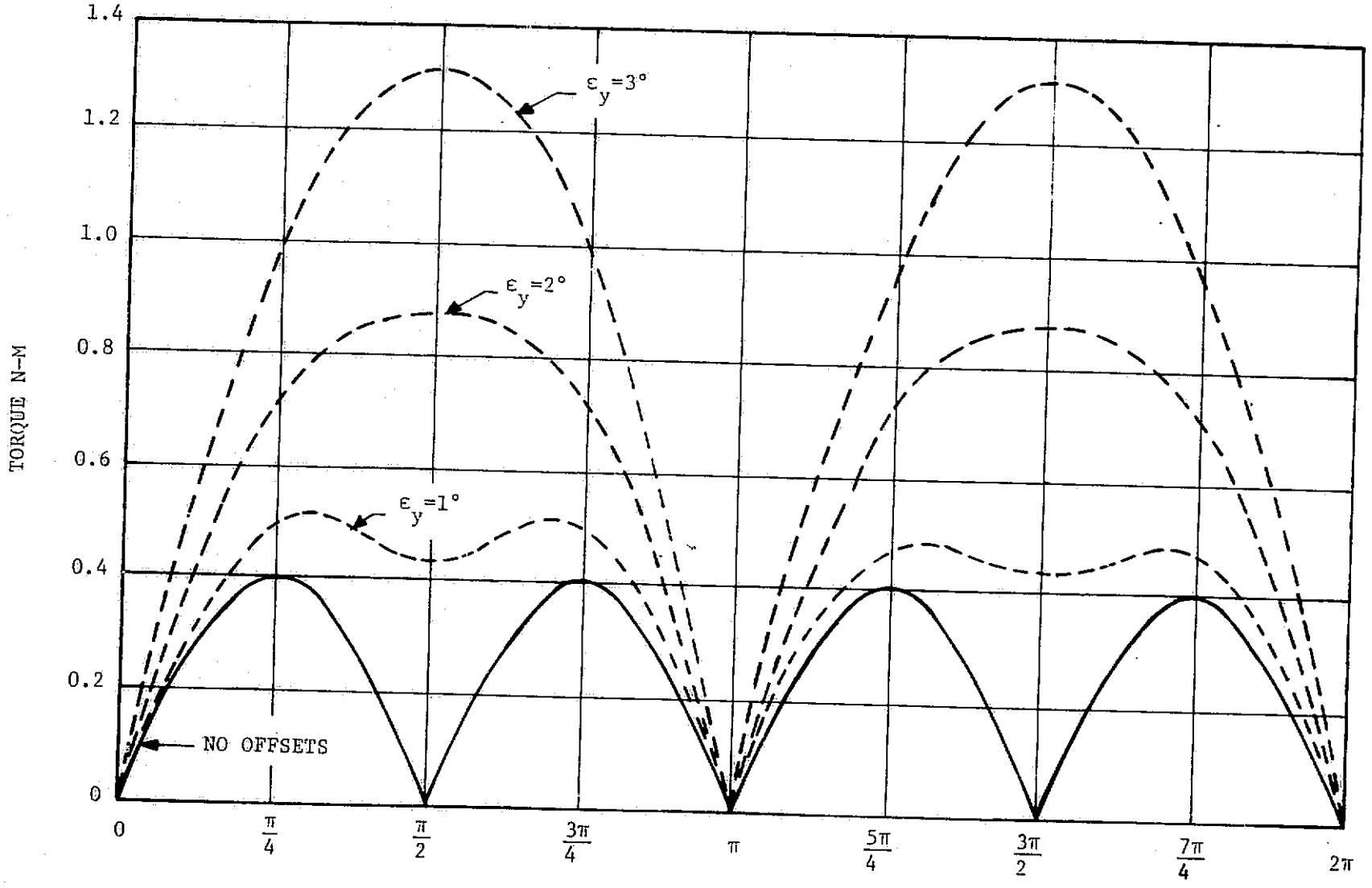

Figure 5-2. XPOP Torque Histories - One Orbit

accumulation per orbit as well. For Y offsets the peak momentum and momentum to be dumped per orbit is 1,200 n-m-sec per degree offset. For Z offsets the corresponding amount is 1,160 n-m-sec per degree offset. For offsets about both Y and Z the momentum accumulation is the root-sum-square of the per axis amounts.

Figure 5-3 is included to indicate the effect of the principle axis offsets on the momentum history if the vehicle geometric axes are used for XPOP. For no offsets, the momentum history is the same as the H_x component of this figure. When the principal angle offsets of eautions 5-1, 5-2, and 5-3 are included in the momentum history, the Y axis momentum dominates due to the large ε_{yp}. The momentum magnitude H is a maximum for $\omega_c t=2\pi$ as described in the previous paragraph.

From information presented in reference 2, the peak aerodynamic torque for XPOP attitudes is on the order of 1.4 n-m with peak transient momentum due to aerodynamics being approximately 1,000 n-m-sec. The net momentum accumulation per orbit is considerably less than this amount.

5.2.2 <u>X Axis in the Orbital Plane (XIOP)</u> - The XIOP vehicle orientation has the advantage of allowing instrument pointing anywhere in the celestial sphere without the need for gimballed payloads with the attendant disadvantage of more severe torque levels and momentum accumulation. With the vehicle X axis constrained to lie in the orbital plane, there always is a rotational degree of freedom about that axis which will be defined as β, $-\pi\leq\beta\leq\pi$, the angle by which the vehicle Y axis is rotated out of the orbital plane. The relation between the vehicle axes and the orbit is shown in figure 5-4. With reference to that figure it can be seen that the coordinates of the unit vector along the local vertical resolved into vehicle coordinates is:

$$\hat{r}=\begin{bmatrix} a_x \\ a_y \\ a_z \end{bmatrix}=\begin{bmatrix} 1 & 0 & 0 \\ 0 & \cos\beta & \sin\beta \\ 0 & -\sin\beta & \cos\beta \end{bmatrix}\begin{bmatrix} \cos\omega_o t \\ \sin\omega_o t \\ 0 \end{bmatrix}=\begin{bmatrix} \cos\omega_o t \\ \cos\beta\sin\omega_o t \\ -\sin\beta\sin\omega_o t \end{bmatrix} \qquad (5\text{-}12)$$

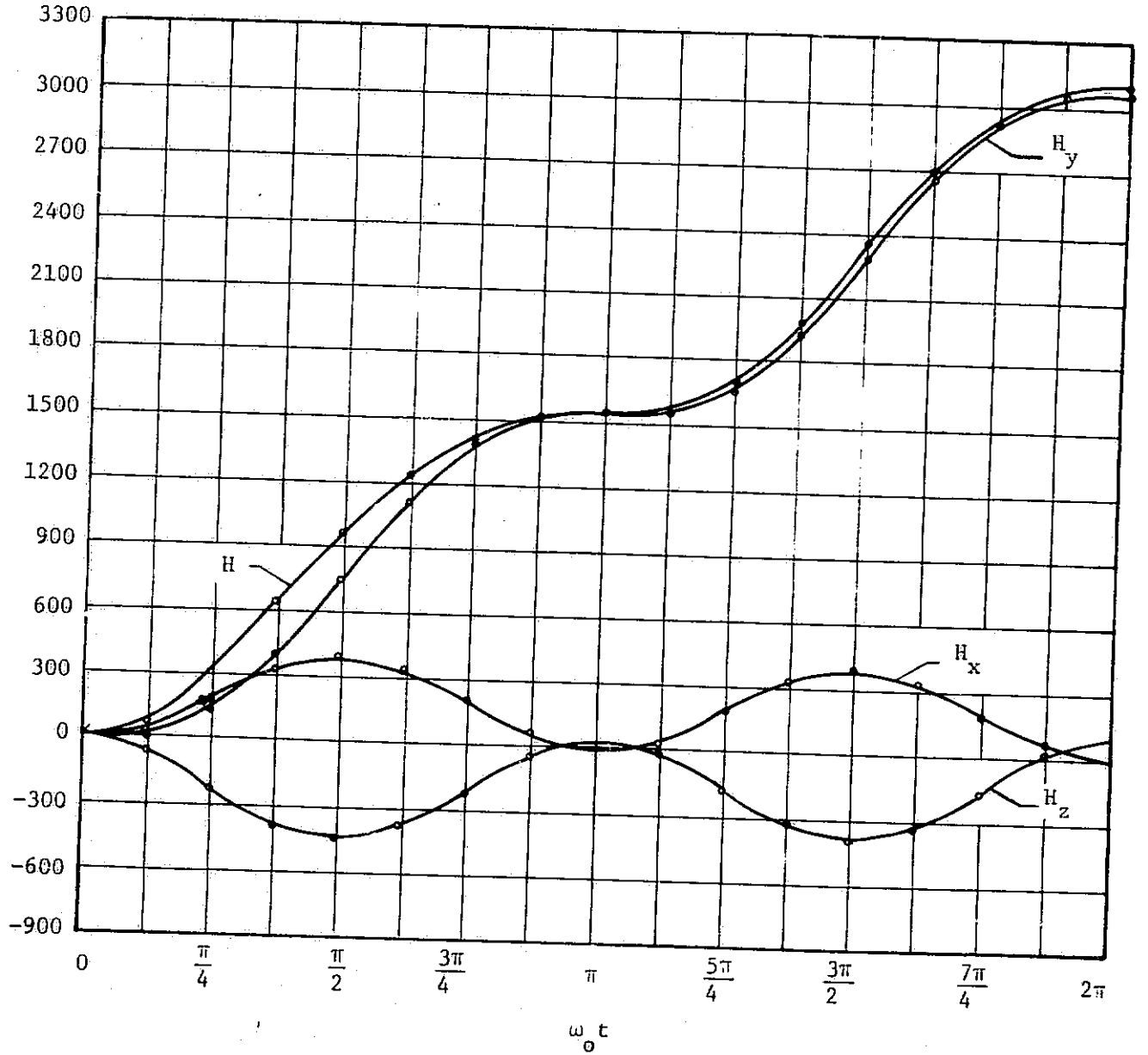

Figure 5-3. XPOP Momentum History With Vehicle Axis Pointing

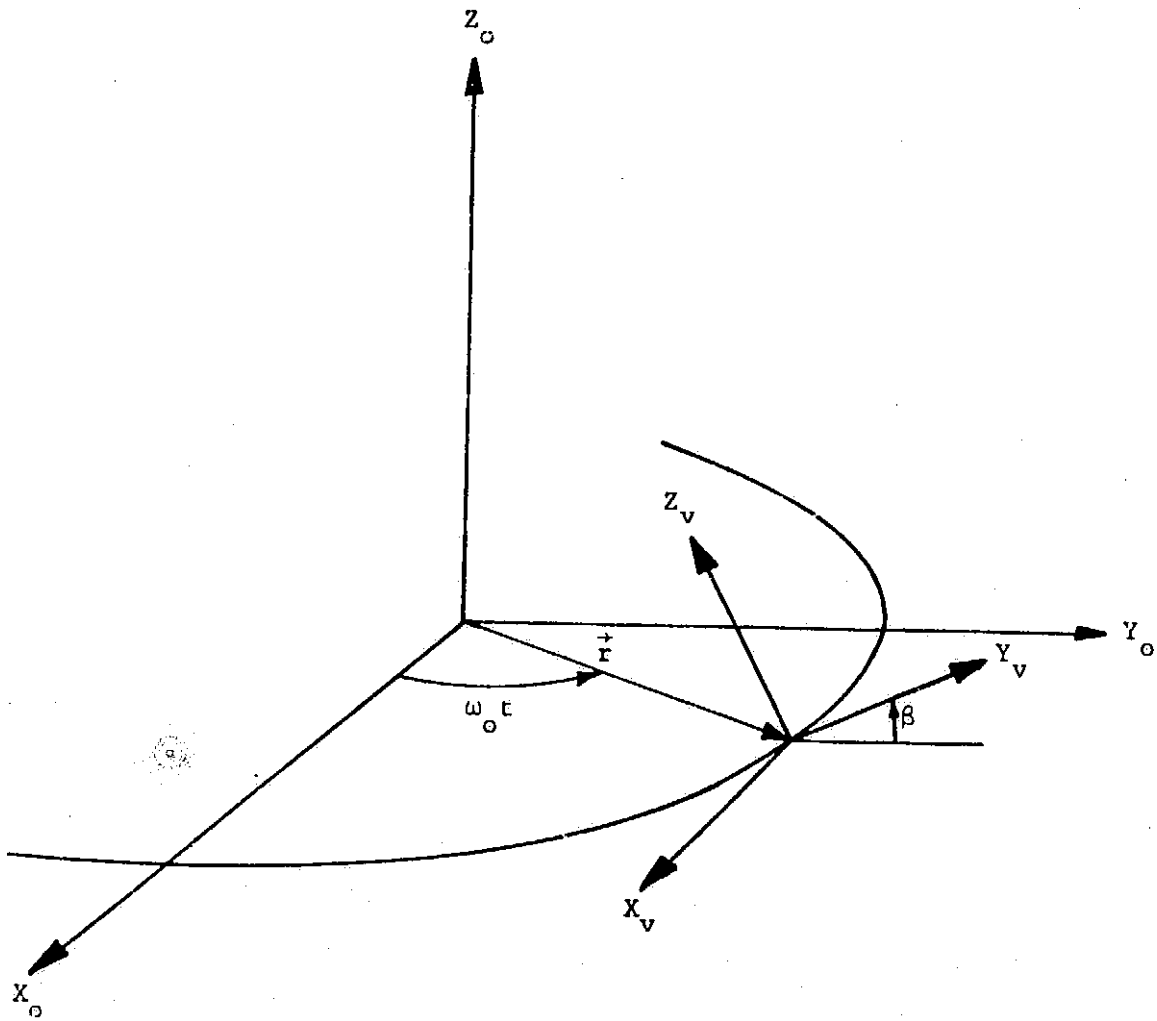

Figure 5-4. XIOP Attitude Geometry

If an offset $\vec{\varepsilon}=(\varepsilon_x,\varepsilon_y,\varepsilon_z)^T$ exists between ideal and actual vehicle attitude the components of the local vertical unit vector can be written:

$$\hat{r}_o=\begin{bmatrix} 1 & \varepsilon_z & -\varepsilon_y \\ -\varepsilon_z & 1 & \varepsilon_x \\ \varepsilon_y & -\varepsilon_x & 1 \end{bmatrix}\begin{bmatrix} a_x \\ a_y \\ a_z \end{bmatrix}=\begin{bmatrix} a_x+\varepsilon_z a_y-\varepsilon_y a_z \\ a_y-\varepsilon_z a_x+\varepsilon_x a_z \\ a_z+\varepsilon_y a_x-\varepsilon_x a_y \end{bmatrix} \tag{5-13}$$

Substituting the components a_i from equation 5-12 into equation 5-4 then yields the gravity gradient torques for the ideal XIOP attitude.

$$\vec{T}_{gg}=\frac{3}{2}\omega_o^2\begin{bmatrix} \frac{1}{2}\sin 2\beta(\cos 2\omega_o t-1)\Delta I_x \\ -\Delta I_y \sin\beta \sin 2\omega_o t \\ \Delta I_z \cos\beta \sin 2\omega_o t \end{bmatrix} \tag{5-14}$$

Substituting the appropriate numerical values for the differences of inertia and the orbital rate then gives:

$$\vec{T}_{gg}=\begin{bmatrix} 0.198\sin 2\beta(\cos 2\omega_o t-1) \\ -12.21\sin\beta\sin 2\omega_o t \\ 11.81\cos\beta\sin 2\omega_o t \end{bmatrix}\ (n\text{-}m) \tag{5-15}$$

Examination of equation 5-15 then indicates that the maximum gravity gradient torque occurs for $\sin 2\omega_o t=\pm 1$, i.e., $\omega_o t=\frac{n\pi}{4}$, n=1,3,5,7. Further, the maximum torque about the vehicle Y axis occurs with $|\sin\beta|=1$, $\beta=\pm\frac{\pi}{2}$ with the value $\vec{T}_{gg}=(0,\pm 12.21,0)^T$. The maximum torque about the Z axis occurs for $|\cos\beta|=1$, $\beta=0,\pm\pi$ yielding at torque $\vec{T}_{gg}=(0,0,\pm 11.81)^T$. The peak torque about the X axis occurs for $|\sin 2\beta|=1$, $\beta=\pm\frac{\pi}{4},\pm\frac{3\pi}{4}$ yielding $\vec{T}_{gg}=(\pm 0.198,\pm 8.63,\pm 8.35)^T$ with a magnitude of 12.01 n-m. The peak gravity gradient torque is thus approximately 12 n-m for the ideal XIOP attitude.

The momentum history as a function of time can be obtained from the time integral of equation 5-15 as:

$$\vec{H}_{gg} = \begin{bmatrix} 89.17\sin 2\beta(\sin 2\omega_o t - 2\omega_o t) \\ 5{,}498\sin\beta(\cos 2\omega_o t - 1) \\ 5{,}320\cos\beta(1-\cos 2\omega_o t) \end{bmatrix} \text{ (n-m-sec)} \qquad (5\text{-}16)$$

For one orbit ($\omega_o t = 2\pi$) the accumulated momentum is:

$$\vec{H}_d = \begin{bmatrix} -4\pi(89.17)\sin 2\beta \\ 0 \\ 0 \end{bmatrix} = \begin{bmatrix} -1{,}120\sin 2\beta \\ 0 \\ 0 \end{bmatrix} \qquad (5\text{-}17)$$

This is clearly maximized when $|\sin 2\beta| = 1$ which is the value of β for which peak torques develop about the X axis. With the principal X axis in the orbital plane, the net momentum accumulation per orbit is approximately 1,120 n-m-sec.

For peak momentum, the Y and Z components of equation 5-16 dominate and both peak when $\cos 2\omega_o t = -1$. Since the X component contains the secular term $2\omega_o t$, the peak momentum must occur near $\omega_o t = \frac{3\pi}{4}$ yielding:

$$\vec{H}_p = \begin{bmatrix} -3\pi(89.17)\sin 2\beta \\ -2(5{,}498)\sin\beta \\ 2(5{,}320)\cos\beta \end{bmatrix} = \begin{bmatrix} -840.4\sin 2\beta \\ -10{,}996\sin\beta \\ 10{,}640\cos\beta \end{bmatrix} \qquad (5\text{-}18)$$

For peak X torque $|\sin 2\beta| = 1$, yielding a peak momentum of $\vec{H}_p = (\pm 840.4, \pm 7776, \pm 7524)^T$ with a magnitude of 10,820 n-m-sec. For

peak Y torque, $|\sin\beta|=1$ with $\vec{H}_p=(0,\pm 10996,0)^T$ and peak Z torque occurs for $|\cos\beta|=1$ with $\vec{H}_p=(0,0,\pm 10640)^T$. Thus the peak momentum stored in the CMG cluster is 10,996 n-m-sec, occuring for $\beta=\pm\frac{\pi}{2}$ for which there is no net accumulation about the X axis. A typical momentum history for one orbit is shown in figure 5-5 for which $\beta=-\pi/4$.

With any pointing offsets $\vec{\varepsilon}$, the components of equation 5-13 must be used in the torque equation 5-4 giving the gravity gradient torques with an offset

$$\vec{T}_{gg}^{\,0}=\vec{T}_{gg}+3\omega_o^2\varepsilon_x\begin{bmatrix}(a_z^2-a_y^2)\Delta I_x\\ -a_xa_y\Delta I_y\\ a_xa_z\Delta I_z\end{bmatrix}+3\omega_o^2\varepsilon_y\begin{bmatrix}a_xa_y\Delta I_x\\ (a_x^2-a_z^2)\Delta I_y\\ -a_ya_z\Delta I_z\end{bmatrix}+3\omega_o^2\varepsilon_z\begin{bmatrix}-a_xa_z\Delta I_x\\ a_ya_z\Delta I_y\\ (a_y^2-a_x^2)\Delta I_z\end{bmatrix} \quad (5\text{-}19)$$

Substituting the appropriate values and adjusting the coefficients for a per degree offset:

$$\vec{T}_{gg}^{\,0}=\vec{T}_{gg}+\varepsilon_x\begin{bmatrix}0.0069\cos2\beta(\cos2\omega_o t-1)\\ 0.2130\cos\beta\sin2\omega_o t\\ -.2061\sin\beta\sin2\omega_o t\end{bmatrix}$$

$$+\varepsilon_y\begin{bmatrix}0.0069\cos\beta\sin2\omega_o t\\ -.1064[(1+\cos2\beta)+(3-\cos2\beta)\cos2\omega_o t]\\ -.1030\sin2\beta(\cos2\omega_o t-1)\end{bmatrix}$$

$$+\varepsilon_z\begin{bmatrix}0.0069\sin\beta\sin2\omega_o t\\ -.1064\sin2\beta(\cos2\omega_o t-1)\\ -.1030[(1-\cos2\beta)+(3+\cos2\beta)\cos2\omega_o t]\end{bmatrix} \quad (5\text{-}20)$$

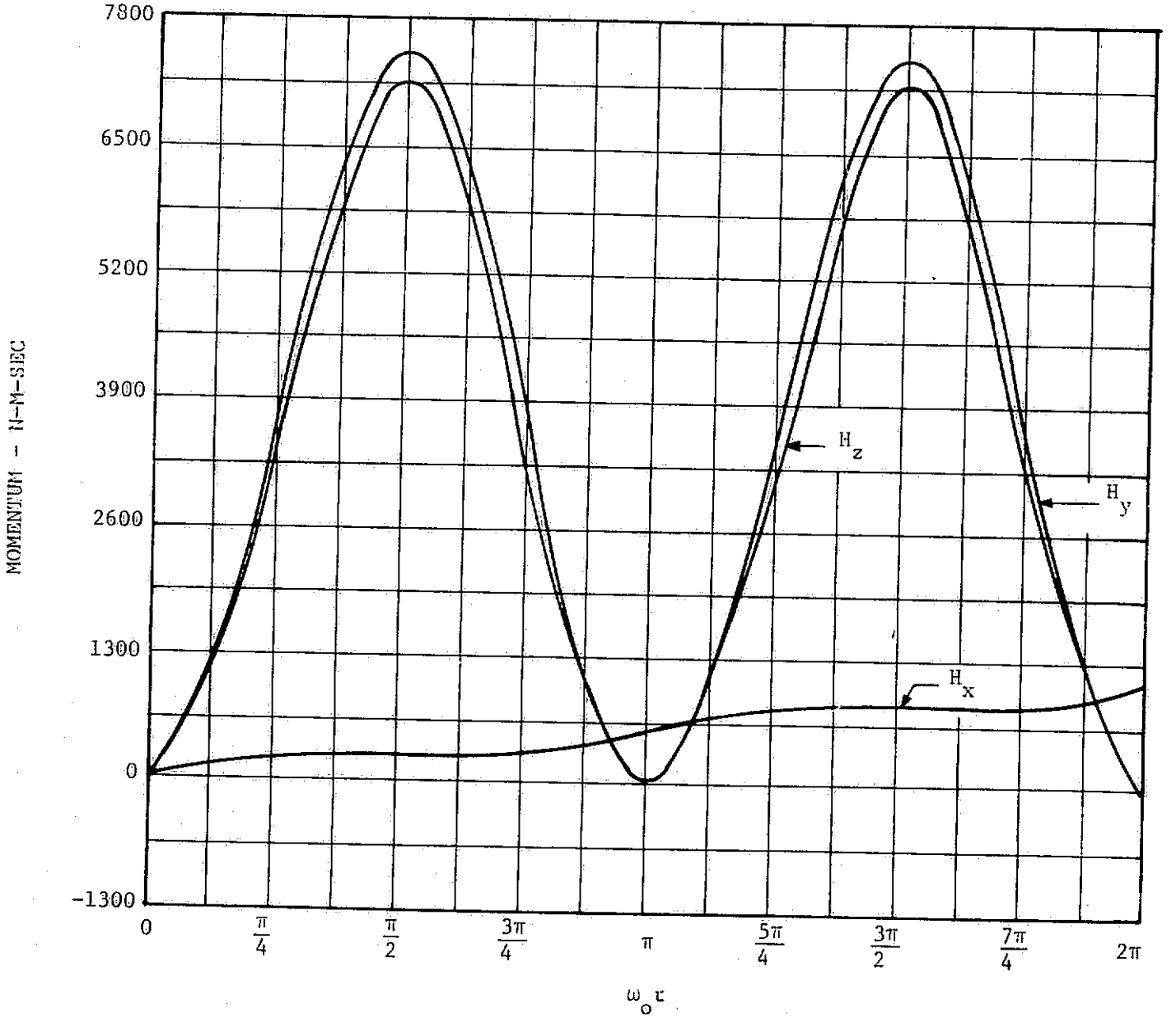

Figure 5-5. XIOP Momentum History for One Orbit, $\beta=-\pi/4$

Examination of equation 5-20 along with the values of peak gravity gradient torques for the ideal case indicates that only an extremely small torque increase will result from offsets on the order of one degree, in actuality approximately 1 percent increase in peak torque per degree offset per axis.

Performing the time integral of equation 5-20 to obtain the momentum history:

$$\vec{H}_{gg}^{0}=\vec{H}_{gg}+\varepsilon_x\begin{bmatrix}3.112\cos2\beta(\sin2\omega_o t-2\omega_o t)\\95.95\cos\beta(1-\cos2\omega_o t)\\92.84\sin\beta(\cos2\omega_o t-1)\end{bmatrix}$$

$$+\varepsilon_y\begin{bmatrix}3.112\cos\beta(1-\cos2\omega_o t)\\-47.96[(1+\cos2\beta)2\omega_o t+(3-\cos2\beta)\sin2\omega_o t]\\46.41\sin2\beta(2\omega_o t-\sin2\omega_o t)\end{bmatrix}$$

$$+\varepsilon_z\begin{bmatrix}3.112\sin\beta(1-\cos2\omega_o t)\\47.96\sin2\beta(2\omega_o t-\sin2\omega_o t)\\-46.41[(1-\cos\beta)2\omega_o t+(3+\cos2\beta)\sin2\omega_o t]\end{bmatrix} \qquad (5\text{-}21)$$

To determine the effect on the dump requirement, $\omega_o t=2\pi$:

$$\vec{H}_d^{0}=\vec{H}_d+\begin{bmatrix}-39.10\cos2\beta\\0\\0\end{bmatrix}\varepsilon_x+\begin{bmatrix}0\\-602.8(1+\cos2\beta)\\583.2\sin2\beta\end{bmatrix}\varepsilon_y+\begin{bmatrix}0\\602.8\sin2\beta\\-583.2(1-\cos2\beta)\end{bmatrix}\varepsilon_z \qquad (5\text{-}22)$$

For $|\sin2\beta|=1$, which gives the maximum momentum to be dumped for the ideal case, $H_d^0=(112.5,\pm602.8,\pm583.2)^T$ with a magnitude of 1,399 n-m-sec, for either Y or Z offsets, an increase in stored momentum of 25 percent per degree offset about the Y or Z axes. Considering an offset of 2.31° about Y and .085° about Z, that is, maintaining the vehicle X axis in the orbital plane as opposed to the principal X axis yields $H_d=(1120.5,1443.7,1396.8)^T$ with a magnitude of 2,301 n-m-sec to be dumped per orbit.

In order to determine the effect on the peak momentum state it is necessary to evaluate equation 5-21 for $\omega_o t=3\pi/2$:

$$\vec{H}_p^0=\vec{H}_p+\begin{bmatrix}-29.33\cos 2\beta\\ 191.9\cos\beta\\ -185.7\sin\beta\end{bmatrix}\varepsilon_x+\begin{bmatrix}6.223\cos\beta\\ -452.1(1+\cos\beta)\\ 437.4\sin 2\beta\end{bmatrix}\varepsilon_y+\begin{bmatrix}6.223\sin\beta\\ 452.1\sin 2\beta\\ -437.4(1-\cos\beta)\end{bmatrix}\varepsilon_z \quad (5\text{-}23)$$

for $\beta=\pm\frac{\pi}{4}$, corresponding to the peak momentum of the nonoffset case:

for ε_x: $\vec{H}_p^0=(869.7,7911,7655)^T$, $H_p=11{,}043$ n-m-sec (5-24a)

ε_y: $=(844.8,8548,7524)^T$, $H_p=11{,}419$ n-m-sec (5-24b)

ε_z: $=(844.8,7776,9270)^T$, $H_p=11{,}383$ n-m-sec (5-24c)

Thus, there is an increase in peak momentum of 2.1 percent per degree offset about X, 5.5 percent per degree offset about Y, and 5.2 percent per degree offset about Z. Again considering the case of vehicle X axis in the orbital plane with a Y offset of 2.31° yields a peak momentum value of 12,194 n-m-sec.

From data contained in reference 2, the peak aerodynamic torque is somewhat less than 1.4 n-m for XIOP with the peak momentum being approximately 950 n-m-sec.

5.2.3 Maneuvering Requirements - While baseline information indicates that gross vehicle maneuvers will not be performed with the CMG system, it is evident that momentum desaturation will require vehicle maneuvering under CMG control. The effects of this maneuvering can be significant in three ways, i.e., 1) the torque level required to accelerate and decelerate the vehicle as the maneuver is established and completed, 2) the momentum that must be absorbed by the CMG system during the maneuver as required by conservation of angular momentum, and 3) the increase in gravity gradient momentum accumulation during the maneuver.

Previous studies (reference 2) have shown that momentum desaturation can be accomplished by means of small angle maneuver laws in which the maximum maneuver is no greater than 10 degrees. In general at least two maneuvers will be required for XPOP desaturation and no more thna 4 for XIOP desaturation with the sum of all maneuver angles in either case probably not exceeding 20 degrees. For the 500 km orbit, the period is 5,676 seconds and

postulating a minimum desaturation period of one-third orbit or 1,892 seconds, no more than 20 percent of the desaturation period or some 378 seconds should be taken by the maneuvers. Thus a maximum desaturation maneuver rate $\omega_m=20/500\approx0.04$ deg/sec seems a practical working value. Referring to table 3-1 it can be seen that the vehicle axis of largest inertia is Z_v, and all following computations will be based on maneuvers about Z_v as the worst case in terms of torque requirements and momentum exchange.

Conservation of momentum requires that the sum of vehicle momentum and CMG momentum must remain constant when no external torques act on the system, which is nearly the case during a maneuver since the gravity gradient torque is quite small. During experiment pointing the vehicle rates are essentially zero, thus the vehicle angular momentum is zero. When a maneuver occurs the CMG system must experience a change in momentum $\Delta H=-J\omega$ where J is the moment of inertia about the axis of rotation and ω is the rotation rate in order to satisfy the conservation law. For $\omega_z=.04$ deg/sec:

$$|\Delta H_z|=I_{zz}|\omega_z|=5,315 \text{ n-m-sec} \tag{5-25}$$

To examine the torque requirement to perform the maneuvers an ideal maneuver strategy consisting of an acceleration to achieve the limiting maneuver rate, a coasting rotation at the maximum rate and a deceleration to zero rate with acceleration and deceleration times equal will be used. This is a time optimal strategy for equal torque applications on acceleration and deceleration. If the torque level of the CMG is defined to be T, the acceleration about the axis of rotation is:

$$\dot{\omega}=T/J \tag{5-26}$$

The time required to accelerate to the maximum rate ω_m or decelerate from ω_m to rest is:

$$t_a=\omega_m/\dot{\omega}=J\omega_m/T \tag{5-27}$$

The angular motion during acceleration and deceleration is:

$$\Delta\psi=\dot{\omega}_a t^2/2=\frac{J\omega_m^2}{2T} \tag{5-28}$$

A total maneuver ψ then will require an angular motion of $\psi-2\Delta\psi$ during the constant rate period which will require a time:

$$t_b = \frac{\psi - 2\Delta\psi}{\omega_m} = \frac{\psi}{\omega_m} - \frac{J\omega_m}{T} \tag{5-29}$$

The total maneuver time is then:

$$t_m = 2t_a + t_b = \frac{\psi}{\omega_m} + \frac{J\omega_m}{T} \tag{5-30}$$

If instantaneous acceleration is assumed, the maneuver time is simply ψ/ω_m thus the increase in time required to perform the maneuver considering a finite torque application is:

$$\Delta t = J\omega_m/T \tag{5-31}$$

Using the maximum rate of 0.04 deg/sec and I_{zz} then gives:

$$\Delta t = 5{,}315/T \text{ sec} \tag{5-32}$$

For an increase of maneuver time of 25 seconds (a 10 percent increase for a 10 degree maneuver) a torque of 213 n-m is required, while for 20 and 10 seconds the values are 266 n-m and 532 n-m, respectively. A minimum torque requirement for maneuvering thus would be 200 n-m with a value of 510 n-m being a practical maximum as larger values decrease the total maneuver time only a small amount for even small maneuvers.

The amount of gravity gradient torque and additional momentum accumulation exerted on the vehicle during a maneuver can be bounded by reference to the torque equation 5-19 which is a general torque equation in terms of the components of the local vertical vector a_i, $i=x,y,z$. Since the orbital position changes only slightly during a maneuver, the a_i can be assumed constant and since they are components of a unit vector; $\max\{a_i a_j\}=0.5$, $\max\{a_i^2 - a_j^2\}=1$, $i \neq j$. The maximum torque thus arises from the ε_y term of equation 5-19 since ΔI_y is the largest inertia difference and in this term has a coefficient bound of unity. Thus the gravity gradient torque during a maneuver is thus bounded by:

$$\vec{T}_{ggm} < 3\omega_o^2 \dot{\varepsilon}_y t \begin{bmatrix} 0.5\Delta I_x \\ \Delta I_y \\ 0.5\Delta I_z \end{bmatrix} \tag{5-33}$$

where $\varepsilon_y = \dot{\omega}_y t$ and it is a strict inequality since all three coefficients cannot attain their maximums simultaneously. The corresponding momentum bound is found from the time integral of equation 5-33:

$$\vec{H}_{ggm} < \frac{3}{2}\,\omega_o^2 \dot{\varepsilon}_y t^2 \begin{bmatrix} 0.5\Delta I_x \\ \Delta I_y \\ 0.5\Delta I_z \end{bmatrix} \qquad (5\text{-}34)$$

For $\dot{\varepsilon}_y = \omega_m = .04$ deg/sec and a maneuver time of 250 seconds:

$$\vec{T}_{ggm} < \begin{bmatrix} 0.069 \\ 4.238 \\ 2.050 \end{bmatrix} \qquad T_{ggm} < 4.70 \text{ n-m} \qquad (5\text{-}35)$$

$$\vec{H}_{ggm} < \begin{bmatrix} 8.542 \\ 529.7 \\ 256.3 \end{bmatrix} \qquad H_{ggm} < 588 \text{ n-m-sec} \qquad (5\text{-}36)$$

5.3 Summary of Torque and Momentum Requirements - The results of the previous sections are summarized in table 5-1, listing all derived torque and momentum requirements. The overwhelming torque requirement is that for desaturation maneuvering. A CMG cluster capable of generating a minimum of 200 n-m of torque about any axis is indicated with torque outputs up to some 540 n-m being helpful in reducing total maneuver times.

The XIOP attitude is clearly the worst with respect to momentum storage requirements. The peak gravity gradient, aerodynamic, momentum exchange and maneuver gravity gradient requirements are 10,980, 950, 5,290, and 580 n-m-sec, respectively, for this case. Each of these values represent a vector magnitude and even in the unlikely case that all peaks would occur simultaneously, there is no chance that the individual vectors would be colinear. Realistically the total momentum storage requirement can thus be estimated by using the root-sum-square of the four values instead of the direct sum resulting in a minimum momentum storage requirement of 12,200 n-m-sec about any axis. It should be noted that the largest contribution to the momentum requirement is that due to gravity gradient for which

Table 5-1. Summary of Torque and Momentum Requirements

	XI OP	XIOP	
Peak Gravity Gradient Torque	0.41	12.20	n-m
Increase per degree offset ε_x	0.00	0.15	n-m
ε_y	0.15	0.15	n-m
ε_z	0.15	0.15	n-m
Peak Aerodynamic Torque	1.50	1.50	n-m
Minimum Maneuver Torque	200.00	200.00	n-m
GG Torque - 250 Second Maneuver	4.75	4.75	n-m
Peak Gravity Gradient Momentum	353	10,980	n-m-sec
Increase per degree offset ε_x	0	68	n-m-sec
ε_y	854	434	n-m-sec
ε_z	813	407	n-m-sec
Peak Aerodynamic Momentum	1,630	950	n-m-sec
Momentum Exchange .04 deg/sec	5,290	5,290	n-m-sec
GG Momentum - 250 Second Maneuver	580	580	n-m-sec
Momentum Accumulation Per Orbit	0	1,125	n-m-sec
Increase per degree offset ε_x	0	41	n-m-sec
ε_y	1,210	270	n-m-sec
ε_z	1,170	270	n-m-sec

the individual components of stored momentum are quite predictable. Since this is the case the initial cluster momentum state can be biased to reduce the magnitude of the peaks, thus easing the total requirement.

From the above analysis it appears that a CMG cluster having a momentum storage capability of 12,200 n-m-sec and a minimum torque capability of 200 n-m can meet the requirements of the orbiter/pallet vehicle both for gravity gradient stabilization during observation and maneuvering for momentum desaturation.

In general, torques and momenta can be minimized for either case by placing the X principal axis either perpendicular to or in the orbital plane, thus insuring some additional system capability to meet any additional disturbance events. This could be accomplished quite easily for XPOP since the major misalignment is about the vehicle Y axis and all experiment configurations show a gimbal or hinge about that axis, thus a simple rotation of approximately 2.3° about the vehicle Y axis will place the X principal axis near the orbit normal and the experiment gimbal could compensate for that directly. In the case of XIOP, the experiments can be hardmounted with the vehicle Z axis being the pointed axis, however, a rotation about the vehicle Z axis could place the principal X axis near the orbital plane.

6. CMG CONFIGURATION STUDY

The CMG cluster requirements of the previous section based on gravity gradient, aerodynamic and manned motion disturbances during experiment pointing and desaturation maneuvering are:

Momentum: 12,200 n-m-sec in the vehicle YZ plane

Torque: 200 n-m about any control axis

In addition to these basic requirements a fail operational, fail safe redundancy requirement is assumed to insure mission continuance for a single actuator failure. A second failure would in all likelihood cause mission termination but would be fail safe in the sense that the shuttle reaction control system (RCS) would still be available for attitude control during de-activation, deorbit, and reentry.

CMG actuators presently available or in late development stages are surveyed and traded by type (double vs single gimbal), size, weight, and power requirements on an actuator and a cluster basis. Consideration is given to both normal and failure modes of operation with some qualitative vibrational aspects discussed.

6.1 CMG Types and Type Selection - The two types of CMGs are the single gimbal CMG (SCMG) with one gimbal between the momentum wheel and the base and the double gimbal CMG (DCMG) with two gimbals between the momentum wheel and the base. A pictorial representation of both CMG types is shown in figure 6-1.

The SCMG has only one rotational degree of freedom and the output torque $\vec{T}_s = \vec{\omega}_g \times \vec{H}_w$ is thus constrained to lie along the line normal to both the gimbal axis and the wheel momentum vector $\vec{H}_w$. This is the SCMG output torque axis, and since it lies normal to the gimbal axis there is no component of output torque about the gimbal torquer axis. The SCMG output torque is thus limited only by the radial load carrying capacity of the gimbal and momentum wheel bearings. The gimbal torquers must only accelerate the gimbal and since there are no large reaction torques about the gimbal axis, relatively large gimbal rates are possible. The SCMG is thus a torque multiplier, i.e., small torques applied about the gimbal axis to establish a gimbal rate $\vec{\omega}_g$ can produce large torques about the output axis. In broad terms the single gimbal CMG is well suited to high torque applications, but has a constrained momentum storage capability.

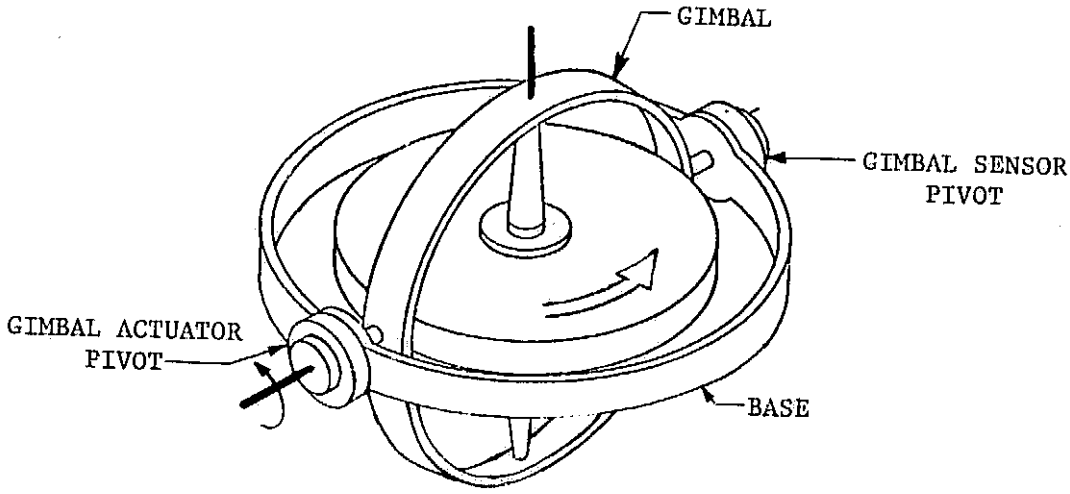

a) Typical Single Gimbal CMG Arrangement

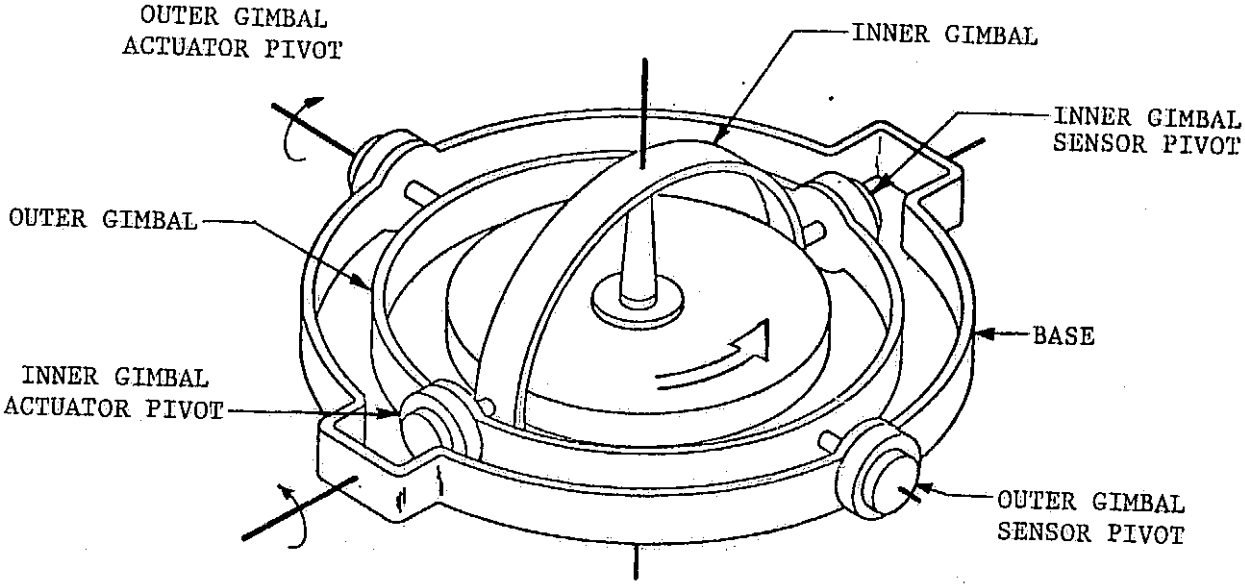

b) Typical Double Gimbal CMG Arrangement

Figure 6-1. Types of Control Moment Gyroscopes

The DCMG has two rotational degrees of freedom, one about each of the two perpendicular gimbal axes. Motion of the two gimbals can produce an effective gimbal rate $\vec{\omega}_g$ anywhere in the plane normal to the wheel momentum $\vec{H}_w$ thus the output torque $\vec{T}_D = \vec{\omega}_g x \vec{H}_w$ can lie anywhere in this plane which can then be called the DCMG output torque plane. However, the output torque always has a component along one of the gimbal axes, therefore it is limited by torque capability of the gimbal torquers. Again in broad terms, the double gimbal CMG is more suited to applications with moderate torque requirements, but has a more flexible (i.e., optimum) momentum storage capability.

The momentum envelope of one CMG is the plane normal to the gimbal axis and the envelope of an actuator cluster is dependent on the mounting configuration of the individual actuators. While the basic cluster can be arranged to give a more or less regular momentum envelope, a single CMG failure strongly distorts the envelope and causes some quite complex software problems in determining desaturation strategies, e.g., a normal gravity gradient desaturation which tends to decrease the stored momentum magnitude could drive the cluster momentum vector into the distorted envelope, thus causing saturation even though decreasing the momentum load. Another severe problem with a SCMG cluster is the existence of singularity surfaces within the momentum envelope occurring when the torque output vectors of the individual actuators are coplanar, i.e., no control torque is possible about the axis normal to the plane. A total analytic solution for the location of these surfaces and general software for singularity avoidance does not exist, and the normal strategy is local avoidance of the surfaces along with varying amounts of excess momentum storage capability over the basic requirements.

The DCMG momentum envelope is spherical in the absence of gimbal stops and even with limited gimbal rotation the envelope of a single actuator is a portion of a sphere. The envelope of a DCMG cluster of any number of actuators is thus also spherical and the failure of a single actuator while decreasing the envelope size does not change its spherical character. Desaturation strategies can thus be devised to decrease or control the stored momentum with the guarantee that the momentum vector is always moving away from the envelope in both normal and failure modes of operation. DCMG singularity occurs only when the individual actuator momentum vectors are colinear and this situation can be avoided through relatively simple logic involving redistribution of the individual momenta through the use of the excess degrees of freedom provided when more than a single actuator is in use.

An examination of the capabilities of currently available actuators as tabulated in reference 3 indicates a maximum SCMG actuator momentum storage capability of 1,350 n-m-sec with units up to 2,050 n-m-sec under study. Remaining within the available or nearly available single gimbal actuators implies the need for a cluster of at least 10 SCMGs, to meet the basic momentum storage requirement of this application (including a margin for singularity avoidance). The attendant mechanical complexity of at least 10 devices with the attendant mounting and connection problems along with the singularity problem and failure mode saturation avoidance indicates that the single gimbal CMG should not be considered further for the floated pallet application, and all further evaluation will be concerned with selection of a double gimbal actuator and specification of a cluster configuration utilizing DCMGs.

6.2 Survey of Double Gimbal CMGs - Examination of the specifications of currently or nearly available DCMG actuators from reference 3 and informal sources shows three devices which will be considered for this application. Basic data for these actuators are shown in table 6-1. The Bendix MA-2300 DCMG is the actuator used on the Skylab vehicle while the Sperry 4500 and Bendix MA-2000 are in the late development stage. Although the MA-2300 actuator experienced spin bearing lubrication difficulties during the Skylab mission, this problem has since been solved and the modified device remains the only double gimbal CMG which is space qualified. In addition the gimbal stops on the MA-2300 have been removed.

6.3 CMG Cluster Definitions - The basic momentum storage requirement of 12,200 n-m-sec defines the low limit of the actuator cluster and thus indicates that 4 Bendix MA-2300 or MA-2000 or 2 Sperry 4500 DCMGs are required. In order to meet the fail operational concept, however, at least 3 CMGs are required since three-axis control is not available with a single actuator, thus 3 of the Sperry actuators would be necessary. The total capabilities and requirements of all four of the above mentioned clusters are given in table 6-2, although the 2 CMG cluster will not be considered further due to the inability to provide "operational" failure mode protection.

6.4 CMG Actuator Recommendations - Referring again to table 6-2, and considering first the two Bendix clusters, it is immediately evident that in the normal operating mode there is little difference in the two systems in basic control capabilities and weight. The MA-2300 cluster has a higher power requirement in steady state operation while the MA-2000 cluster shows higher transient requirements although both are moderate. The variable

Table 6-1. Candidate Double Gimbal CMG Actuators

	BENDIX MA-2300	SPERRY 4500	BENDIX MA-2000
Stored Angular Momentum	3,120	6,100 (d)	1,355 to 4,070 (f)
Peak Output Torque (n-m)	165	340	240
Wheel Rotation Rate (rpm)	9,080	6,520 (d)	3,950 to 11,850 (f)
Actuator Weight (kg)	190 (a)	295 (c)	205
Actuator Dimensions (m)	1x1.07x1	1.17x1.22x0.53	1x1.07x1
Gimbal Freedom	*	Unlimited	Unlimited
Actuator Bandwidth (Hz)	4 to 10	15	5 to 10
Wheel Spinup Time (hr)	14	4	2.5
Power Requirements (watts)			
Wheel Spin Control	80	55 to 102 (e)	50
Spinup Peak	170	450	400
Gimbal Torquers at Peak	170	500	300
Spin Bearing Heaters (peak)	52	Unknown	52
Other (peak)	70 (b)	Unknown	Unknown
Spin Motor Type	AC	Brushless DC	Brushless DC
Torquer Type	Brush type DC	Brushless DC	Brushless DC
Torquer/Gimbal Drive	Geared	Direct	Geared
Status	Space qualified Available "off-the-shelf"	Development	Development

Notes:
a) Does not include inverter assembly weight of 23 kg, 2 required per cluster.
b) Allocated to inverter assembly functions.
c) Does not include external control electronics of unknown weight.
d) Nominal values (4 discrete speeds possible).
e) Larger value required at peak output torque.
f) Nominal values 2,700 n-m-sec, 7,900 rpm.
* Unlimited gimbal freedom in modified actuator.

Table 6-2. Candidate Actuator Clusters

	4 BENDIX MA-2300	4 BENDIX MA-2000	3 SPERRY 4500	2 SPERRY 4500
Normal Operation				
Momentum Storage Capacity (n-m-sec)	12,480	12,200	18,300	12,200
Peak Torque Output (n-m)	660	960	1,020	680
Cluster Weight (kg)	760 (b)	820	885 (c)	590 (c)
Power Required for Spin Control (watts)	320	200	165	110
Peak Power Required During Spinup (watts)	680	1,600	1,350	900
Torquer Power Required at 10 ft-lb-sec (watts) (d)	15	16	25 (e)	25 (e)
Torquer Power Required at 150 ft-lb-sec (watts) (d)	215	255	330 (e)	330 (e)
Torquer Power Required at 400 ft-lb-sec (watts) (d)	560	690	875 (e)	875 (e)
Single Actuator Failure				
Momentum Storage Capacity (n-m-sec)	9,360	12,200	12,200	6,100
Peak Torque Output (n-m)	495	720	680	340
Control Law Modifications Required for Failure	Minimal	Minimal	Moderate	(g)

Notes: a) Run at 3,050 n-m-sec each instead of nominal 2,700 n-m-sec.
b) Does not include 46 kg for 2 inverter assemblies.
c) Does not include weight of external control electronics.
d) Estimated from peak values.
e) Includes increase in spin control power required.
f) Based on increase to 4,067 n-m-sec for remaining actuators.
g) Three axis control impossible.

momentum storage feature of the MA-2000 actuator allows the cluster storage capability to be returned to 12,200 n-m-sec in case of a single failure, however, this is not the overwhelming advantage it appears to be since the gravity gradient momentum peaks which dominate the transient momentum are highly predictable and the cluster momentum state can be biased to provide the necessary momentum storage capability in the required direction. Thus, since the actuator capabilities and requirements are quite similar and the decreased momentum capability of the MA-2300 cluster in the failure mode is not a serious problem, the MA-2300 cluster is to be preferred to the MA-2000 on the basis of the space qualificatio and off-the-shelf availability of the actuators.

Comparison of the cluster of four Bendix MA-2300 actuators and that of three Sperry 4500 actuators shows that the Sperry cluster has higher torque and momentum storage capabilities both in the normal and failure modes, however, as stated above the peak momentum is predictable, thus the excess storage capability is not an overriding consideration. The Bendix cluster shows a higher steady state power requirement with the Sperry showing higher transient power needs, although both are nominal for this application. The basic cluster weight is significantly less for the Bendix actuators and since both CMGs under consideration require additional electronic gear, the net weight advantage for the MA-2300 cluster should exist even after adding the weights of the inverter and external electronics assemblies. Another factor to be considered in this comparison is the momentum wheel rotation rate of the actuators which defines the basic vibration frequencies arising from wheel imbalance. As can be seen from table 6-1, the Bendix actuator wheel spins at over 9,000 rpm while the Sperry spin rate is around 6,500 rpm, nearly 30 percent slower. In general as the vibration disturbance frequency increases, the effect on pointing accuracy due to structural propagation of the vibration decreases. Another factor to be considered, however, is the fact that although the Sperry actuator has a lower vibration frequency, there is one less rotating wheel in the cluster which could tend to compensate for the lower rate. The effects of vibration must thus be left open pending some study of the CMG cluster/pallet structure interaction and the net effect on pointing.

In summary, the comparison of the Bendix MA-2300 and Sperry 4500 clusters shows a slight weight and probable better vibration characteristics for the Bendix cluster while the Sperry cluster has somewhat lower power requirements. Since detailed cost information is not available for the Sperry actuators, this factor cannot be evaluated. In the absence of any clear-cut disadvantages for the MA-2300 actuator, this actuator is to be preferred due to its availability and space qualification.

6.5 CMG Cluster Configuration - With the selection of the Bendix MA-2300 CMG (the modified Skylab ATM actuator) for this application, the next problem to be considered is the mounting configuration of the four actuators required in the cluster. In general, the mounting arrangement is not critical for a double gimbal CMG with unlimited gimbal freedom and the purely hardware constraints of physical clearances, torque paths, etc., will be the primary consideration in determining the actuator locations and orientations. This aspect of the configuration is treated in detail in volume III of this final report.

For the purposes of implementing a simulation of the total orbiter-pallet-suspension dynamics with detailed shockmounted CMG models, a cluster configuration was required prior to completion of the hardware studies. Since orientation is not a critical problem within the scope of the overall study, a representative configuration was selected for use in the simulation studies.

The simplest arrangement for any number of CMGs would be an in-line configuration with the output axes of all the actuators aligned, leading also to a relative simple CMG control law (gimbal steering law). However, placement in this orientation would require that the initial conditions on the gimbal angles would have to vary in each actuator to avoid starting with all wheel momentum vectors aligned (a singularity condition, actually a saturation). In order to avoid this problem while retaining a simple configuration, a rotated in-line configuration was selected in which each CMG is rotated by $n\pi/2$, $n=0,1,2,3$ about the base X axis as shown in figure 6-2. This configuration is also a worst case in the sense of qualitative actuator bandwidth since operation will be near zero gimbal angles for all CMGs.

6.6 CMG Control Law - With the selection of an actuator cluster configuration to be utilized in the simulation study of the floated pallet, it is necessary to derive a CMG control law which will generate a set of gimbal rate commands that will result in a CMG cluster torque output equal to the desired command torque. For the purposes of this study there is no requirement to include singularity avoidance logic and failure mode alterations to the basic CMG control law, however, these items could easily be added to the law derived in this section.

The CMG control law to be used is a pseudo-inverse law which is optimized and decoupled and must be implemented digitally. The eight CMG gimbal rate commands are computed by minimizing the sum of the squares of the commands with the constraint that the ideal CMG output torque equals the command torque desired. The extremization is carried out by the technique of Lagrange multipliers.

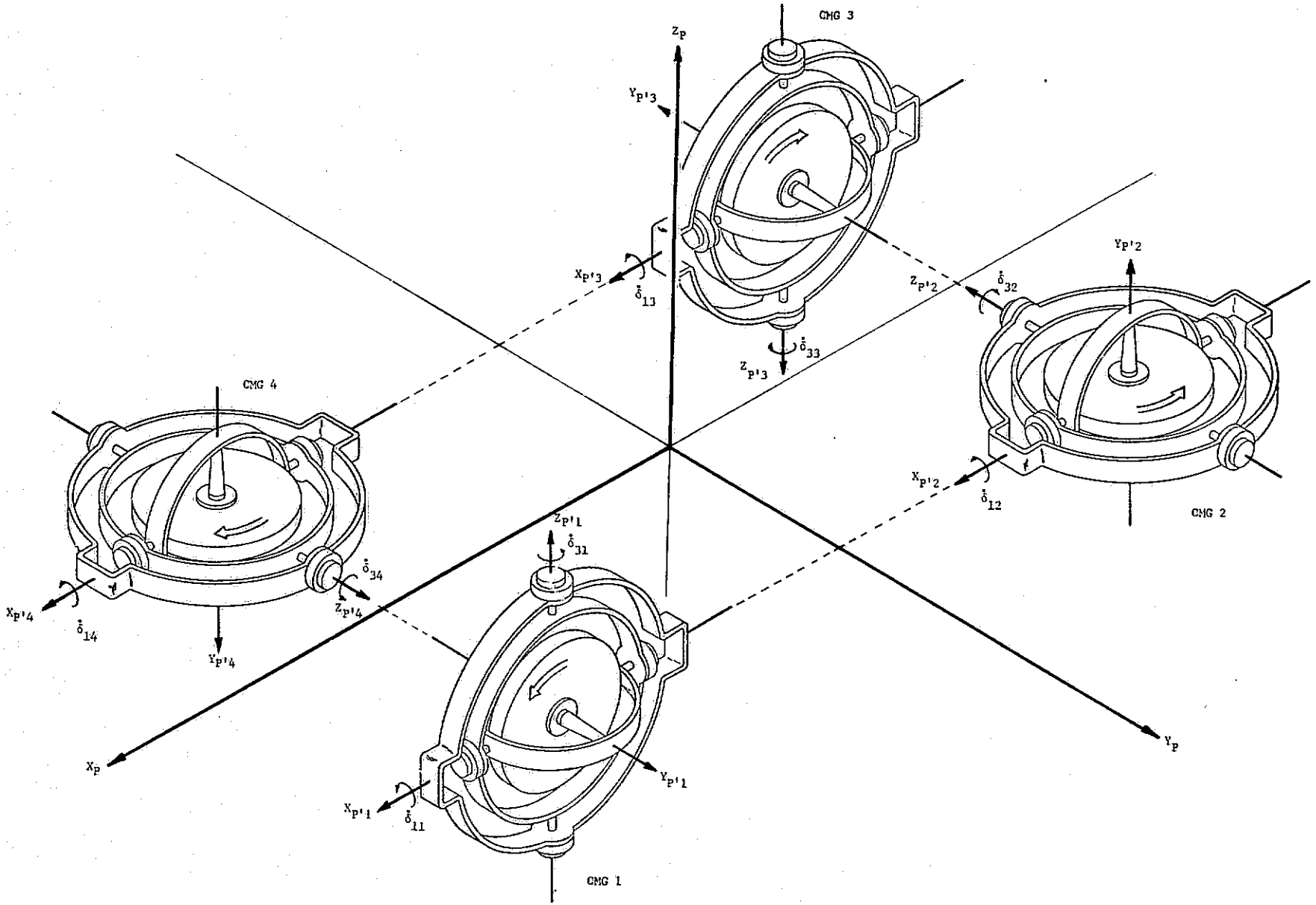

Figure 6-2. Rotated In-Line CMG Cluster Configuration

The pseudo-inverse steering law will be derived under the assumptions that all wheel momenta are equal and that the pallet is inertially held, i.e., all pallet rates are assumed zero. With reference to the recommended cluster configuration, the CMG output (P') axes are located with respect to the pallet (P) axes as shown in figure 6-3. The transformations from the CMG output axes (P'j, j=1,2,3,4) to the pallet coordinates (P) are:

$$[{}_{P}T_{P'1}]=\begin{bmatrix}1 & 0 & 0\\ 0 & 1 & 0\\ 0 & 0 & 1\end{bmatrix} \tag{6-1}$$

$$[{}_{P}T_{P'2}]=\begin{bmatrix}1 & 0 & 0\\ 0 & 0 & -1\\ 0 & 1 & 0\end{bmatrix} \tag{6-2}$$

$$[{}_{P}T_{P'3}]=\begin{bmatrix}1 & 0 & 0\\ 0 & -1 & 0\\ 0 & 0 & -1\end{bmatrix} \tag{6-3}$$

$$[{}_{P}T_{P'4}]=\begin{bmatrix}1 & 0 & 0\\ 0 & 0 & 1\\ 0 & -1 & 0\end{bmatrix} \tag{6-4}$$

For each actuator the transformations from output (P'j) to outer gimbal (Cj) and outer gimbal to inner gimbal (Aj) coordinates are:

$$[{}_{Cj}T_{P'j}]=\begin{bmatrix}\cos\delta_{3j} & \sin\delta_{3j} & 0\\ -\sin\delta_{3j} & \cos\delta_{3j} & 0\\ 0 & 0 & 1\end{bmatrix} \tag{6-5}$$

$$[{}_{Aj}T_{Cj}]=\begin{bmatrix}1 & 0 & 0\\ 0 & \cos\delta_{1j} & \sin\delta_{1j}\\ 0 & -\sin\delta_{1j} & \cos\delta_{1j}\end{bmatrix} \tag{6-6}$$

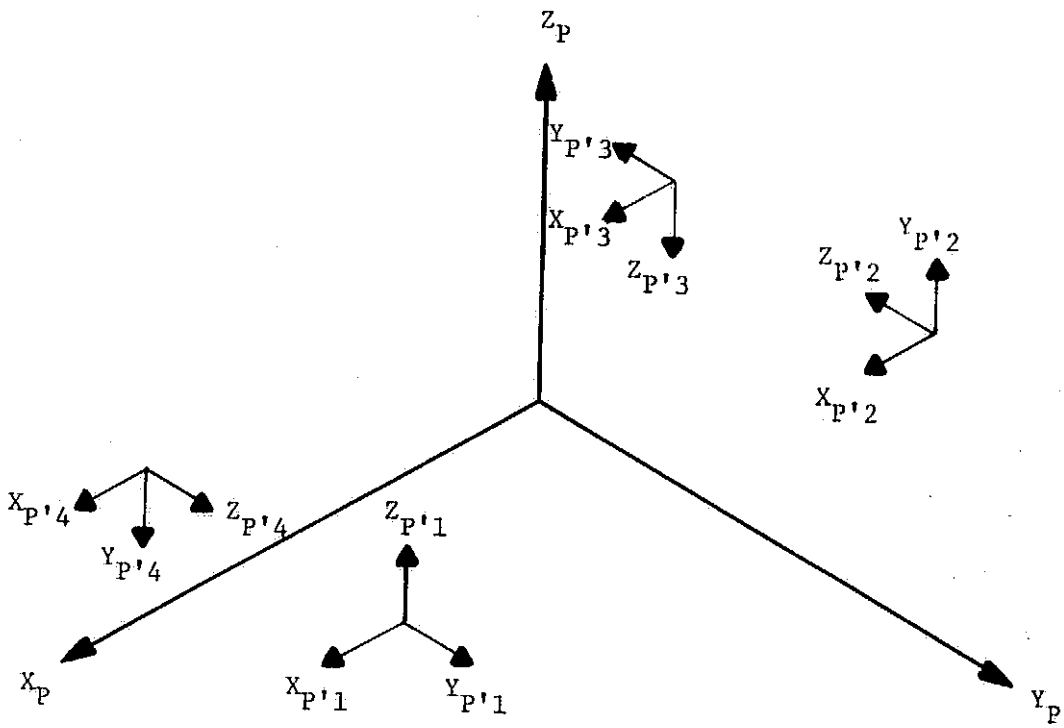

Figure 6-3. Relation of CMG Output Axes to Pallet Axes

where the gimbal angle δ_{ij} refers to the ith gimbal (i=1 inner, i=3 outer) of the jth CMG (j=1,2,3,4).

With the assumption of small vehicle rates and ideal actuators, the total angular rate applied to the wheel of the jth CMG is due to the gimbal rates $\dot{\delta}_{1j}$ and $\dot{\delta}_{3j}$, explicitly:

$$\vec{\omega}_{Aj} = \begin{bmatrix} \dot{\delta}_{1j} \\ 0 \\ 0 \end{bmatrix} + [{}_{Aj}T_{Cj}] \begin{bmatrix} 0 \\ 0 \\ \dot{\delta}_{3j} \end{bmatrix} = \begin{bmatrix} \dot{\delta}_{1j} \\ \dot{\delta}_{3j}\sin\delta_{1j} \\ \dot{\delta}_{3j}\cos\delta_{ij} \end{bmatrix} \tag{6-7}$$

In the inner gimbal space the wheel momentum $\vec{H}_{Aj}=(0,h,0)^T$ and the external torque applied to the wheel is the inertial derivative of $\vec{H}_{Aj}$.

$$\frac{D\vec{H}_{Aj}}{Dt} = \dot{\vec{H}}_{Aj} + \vec{\omega}_{Aj} x \vec{H}_{Aj} = H \begin{bmatrix} -\dot{\delta}_{3j}\cos\delta_{1j} \\ 0 \\ \dot{\delta}_{1j} \end{bmatrix}$$

The individual CMG control torque is simply the negative of the external torque acting on the wheel. Transforming to the CMG output space:

$$\vec{T}_{P'j} = H[{}_{P'j}T_{Cj}][{}_{Cj}T_{Aj}] \begin{bmatrix} \dot{\delta}_{3j}\cos\delta_{1j} \\ 0 \\ -\dot{\delta}_{1j} \end{bmatrix} = H \begin{bmatrix} -\dot{\delta}_{1j}\sin\delta_{1j}\sin\delta_{3j} + \dot{\delta}_{3j}\cos\delta_{1j}\cos\delta_{3j} \\ \dot{\delta}_{1j}\sin\delta_{1j}\cos\delta_{3j} + \dot{\delta}_{3j}\cos\delta_{1j}\sin\delta_{3j} \\ -\dot{\delta}_{1j}\cos\delta_{1j} \end{bmatrix} \tag{6-8}$$

The total control torque exerted on the pallet by the CMG cluster resolved into pallet coordinates is then:

$$\vec{T}_{CP} = \sum_{i=1}^{4} [{}_{P}T_{P'j}]\vec{T}_{P'j} \tag{6-9}$$

or:

$$\vec{T}_{CP} = H\{[A]\dot{\vec{\delta}}_1 + [B]\dot{\vec{\delta}}_3\} \tag{6-10}$$

where:

$$\dot{\vec{\delta}}_1 \triangleq (\dot{\delta}_{11}, \dot{\delta}_{12}, \dot{\delta}_{13}, \dot{\delta}_{14})^T \tag{6-11}$$

$$\dot{\vec{\delta}}_3 \triangleq (\dot{\delta}_{31}, \dot{\delta}_{32}, \dot{\delta}_{33}, \dot{\delta}_{34})^T \tag{6-12}$$

$$[A] \triangleq \begin{bmatrix} -\sin\delta_{11}\sin\delta_{31} & -\sin\delta_{12}\sin\delta_{32} & -\sin\delta_{13}\sin\delta_{33} & -\sin\delta_{14}\sin\delta_{34} \\ \sin\delta_{11}\cos\delta_{31} & \cos\delta_{12} & -\sin\delta_{13}\cos\delta_{33} & -\cos\delta_{14} \\ -\cos\delta_{11} & \sin\delta_{12}\cos\delta_{32} & \cos\delta_{13} & -\sin\delta_{14}\cos\delta_{34} \end{bmatrix} \tag{6-13}$$

$$[B] \triangleq \begin{bmatrix} \cos\delta_{11}\cos\delta_{31} & \cos\delta_{12}\cos\delta_{32} & \cos\delta_{13}\cos\delta_{33} & \cos\delta_{14}\cos\delta_{34} \\ \cos\delta_{11}\sin\delta_{31} & 0 & -\cos\delta_{13}\sin\delta_{33} & 0 \\ 0 & \cos\delta_{12}\sin\delta_{32} & 0 & -\cos\delta_{14}\sin\delta_{34} \end{bmatrix} \tag{6-14}$$

In order to derive the control law it is necessary to find the gimbal rate commands $\dot{\delta}_{1C}$ and $\dot{\delta}_{3C}$ such that the control torque $\vec{T}_{CP}$ is equal to the command torque $\vec{T}'_C$ while minimizing the generated command rates. This can be done by selecting a performance index P which is the sum of the squares of the rate commands:

$$P = \frac{1}{2}\sum_{i=1}^{4} (\dot{\delta}^2_{1iC} + \dot{\delta}^2_{3iC}) = \frac{1}{2}(\dot{\vec{\delta}}_{1C}\cdot\dot{\vec{\delta}}_{1C} + \dot{\vec{\delta}}_{3C}\cdot\dot{\vec{\delta}}_{3C}) \tag{6-15}$$

where the $\cdot$ indicates the vector dot product (inner product). The constraint is simply:

$$\vec{T}_{CP} - \vec{T}'_C = 0 \tag{6-16}$$

The optimization is carried out by using the Lagrange multiplier $\vec{\lambda} = (\lambda_1, \lambda_2, \lambda_3)^T$. Forming the Lagrangian adjoint equation using equations 6-14, 6-15, and 6-16:

$$L = P - \vec{\lambda}\cdot(\vec{T}_{CP} - \vec{T}'_C)$$

$$L = \frac{1}{2}(\dot{\vec{\delta}}_{1C}\cdot\dot{\vec{\delta}}_{1C} + \dot{\vec{\delta}}_{3C}\cdot\dot{\vec{\delta}}_{3C}) - \vec{\lambda}\cdot\{H[A]\dot{\vec{\delta}}_{1C} + H[B]\dot{\vec{\delta}}_{3C} - \vec{T}'_C\} \tag{6-17}$$

To minimize L, the partial derivatives $\frac{\partial L}{\partial \dot{\vec{\delta}}_{1C}}$, $\frac{\partial L}{\partial \dot{\vec{\delta}}_{3C}}$, and $\frac{\partial L}{\partial \vec{\lambda}}$ are set to zero, resulting in 11 equations in the 11 unknowns ($4\dot{\delta}_{1iC}$, $4\dot{\delta}_{3iC}$, and $3\lambda_i$). The notation of the derivative of the scalar function L with respect to a vector is understood to be the vector whose components are the derivatives of L with respect to the vector components, i.e., for any $\vec{\alpha}$, $\frac{\partial L}{\partial \vec{\alpha}} \triangleq (\frac{\partial L}{\partial \alpha_1}, \frac{\partial L}{\partial \alpha_2}, \ldots, \frac{\partial L}{\partial \alpha_n})^T$.

The derivatives are reasonably straightforward perhaps with the exception of the form $\frac{\partial}{\partial \dot{\vec{\delta}}_{iC}}(\vec{\lambda} \cdot [C]\dot{\vec{\delta}}_{iC})$ where [C]=[A] for i=1 and [B] for i=3. Expanding:

$$\begin{aligned}\vec{\lambda} \cdot [C]\dot{\vec{\delta}}_{iC} = &\lambda_1(C_{11}\dot{\delta}_{i1C}+C_{12}\dot{\delta}_{i2C}+C_{13}\dot{\delta}_{i3C}+C_{14}\dot{\delta}_{i4C})\\ &+\lambda_2(C_{21}\dot{\delta}_{i1C}+C_{22}\dot{\delta}_{i2C}+C_{23}\dot{\delta}_{i3C}+C_{24}\dot{\delta}_{i4C})\\ &+\lambda_3(C_{31}\dot{\delta}_{i1C}+C_{32}\dot{\delta}_{i2C}+C_{33}\dot{\delta}_{i3C}+C_{34}\dot{\delta}_{i4C})\end{aligned}$$

$$\frac{\partial}{\partial \dot{\vec{\delta}}_{iC}}(\vec{\lambda} \cdot [C]\dot{\vec{\delta}}_{iC}) = \begin{bmatrix} C_{11}\lambda_1+C_{21}\lambda_2+C_{31}\lambda_3 \\ C_{12}\lambda_1+C_{22}\lambda_2+C_{32}\lambda_3 \\ C_{13}\lambda_1+C_{23}\lambda_2+C_{33}\lambda_3 \\ C_{14}\lambda_1+C_{24}\lambda_2+C_{34}\lambda_3 \end{bmatrix} \equiv [C]^T\vec{\lambda}$$

where the superscript T indicates the transposed matrix. Thus,

$$\frac{\partial L}{\partial \dot{\vec{\delta}}_{1C}} = \dot{\vec{\delta}}_{1C} - H[A]^T\vec{\lambda} = 0 \qquad (6\text{-}18)$$

$$\frac{\partial L}{\partial \dot{\vec{\delta}}_{3C}} = \dot{\vec{\delta}}_{3C} - H[B]^T\vec{\lambda} = 0 \qquad (6\text{-}19)$$

$$\frac{\partial L}{\partial \vec{\lambda}} = T'_C - H[A]\dot{\vec{\delta}}_{1C} - H[B]\dot{\vec{\delta}}_{3C} = 0 \qquad (6\text{-}20)$$

Substituting 6-18 and 6-19 into 6-20:

$$\vec{T}'_C = H[A]H[A]^T\vec{\lambda} + H[B]H[B]^T\vec{\lambda}$$
$$= H^2\{[A][A]^T + [B][B]^T\}\vec{\lambda} \qquad (6\text{-}21)$$

Defining:

$$[G] \triangleq [A][A]^T + [B][B]^T \qquad (6\text{-}22)$$

[G] is a 3x3 matrix and is symmetric by examination of equation 6-22, further, since it is square, equation 6-21 can be solved for $\vec{\lambda}$:

$$\vec{\lambda} = \frac{1}{H^2}[G]^{-1}\vec{T}'_C \qquad (6\text{-}23)$$

Finally, substituting into equations 6-18 and 6-19 and rearranging:

$$\dot{\vec{\delta}}_{1C} = \frac{1}{H}[A]^T[G]^{-1}\vec{T}'_C \qquad (6\text{-}24)$$

$$\dot{\vec{\delta}}_{3C} = \frac{1}{H}[B]^T[G]^{-1}\vec{T}'_C \qquad (6\text{-}25)$$

In summary, the CMG control law must be implemented digitally. The gimbal angle state is required to form the matrices [A] and [B] as defined in equations 6-13 and 6-14, respectively. The matrix [G] is formed using equation 6-22. Then, given the command torque $\vec{T}'_C$, the gimbal rate commands are computed from equations 6-24 and 6-25.

It should be noted that the basic steering law presented in this paragraph can easily be altered for changes in CMG mounting arrangements. Once a cluster configuration has been defined, the output to pallet transformations can be determined and these will replace equations 6-1 through 6-4. These new transformations are used in equation 6-9 to generate new forms of the matrices [A] and [B] and the balance of the computation remains as given above.

7. CONTROL MOMENT GYRO (CMG) MODEL

The CMG used in this study is the Skylab Apollo Telescope Mount (ATM) CMG. The unique aspect of this study, when compared to previous studies utilizing the ATM CMG model, is that the CMG is attached to the floated pallet through shockmount isolators. In previous studies associated with the ATM CMG, the CMG is considered to be rigidly mounted to the vehicle. Also in previous studies vehicle rates have been considered small when compared to CMG gimbal rates, therefore CMG base rates were assumed to be zero.

Since in the present study the base of the CMG is mounted on springs, the base rates have values comparable to the gimbal rates.

The primary purpose of developing a CMG model for this study is to determine how the CMG base rates ($\vec{\omega}_b$), caused by shockmount dynamics, change the six-mass CMG dynamic model.

7.1 Compliances - All structures of the CMG are considered to be rigid with the exception of the gear train compliance and the compliance between the inner gimbal and the CMG rotor.

7.2 Shockmount - The CMG is mounted on shockmounts along each axis. The purpose of this shockmount system is to isolate the high frequency vibrations within the CMG from reaching the pallet. These shockmounts have a bandwidth of 20 Hz with a damping ratio of 0.15. Effect of these springs on the CMG system will be to lower the bandwidth of the CMG. This will require that the CMG/shockmount system be frequency compensated to increase the bandwidth of the overall CMG/shockmount system.

7.3 CMG Friction - The CMG friction is modeled classically to switch between static (stiction) and running (coulomb) friction. Ideally, this switch occurs whenever the motor rate $\dot{\delta}_{mi}$ (i=1,3) or gimbal rate $\dot{\delta}_i$ is driven to or away from a zero value. The following discussion pertains to inner gimbal bearing friction, however, inner gimbal torque motor friction, outer gimbal torque motor friction, and outer gimbal bearing friction are similar. The friction torque T_{fg1} (see figure 10-2) is equal to the static level T_{sg1} during stiction and equal to the running level $T_{Rg1} = \pm R_g$ during coulomb friction.

During stiction, the friction torque $T_{fg1}=T_{sg1}$ achieves whatever instantaneous value is required to maintain the inner gimbal fixed relative to the outer gimbal, i.e., $\dot{\delta}_1=0$, so long as this torque never exceeds the maximum static level S_g. Thus, during stiction

$$\omega_{ax}=\omega_{cx}$$

and

$$\dot{\omega}_{ax}=\dot{\omega}_{cx}$$

where

ω_{ax} = inertial inner gimbal angular rate about inner gimbal x axis

ω_{cx} = inertial outer gimbal angular rate about inner gimbal x axis

The torque required to maintain this condition is therefore obtained as follows:

$$-T_{sg1}=T_{g1}-T_{wx}-J_{all}\dot{\omega}_{cx}$$

where

T_{g1} = inner gimbal gear train output torque

T_{wx} = wheel momentum reaction torque about inner gimbal x axis

J_{all} = inertia of inner gimbal and motor rotor assembly about inner gimbal x axis

As a practical matter, each CMG friction model was implemented on the analog portion of the hybrid computer as shown in figure 10-2. The friction torque T_{fg1} switches from a running condition to a static condition whenever

$$|\dot{\delta}_1|<\varepsilon_g$$

and

$$|T_{sg1}|<S_g$$

where ε_g is a small value slightly larger than the noise level of the computer. Once in a static condition, the friction torque T_{fg1} switches to a running level only when

$$|T_{sg1}|>S_g$$

This insures that only the required breakaway torque will initiate a running condition and not $\dot{\delta}_1$ noise. The value for T_{sg1} is monitored and tested continuously in order to implement these switching decisions.

Rather than feed $T_{fg1}=T_{sg1}$ to the inner gimbal inertia integrator during stiction, and thus introduce the possibility of drift between inertial inner and outer gimbal angular rates, the inner gimbal inertial rate ω_{ax} is forced to equal ω_{cx} (i.e., $\dot{\delta}_1=0$) by disabling the inner gimbal integrator and causing the initial condition to equal ω_{cx} at any instant of time. Once switching to the running condition has occurred, the integrator is then freed to follow the input

$$T_{g1}-T_{wx}+T_{fg1}=T_{g1}-T_{wx}+T_{Rg1}$$

Furthermore to avoid gear train stiffness integrator drift, the gear train stiffness integrator is placed in hold when both motor and gimbal are stuck.

Finally, to avoid an algebraic loop in implementing the outer gimbal static friction, the following calculation is made. The expression for T_{sg3} is

$$T_{sg3}=-T_{g3}+c\delta_1 T_{wz}+J'_{c33}\dot{\omega}_{bz}$$

where

T_{sg3} = outer gimbal static friction torque

T_{g3} = outer gimbal gear train output torque

T_{wz} = wheel momentum reactiontorque about inner gimbal z axis

J'_{c33} = equivalent outer gimbal inertia about outer gimbal z axis

ω_{bz} = inertial CMG base angular rate about outer gimbal z axis

Now, $\dot{\omega}_{bz}$ can be evaluated from the z axis base equation of motion as follows:

$$\dot{\omega}_{bz} = -\frac{1}{J_{b33}}(T_{g3}+T_{sg3}+T_{pz})$$

where:

J_{b33} = CMG base inertia about base z axis

$T_{p'z}$ = torque exerted on pallet about CMG base z axis

Substituting into the expression for T_{sg3} and solving for T_{sg3} gives

$$T_{sg3} = -T_{g3} - \frac{J'_{c33}}{J_{b33}+J'_{c33}} T_{pz} + \frac{J_{b33}}{J_{b33}+J'_{c33}} \cos\delta_1 T_{wz}.$$

This expression for T_{sg3} is used in the friction logic on a continuous basis, and is also substituted for T_{fg3} in the shockmount dynamics during outer gimbal stiction.

7.4 Coordinate Systems - There are five coordinate systems used to define the shockmounted CMG: 1) the wheel coordinate frame (W-space), 2) inner gimbal coordinate frame (A-space), 3) outer gimbal coordinate frame (C-space), 4) CMG base coordinate frame (B-space), and 5) the pallet end of the shockmount (P'-space). Figure 7-1 shows the general relationship of these five coordinate systems. When both CMG gimbal angles (δ_1,δ_3) are in the zero position and the two spring equivalent systems (γ_i,θ_{Si}) are in the relaxed state, then all five systems are aligned.

Each of the systems are discussed below with the appropriate transformations defined.

7.4.1 Wheel Coordinate System (W-space) - The wheel coordinate frame is fixed in the rotor of the CMG. The spin vector of the rotor is in the positive y direction of the W-frame, the x axis of the W-system points out through the inner gimbal torquer, and the right-hand system is completed by the z axis.

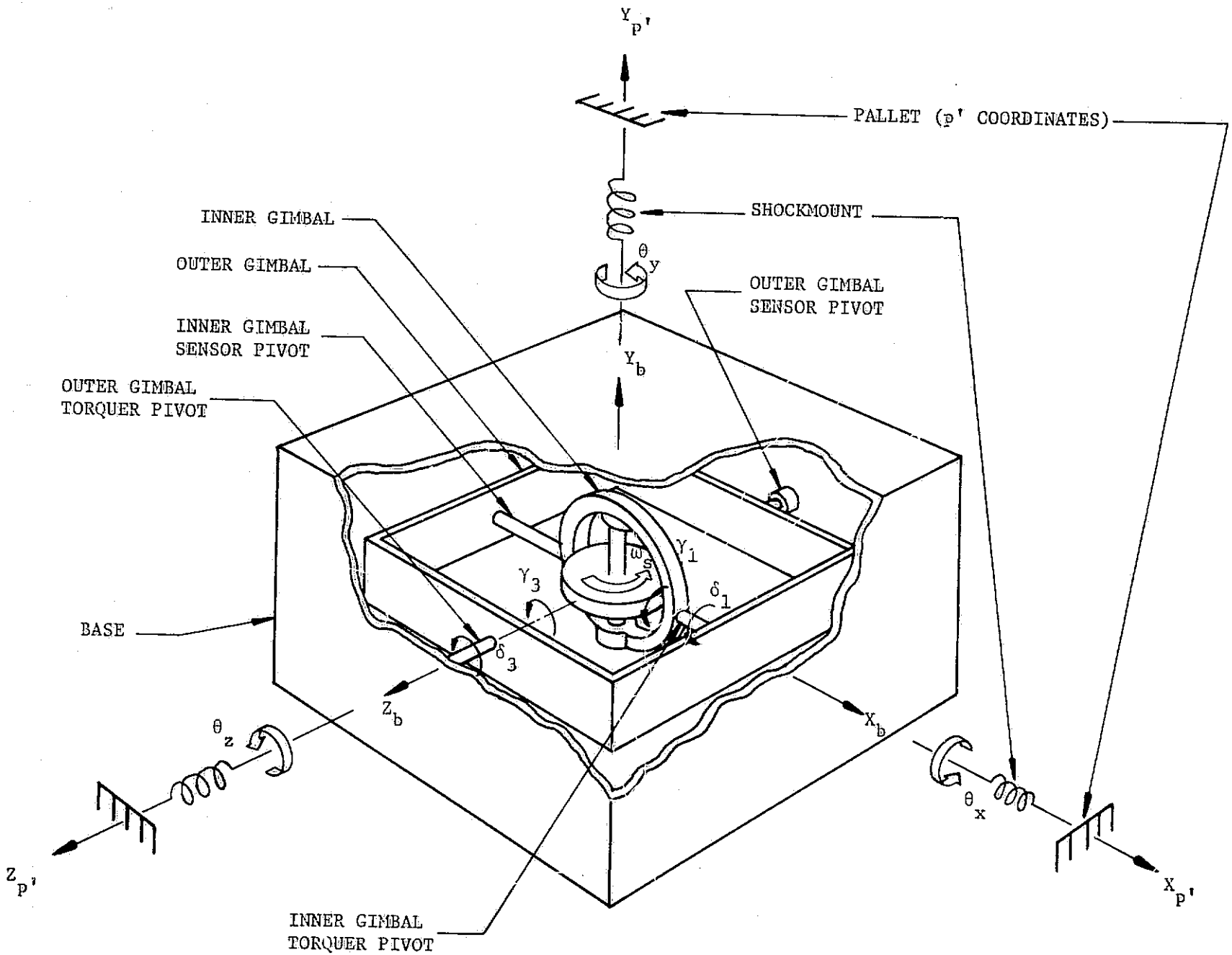

Figure 7-1. Coordinate Frame Relationship With No Deflections

7.4.2 Inner Gimbal Coordinate System (A-space) - This coordinate system is fixed in the inner gimbal frame of the CMG. The system is defined with the x axis along the axis of the inner gimbal torquer, the y axis along the spin vector of the rotor and the z axis completing the right-hand system.

Compliance springs (γ_i) provide the connection between the rotor and the inner gimbal. These springs provide support along the x and z axis only with the rotor free to spin about the y axis. Deflection about the x axis is defined as γ_1 and deflection about the z axis is defined by γ_3. Deflections are considered to be small angle and the transformation from A-space to W-space is given by equation 7-1.

$$[{}_wT_a]=\begin{bmatrix} 1 & \gamma_3 & 0 \\ -\gamma_3 & 1 & \gamma_1 \\ 0 & -\gamma_1 & 1 \end{bmatrix} \approx \begin{bmatrix} 1 & 0 & 0 \\ 0 & 1 & 0 \\ 0 & 0 & 1 \end{bmatrix} \qquad (7\text{-}1)$$

7.4.3 Outer Gimbal Coordinate System (C-space) - This system is fixed in the outer gimbal defined with the x axis through the inner gimbal torquer, the z axis through the outer gimbal torquer, and the y axis completing the right-hand coordinate system. The inner gimbal (A-space) and outer gimbal (C-space) are related by the rotation of the inner gimbal through the angle δ_1. Equation 7-2 gives the transformation from C-space to A-space.

$$[{}_aT_c]=\begin{bmatrix} 1 & 0 & 0 \\ 0 & \cos\delta_1 & \sin\delta_1 \\ 0 & -\sin\delta_1 & \cos\delta_1 \end{bmatrix} \qquad (7\text{-}2)$$

7.4.4 Base Coordinate System (B-space) - The base system is fixed in the CMG base with the z axis along the centerline of the outer gimbal torquer. The base is related to the outer gimbal system through the rotation of the outer gimbal through the angle δ_3. When $\delta_3=0$, the base (B) and outer gimbal (C) systems are aligned. The transformation relating the B and C system is given by equation 7-3.

$$[{}_cT_b] = \begin{bmatrix} \cos\delta_3 & \sin\delta_3 & 0 \\ -\sin\delta_3 & \cos\delta_3 & 0 \\ 0 & 0 & 1 \end{bmatrix} \tag{7-3}$$

7.4.5 Shockmount Coordinate System (P'-space) - The shockmount coordinate system is fixed on the pallet end of the shockmount. This system is related to the pallet system (P-space) by the transformation defined in section 6.6. Also this system is essentially aligned with the base system, displaced only by the small angle θ rotations. Equation 7-4 gives the transformation from the P'-space to B-space.

$$[{}_bT_{p'}] = \begin{bmatrix} 1 & \theta_z & -\theta_y \\ -\theta_z & 1 & \theta_x \\ \theta_y & -\theta_x & 1 \end{bmatrix} \approx \begin{bmatrix} 1 & 0 & 0 \\ 0 & 1 & 0 \\ 0 & 0 & 1 \end{bmatrix} \tag{7-4}$$

7.5 CMG Dynamics - Dynamic equations are written for the rotor (γ-dynamics), inner gimbal, outer gimbal, and CMG base. These equations are used to develop the CMG rate loops and the torque output exerted on the pallet from the CMG. All product of rate terms are considered to be small and are not used throughout the development.

7.5.1 Inner Gimbal/Rotor Compliance (γ) Dynamics - In this section the equations are developed which relate the rotor (W-space) dynamics to the inner gimbal. The angular momentum of the rotor ($\vec{H}_r$) written in W-space is

$$\vec{H}_r = \begin{bmatrix} J_d & 0 & 0 \\ 0 & J_r & 0 \\ 0 & 0 & J_d \end{bmatrix} \left\{ \vec{\omega}_w + \begin{bmatrix} 0 \\ \omega_s \\ 0 \end{bmatrix} \right\} = \begin{bmatrix} J_d\omega_{wx} \\ J_r(\omega_{wy}+\omega_s) \\ J_d\omega_{wz} \end{bmatrix} \tag{7-5}$$

where J_d and J_r are the moments of inertia of the rotor about a diameter and the spin axis, respectively, $\vec{\omega}_w$ is the inertial rate of the wheel frame and ω_s is the spin rate of the rotor. Torque ($\vec{T}_w$) exerted onto the wheel frame written in W-space is

$$\vec{T}_w = \frac{d\vec{H}_r}{dt} + \vec{\omega}_w x \vec{H}_r$$

$$\begin{bmatrix} T_{wx} \\ T_{wy} \\ T_{wz} \end{bmatrix} = \begin{bmatrix} J_d \dot{\omega}_{wx} \\ J_r(\dot{\omega}_{wy} + \dot{\omega}_s) \\ J_d \dot{\omega}_{wz} \end{bmatrix} + \begin{bmatrix} -\omega_{wz} H_r \\ 0 \\ \omega_{wx} H_r \end{bmatrix} \tag{7-6}$$

All product of rate terms have been neglected because torques from this source are small compared to the gyroscopic torques.

Torques exerted onto the wheel frame (i.e., $\vec{T}_{wi}$; i=x,y,z) are from the γ compliance springs and are

$$\begin{bmatrix} T_{wx} \\ T_{wy} \\ T_{wz} \end{bmatrix} = \begin{bmatrix} -K_{\gamma 1}\gamma_1 - \beta_{\gamma 1}\dot{\gamma}_1 \\ -K_{\gamma 2}\gamma_2 - \beta_{\gamma 2}\dot{\gamma}_2 \\ -K_{\gamma 3}\gamma_3 - \beta_{\gamma 3}\dot{\gamma}_3 \end{bmatrix} \tag{7-7}$$

where γ_i is the displacement between the wheel frame and the inner gimbal frame, and

$$\begin{bmatrix} \dot{\gamma}_1 \\ \dot{\gamma}_2 \\ \dot{\gamma}_3 \end{bmatrix} = \begin{bmatrix} \omega_{wx} - \omega_{ax} \\ \omega_{wy} - \omega_{ay} \\ \omega_{wz} - \omega_{az} \end{bmatrix} \tag{7-8}$$

where ω_{ai} is the inertial rate of the inner gimbal. From equations 7-6 and 7-7, the following relationship exists

$$J_d \dot{\omega}_{wx} = -K_{\gamma 1}\gamma_1 - \beta_{\gamma 1}\dot{\gamma}_1 + H_r \omega_{wz}$$

$$J_d \dot{\omega}_{wz} = -K_{\gamma 3}\gamma_3 - \beta_{\gamma 3}\dot{\gamma}_3 - H_r \omega_{wx}$$

Using these relationships and equation 7-8, figure 7-2 gives the γ dynamics in block diagram form.

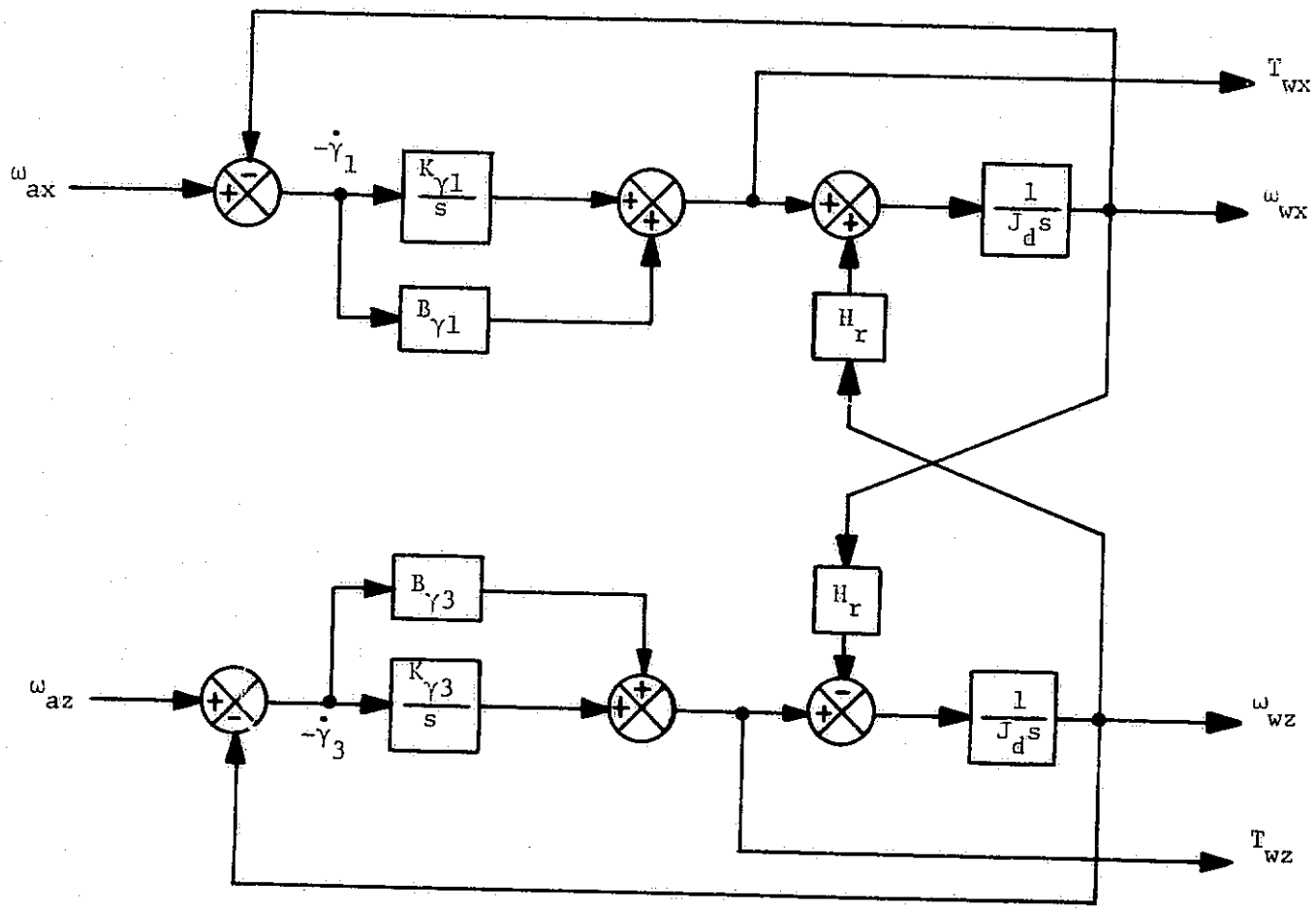

Figure 7-2. Inner Gimbal/Rotor Compliance (γ) Dynamics

7.5.2 Inner Gimbal Dynamics - Angular momentum ($\vec{H}_a$) of the inner gimbal written in A-space is

$$\vec{H}_a = \begin{bmatrix} J_{a11} & 0 & 0 \\ 0 & J_{a22} & 0 \\ 0 & 0 & J_{a33} \end{bmatrix} \vec{\omega}_a = \begin{bmatrix} J_{a11}\omega_{ax} \\ J_{a22}\omega_{ay} \\ J_{a33}\omega_{az} \end{bmatrix} \tag{7-9}$$

where J_{ai} are the principal axis inertial terms for the inner gimbal.

The inner gimbal dynamic equation written in A-space is

$$\vec{T}_{ext} = \frac{d\vec{H}_a}{dt} + \vec{\omega}_a x \vec{H}_a$$

where $\vec{T}_{ext}$ is the sum of all external torques acting on the inner gimbal. External torques acting on the inner gimbal consist of two components, the torque exerted by the outer gimbal ($\vec{T}_a$) onto the inner gimbal and the torques exerted from the wheel frame onto the inner gimbal. This second torque will be the negative of the torque $\vec{T}_w$. Therefore

$$\begin{bmatrix} T_{ax} \\ T_{ay} \\ T_{az} \end{bmatrix} - \begin{bmatrix} T_{wx} \\ T_{wy} \\ T_{wz} \end{bmatrix} \cong \begin{bmatrix} J_{a11}\dot{\omega}_{ax} \\ J_{a22}\dot{\omega}_{ay} \\ J_{a33}\dot{\omega}_{az} \end{bmatrix} \tag{7-10}$$

with the product of rate terms being neglected.

7.5.3 Outer Gimbal Dynamics - Equations representing the outer gimbal dynamics are developed in a similar manner as those for the inner gimbal. External torques acting on the outer gimbal are $\vec{T}_c$ (torques from the base onto the outer gimbal) and the reaction torques from the inner gimbal $-\vec{T}_a$ transformed to C-space.

The angular momentum ($\vec{H}_c$) of the outer gimbal written in C-space is

$$\vec{H}_c = \begin{bmatrix} J_{c11} & 0 & 0 \\ 0 & J_{c22} & 0 \\ 0 & 0 & J_{c33} \end{bmatrix} \vec{\omega}_c = \begin{bmatrix} J_{c11}\omega_{cx} \\ J_{c22}\omega_{cy} \\ J_{c33}\omega_{cz} \end{bmatrix} \tag{7-11}$$

where J_{ci} are the principal axis inertia terms for the outer gimbal and $\vec{\omega}_c$ is the inertial rate of the outer gimbal.

Again, neglecting product of rate terms and writing the outer gimbal dynamic equation in C-space

$$\vec{T}_c - [{}_cT_a]\vec{T}_a = \frac{d\vec{H}_c}{dt} + \vec{\omega}_c x \vec{H}_c \tilde{=} \begin{bmatrix} J_{c11}\dot{\omega}_{cx} \\ J_{c22}\dot{\omega}_{cy} \\ J_{c33}\dot{\omega}_{cz} \end{bmatrix} \tag{7-12}$$

Now, writing the inner gimbal inertial rate ($\vec{\omega}_a$) in terms of outer gimbal inertia rate ($\vec{\omega}_c$) plus the inner gimbal rate

$$\vec{\omega}_a = [{}_aT_c] \quad \vec{\omega}_c + \begin{bmatrix} \dot{\delta}_1 \\ 0 \\ 0 \end{bmatrix}$$

or

$$\begin{bmatrix} \omega_{ax} \\ \omega_{ay} \\ \omega_{az} \end{bmatrix} = \begin{bmatrix} 1 & 0 & 0 \\ 0 & c\delta_1 & s\delta_1 \\ 0 & -s\delta_1 & c\delta_1 \end{bmatrix} \begin{bmatrix} \omega_{cx}+\dot{\delta}_1 \\ \omega_{cy} \\ \omega_{cz} \end{bmatrix} \tag{7-13}$$

Now by taking the derivative of equation 7-13 again neglecting product of rate terms

$$\begin{bmatrix} \dot{\omega}_{ax} \\ \dot{\omega}_{ay} \\ \dot{\omega}_{az} \end{bmatrix} = \begin{bmatrix} 1 & 0 & 0 \\ 0 & c\delta_1 & s\delta_1 \\ 0 & -s\delta_1 & c\delta_1 \end{bmatrix} \begin{bmatrix} \dot{\omega}_{cx}+\ddot{\delta}_1 \\ \dot{\omega}_{cy} \\ \dot{\omega}_{cz} \end{bmatrix} \tag{7-14}$$

Substituting equation 7-14 into equation 7-10, and then 7-10 into 7-12, produces the dynamic equation for the outer gimbal written in C-space.

$$\begin{bmatrix} T_{cx} \\ T_{cy} \\ T_{cz} \end{bmatrix} - \begin{bmatrix} 1 & 0 & 0 \\ 0 & c\delta_1 & -s\delta_1 \\ 0 & s\delta_1 & c\delta_1 \end{bmatrix} \left\{ \begin{bmatrix} T_{wx} \\ T_{ms} \\ T_{wz} \end{bmatrix} + \begin{bmatrix} J_{a11} & 0 & 0 \\ 0 & J_{a22} & 0 \\ 0 & 0 & J_{a33} \end{bmatrix} \begin{bmatrix} 1 & 0 & 0 \\ 0 & c\delta_1 & s\delta_1 \\ 0 & -s\delta_1 & c\delta_1 \end{bmatrix} \begin{bmatrix} \dot{\omega}_{cx}+\ddot{\delta}_1 \\ \dot{\omega}_{cy} \\ \dot{\omega}_{cz} \end{bmatrix} \right\}$$

$$\approx \begin{bmatrix} J_{c11}\dot{\omega}_{cx} \\ J_{c22}\dot{\omega}_{cy} \\ J_{c33}\dot{\omega}_{cz} \end{bmatrix} \quad (7-$$

Equation 7-15 reduces to

$$\begin{bmatrix} T_{cx} \\ T_{cy} \\ T_{cz} \end{bmatrix} - \begin{bmatrix} 1 & 0 & 0 \\ 0 & c\delta_1 & -s\delta_1 \\ 0 & s\delta_1 & c\delta_1 \end{bmatrix} \begin{bmatrix} T_{wx} \\ 0 \\ T_{wz} \end{bmatrix} \approx \begin{bmatrix} J'_{c11} & 0 & 0 \\ 0 & J'_{c22} & 0 \\ 0 & 0 & J'_{c33} \end{bmatrix} \begin{bmatrix} \dot{\omega}_{cx} \\ \dot{\omega}_{cy} \\ \dot{\omega}_{cz} \end{bmatrix} + \begin{bmatrix} J_{a11}\ddot{\delta}_1 \\ 0 \\ 0 \end{bmatrix} \tag{7-16}$$

where T_{ms} (torque about rotor spin axis) and $(J_{a22}-J_{a33})$ are considered small and

$$J'_{c11}=J_{c11}+J_{a11}$$

$$J'_{c22}=J_{c22}+\frac{1}{2}(J_{a22}+J_{a33})$$

$$J'_{c33}=J_{c33}+\frac{1}{2}(J_{a22}+J_{a33})$$

7.5.4 <u>CMG Base Dynamics</u> - Angular momentum ($\vec{H}_b$) of the base written in base space is

$$\vec{H}_b = \begin{bmatrix} J_{b11} & 0 & 0 \\ 0 & J_{b22} & 0 \\ 0 & 0 & J_{b33} \end{bmatrix} \vec{\omega}_b = \begin{bmatrix} J_{b11}\omega_{bx} \\ J_{b22}\omega_{by} \\ J_{b33}\omega_{bz} \end{bmatrix} \tag{7-17}$$

where $\vec{\omega}_b$ is the inertial rate of the base frame, and J_{bii} are the principal axis inertia terms of the base.

Writing the base dynamic equation in B-space

$$\vec{T}_b - [{}_bT_c]\vec{T}_c = \frac{d\vec{H}_b}{dt} + \vec{\omega}_b x \vec{H}_b$$

where $\vec{T}_b$ is the torque exerted on the base by the shockmount springs and $-[{}_bT_c]\vec{T}_c$ is the reaction torque from the outer gimbal onto the base expressed in B-space. This equation readily reduces to

$$\begin{bmatrix} T_{bx} \\ T_{by} \\ T_{bz} \end{bmatrix} - \begin{bmatrix} c\delta_3 & -s\delta_3 & 0 \\ s\delta_3 & c\delta_3 & 0 \\ 0 & 0 & 1 \end{bmatrix} \begin{bmatrix} T_{cx} \\ T_{cy} \\ T_{g3}+T_{fg3} \end{bmatrix} \approx \begin{bmatrix} J_{b11}\dot{\omega}_{bx} \\ J_{b22}\dot{\omega}_{by} \\ J_{b33}\dot{\omega}_{bz} \end{bmatrix} \tag{7-18}$$

and the outer gimbal acceleration is related to base acceleration by

$$\begin{bmatrix} \dot{\omega}_{cx} \\ \dot{\omega}_{cy} \\ \dot{\omega}_{cz} \end{bmatrix} = \begin{bmatrix} c\delta_3 & s\delta_3 & 0 \\ -s\delta_3 & c\delta_3 & 0 \\ 0 & 0 & 1 \end{bmatrix} \begin{bmatrix} \dot{\omega}_{bx} \\ \dot{\omega}_{by} \\ \dot{\omega}_{bz}+\ddot{\delta}_3 \end{bmatrix} \tag{7-19}$$

when product of rate terms are neglected.

7.5.4.1 Base Rate About the z-Axis - Base rate about the z-axis (ω_{bz}) is obtained directly from equation 7-18 since all torques are readily available.

T_{bz} is the torque exerted on the base by the shockmount spring and $T_{g3}+T_{fg3}$ is the resultant torque generated by the outer gimbal torquer. Since both of these torques are known and act directly along the base z axis, the following relationship is written

$$T_{bz}-(T_{g3}+T_{fg3})=J_{b33}\dot{\omega}_{bz}$$

and $\dot{\omega}_{bz}$ and ω_{bz} are obtained directly as shown in figure 7-3.

7.5.4.2 Base Rate About the x and y Axes - Base rates about x (ω_{bx}) and y (ω_{by}) axes is not obtained as easily as was ω_{bz}. T_{cx} and T_{cy} in equation 7-18 must be obtained by combining equations 7-16 through 7-19 as follows

$$\begin{bmatrix} T_{bx} \\ T_{by} \\ T_{bz} \end{bmatrix} - \begin{bmatrix} c\delta_3 & -s\delta_3 & 0 \\ s\delta_3 & c\delta_3 & 0 \\ 0 & 0 & 1 \end{bmatrix} \left\{ \begin{bmatrix} 1 & 0 & 0 \\ 0 & c\delta_1 & -s\delta_1 \\ 0 & s\delta_1 & c\delta_1 \end{bmatrix} \begin{bmatrix} T_{wx} \\ 0 \\ T_{wz} \end{bmatrix} + \begin{bmatrix} J'_{c11} & 0 & 0 \\ 0 & J'_{c22} & 0 \\ 0 & 0 & J'_{c33} \end{bmatrix} \begin{bmatrix} c\delta_3 & s\delta_3 & 0 \\ -s\delta_3 & c\delta_3 & 0 \\ 0 & 0 & 1 \end{bmatrix} \begin{bmatrix} \dot{\omega}_{bx} \\ \dot{\omega}_{by} \\ \dot{\omega}_{bz}+\ddot{\delta}_3 \end{bmatrix} + \begin{bmatrix} J_{a11}\ddot{\delta}_1 \\ 0 \\ 0 \end{bmatrix} \right\} \approx \begin{bmatrix} J_{b11}\dot{\omega}_{bx} \\ J_{b22}\dot{\omega}_{by} \\ J_{b33}\dot{\omega}_{bz} \end{bmatrix} \quad (7\text{-}20)$$

Expanding equation 7-20 gives

$$\begin{bmatrix} T_{bx} \\ T_{by} \\ T_{bz} \end{bmatrix} - \begin{bmatrix} c\delta_3 T_{wx}+s\delta_1 s\delta_3 T_{wz} \\ s\delta_3 T_{wx}-s\delta_1 c\delta_3 T_{wz} \\ c\delta_1 T_{wz} \end{bmatrix} \approx [J'] \begin{bmatrix} \dot{\omega}_{bx} \\ \dot{\omega}_{by} \\ \dot{\omega}_{bz} \end{bmatrix} + \begin{bmatrix} J_{a11} c\delta_3 \ddot{\delta}_1 \\ J_{a11} s\delta_3 \ddot{\delta}_1 \\ J'_{c33}\ddot{\delta}_3 \end{bmatrix} \quad (7\text{-}21)$$

where

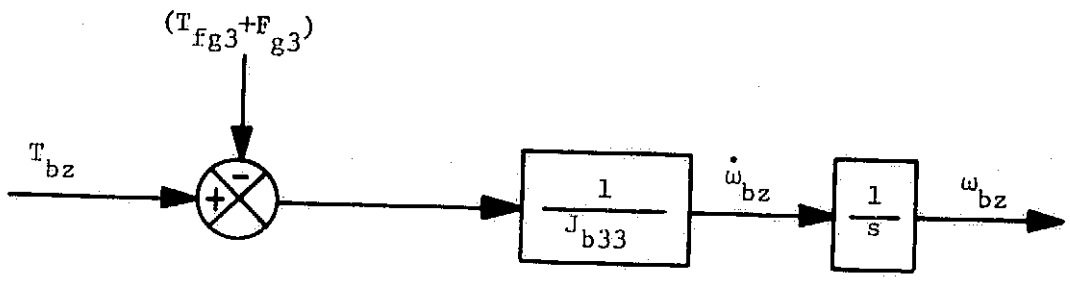

Figure 7-3. Z Axis Dynamics of the CMG Base

$$[J'] = \begin{bmatrix} J'_{11} & J'_{12} & J'_{13} \\ J'_{21} & J'_{22} & J'_{23} \\ J'_{31} & J'_{32} & J'_{33} \end{bmatrix}$$

and

$$J'_{11} = J_{b11} + \frac{1}{2}(J'_{c11} + J'_{c22}) + \frac{1}{2}(J'_{c11} - J'_{c22})c2\delta_3$$

$$J'_{12} = J'_{21} = \frac{1}{2}(J'_{c11} - J'_{c22})s2\delta_3$$

$$J'_{13} = J'_{23} = J'_{31} = J'_{32} = 0$$

$$J'_{22} = J_{b22} + \frac{1}{2}(J'_{c11} + J'_{c22}) - \frac{1}{2}(J'_{c11} - J'_{c22})c2\delta_3$$

$$J'_{33} = J_{b33} + J'_{c33}$$

Considering only the x and y component of equation 7-21, and rearranging

$$\begin{bmatrix} J'_{11} & J'_{12} \\ J'_{21} & J'_{22} \end{bmatrix} \begin{bmatrix} \dot{\omega}_{bx} \\ \dot{\omega}_{by} \end{bmatrix} = \begin{bmatrix} T_{bx} \\ T_{by} \end{bmatrix} - \begin{bmatrix} c\delta_3 T_{wx} + s\delta_1 s\delta_3 T_{wz} \\ s\delta_3 T_{wx} - s\delta_1 c\delta_3 T_{wz} \end{bmatrix} - \begin{bmatrix} J_{a11} c\delta_3 \ddot{\delta}_1 \\ J_{a11} s\delta_3 \ddot{\delta}_1 \end{bmatrix} . \quad (7\text{-}22)$$

For the purposes of this study, J'_{12} (therefore J'_{21}) is considered negligible when compared to J'_{11} and J'_{22}; J'_{11} and J'_{22} can be approximated as

$$J'_{11} \approx J_{b11} + \frac{1}{2}(J_{c11} + J_{c22} + J_{a11}) + \frac{1}{4}(J_{a22} + J_{a33})$$

$$J'_{22} \approx J_{b22} + \frac{1}{2}(J_{c11} + J_{c22} + J_{a11}) + \frac{1}{4}(J_{a22} + J_{a33})$$

Therefore equation 7-22 can be solved directly for $\dot{\omega}_{bx}$ and $\dot{\omega}_{by}$. Figure 7-4 gives the block diagram showing the solution of equation 7-22.

7.5.5 Shockmount Dynamics - Shockmount spring stiffness K_{si} and damping D_{si} have been chosen to give a natural frequency of approximately 20 Hz with a damping of 0.15. Since the rotation of the shockmount system is small angle, the torque exerted on the pallet via the shockmount is given as

$$T_{P'i}=K_{Si}\theta_i+D_{Si}\dot{\theta}_i \tag{7-23}$$

where $\dot{\vec{\theta}}=\vec{\omega}_b-\vec{\omega}_P$ and $\vec{\omega}_b$ and $\vec{\omega}_P$ are the inertial rate of the CMG base and pallet, respectively.

The torque exerted on the base (T_{bi}) via the shockmount is the negative of equation 7-23, therefore both torques are generated as shown in figure 7-5. Also, since the pallet rate is small compared to the base rate, $\dot{\vec{\theta}}\approx\vec{\omega}_b$.

7.6 CMG/Shockmount Dynamic Model - The entire CMG/dynamic shockmount model as simulated for this study is shown in section 10 (figure 10-2). The tachometer loop and the motor gear train model is shown in figure 7-6 as established in previous studies (references 4 and 5). Some simplifications have been made to conserve computer space, however, these simplifications have no effect for purposes of this study. Figure 7-6 shows the tachometer loop including voltage limiters, current limiters, and torque limiters which were not included in the simulation model. Signal levels in this study were below those of these limiters, therefore these limiters along with the back emf gain (K_{B1}) were eliminated from the simulation model (figure 10-1).

Effects of the CMG being shockmounted are evident in figure 10-2. Outer gimbal rates are related to base rates by equation 7-24

$$\begin{bmatrix}\omega_{cx}\\ \omega_{cy}\\ \omega_{cz}\end{bmatrix}=\begin{bmatrix}c\delta_3 & s\delta_3 & 0\\ -s\delta_3 & c\delta_3 & 0\\ 0 & 0 & 1\end{bmatrix}\begin{bmatrix}\omega_{bx}\\ \omega_{by}\\ \omega_{bz}\end{bmatrix}+\begin{bmatrix}0\\ 0\\ \dot{\delta}_3\end{bmatrix} \tag{7-24}$$

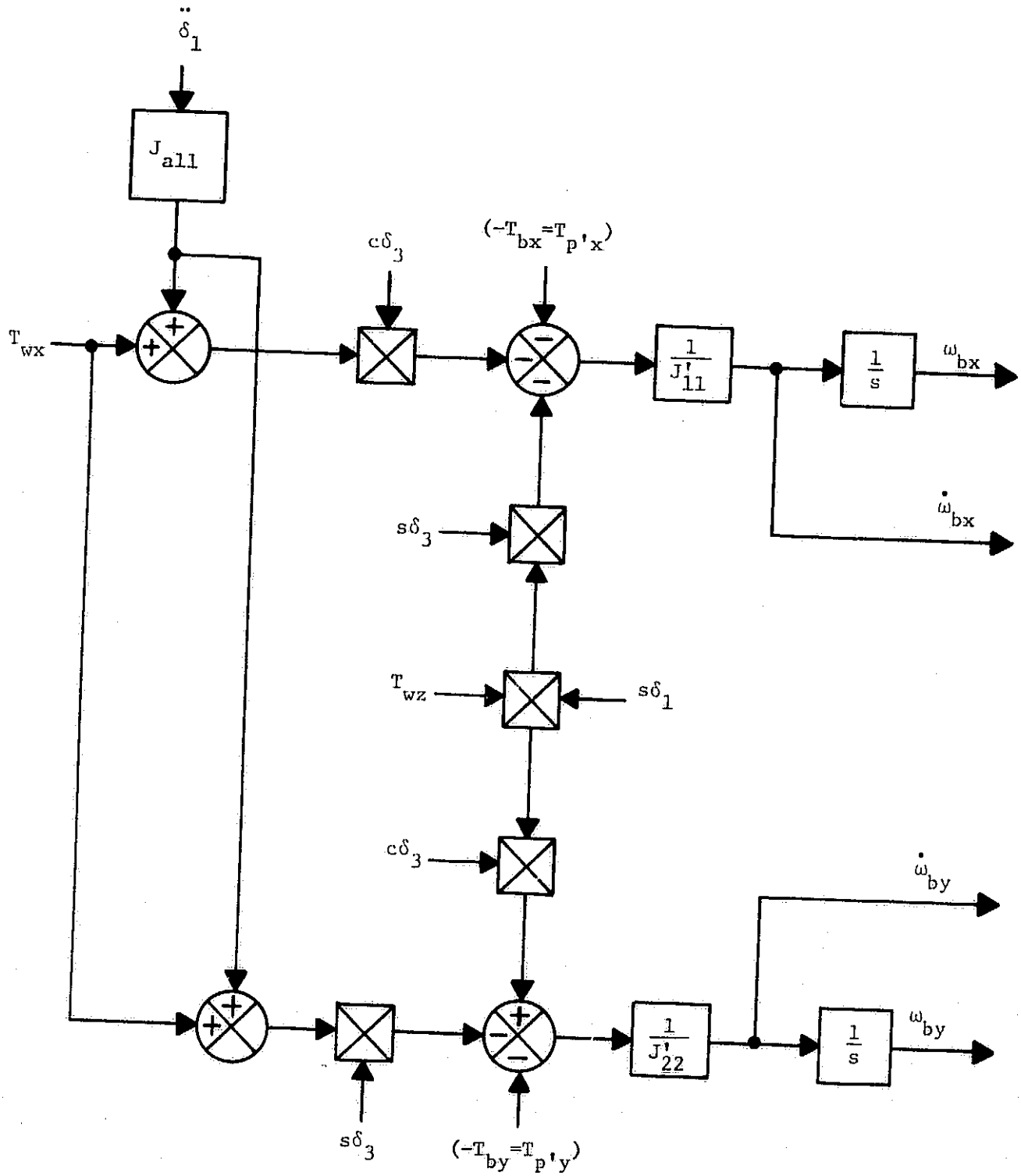

Figure 7-4. Block Diagram of Base Dynamics for X and Y Axes

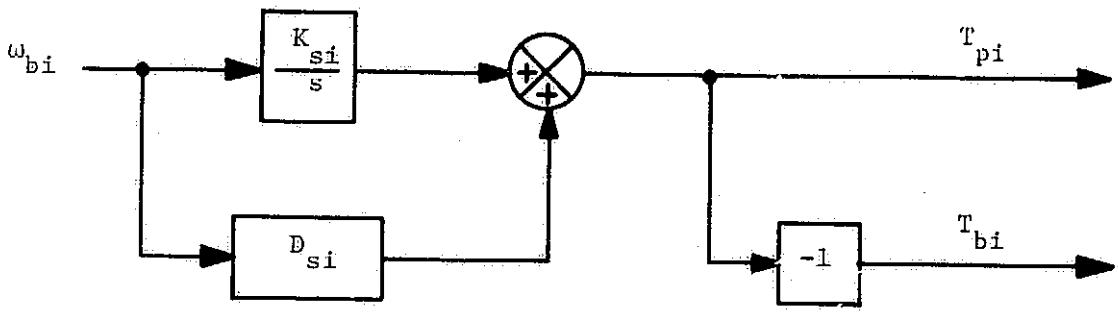

Figure 7-5. Generation of Shockmount Torques

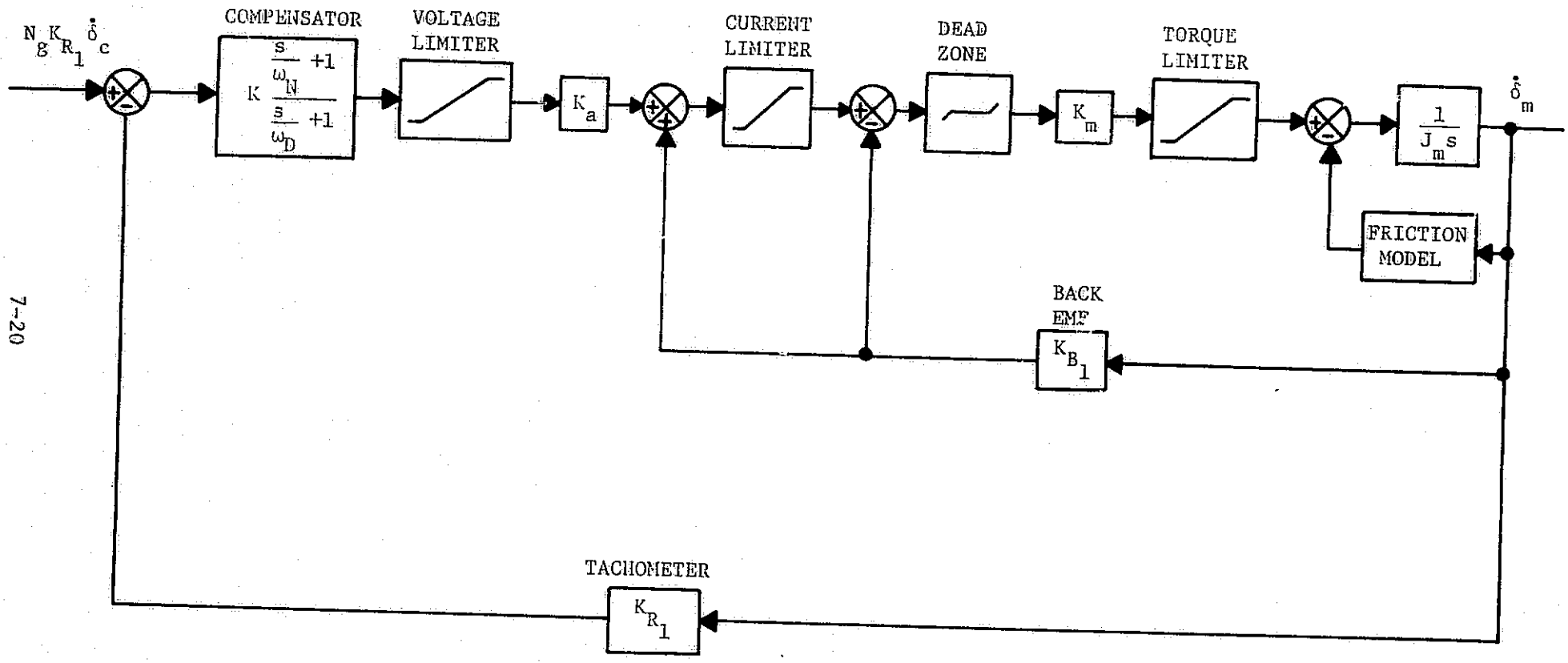

Figure 7-6. CMG Rate Loop

which says that if $\vec{\omega}_b=0$, then $\omega_{cx}=\omega_{cy}=0$ and $\omega_{cz}=\dot{\delta}_3$. Therefore, applying these simplifications to figure 10-2 shows the effect of base rates being non-zero.

7.7 <u>CMG Frequency Response</u> - Studies have been made in which the Skylab ATM CMG was determined to have a bandwidth of approximately 30 radians per second. When the CMG is mounted so that the base is free to move, the effect is to lower the bandwidth of the total system (i.e., torque out to torque input) where torque output is now on the pallet side of the shockmount.

8. CMG-PALLET CONTROL LOOP STUDIES

The objective of the control loop studies is the specification of analytically determined rate, position, and position integral gains in the vehicle control law such that the pallet control loop is stable, has the required 2 Hz bandwidth, and such that the pallet can meet the pointing accuracy requirements. In addition a compensation network analysis is performed to insure that the above requirements can be met when the specified CMGs are placed in the control loop.

While the analyses of this section are based on a nominal 2 Hz pallet control loop, the definition of gains for other bandwidths parallels these derivations. Indeed, gains were derived for several bandwidths above and below the nominal for use in the simulation study which is discussed in section 10 of this volume.

8.1 Vehicle Control Law - The function of the vehicle control law is to compute a CMG torque command $\vec{T}_c$ from sensed body motion that will compensate for unwanted vehicle motion caused by disturbance torques acting on the vehicle. The vehicle control law is also used to generate torque commands required to implement vehicle maneuvers or attitude offsets. The specified vehicle control law is a standard rate plus position plus position integral law which in complete form would be:

$$\vec{T}_c=[K_R](\vec{\omega}_D-\vec{\omega})+[K_P](\vec{\theta}_D-\vec{\theta}+\vec{\varepsilon})+[K_{PI}]\{\int(\vec{\theta}_D-\vec{\theta}+\vec{\varepsilon})dt\}$$

where the gain matrices $[K_R]$, $[K_P]$, and $[K_{PI}]$ are diagonal, the vectors $\vec{\omega}_D$ and $\vec{\theta}_D$ are the desired vehicle rates and positions which would be obtained from maneuver control logic, $\vec{\omega}$ and $\vec{\theta}$ are the sensed vehicle rates and positions and $\vec{\varepsilon}$ represents any small angle attitude offset command, e.g., a CMG desaturation maneuver.

Since the scope of this study includes only pointing performance, all maneuver considerations will be ignored, thus in particular $\vec{\omega}_D$ and $\vec{\varepsilon}$ will be defined to be zero. During any period of inertial pointing the control axes will be held in some constant relationship to a set of references or ideal pointing axes. For the purposes of this study this relationship can be assumed an identity, thus $\vec{\theta}_D$ can also be set to zero giving:

$$\vec{T}_c = -[K_R]\vec{\omega} - [K_P]\vec{\theta} - [K_{PI}]\int \vec{\theta}dt$$

Finally, since perfect sensors are assumed for the purposes of this study, the sensed rate is simply the actual rotation rate of the pallet about any axis. Further since only small angle rotations are under consideration the position and position integral about each axis can be obtained by direct integration of the rate about that axis, thus identifying $\vec{\omega}$ as $\dot{\vec{\theta}}_P$, the control law becomes:

$$\vec{T}_c = -[K_R]\dot{\vec{\theta}}_P - [K_P]\int \dot{\vec{\theta}}_P dt - [K_{PI}]\iint \dot{\vec{\theta}}_P dt$$

In terms of the Laplace operator s this becomes on a per axis basis:

$$T_{ci} = -K_{Ri}\dot{\theta}_{Pi} - K_{Pi}\frac{\dot{\theta}_{Pi}}{s} - K_{PIi}\frac{\dot{\theta}_{Pi}}{s^2} \quad i=x,y,z$$

or,

$$G_1(s) \triangleq \frac{T_{ci}}{\dot{\theta}_{Pi}} = -K_{Ri} - \frac{K_{Pi}}{s} - \frac{K_{PIi}}{s^2} \quad i=x,y,z \qquad (8\text{-}1)$$

8.2 <u>CMG-Pallet Control Loop</u> - For the purposes of this study it is assumed that the pallet is an independent body under the control of the CMG cluster, i.e., the shuttle dynamics are ignored except as they affect the pallet as disturbance torques applied through the suspension system. Since the pallet products of inertia are quite small as compared with the moments of inertia about the control axes they are neglected making possible linear single-axis control loop studies. Under these assumptions and the additional assumption that the CMG cluster shows minimal cross-axis torque output, the basic control loop for each pallet axis is as shown in figure 8-1, where the negative sign occurring in the vehicle control law (equation 8-1) has been carried around the loop to the summing junction where the disturbance torque T_D is applied. The subscript i representing the axis under consideration will not be used in the succeeding paragraphs for simplicity in notation. The disturbance torque T_D acting on the pallet arises from torques applied by the suspension system. Gravity gradient torques are sinusoidal with a frequency of twice the orbital period, or approximately 0.0022 rad/sec, and will thus be transmitted through the suspension with no alteration, being well inside the suspension bandwidth of 0.1 rad/sec, indeed the frequency is so low that it can be assumed a constant torque with the magnitude taken as the peak value of 15 n-m about the vehicle y and z axes as determined in section 5. On the other

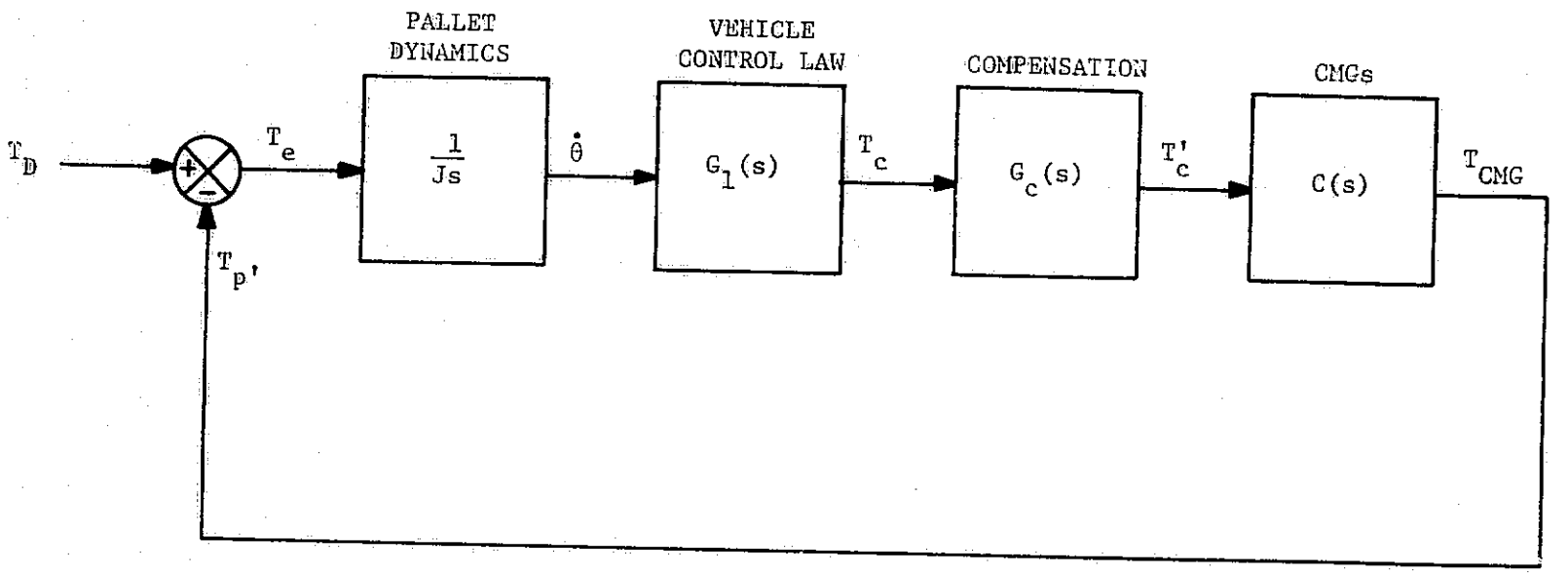

Figure 8-1. CMG-Pallet Linearized Control Loop

hand, torques due to crew motion are of relatively high frequency and will be filtered both by the shuttle dynamics and the suspension characteristics before acting on the pallet. The vehicle control law $G_1(s)$ is the rate plus position plus position integral law described in section 8.1. The CMG torque transfer function is defined as C(s) and will be discussed in section 8.4. The compensation $G_c(s)$ is discussed in the following sections, 8.5 and 8.6.

8.3 Analysis With Ideal CMG - In order to make an initial determination of the loop gains it will be assumed that the CMG transfer $C(s)\equiv 1$. The compensation $G_c(s)$ is thus also unity and the open loop transfer from figure 8-1 is thus:

$$G(s)=\frac{T_c}{T_\varepsilon}=\frac{G_1(s)}{Js}$$

The design approach to be followed is to determine the rate and position gains K_R and K_P, i.e., setting $K_{PI}=0$, with the constraints of a 2 Hz closed loop bandwidth and .707 damping on the dominant roots, then to add the position integral gain K_{PI} determining its value such that the bandwidth and damping are not significantly affected.

8.3.1 Determination of Rate and Position Gains - Setting the position integral gain K_{PI} to zero, the open loop transfer is:

$$G(s)=\frac{1}{Js}(K_R+\frac{K_P}{s})=\frac{K_R}{J}\frac{s+K_P/K_R}{s^2}$$

Defining:

$$R\triangleq K_R/J \tag{8-2}$$

$$a\triangleq K_P/K_R \tag{8-3}$$

G(s) then becomes

$$G(s)=R\frac{s+a}{s^2} \tag{8-4}$$

The characteristic equation of the loop is:

$$\Delta(s)=1+G(s)=1+R\frac{s+a}{s^2} \tag{8-5}$$

It is evident from equation 8-5 that the system is stable for all $R>0$ and $a\geq 0$. The root locus plot of equation 8-5 is given in figure 8-2, showing the double pole at the origin and the zero at $-a$. For values of $R<4a$, the locus is a circle of radius a centered at the open loop zero, and the locus is on the negative real axis to the left of the zero for $R>4a$.

For loop damping $\zeta=.707$, the angle θ is 45° and the desired root is directly above the zero at $-a$ for which $s=-a+ja$. The gain R at that point can be determined in several ways, the most direct being from the magnitude requirement:

$$R\frac{|s+a|}{|s^2|}=1, \quad s=-a+ja$$

or,

$$R=2a \tag{8-6}$$

The closed loop transfer of the simplified loop is:

$$\frac{T(s)}{T_D(s)}=\frac{R(s+a)}{s^2+Rs+Ra} \tag{8-7}$$

By definition, the bandwidth ω_B is that frequency at which the closed loop log magnitude passes through -3 db or,

$$\left|\frac{T(j\omega)}{T_D(j\omega)}\right|=\frac{\sqrt{2}}{2} \tag{8-8}$$

From equation 8-7:

$$\frac{T(j\omega)}{T_D(j\omega)}=\frac{R(a+j\omega)}{Ra-\omega^2+jR\omega}$$

Using equation 8-8:

$$\frac{R^2(a^2+\omega_B^2)}{(Ra-\omega_B^2)^2+R^2\omega_B^2}=\frac{1}{2} \tag{8-9}$$

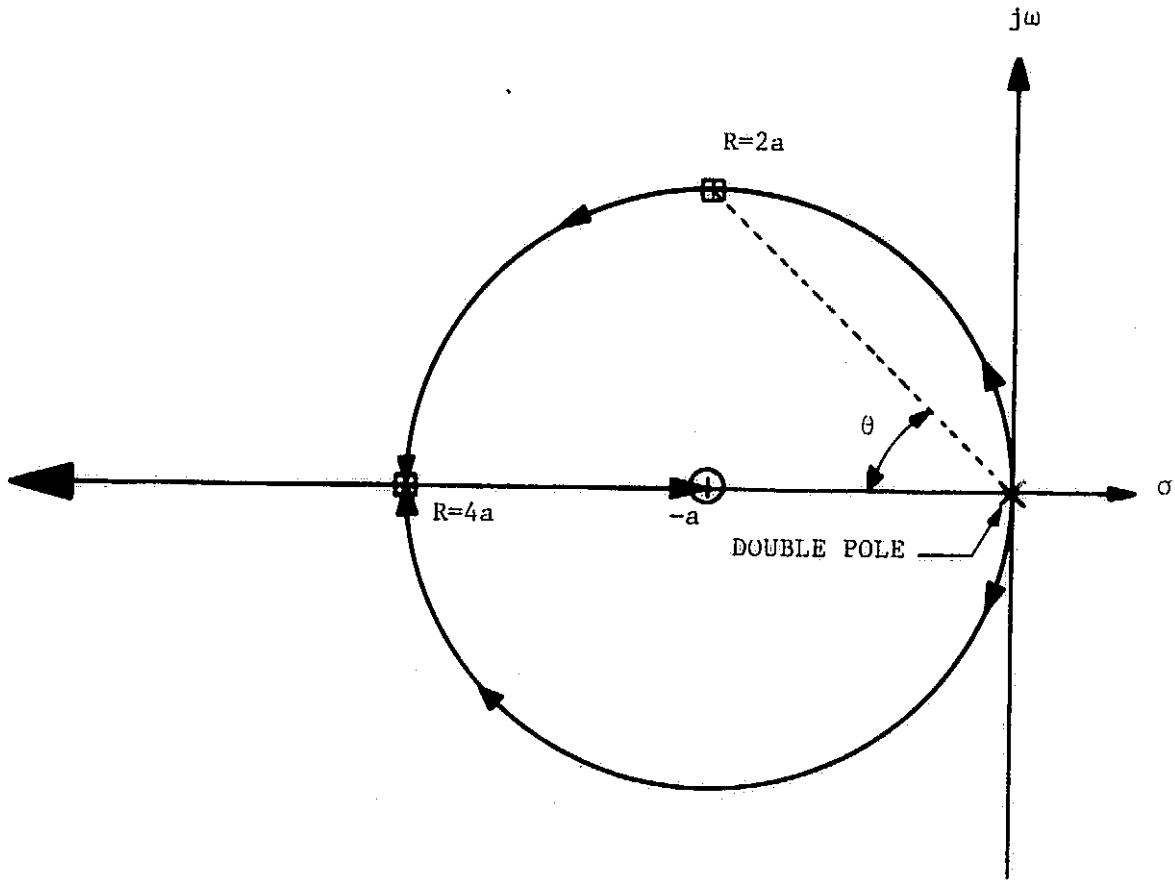

Figure 8-2. Root Locus of the Ideal Loop With $K_{PI}=0$

Rearranging equation 8-9 and substituting the damping requirement from equation 8-6 then gives:

$$(R/\omega_B)^4+8(R/\omega_B)^2-4=0$$

or,

$$(R/\omega_B)^2=-4\pm2\sqrt{5}$$

Since R and ω_B are both real, the upper sign must be used and for any desired bandwidth ω_B with a damping ratio of .707:

$$R=(2\sqrt{5}-4)^{1/2}\omega_B \tag{8-10}$$

$$a=R/2 \tag{8-11}$$

For the 2 Hz requirement $\omega_B=4\pi$ and:

$$R=8.6346 \tag{8-12}$$

$$a=4.3173 \tag{8-13}$$

Substituting these values into equation 8-7 then gives:

$$\frac{T(s)}{T_D(s)} = \frac{1+s/4.3173}{1+\sqrt{2}s/6.1056+(s/6.1056)^2} \tag{8-14}$$

Equation 8-14 explicitly shows the dominant root damping of $\sqrt{2}/2=.707...$ in the closed loop transfer and further that the transfer includes a lead term at $\omega=4.3173$ radians and the quadratic lag at 6.1056 radians. The bandwidth by derivation is $\omega_B=4\pi=12.566$ radians.

8.3.2 <u>Determination of Position Integral Gain</u> - To determine the position integral gain K_{PI} we now return to the complete vehicle control law with:

$$G_1(s)=K_R+\frac{K_P}{s}+\frac{K_{PI}}{s^2}$$

The open loop transfer is thus:

$$G(s)=\frac{K_R}{J}\,\frac{s^2+sK_P/K_R+K_{PI}/K_R}{s^3}$$

$$G(s)=R\,\frac{s^2+as+b}{s^3} \tag{8-15}$$

where R and a are as defined in equations 8-2 and 8-3 and:

$$b\triangleq K_{PI}/K_R \tag{8-16}$$

The characteristic equation becomes:

$$\Delta(s)=1+R\,\frac{s^2+as+b}{s^3} \tag{8-17}$$

which for b=0 reduces to equation 8-5. Forming the Routh array for equation 8-17:

s^3	1	Ra
s^2	R	Rb
s^1	Ra−b	0
s^0	Rb	0

The Routh-Hurwitz stability criterion requires that no sign changes occur in the first column of the array, thus the allowable values of b are:

$$0\leq b\leq Ra \tag{8-18}$$

or,

$$0\leq b\leq 37.278 \tag{8-19}$$

The closed loop transfer function is now:

$$\frac{T(s)}{T_R(s)}=R\,\frac{s^2+as+b}{s^3+Rs^2+Ras+Rb} \tag{8-20}$$

$$\frac{T(j\omega)}{T_D(j\omega)}=R\,\frac{(b-\omega^2)+ja\omega}{R(b-\omega^2)+j\omega(Ra-\omega^2)} \tag{8-21}$$

In order to evaluate the effect of adding the position integral gain, the magnitude of the transfer function 8-21 is evaluated for various values of b at the desired bandwidth frequency of 2 Hz (4π radians) using the values of R and a previously derived.

It is evident from examination of table 8-1 that the addition of the position integral gain has only a minimal effect on the logarithmic gain of the closed loop transfer, i.e., the bandwidth ω_B is a very weak function of b. Indeed, for a selection of b=2, the gain is down only .005 db from the desired -3.01 db at $\omega=4\pi$. To determine the effect on the dominant root damping the values of R and a from equations 8-12 and 8-13 along with the values of b from table 8-1 are substituted into equation 8-20. The resulting cubic in the denominator can be factored as can the quadratic numerator yielding the critical frequencies of the transfer function shown in table 8-2.

Examination of table 8-2 shows that the effect of adding the position integral gain is twofold: 1) a lag-lead factor pair is superimposed on the basic rate plus position control law, and 2) the lead and quadratic lag critical frequencies are decreased with increasing K_{PI}. The dominant root damping is little affected by the position integral gain, however, as b increases the locations of the position integral lag-lead pole zero pair diverge and the resonant peak resulting from the position gain lead and the position integral lead increases in magnitude. The selection of b and thus K_{PI} is necessarily qualitative, however, a value of 2 seems a good compromise showing almost no alteration in either bandwidth or dominant root damping and virtually no change in the closed loop response of the system as can be seen in figure 8-3 which shows the closed loop Bode plot for b=0 and b=2. Utilizing the pallet inertia data from section 3, the preliminary design values of R, a, and b, and equations 8-12, 8-13, and 8-16, the numerical values of K_R, K_P, and K_{PI} for each vehicle axis can be determined for the 2 Hz loop. The development for other bandwidths is similar and is not presented here. Gain values for all bandwidths considered are given in table 10-3.

8.4 <u>CMG Characteristics</u> - The Skylab ATM CMG has a bandwidth of approximately 30 radians per second when mounted on a rigid base. However, the bandwidth of the CMG is lower in this application since the CMG is mounted on shocks. Measurements made on the hybrid simulation show the CMG can be approximated as a second order lag with a damping ratio of 0.25 and a bandwidth of 20 rad/sec over the frequency range of interest. More detailed analysis of the CMG is given in section 10.

Table 8-1. Closed Loop Gain at $\omega=4\pi$ for Various K_{PI}/K_R (Ideal CMG)

b	$\lvert T(j\omega)/T_D(j\omega)\rvert$	$20 \log \lvert T(j\omega)/T_D(j\omega)\rvert$
0	0.7071	-3.01 db
1	0.7051	-3.04 db
2	0.7031	-3.06 db
3	0.7010	-3.08 db
4	0.6990	-3.11 db
5	0.6969	-3.14 db

Table 8-2. Factors of the Closed Loop Transfer for Various K_{PI}/K_R (Ideal CMG)

b	NUMERATOR		DENOMINATOR	
0	-	s+4.3173	-	$s^2+8.6346s+37.278(\zeta=.70711,\omega_n=6.1056)$
1	s+0.24560	s+4.0717	s+0.24515	$s^2+8.3895s+35.221(\zeta=.70681,\omega_n=5.9347)$
2	s+0.52777	s+3.7895	s+0.52271	$s^2+8.1119s+33.038(\zeta=.70565,\omega_n=5.7479)$
3	s+0.87033	s+3.4470	s+0.84363	$s^2+7.7910s+30.705(\zeta=.70300,\omega_n=5.5412)$
4	s+1.3464	s+2.9709	s+1.2246	$s^2+7.4100s+28.207(\zeta=.69765,\omega_n=5.3107)$
5	$s^2+4.3173s+5(\zeta=.96538,\omega_n=2.2361)$		s+1.6905	$s^2+6.9441s+25.539(\zeta=.68704,\omega_n=5.0536)$

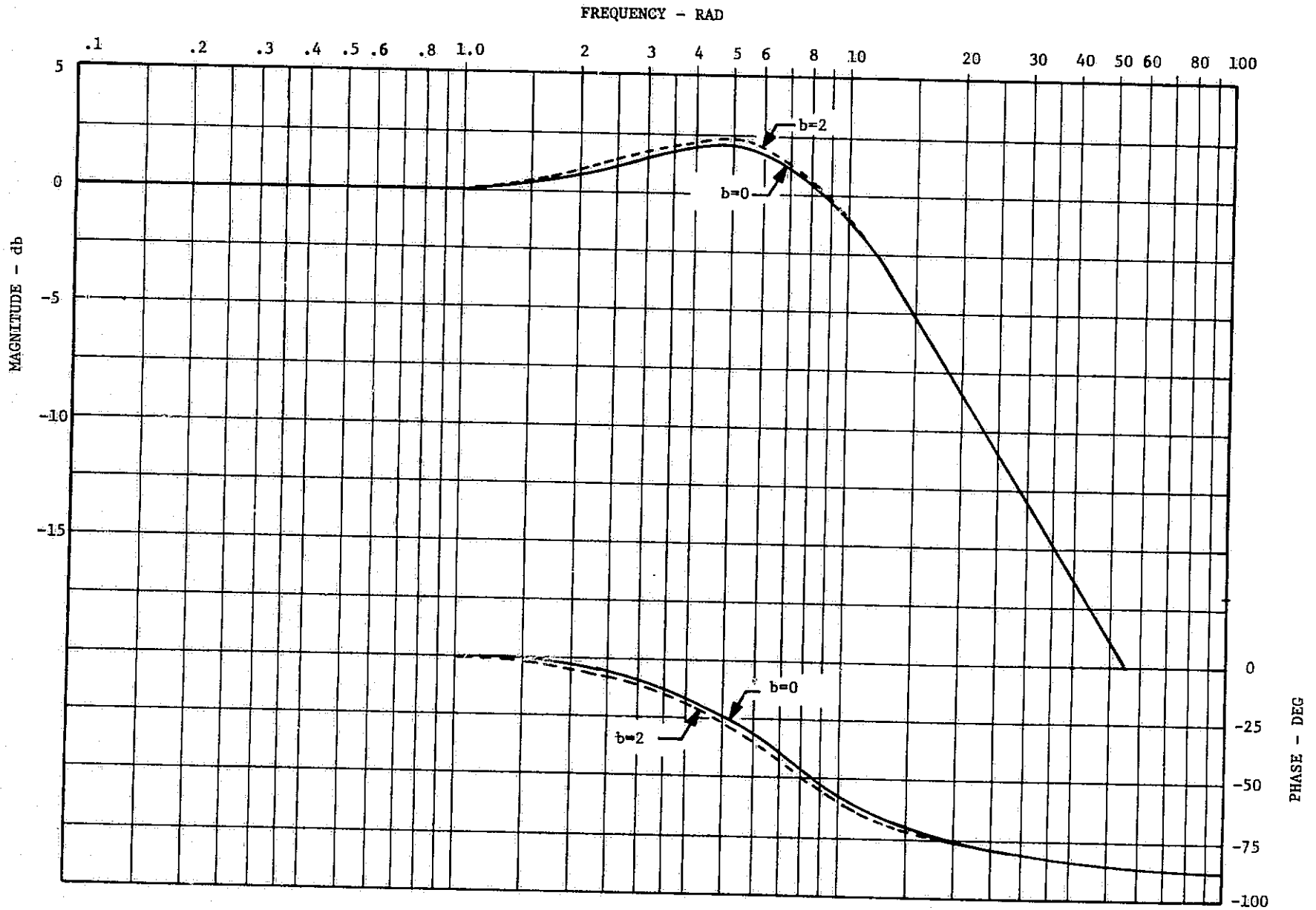

Figure 8-3. Closed Loop Response for K_{PI}/K_P of 0 and 2 With Ideal CMG

8.5 Loop Stability Investigation - Stability analysis performed in this section is based on the assumption that the CMG can be approximated by a second-order lag with a natural frequency of 13 rad/sec (bandwidth=20 rad/sec) and a damping ratio of 0.25. In figure 8-1 the CMG is represented as C(s), the compensation network as $G_c(s)$, and the control law as $G_1(s)$.

The control analysis given in section 8.2 establishes the criteria for a system in which the CMG was assumed to have a transfer function of 1. Since the shockmounted CMG has the characteristics described above, a problem will exist which has not been considered in the section 8.2 analysis.

Writing the transfer function of the CMG as:

$$C(s)=\frac{\omega_n^2}{s^2+2\zeta_n\omega_n s+\omega_n^2}, \text{ where: } \omega_n = 13 \text{ (rad/sec)} \quad \zeta = 0.25 \tag{8-22}$$

the compensator as:

$$G_c(s)=1$$

and the control law as:

$$G_1(s)=R\left(\frac{s+a}{s^2}\right) \tag{8-23}$$

the open loop transfer function becomes:

$$\frac{T_{CMG}(s)}{T_\varepsilon(s)} =37.3\ \frac{(1+s/4.3)}{s^2}\ \frac{1}{\left[1+\frac{0.5}{13}\ s+\left(\frac{s}{13}\right)^2\right]} \tag{8-24}$$

The Bode diagram of equation 8-24 is given in figure 8-4. It is evident from the figure that the CMG has changed the stable system described in section 8.2.1 into an unstable system. Therefore compensation will be required to make the loop stable. Compensation analysis is discussed in the following section.

8.6 Compensation Analysis - Two candidates were considered for the compensation network, $G_c(s)$. The two were of the form:

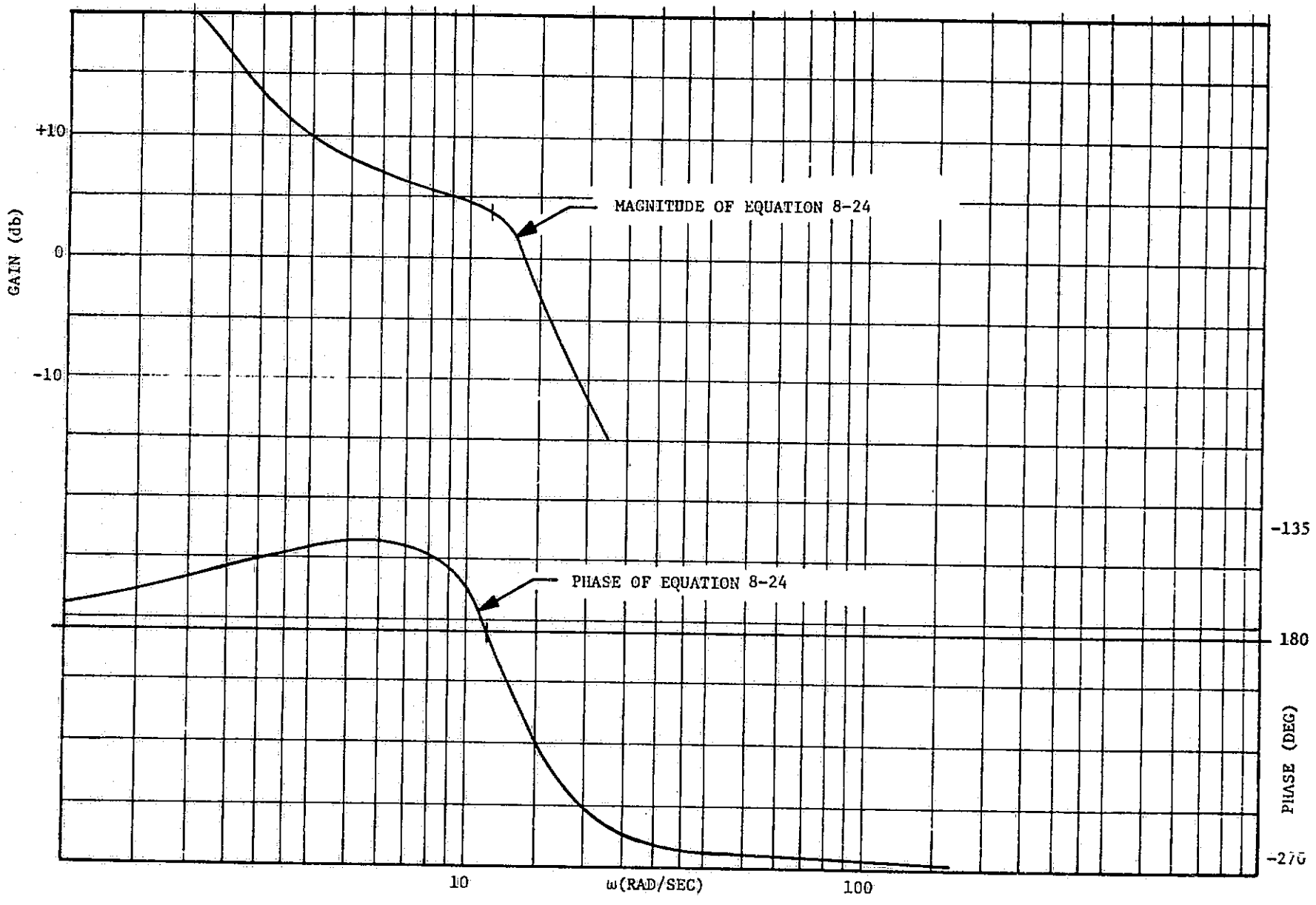

Figure 8-4. Bode Diagram of Open Loop Rate Plus Position Control Law With Second-Order CMG

$$G_c(s)=\frac{s+b}{s+d} \quad d>b \tag{8-25}$$

and

$$G_c(s)=\frac{\left[1+\frac{2\zeta_1 s}{\omega_1}+\frac{s^2}{\omega_1^2}\right]}{\left[1+\frac{2\zeta_2 s}{\omega_2}+\frac{s^2}{\omega_2^2}\right]} \tag{8-26}$$

The second order compensator (equation 8-26) is used in this study. This type compensator is chosen so that the lead term of the compensator can be chosen as the reciprocal of the second order lag characteristic of the CMG, and the compensator lag can be 0.7 damped with an ω_n of 100 radians per second.

8.6.1 Combined CMG/Compensator System - Since the CMG can be approximated by a second order lag over the critical frequency range and a compensator can be used as described in section 8.6, then the open loop transfer will again be described by equation 8-24. Now, however, ζ=0.707 and ω_n=100 radians per second since the CMG lag and compensator lead cancel. Substituting these values into equation 8-24, the open loop transfer function is:

$$G(s)=37.3\,\frac{(1+s/4.3)}{s^2}\left(\frac{1}{1+.014s+10^{-4}s^2}\right) \tag{8-27}$$

Figure 8-5 is a plot of equation 8-27 and shows that this function generates a gain margin (K_m) of 24 db and a phase margin (ϕ_m) of 60 degrees.

A root locus plot is given in figure 8-6 of the rate plus position control law, the second order CMG and the compensator described by equation 8-26. The loop function for the root locus is:

$$\frac{T_{CMG}(s)}{T_\varepsilon(s)}=R\left(\frac{s+a}{s^2}\right)\frac{1}{\left[1+\frac{2\zeta_n}{\omega_n}s+\frac{s^2}{\omega_n^2}\right]}\frac{\left[1+\frac{2\zeta_1}{\omega_1}s+\frac{s^2}{\omega_1^2}\right]}{\left[1+\frac{2\zeta_2}{\omega_2}s+\frac{s^2}{\omega_2^2}\right]} \tag{8-28}$$

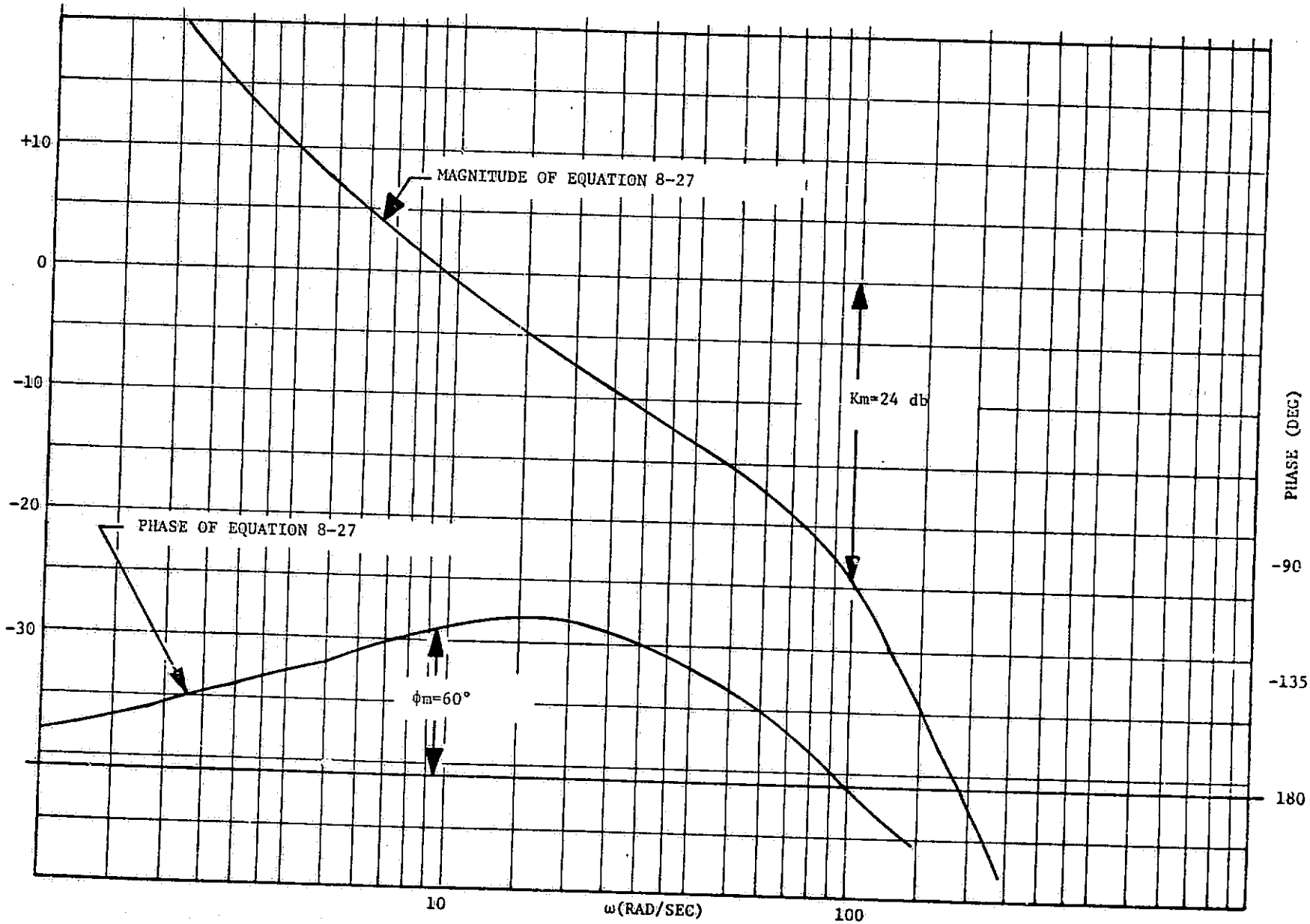

Figure 8-5. Bode Diagram of Open Loop Rate Plus Position Control Loop With Compensated CMG

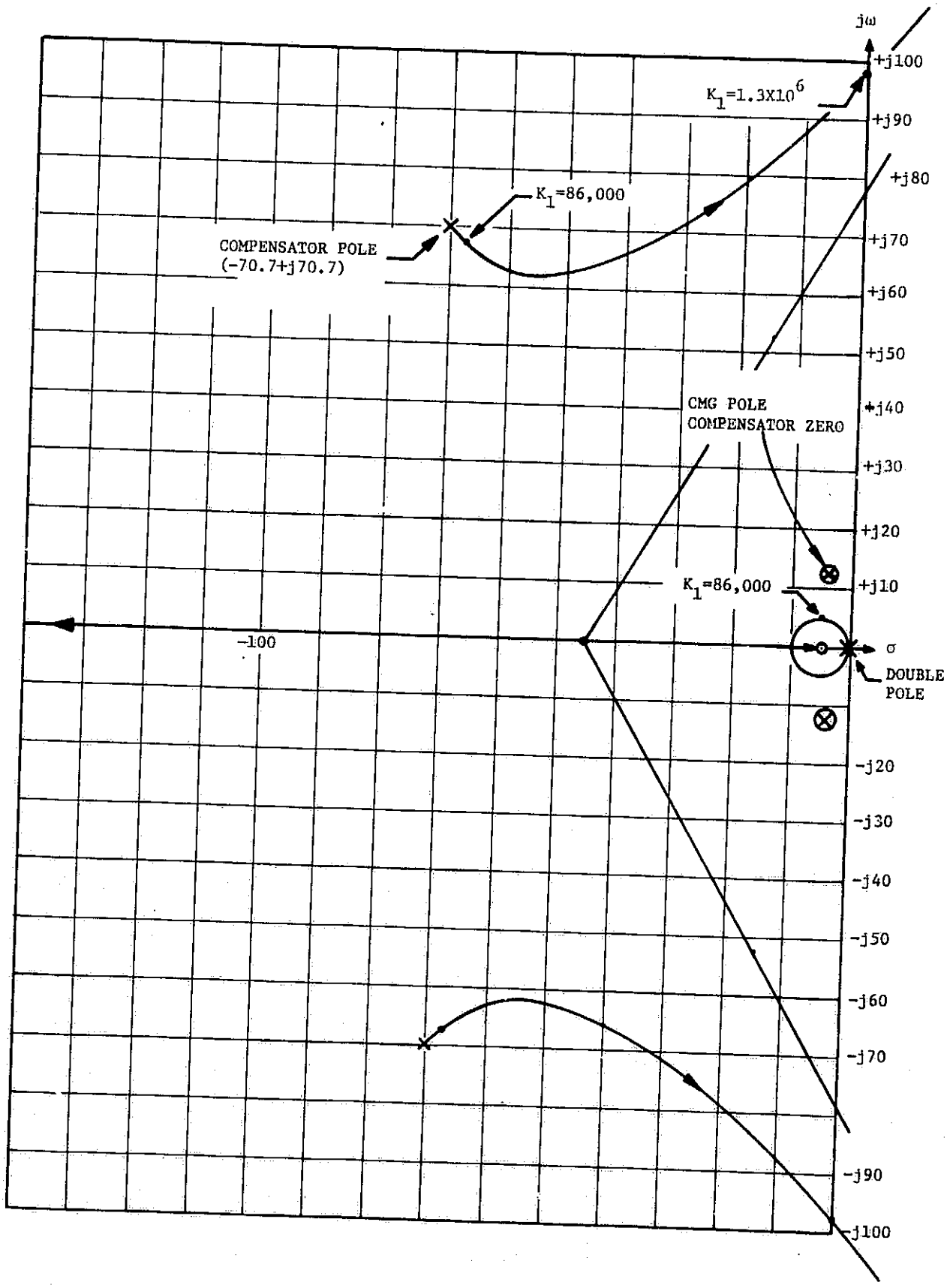

Figure 8-6. Root Locus Diagram of Rate Plus Position Control Loop, CMG, and Compensator

where:

$$\zeta_n = 0.25, \ \omega_n = 13 \text{ rad/sec}$$

$$\zeta_1 = 0.25, \ \omega_1 = 13 \text{ rad/sec}$$

$$\zeta_2 = .707, \ \omega_2 = 100 \text{ rad/sec}$$

$$R = K_R/J$$

$$a = K_P/K_R$$

Rearranging equation 8-28 and substituting values suitable for constructing a root locus diagram:

$$\frac{T_{CMG}(s)}{T_\varepsilon(s)} = K_1 \left(\frac{s+4.3}{s^2}\right)\left(\frac{13^2}{s^2+6.5s+13^2}\right)\left(\frac{s^2+6.5s+13^2}{13^2}\right)\left(\frac{1}{s^2+140s+100^2}\right) \quad (8\text{-}29)$$

where:

$$K_1 = \omega_2^2 R = 10{,}000 \ R$$

Equation 8-29 shows the following pole and zero configuration exists. A double pole at the origin, poles at $-3.25 \pm j12.56$, $-70.7 \pm j70.7$ and zeros at $s=-4.3$, $s=-3.25 \pm j12.56$. The one pole/zero combination cancels, leaving the double pole at the origin and the zero at -4.3 essentially the same as described in figure 8-2. The complex pole pair at $s=-70 \pm j70$ has a locus which crosses the $j\omega$ axis and approaches the asymptotes at $\pm 60°$.

The locus near the origin will travel in a circular path. Therefore a value of gain (K_1) will be chosen to put the closed loop roots on the $\theta=45°$ line to give 0.707 dominant root damping. This will give a set of closed loop roots at $s=-4.6 \pm j4.6$ for a value of $K_1=86{,}000$.

Using the assumption that the lead term of the compensator will nullify the CMG characteristics, equation 8-29 reduces to

$$G(s) = \frac{K_1(s+4.3)}{s^2(s^2+2\zeta_2\omega_2 s+\omega_2^2)} \quad (8\text{-}30)$$

The closed loop transfer function of this compensated system is:

$$\frac{T_{CMG}(s)}{T_D(s)} = \frac{K_1(s+4.3)}{s^4+2\zeta_2\omega_2 s^3+\omega_2^2 s^2+K_1 s+4.3K_1} \tag{8-31}$$

Using previously chosen value of K_1, equation 8-31 becomes:

$$\frac{T_{CMG}(s)}{T_D(s)} = \frac{K_1(s+4.3)}{s^4+140s^3+10,000s^2+86,000s+369,800} \tag{8-32}$$

The denominator of equation 8-32 factors into the four roots $s=-4.6\pm j4.6$ and $s=-66.1\pm j66.1$. Therefore both sets of closed loop roots have a damping ratio of 0.707. Equation 8-33 gives the closed loop response in factored form.

$$\frac{T_{CMG}(s)}{T_D(s)} = \frac{K_1(s+4.3)}{(s^2+9.2s+42.3)(s^2+132s+8,738)} \tag{8-33}$$

A plot of equation 8-33 will give the system closed loop response which is essentially the same as the solid lines on figure 8-3 over the frequency range of concern.

8.6.2 Combined System With Integral Gain - The effects of adding integral gain to the rate plus position control law using the ideal CMG was discussed in section 8.2.2 Adding integral gain to the combined system discussed in section 8.6.1 will not affect the performance of the system appreciably. Equation 8-34 is the open loop transfer function of the rate plus position plus integral control law with a second order approximation of the CMG and with the compensator described in section 8.6.

$$\frac{T_{CMG}(s)}{T_\varepsilon(s)} =$$

$$K_1\left[\frac{s^2+4.3s+2}{s^3}\right]\left[\frac{\omega_n^2}{s^2+2\zeta\omega_n s+\omega_n^2}\right]\left[\frac{s^2+2\zeta_1\omega_1 s+\omega_1^2}{\omega_1^2}\right]\left[\frac{1}{s^2+2\zeta_2\omega_2 s+\omega_2^2}\right] \tag{8-34}$$

Figure 8-7 is a root locus diagram of equation 8-34. This diagram is essentially the same as figure 8-6, however, there are now three poles at the origin and an additional zero on the real axis near the origin. One locus leaves the origin and goes to the real zero near the origin. The other travels into the right half plane, then cross the $j\omega$ axis and travel in the left half plane in a near circular locus. It is evident that the system would be unstable for a low or high value of K_1, but if a value of K_1=86,000 is chosen, the closed loop roots are found to be at s=-0.525, s=-4.05±j4.05, and s=-65.6±j65.6.

The closed loop transfer function is:

$$\frac{T_{CMG}(s)}{T_D(s)} = \frac{K_1(s+0.53)(s+3.77)}{(s+0.525)(s^2+8.1s+33)(s^2+131s+8,596)} \qquad (8\text{-}35)$$

The two second order roots in equation 8-35 have a damping ratio of 0.7 and the plot of equation 8-35 is essentially that given by the dotted line in figure 8-3 over the 2 Hz bandwidth of interest.

8.7 Pointing Error Estimation - The pointing error can be estimated by assuming an ideal CMG. Considering the control law only, pallet position (θ) is given as a function of disturbing torque (T_D) by equation 8-36.

$$\theta(s) = \frac{s}{Js^3+K_R s^2+K_P s+K_I}\,[T_D(s)] \qquad (8\text{-}36)$$

It has been established in section 5 that the major disturbances can be approximated by a step input with a magnitude of 15 n-m about the y and z axes. Applying the final value theorem

$$\lim_{t\to\infty}\theta(t) = \lim_{s\to 0} s\,\theta(s)$$

to equation 8-36 for a step input

$$\lim_{t\to\infty}\theta(t) = \lim_{s\to 0}\left\{s\,\frac{s}{Js^3+K_R s^2+K_P s+K_I}\left(\frac{15}{s}\right)\right\}$$

$$\lim_{t\to\infty}\theta(t) = 0$$

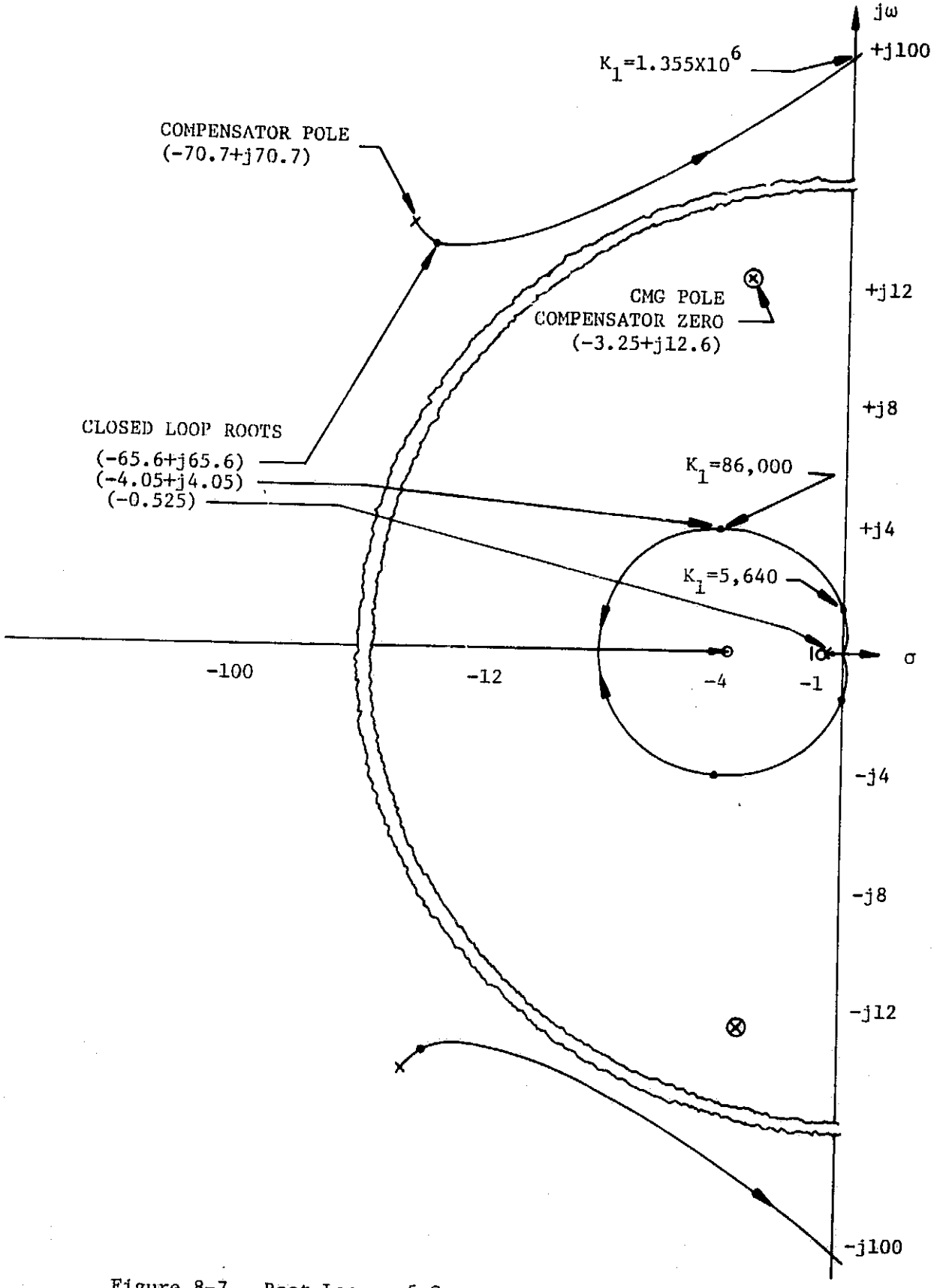

Figure 8-7. Root Locus of Compensated CMG With Rate, Position and Integral Control Law

which says that the pointing error should be equal to zero for a step disturbance input when position integral is used in the control law.

The preceding analysis is valid for linear systems, however, there are nonlinearities present in the system which will cause pointing errors. These pointing errors will appear as limit cycles caused primarily by CMG friction. Results showing these effects are given in section 10 of this volume.

9. VEHICLE DYNAMIC MODEL

In order to study the pointing performance realizable with the floated pallet under the control of the recommended CMG actuator cluster, it is necessary to formulate a model of the pallet/suspension/orbiter dynamics to be used in conjunction with the CMG model developed in section 7. Since only pointing performance is to be investigated, the vehicle is essentially in an inertially held attitude, therefore a primary assumption used throughout this section is that all angular motions are very small, allowing the small angle transformation to be used.

Separate rotational dynamics are developed for the pallet and orbiter, along with relative translation. Disturbance torques and forces and gravity gradient torques act on both bodies, the CMG control torques act directly on the pallet, and forces and torques generated by the action of the suspension system act on both bodies.

The total simulation will include the digital CMG control law developed in section 6.6, four of the CMG models as given in section 7, and the vehicle dynamic model of this section. The pallet angular rates are picked off and processed through the vehicle control law discussed in section 8, in order to generate torque commands for use in the CMG control law.

9.1 <u>Resolution of CMG Control Torques</u> - Although the control torque acting on the pallet is physically only an input to the dynamics of the combined vehicle, the resolution of the torques from the individual actuators into a single torque vector is necessary, and conveniently discussed at this point. Given the output torque of the ith actuator as defined in equation 7-23 as $\vec{T}_{P'i}$, and using the CMG output to pallet transformations of equations 6-1 through 6-4, the control torque $\vec{T}_{CP}$ acting on the pallet resolved into pallet coordinates is:

$$\vec{T}_{CP} = \sum_{i=1}^{4} [{}_{P}T_{P'i}]\vec{T}_{P'i}$$

$$\vec{T}_{CP} = \begin{bmatrix} T_{P'x1}+T_{P'x2}+T_{P'x3}+T_{P'x4} \\ T_{P'y1}+T_{P'z2}-T_{P'y3}+T_{P'z4} \\ T_{P'z1}+T_{P'y2}-T_{P'z3}-T_{P'y4} \end{bmatrix} \qquad (9\text{-}1)$$

9.2 Derivation of the Detailed Dynamics - The vehicle and sus-suspension system dynamics are derived in the following paragraphs, first with only the assumption of small angle restrictions in rotation and linear characteristics in the individual isolators of the suspension system. In section 9.3 the suspension dynamics are simplified based on the selection in volume III of an uncoupled four-point system.

9.2.1 Suspension System Dynamics - When the pallet is inertially held under the control of the CMG system, the only connection between the pallet and orbiter is through the suspension system. The suspension system exerts forces and torques on both the orbiter and pallet as a function of the relative rates and displacements of the two bodies. The dynamics of the suspension system are derived by considering each suspension point individually. It is assumed that each suspension point (isolator) exhibits only linear spring rate and damping characteristics along each vehicle axis with no coupling, i.e., a linear deflection or rate at any isolator location will result in a force acting along the deflection or rate. In addition it is assumed that the individual isolators exhibit no rotational compliance or damping and finally that the undeflected isolator length is small compared to the distance from the pallet center-of-mass.

In order to determine the forces applied to the orbiter and pallet by each isolator it is necessary to derive the deflection $\vec{\delta}_i$ of the ith isolator as a function of relative translation of the orbiter and pallet and the rotations of both bodies. Figure 9-1 shows a representation of the isolator body geometry when the suspension system is relaxed and there is no translation of the orbiter or pallet with respect to the ideal (I) coordinate system. The vectors $\vec{\rho}_{Po}$ and $\vec{\rho}_{So}$ locate the pallet and orbiter mass centers with respect to the origin of the I coordinate system. The vector $\vec{R}_o$ locates the pallet mass center with respect to the orbiter mass center when the suspension system is relaxed. The vector $\vec{\beta}_i$ locates the orbiter end of the ith isolator and $\vec{\alpha}_i$ the pallet end. $\vec{R}_o$ and $\vec{\beta}_i$ are fixed in the orbiter and rotate with it and $\vec{\alpha}_i$ is fixed in the pallet. The vector $\vec{\rho}_o$ coincides with $\vec{R}_o$ when the suspension is relaxed and is constant in I coordinates. From the figure, using assumption that the isolator relaxed length is negligible:

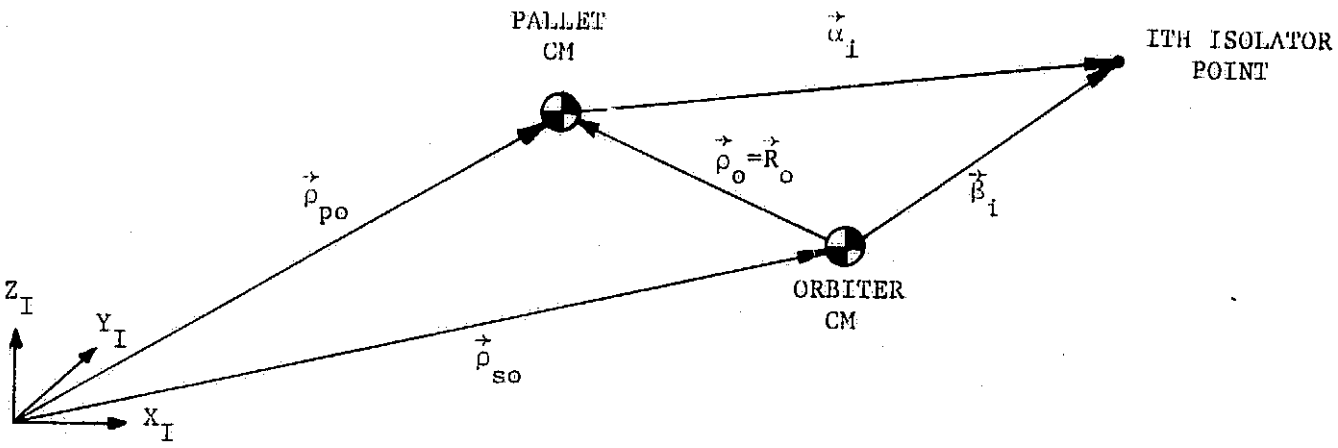

Figure 9-1. Geometry of One Suspension Point With No Deflection

$$\vec{R}_o+\vec{\alpha}_i=\vec{\beta}_i \tag{9-2}$$

$$\vec{\rho}_o=\vec{\rho}_{Po}-\vec{\rho}_{So}$$

Now, consider the case when both the pallet and orbiter have been rotated with respect to I through the small angles $\vec{\theta}_P=(\theta_{Px},\theta_{Py},\theta_{Pz})^T$ and $\vec{\theta}_S=(\theta_{Sx},\theta_{Sy},\theta_{Sz})^T$, respectively, and both bodies translated with respect to I coordinates as shown in figure 9-2. The pallet and orbiter mass centers are located by the vectors $\vec{\rho}_P$ and $\vec{\rho}_S$, respectively, with:

$$\vec{\rho}=\vec{\rho}_P-\vec{\rho}_S \tag{9-3}$$

The vector $\vec{\delta}_i$ now represents the opening between the pallet and orbiter ends of the ith isolator, i.e., it is the deflection of the ith isolator. Expressing all vectors in their I space coordinates and noting that $\vec{\alpha}_i$, $\vec{\beta}_i$, and $\vec{R}_o$ have undergone rotations:

$$\vec{\rho}+[{}_IT_P]\vec{\alpha}_i=[{}_IT_S]\vec{\beta}_i+\vec{\delta}_i \tag{9-4}$$

The vector $\vec{\varepsilon}$ is a measure of the translation of the pallet center of mass from its position when neither orbiter rotation or relative orbiter/pallet translation has occurred, thus:

$$\vec{\rho}=[{}_IT_S]\vec{R}_o+\vec{\varepsilon} \tag{9-5}$$

Substituting equation 9-5 into 9-4 and solving for $\vec{\delta}_i$:

$$\vec{\delta}_i=\vec{\varepsilon}+[{}_IT_S](\vec{R}_o-\vec{\beta}_i)+[{}_IT_P]\vec{\alpha}_i$$

From equation 9-1, $\vec{R}_o-\vec{\beta}_i=-\vec{\alpha}_i$ and:

$$\vec{\delta}_i=\vec{\varepsilon}+\{[{}_IT_P]-[{}_IT_S]\}\vec{\alpha}_i \tag{9-6}$$

Noting:

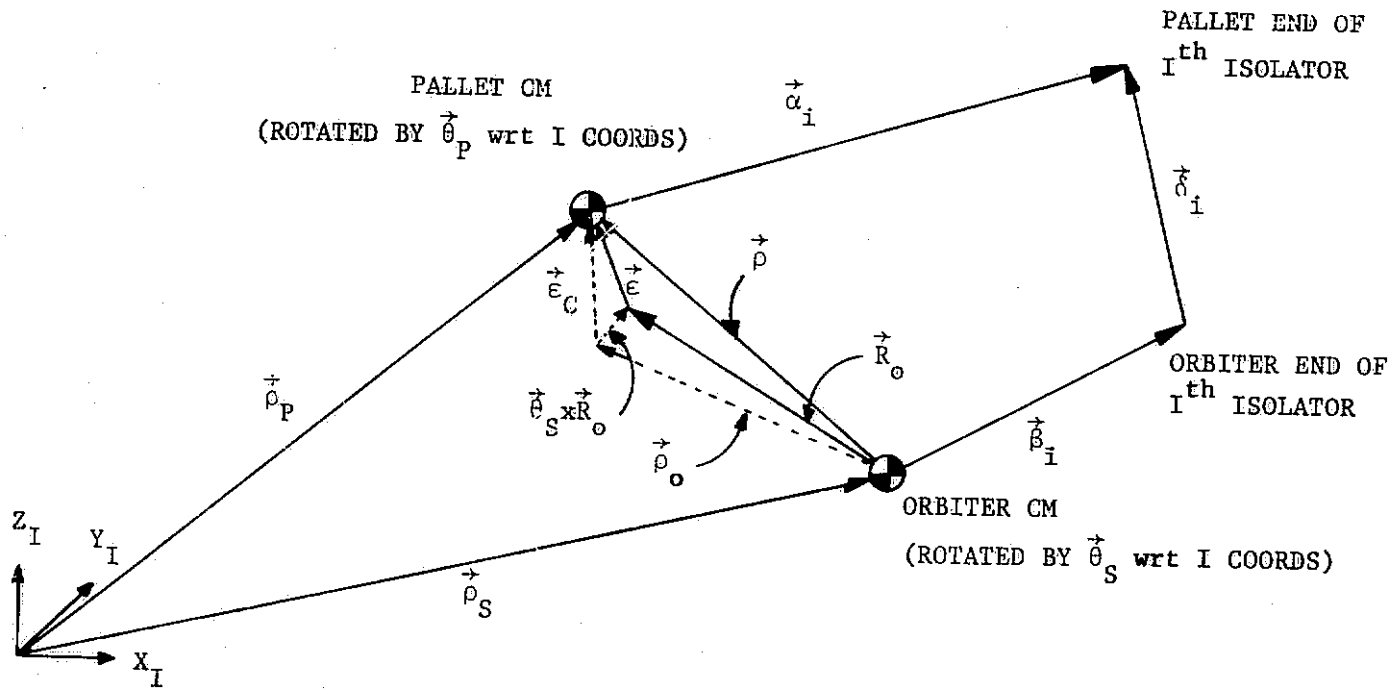

Figure 9-2. Geometry of One Suspension Point With a General Deflection

$$[{}_I T_P] = \begin{bmatrix} 1 & -\theta_{Pz} & \theta_{Py} \\ \theta_{Pz} & 1 & -\theta_{Px} \\ -\theta_{Py} & \theta_{Px} & 1 \end{bmatrix}$$

$$[{}_I T_S] = \begin{bmatrix} 1 & -\theta_{Sz} & \theta_{Sy} \\ \theta_{Sz} & 1 & -\theta_{Sx} \\ -\theta_{Sy} & \theta_{Sx} & 1 \end{bmatrix}$$

$$\{[{}_I T_P]-[{}_I T_S]\}\vec{\alpha}_i = \begin{bmatrix} 0 & -(\theta_{Pz}-\theta_{Sz}) & (\theta_{Py}-\theta_{Sy}) \\ (\theta_{Pz}-\theta_{Sz}) & 0 & -(\theta_{Px}-\theta_{Sx}) \\ -(\theta_{Py}-\theta_{Sy}) & (\theta_{Px}-\theta_{Sx}) & 0 \end{bmatrix} \vec{\alpha}_i \equiv (\vec{\theta}_P - \vec{\theta}_S) x \vec{\alpha}_i$$

defining:

$$\vec{\phi} \triangleq \vec{\theta}_P - \vec{\theta}_S \tag{9-7}$$

Equation 9-6 can be written as:

$$\vec{\delta}_i = \vec{\varepsilon} + \vec{\phi} x \vec{\alpha}_i \tag{9-8}$$

where $\vec{\delta}_i$ is given in terms of its I space coordinates. Under the assumption of small angle rotations and small deflections $\vec{\delta}_i$, the resolution of $\vec{\delta}_i$ into orbiter coordinates is:

$$\vec{\delta}_i \big|_S = [{}_S T_I]\vec{\delta}_i = \vec{\delta}_i - \vec{\theta}_S x \vec{\delta}_i \approx \vec{\delta}_i$$

where $\vec{\theta}_S x \vec{\delta}_i$ is essentially a second order term and similarly for resolution into pallet coordinates. Thus, the isolator deflection can be expressed in both S and P coordinates by means of equation 9-8. Under the small angle assumption, ignoring second order products, the deflection rate $\dot{\vec{\delta}}_i$ can be given as:

$$\dot{\vec{\delta}}_i = \dot{\vec{\varepsilon}} + \dot{\vec{\phi}} x \vec{\alpha}_i \tag{9-9}$$

The vectors $\vec{\delta}_i$ and $\dot{\vec{\delta}}_i$ are defined as directed from the orbiter to the pallet, resulting in forces on the orbiter along those vectors and in the same direction. Defining the spring constant and damping matrices describing the ith isolator characteristics as:

$$[K_i] \triangleq \mathrm{diag}\{K_{xi}, K_{yi}, K_{zi}\} \tag{9-10}$$

$$[C_i] \triangleq \mathrm{diag}\{C_{xi}, C_{yi}, C_{zi}\} \tag{9-11}$$

The force on the orbiter due to the ith suspension point is:

$$\vec{F}_{Si} = [K_i]\vec{\delta}_i + [C_i]\dot{\vec{\delta}}_i + \vec{f}_i \tag{9-12}$$

where the vector $\vec{f}_i = (f_{xi}, f_{yi}, f_{zi})$ represents the friction of the suspension point, which for the purposes of this derivation is assumed to be of constant magnitude in each coordinate direction acting in the direction of the proper velocity component, i.e.:

$$\left.\begin{aligned} f_{ki} &= F_{ki}, \quad \dot{\delta}_{ki} > 0 \\ &= 0 \quad\;\; , \quad \dot{\delta}_{ki} = 0 \\ &= -F_{ki}, \quad \dot{\delta}_{ki} < 0 \end{aligned}\right\} \; k = x, y, z \tag{9-13}$$

The force on the pallet due to the ith suspension point is simply the negative $\vec{F}_{Si}$:

$$\vec{F}_{Pi} = -\vec{F}_{Si} \tag{9-14}$$

The torque exerted on the pallet by the isolator is due to the force $\vec{F}_{Si}$ acting on the lever arm $\vec{\alpha}_i$:

$$\vec{T}_{Pi} = \vec{\alpha}_i \times \vec{F}_{Pi} = -\alpha_i \times \vec{F}_{Si} \tag{9-15}$$

The torque applied to the shuttle is:

$$\vec{T}_{Si}=\vec{\beta}_i x\vec{F}_{Si}=(\vec{R}_o+\vec{\alpha}_i)x\vec{F}_{Si}$$

$$\vec{T}_{Si}=\vec{R}_o x\vec{F}_{Si}-\vec{T}_{Pi} \tag{9-16}$$

The total forces and torques acting on each body due to n isolators is then:

$$\vec{F}_{SS}=\sum_{i=1}^{n}\vec{F}_{Si} \tag{9-17}$$

$$\vec{F}_{SP}=-\vec{F}_{SS} \tag{9-18}$$

$$\vec{T}_{SP}=\sum_{i=1}^{n}\vec{T}_{Pi} \tag{9-19}$$

$$\vec{T}_{SS}=\vec{R}_o x\vec{F}_{SS}-\vec{T}_{SP} \tag{9-20}$$

where the subscript "SS" indicates action of the suspension on the orbiter and "SP" on the pallet.

9.2.2 Orbiter Rotational Dynamics - Under the assumption of small angle rotations, the rotational equations of motion of the orbiter are simply:

$$[J_S]\ddot{\vec{\theta}}_S=\vec{T}_{SS}+\vec{T}_{GS}+\vec{T}_{DS} \tag{9-21}$$

where the Euler term involving the cross product of rates has been neglected, and the external torques are the suspension torque $\vec{T}_{SS}$ (equation 9-20), gravity gradient torque acting on the orbiter $\vec{T}_{GS}$ and disturbance torque acting on the orbiter $\vec{T}_{DS}$. The matrix $[J_S]$ represents the inertia tensor of the orbiter. The orbiter rates and displacements $\dot{\vec{\theta}}_S$ and $\vec{\theta}_S$ are obtained by integration of the acceleration components.

9.2.3 Pallet Rotational Dynamics - In a similar statement, the pallet equations of motion in rotation are:

$$[J_P]\ddot{\vec{\theta}}_P=\vec{T}_{SP}+\vec{T}_{GP}+\vec{T}_{DP}+\vec{T}_{CP} \tag{9-22}$$

where $[J_P]$ represents the inertia of the pallet and the external torques are those due to suspension, gravity gradient, disturbance and control output torque from the CMG cluster, respectively. The pallet rates and displacements are obtained from the time integrals of equation 9-22.

9.2.4 Translational Dynamics - Although both the orbiter and the pallet can translate with respect to the I coordinate frame, a complete solution of the translational equations of motion for both bodies is not required. Referring to section 9.1.1 it can be seen that only the relative translation of the pallet with respect to the orbiter is required to determine the suspension dynamics, in particular the vector $\vec{\varepsilon}$ shown in figure 9-2. In general, the vector $\vec{\varepsilon}$ expressed in I space components can be related to $\vec{\rho}$ and $\vec{R}_o$, recalling $\vec{R}_o$ rotates with the orbiter by:

$$\vec{\rho}=\vec{\varepsilon}+[{}_IT_S]\vec{R}_o=\vec{\varepsilon}+\vec{R}_o+\vec{\theta}_S x\vec{R}_o$$

from which:

$$\vec{\varepsilon}=\vec{\rho}-\vec{R}_o-\vec{\theta}_S x\vec{R}_o$$

and, recalling $\vec{R}_o$ is a constant magnitude vector, and again using the small angle assumption:

$$\dot{\vec{\varepsilon}}=\dot{\vec{\rho}}-\dot{\vec{\theta}}_S x\vec{R}_o \tag{9-24}$$

It should be noted here that the vector $\vec{\varepsilon}_C$ which appears on figure 8-2 which is given by $\vec{\varepsilon}_C=\vec{\varepsilon}+\vec{\theta}_S xR_o$ is the relative translation used in volume I of this final report in the derivation of equations of motion and is mentioned here for the sake of compatibility between the two derivations.

Again, referring to figure 9-2 it can be seen that the vector $\vec{\rho}$ can be expressed in terms of $\vec{\rho}_P$ and $\vec{\rho}_S$ which locate the pallet and orbiter mass centers as:

$$\vec{\rho}=\vec{\rho}_P-\vec{\rho}_S$$

and thus,

$$\ddot{\vec{\rho}}=\ddot{\vec{\rho}}_P-\ddot{\vec{\rho}}_S \tag{9-25}$$

Considering each body separately, the equations of motion in translation are:

$$m_P\ddot{\vec{\rho}}_P=\vec{F}_{SP}+\vec{F}_{DP} \tag{9-26}$$

$$m_S\ddot{\vec{\rho}}_S=\vec{F}_{SS}+\vec{F}_{DS} \tag{9-27}$$

where m_P and m_S are the masses of the pallet and orbiter, $\vec{F}_{SS}$ and $\vec{F}_{SP}$ the forces of the suspension and $\vec{F}_{DP}$ and $\vec{F}_{DS}$ disturbance forces. Solving equations 9-26 and 9-27 for the acceleration, substituting into equation 9-25 recalling $\vec{F}_{SP}=-\vec{F}_{SS}$:

$$\ddot{\vec{\rho}}=\frac{\vec{F}_{DP}}{m_P}-\frac{\vec{F}_{DS}}{m_S}-\frac{m_P+m_S}{m_Pm_S}\vec{F}_{SS} \tag{9-28}$$

The time integral of equation 9-28 gives $\ddot{\vec{\rho}}$ for use in equation 9-24, since the initial condition on $\dot{\vec{\rho}}=0$. However, to determine $\vec{\rho}$:

$$\vec{\rho}=\int_0^t \dot{\vec{\rho}}(\tau)d\tau+\vec{\rho}_o$$

and, since the I space representation of $\vec{\rho}_o$ is the same as the S space representation of $\vec{R}_o$:

$$\int_0^t \dot{\vec{\rho}}(\tau)d\tau=\vec{\rho}-\vec{\rho}_o\equiv\vec{\varepsilon}_c\equiv\vec{\rho}-\vec{R}_o \tag{9-29}$$

Thus, the integral of $\dot{\vec{\rho}}$ is substituted into equation 9-23 to determine $\vec{\varepsilon}$.

9.2.5 Summary of the Detailed Dynamics - All external forces and torques acting on the bodies are put into the equations of motion. The pallet rates $\dot{\vec{\theta}}_P$ are picked off and processed through the vehicle control law, CMG control law and CMG dynamics to obtain the control torque $\vec{T}_{CP}$. The suspension forces and torques are fed back into the dynamics to complete the dynamic loops. In vector representation, the equations of motion are given as:

Pallet Rotation: $$\ddot{\vec{\theta}}_P=[J_P]^{-1}(\vec{T}_{SP}+\vec{T}_{GP}+\vec{T}_{DP}+\vec{T}_{CP}) \tag{9-30}$$

Orbiter Rotation: $$\ddot{\vec{\theta}}_S=[J_S]^{-1}(\vec{T}_{SS}+\vec{T}_{GS}+\vec{T}_{DS}) \tag{9-31}$$

Translation: $$\ddot{\vec{\rho}}=\frac{\vec{F}_{DP}}{m_P}-\frac{\vec{F}_{DS}}{m_S}-\frac{m_P+m_S}{m_P m_S}\vec{F}_{SS} \tag{9-32}$$

Integrating:

$$\dot{\vec{\theta}}_P=\int \ddot{\vec{\theta}}_P d\tau \qquad \vec{\theta}_P=\int \ddot{\vec{\theta}}_P d\tau \tag{9-33}$$

$$\dot{\vec{\theta}}_S=\int \ddot{\vec{\theta}}_S d\tau \qquad \vec{\theta}_S=\int \dot{\vec{\theta}}_S d\tau \tag{9-34}$$

$$\dot{\vec{\rho}}=\int \ddot{\vec{\rho}} d\tau \qquad \vec{\varepsilon}_C=\vec{\rho}-\vec{R}_o=\int \dot{\vec{\rho}} d\tau \tag{9-35}$$

The suspension dynamics are then determined by:

$$\dot{\vec{\phi}}=\dot{\vec{\theta}}_P-\dot{\vec{\theta}}_S \qquad \vec{\phi}=\vec{\theta}_P-\vec{\theta}_S \tag{9-36a}$$

$$\dot{\vec{\varepsilon}}=\dot{\vec{\rho}}-\dot{\vec{\theta}}_S x\vec{R}_o \qquad \vec{\varepsilon}=\vec{\varepsilon}_C-\vec{\theta}_S x\vec{R}_o \tag{9-36b}$$

For i=1, n where n is the number of suspension points:

$$\dot{\vec{\delta}}_i=\dot{\vec{\varepsilon}}+\dot{\vec{\phi}}x\vec{\alpha}_i \qquad \vec{\delta}_i=\vec{\varepsilon}+\vec{\phi}x\vec{\alpha}_i \tag{9-37}$$

$$\vec{F}_{Si}=[K_i]\vec{\delta}_i+[C_i]\dot{\vec{\delta}}_i+\vec{f}_i \tag{9-38}$$

$$\vec{T}_{Pi}=-\vec{\alpha}_i x\vec{F}_{Si} \tag{9-39}$$

Finally, the required forces and torques to be fed back to equations 9-30, 9-31, and 9-32 are:

$$\vec{F}_{SS}=\sum_{i=1}^{n}\vec{F}_{Si} \tag{9-40}$$

$$\vec{T}_{SP}=\sum_{i=1}^{n}\vec{T}_{Pi} \tag{9-41}$$

$$\vec{T}_{SS}=\vec{R}_o x\vec{F}_{SS}-\vec{T}_{SP} \tag{9-42}$$

9.3 Simplified Vehicle Dynamics - The previous derivation if implemented for simulation would result in a dynamic simulation which would allow parametric variation of the number of isolators and their characteristics and locations, as well as center-of-mass locations of both the orbiter and pallet. Within the scope of this study, however, such generalizations are not needed and significant savings can be made in the computations required by making additional assumptions and using the four-point suspension configuration recommended in volume III of this report.

The four-point configuration is shown schematically in figure 9-3 which illustrates the near symmetrical placement of the isolators about the pallet center-of-mass and in a plane containing the center-of-mass. Under these conditions, the locations of the isolators $\vec{\alpha}_i$, i=1,4 can be expressed in terms of two lengths, i.e., the longitudinal and lateral distances from the mass center. Assuming perfect symmetry which implies uncoupled translation and rotation for the pallet, the isolator locating vectors $\vec{\alpha}_i$ can be

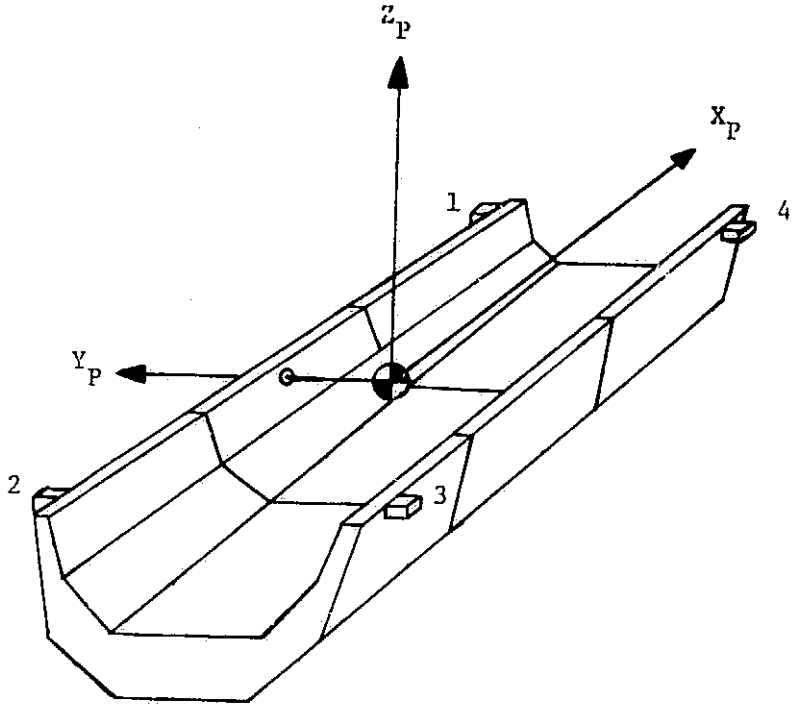

Figure 9-3. Suspension Point Identification - Four Point System

given in terms of the location of the number 1 isolator. Noting the isolators are numbered in terms of the quadrant of the $X_P Y_P$ plane in which they lie, the $\vec{\alpha}_i$ become under this assumption:

$$\vec{\alpha}_1=(\alpha_x,\alpha_y,0) \tag{9-43a}$$

$$\vec{\alpha}_2=(-\alpha_x,\alpha_y,0) \tag{9-43b}$$

$$\vec{\alpha}_3=(-\alpha_x,-\alpha_y,0) \tag{9-43c}$$

$$\vec{\alpha}_4=(\alpha_x,-\alpha_y,0) \tag{9-43d}$$

and,

$$\sum_{i=1}^{4} \vec{\alpha}_i \equiv 0 \tag{9-44}$$

If in addition it is assumed that each isolator exhibits identical spring rate and damping characteristics such that all $[K_i]=[K]$, $[C_i]=[C]$ and $F_{ki}=F_k$, the expression for the forces and torques applied by the suspension can be greatly simplified. With these assumptions, the force equation 9-40 can be written:

$$\vec{F}_{SS}=\sum_{i=1}^{4}\{[K](\vec{\varepsilon}+\vec{\phi}x\vec{\alpha}_i)+[C](\dot{\vec{\varepsilon}}+\dot{\vec{\phi}}x\vec{\alpha}_i)+f_i\}$$

$$=4[K]\vec{\varepsilon}+[K]\vec{\phi}x\sum_{i}^{4}\vec{\alpha}_i+4[C]\dot{\vec{\varepsilon}}+[C]\dot{\vec{\phi}}x\sum_{i}^{4}\vec{\alpha}_i+\sum_{i}^{4}\vec{f}_i$$

or,

$$\vec{F}_{SS}=4[K]\vec{\varepsilon}+4[C]\dot{\vec{\varepsilon}}+\sum_{1}^{4}\vec{f}_i \tag{9-45}$$

It should be noted that although the quantities δ_i are no longer required, $\dot{\vec{\delta}}_i$ must be calculated to determine the frictional forces $\vec{f}_i$, however, expanding the various $\dot{\vec{\delta}}_i$:

$$\dot{\vec{\delta}}_1=\dot{\vec{\varepsilon}}+\begin{bmatrix} -\alpha_y\dot{\phi}_z \\ \alpha_x\dot{\phi}_z \\ \alpha_y\dot{\phi}_x-\alpha_x\dot{\phi}_y \end{bmatrix}$$

$$\dot{\vec{\delta}}_2=\dot{\vec{\varepsilon}}+\begin{bmatrix} -\alpha_y\dot{\phi}_z \\ -\alpha_x\dot{\phi}_z \\ \alpha_x\dot{\phi}_y+\alpha_y\dot{\phi}_x \end{bmatrix}$$

$$\dot{\vec{\delta}}_3=\dot{\vec{\varepsilon}}+\begin{bmatrix} \alpha_y\dot{\phi}_z \\ -\alpha_x\dot{\phi}_z \\ \alpha_x\dot{\phi}_y-\alpha_y\dot{\phi}_x \end{bmatrix}$$

$$\dot{\vec{\delta}}_4=\dot{\vec{\varepsilon}}+\begin{bmatrix} \alpha_y\dot{\phi}_z \\ \alpha_x\dot{\phi}_z \\ -\alpha_x\dot{\phi}_y-\alpha_y\dot{\phi}_x \end{bmatrix}$$

By making the following definitions of individual components:

$$\dot{\delta}_{x1}=\dot{\varepsilon}_x-\alpha_y\dot{\phi}_z \tag{9-46a}$$

$$\dot{\delta}_{x3}=\dot{\varepsilon}_x+\alpha_y\dot{\phi}_z \tag{9-46b}$$

$$\dot{\delta}_{y1}=\dot{\varepsilon}_y+\alpha_x\dot{\phi}_z \tag{9-46c}$$

$$\dot{\delta}_{y2}=\dot{\varepsilon}_y-\alpha_x\dot{\phi}_z \tag{9-46d}$$

$$\dot{\delta}_{z1}=\dot{\varepsilon}_z+(\alpha_y\dot{\phi}_x-\alpha_x\dot{\phi}_y) \tag{9-46e}$$

$$\dot{\delta}_{z2}=\dot{\varepsilon}_z+(\alpha_y\dot{\phi}_x+\alpha_x\dot{\phi}_y) \tag{9-46f}$$

$$\dot{\delta}_{z3}=\dot{\varepsilon}_z-(\alpha_y\dot{\phi}_x-\alpha_x\dot{\phi}_y) \tag{9-46g}$$

$$\dot{\delta}_{z4}=\dot{\varepsilon}_z-(\alpha_y\dot{\phi}_x+\alpha_x\dot{\phi}_y) \tag{9-46h}$$

The twelve individual components of the δ_i can thus be given in terms of the above eight calculations which in turn involve sums and difference of many identical quantities. Denoting f_{ai} as the friction resulting from the rate $\dot{\delta}_{ai}$, a=x,y,z; i=1,2,3,4, the total friction force becomes:

$$\vec{F}_f \triangleq \sum_{i=1}^{4} \vec{f}_i = \begin{bmatrix} 2(f_{x1}+f_{x3}) \\ 2(f_{y1}+f_{y2}) \\ f_{z1}+f_{z2}+f_{z3}+f_{z4} \end{bmatrix} \tag{9-47}$$

Consider next the torque equation 9-41:

$$\vec{T}_{SP}=-\sum_{i=1}^{4} \vec{\alpha}_i x\{[K](\vec{\varepsilon}+\vec{\phi}x\vec{\alpha}_i)+[C](\dot{\vec{\varepsilon}}+\dot{\vec{\phi}}x\vec{\alpha}_i)+\vec{f}_i\}$$

$$=[K]\vec{\varepsilon}x\sum_{1}^{4}\vec{\alpha}_i x[K](\vec{\phi}x\vec{\alpha}_i)+[C]\dot{\vec{\varepsilon}}x\sum_{1}^{4}\vec{\alpha}_i-\sum_{1}^{4}\vec{\alpha}_i x[C](\dot{\vec{\phi}}x\vec{\alpha}_i)-\sum_{1}^{4}\vec{\alpha}_i x\vec{f}_i$$

The terms involving only sums of the $\vec{\alpha}_i$ clearly disappear, then expanding:

$$\sum_{1}^{4}\vec{\alpha}_i x[K](\vec{\phi}x\vec{\alpha}_i)=\sum_{1}^{4}\begin{bmatrix} K_z(\alpha_{yi}^2\phi_x-\alpha_{xi}\alpha_{yi}\phi_y) \\ K_z(\alpha_{xi}^2\phi_y-\alpha_{xi}\alpha_{yi}\phi_z) \\ (K_x\alpha_{yi}^2+K_y\alpha_{xi}^2)\phi_z \end{bmatrix} = \begin{bmatrix} 4K_z\alpha_y^2\phi_x \\ 4K_z\alpha_x^2\phi_y \\ 4(K_x\alpha_y^2+K_y\alpha_x^2)\phi_z \end{bmatrix}$$

with a parallel expansion for the damping term. Defining a friction torque:

$$\vec{T}_f \triangleq \sum_1^4 \vec{\alpha}_i x \vec{f}_i = \begin{bmatrix} -\alpha_y(f_{z1}+f_{z2}-f_{z3}-f_{z4}) \\ \alpha_x(f_{z1}-f_{z2}-f_{z3}+f_{z4}) \\ 2\alpha_y(f_{x1}-f_{x3})-2\alpha_x(f_{y1}-f_{y2}) \end{bmatrix} \tag{9-48}$$

Then, defining:

$$[K_C] \triangleq 4[K] \tag{9-49a}$$

$$[D_C] \triangleq 4[C] \tag{9-49b}$$

$$[K_\phi] \triangleq \mathrm{diag}\{4\alpha_y^2 K_z, 4\alpha_x^2 K_z, 4(\alpha_y^2 K_x + \alpha_x^2 K_y)\} \tag{9-49c}$$

$$[D_\phi] \triangleq \mathrm{diag}\{4\alpha_y^2 D_z, 4\alpha_x^2 D_z, 4(\alpha_y^2 D_x + \alpha_x^2 D_y)\} \tag{9-49d}$$

The suspension torque and force equations become:

$$\vec{F}_{SS} = [K_C]\vec{\epsilon} + [C_C]\dot{\vec{\epsilon}} + \vec{F}_f \tag{9-50}$$

$$\vec{T}_{SP} = -[K_\phi]\vec{\phi} - [C_\phi]\dot{\vec{\phi}} - \vec{T}_f \tag{9-51}$$

and as before,

$$\vec{T}_{SS} = -\vec{T}_{SP} + \vec{R}_o x \vec{F}_S \tag{9-52}$$

The equations of motion cannot be further simplified in vector form, however, since the cross products of inertia are small, some computational relief can be obtained by assuming a diagonal inertia tensor. The simplified dynamic equations excluding the resolution of CMG control torques are shown in block diagram form in figure 9-4.

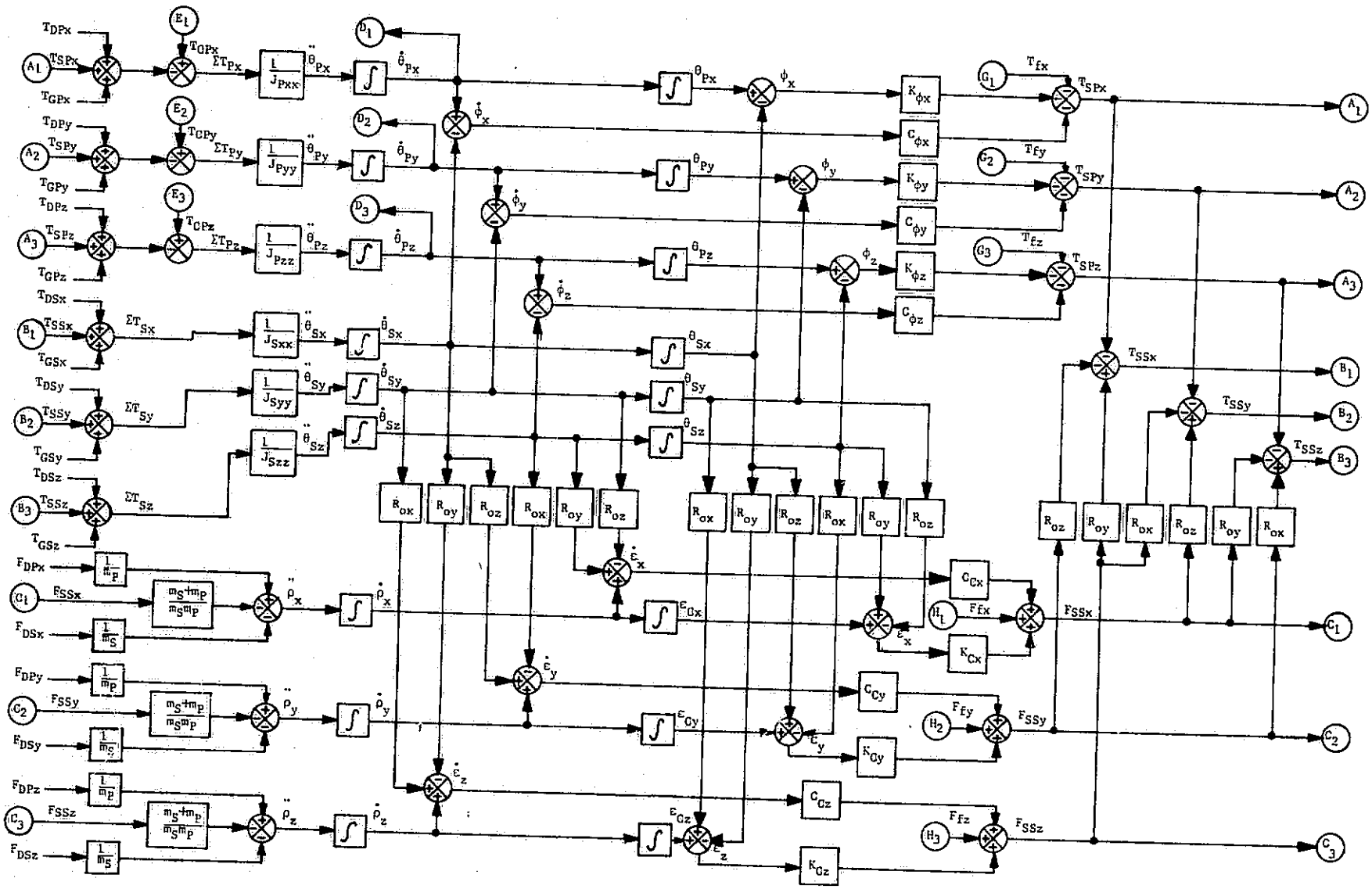

Orbiter/Suspension/Pallet Dynamics

Figure 9-4. Vehicle Dynamics Block Diagram (Sheet 1 of 2)

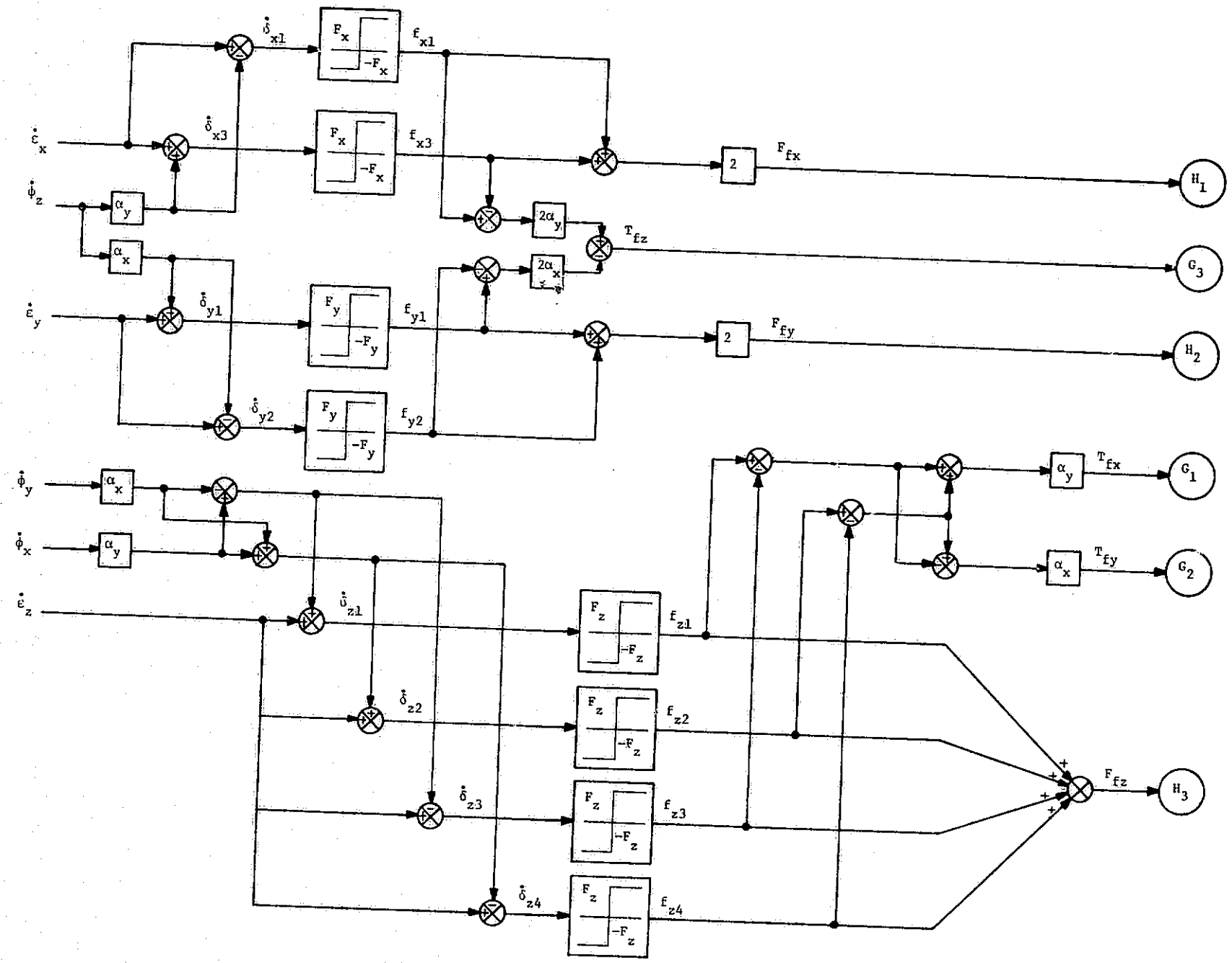

Suspension Friction

Figure 9-4. Vehicle Dynamics Block Diagram (Sheet 2 of 2)

10. COMPUTER STUDY

This section gives the computer results obtained from the hybrid simulation of the orbiter vehicle and the suspended pallet controlled by the shockmounted ATM CMG. The results described in this section were obtained from the pointing accuracy model defined in the preceding sections with the exceptions that CMG gimbal angle change, translational dynamics and suspension torque on the shuttle were neglected since they had negligible effect on the overall system response.

The main purpose of this study was to determine pallet pointing capability as a function of CMG nonlinearities, crew motion disturbance, GG effects, and system bandwidth. Studies determined that the only significant CMG nonlinearity was friction, discussed in section 7.3, and that GG disturbances would not affect pallet pointing appreciably. Therefore pointing studies were parameterized as a function of friction level, crew motion disturbance, system bandwidth and CMG gimbal angle. Limit cycle levels were obtained with no torque input and then the torque input level required to eliminate limit cycles was determined. These results are presented in this section with a summary of results given in table 10-4.

10.1 Hybrid Simulation Details - Figure 10-1 is a block diagram of the complete simulation showing the interrelationships of the vehicle control law (equation 8-1), the compensator (equation 8-26), the CMG control law (equations 6-13, 6-14, 6-22, 6-24 and 6-25), torque resolution (equation 9-1), the vehicle dynamics and the CMG models, both of the latter are discussed below. The model was implemented on a hybrid computer facility comprised of a Scientific Data Systems 86 digital computer interfaced with two Applied Dynamics AD-4 analog consoles and a Beckman Ease analog computer. The simulation was run in real time with the fastest possible sample period which was 7 msec. No quantization was present in the runs other than that of the computer A/D and D/A interfaces, approximately 0.006 percent of maximum value.

10.1.1 CMG Models - A detailed block diagram of the CMG model is given in figure 10-2. The only simplification of the model derived in section 7 is the deletion of the various limiters present in the rate loops. This was done since the region of operation of the CMGs in this study involves low signal levels throughout, thus obviating the need for the limiters. The CMG parameter values used in the frequency response runs and in all pointing performance runs with the exception of those involving variations of the CMG friction are listed in table 10-1.

The four CMG models incorporated into the complete simulation were altered somewhat to minimize the analog hardware requirement. This simplification consisted of replacement of the sines and cosines of gimbal angles with direct gains which could be preset to represent any arbitrary gimbal state. This simplification was made possible due to the short time periods and slow gimbal rates involved which validates the use of linear approximations to these functions.

10.1.2 Vehicle Dynamics Model - Figure 10-3 is a block diagram of the simplified vehicle dynamics used in the simulation study. The dynamics finally used in the computer study are those derived in section 9.3 with the translational dynamics and suspension torque acting on the orbiter being neglected due to the very low magnitudes of these items compared with the other parameters existing in the simulation.

Table 10-2 lists the vehicle dynamics parameter values used in all pointing performance runs.

10.2 CMG Frequency Response - The CMG model frequency response for zero inner and outer gimbal angles and 0.01 rad/sec gimbal rate command amplitude is given in figures 10-4 and 10-5. The quantity T_c is the CMG output torque in the direction of the torque command and perpendicular to the CMG momentum vector divided by the amplitude of the command torque and is theoretically one. The quantity T_x is the CMG output torque in the direction perpendicular to both the command torque and the CMG momentum vector divided by the amplitude of the command torque and is theoretically zero. The third component of CMG output torque, the component in the direction of the CMG momentum vector, was judged to be small and therefore not monitored.

To compensate for the CMG dynamics of figures 10-4 and 10-5, the following compensator parameters (equation 8-26) were employed in all pointing performance runs: ω_1=12.5 rad/sec, ζ_1=0.125, ω_2=70 rad/sec and ζ_2=0.707.

10.3 Simulation Study Outline - Pallet control loop bandwidths of 1/2, 1, 2 and 4 Hz were considered in this study. The vehicle control law rate, position, and position integral gains corresponding to these bandwidths were determined from the analysis of section 8 and are given in table 10-3.

There were three types of runs made for the various system bandwidths and at CMG gimbal angle combinations of 0° and 45°. The three types of pointing performance runs which were made are:

1. No torque disturbance acting on the pallet or orbiter.

2. Step torque disturbance acting on the pallet.

   a) Each axis individually at the minimum value necessary to eliminate the undisturbed limit cycle on that axis.

   b) All axes simultaneously at the values determined in part a.

3. Crew motion torque disturbance acting on the orbiter as given by $\vec{T}_{DS}=\vec{R}x\vec{F}_{DS}$ where $\vec{R}=(-15,0,0)^T$ meter, and

   Case I $\quad \vec{F}_{DS}=(0,F_D,0)^T$ n

   Case II $\quad \vec{F}_{DS}=(0,0,F_D)^T$ n

   Case III $\quad \vec{F}_{DS}=(0,\frac{F_D}{\sqrt{2}},\frac{F_D}{\sqrt{2}})^T$ n

   where: F_D ramps from zero to 100 newtons during the first 0.8 seconds, is zero between 0.8 seconds and 2.4 seconds, ramps from -100 newtons to zero during the last 0.8 seconds.

The above runs were made for:

a) The 1/2, 1, 2, and 4 Hz systems with all gimbal angles equal to 0°.

b) The 1/2 and 1 Hz systems with all gimbal angles equal to 45°.

c) The 2 and 4 Hz systems with the inner gimbal angles equal to 0° and outer gimbal angles equal to 45°.

In addition, type one runs were made for the 1, 2 and 4 Hz systems with all gimbal angles equal 0 and with the CMG friction adjusted to 1/2 the nominal friction level and to 2 times the

nominal friction level. Time histories of various system variables were plotted on strip chart recorders. The variables chosen for display were the following:

$\dot{\delta}_{1j}, j = 1,2,3,4$	CMG inner gimbal rates
$\dot{\delta}_{3j}, j = 1,2,3,4$	CMG outer gimbal rates
$\dot{\theta}_{Si}, i = x,y,z$	orbiter angular rates
$\theta_{Si}, i = x,y,z$	orbiter attitude
$T_{DPi}, i = x,y,z$	torque disturbance on pallet
$T_{Ci}, i = x,y,z$	torque command from vehicle control law
$T'_{Ci}, i = x,y,z$	torque command from compensator
$T_{CPi}, i = x,y,z$	net CMG torque applied to pallet
$\dot{\theta}_{Pi}, i = x,y,z$	pallet angular rates
$\theta_{Pi}, i = x,y,z$	pallet attitude

10.4 Pointing Performance Study Results - Reproductions of selected computer runs are shown in figures 10-6 through 10-46. In reading the runs, time can be read from the marks at the top and bottom of each run where each mark corresponds to 1 second.

10.4.1 CMG Friction Study - The primary nonlinearity of the CMG is friction. When no vehicle disturbances are present, the CMG friction causes limit cycles as evidenced by observing θ_{Pi} on figures where no disturbance torque is applied (i.e., figure 10-6 for example). As can be seen by comparison (figure 10-6 vs 10-16), the limit cycle amplitude decreases as the system bandwidth increases. Figure 10-47 summarizes how pallet attitude (θ_{Pi}) varies with bandwidth.

Studies were also made to determine the effect of friction level on limit cycle amplitude. (See figures 10-41 through 10-46.) For a 2 Hz system with gimbal angles set equal to zero, the pallet attitude error due to nominal CMG friction was approximately 0.1 arc-second about the pallet Y and Z axes, and approximately 1.1 arc-second about the pallet X-axis. As the CMG friction level increases or decreases, the limit cycle amplitude varies proportionately. The effect of friction level for various system bandwidths is summarized in figure 10-48.

10.4.2 Vehicle Disturbance - When small vehicle disturbance torques (T_{DPi}) are applied, approxiamtely 1 n-m, steady CMG gimbal rates occur and the system stops limit cycling (i.e, figure 10-37). Disturbance torques (T_{DPi}) required to stop limit cycling at various system bandwidths are summarized in figure 10-49.

10.4.3 Crew Motion Disturbances - Crew motion is the largest disturbance expected which will affect pallet pointing performance. For the 2 Hz system with CMG gimbal angles at zero, the worst case crew motion disturbance error is 0.25 arc-second about the pallet Z-axis (see figure 10-28). As can be seen from the computer runs, pointing error introduced as a result of crew motion disturbance decreases as system bandwidth increases. These results are summarized in figure 10-50.

10.5 Summary - Data presented in this section shows that the system will have a limit cycle attitude error due to the CMG friction when no external torques act on the vehicle. It also shows that the limit cycle amplitude to be a function of friction level and system bandwidth. This limit cycling can be stopped by applying torques to the vehicle which cause CMG gimbal rates to be required. In addition, crew motion disturbance causes attitude error which is reduced by increasing system bandwidth.

Due to what has been said in the above paragraph, it would seem that the higher the system bandwidth the better the system performance; however, the higher the system bandwidth the less stable the system becomes. In fact, the 2 Hz system was unstable at 45 degree inner and outer gimbal angles and the 4 Hz system was unstable at both 45 degree inner and outer gimbal angles and zero inner gimbal angles and 45 degree outer gimbal angles. This instability was not predicted by an idealized CMG system analysis and thus must be attributed to CMG dynamics. However, it is anticipated that a redesign of the CMG rate loops, taking into account the effects of the CMG shockmount, will eliminate these instabilities.

In summary, the 2 Hz system could easily meet the 1 arc-second pointing requirement considering the fact that an orbital vehicle almost always has disturbance torques acting upon it. Redesign of the CMG rate loop is recommended to take into account the effects of the CMG shockmounts and eliminate system instabilities presently observed for the ATM CMG rate loop design. In addition a redesign of the rate loops, to better compensate for the effects of friction at zero gimbal rate commands, will allow lower vehicle loop bandwidths (i.e., approximately 1 Hz) while still meeting the 1 arc-second pointing stability performance desired for all system states.

Table 10-1. Floated Pallet Pointing Performance Study CMG Parameters

Parameter	Symbol	Nominal Magnitude	Units
Inner Axis Compensator Gain	K_1	10.54	vdc/vdc
Outer Axis Compensator Gain	K_3	12.80	vdc/vdc
Inner Gimbal Amplifier Gain	K_{a1}	10.0	amp/vdc
Outer Gimbal Amplifier Gain	K_{a3}	10.0	amp/vdc
Inner Gimbal Motor Gain	K_{m1}	1.559	N-m/amp
Outer Gimbal Motor Gain	K_{m3}	1.559	N-m/amp
Inner Gimbal Tachometer Gain	K_{R1}	0.995	vdc/rad/sec
Outer Gimbal Tachometer Gain	K_{R3}	0.995	vdc/rad/sec
Compensator Lead Corner Frequency	ω_N	20.0	rad/sec
Compensator Lag Corner Frequency	ω_D	0.2	rad/sec
Motor Deadzone	-	0.003	ampere
Gimbal Motor Static Friction	S_m	0.1	N-m
Gimbal Motor Running Friction	R_m	0.08	N-m
Zero Gimbal Rate Band	ε_g	0.00005	rad/sec
Zero Motor Rate Band	ε_m	0.002828	rad/sec
Gear Ratio	N_g	56.55	
Inner Gimbal Motor Inertia	J_{m1}	0.0068	kg-m^2
Outer Gimbal Motor Inertia	J_{m3}	0.0068	kg-m^2
Inner Gimbal Gear Train Stiffness	K_{g1}	203,370	N-m/rad
Outer Gimbal Gear Train Stiffness	K_{g3}	203,370	N-m/rad
Moment of Inertia of Wheel About Axis Perpendicular to Spin Axis	J_d	1.803	kg-m^2
Gimbal Static Friction	S_g	0.5	N-m
Gimbal Running Friction	R_g	0.4	N-m
Bearing Compliance	$K_{\gamma 1}$	542,320	N-m/rad
Bearing Compliance	$K_{\gamma 3}$	542,320	N-m/rad
Compliance Damping	$\beta_{\gamma 1}$	20	(N-m-sec)/rad
Compliance Damping	$\beta_{\gamma 3}$	20	(N-m-sec)/rad
Angular Momentum of Wheel	H_r	3115.0	N-m-sec
Inner Gimbal Inertia	J_{a11}	0.746	kg-m^2
Inner Gimbal Inertia	J_{a22}	0.868	kg-m^2
Inner Gimbal Inertia	J_{a33}	1.003	kg-m^2

Table 10-1. Floated Pallet Pointing Performance Study CMG Parameters (Concluded)

Parameter	Symbol	Nominal Magnitude	Units
Outer Gimbal Inertia	J_{c11}	0.76	$kg\text{-}m^2$
Outer Gimbal Inertia	J_{c22}	4.3	$kg\text{-}m^2$
Outer Gimbal Inertia	J_{c33}	3.9	$kg\text{-}m^2$
Equivalent Outer Gimbal Inertia	J'_{c33}	4.834	$kg\text{-}m^2$
CMG Base Inertia	J_{b11}	5.35	$kg\text{-}m^2$
CMG Base Inertia	J_{b22}	7.9	$kg\text{-}m^2$
CMG Base Inertia	J_{b33}	3.63	$kg\text{-}m^2$
Shockmount Spring Const.	K_{Sx}	170,000	N-m/rad
Shockmount Spring Const.	K_{Sy}	208,000	N-m/rad
Shockmount Spring Const.	K_{Sz}	58,000	N-m/rad
Shockmount Damping	D_{Sx}	402	(N-m-sec)/rad
Shockmount Damping	D_{Sy}	490	(N-m-sec)/rad
Shockmount Damping	D_{Sz}	137	(N-m-sec)/rad

Table 10-2. Floated Pallet Pointing Performance Study Vehicle Parameters

Parameter	Symbol	Nominal Magnitude	Units
Reciprocal of Pallet Inertia	A_{Pxx}	4.696×10^{-5}	$1/kg\text{-}m^2$
Reciprocal of Pallet Inertia	A_{Pyy}	7.204×10^{-6}	$1/kg\text{-}m^2$
Reciprocal of Pallet Inertia	A_{Pzz}	7.384×10^{-6}	$1/kg\text{-}m^2$
Reciprocal of Shuttle Inertia	A_{Sxx}	1.015×10^{-6}	$1/kg\text{-}m^2$
Reciprocal of Shuttle Inertia	A_{Syy}	1.385×10^{-7}	$1/kg\text{-}m^2$
Reciprocal of Shuttle Inertia	A_{Szz}	1.354×10^{-7}	$1/kg\text{-}m^2$
Suspension Spring Const.	$K_{\phi x}$	8,420	N-m
Suspension Spring Const.	$K_{\phi y}$	21,555	N-m
Suspension Spring Const.	$K_{\phi z}$	53,432	N-m
Suspension Damping	$C_{\phi x}$	2,679	N-m-sec
Suspension Damping	$C_{\phi y}$	6,860	N-m-sec
Suspension Damping	$C_{\phi z}$	17,007	N-m-sec

Table 10-3. Floated Pallet Pointing Performance Study
Vehicle Control Law Gains

GAIN \ BANDWIDTH		(Hz)			
		0.5	1.0	2.0	4.0
N-m-sec/rad	K_{Rx}	4.60×10^4	9.18×10^4	1.84×10^5	3.67×10^5
	K_{Ry}	3.00×10^5	5.98×10^5	1.20×10^6	2.40×10^6
	K_{Rz}	3.00×10^5	5.84×10^5	1.17×10^6	2.34×10^6
N-m/rad	K_{Px}	5.00×10^5	1.98×10^5	7.94×10^5	3.17×10^6
	K_{Py}	3.20×10^5	1.29×10^6	5.18×10^6	2.00×10^7
	K_{Pz}	3.20×10^5	1.26×10^6	5.05×10^6	2.00×10^7
N-m/rad-sec	K_{PIx}	5.75×10^3	4.59×10^4	3.68×10^5	7.40×10^5
	K_{PIy}	3.75×10^4	2.99×10^5	2.40×10^6	4.80×10^6
	K_{PIz}	3.65×10^4	2.92×10^5	2.34×10^6	4.60×10^6

Table 10-4. Floated Pallet Hybrid Simulation Study Results

			SYSTEM BANDWIDTH	0.5 Hz	1.0 Hz	2.0 Hz	4.0 Hz
ZERO GIMBAL ANGLES	UNLOADED LIMIT CYCLE (PEAK VALUE) $\widehat{SEC}$	2 TIMES NOMINAL FRICTION	X axis	-	3.0	2.3	1.4
			Y axis	-	0.3	0.2	0.1
			Z axis	-	0.3	0.2	0.1
		NOMINAL FRICTION	X axis	4.0	1.5	1.1	0.6
			Y axis	0.4	0.15	0.1	0.05
			Z axis	0.4	0.15	0.1	0.05
		0.5 TIMES NOMINAL FRICTION	X axis	-	0.7	0.5	0.4
			Y axis	-	0.1	0.05	0.03
			Z axis	-	0.1	0.05	0.03
	TORQUE DISTURBANCE REQUIRED TO ELIMINATE LIMIT CYCLE (N-m)		X axis	0.5	0.6	1.0	2.2
			Y axis	1.2	1.1	0.8	1.4
			Z axis	1.2	0.6	0.6	1.4
	CREW MOTION DISTURBANCE (PEAK VALUE) $\widehat{SEC}$		Case I (Z axis)	5.0	1.2	0.25	0.05
			Case II (Y axis)	2.0	0.5	0.1	nil
			Case III (X axis)	1.5	0.35	0.05	nil
			(Z axis)	3.5	0.8	0.1	0.05
45 DEGREE GIMBAL ANGLES 0.5 and 1.0 Hz 45,45 2.0 and 4.0 Hz 0,45	UNLOADED LIMIT CYCLE (PEAK VALUE) $\widehat{SEC}$		X axis	1.5	0.1	0.5	*
			Y axis	0.5	0.25	0.2	*
			Z axis	0.5	0.2	0.2	*
	TORQUE DISTURBANCE REQUIRED TO ELIMINATE LIMIT CYCLE (N-m)		X axis	5.0	0.6	1.0	*
			Y axis	1.2	1.1	1.2	*
			Z axis	1.2	0.6	1.0	*
	CREW MOTION DISTURBANCE (PEAK VALUE) $\widehat{SEC}$		Case I (Z axis)	5.0	1.2	0.2	*
			Case II (Y axis)	2.0	0.5	nil	*
			Case III (Y axis)	1.5	0.4	nil	*
			(Z axis)	3.0	0.8	0.15	

*Unstable system, not run.

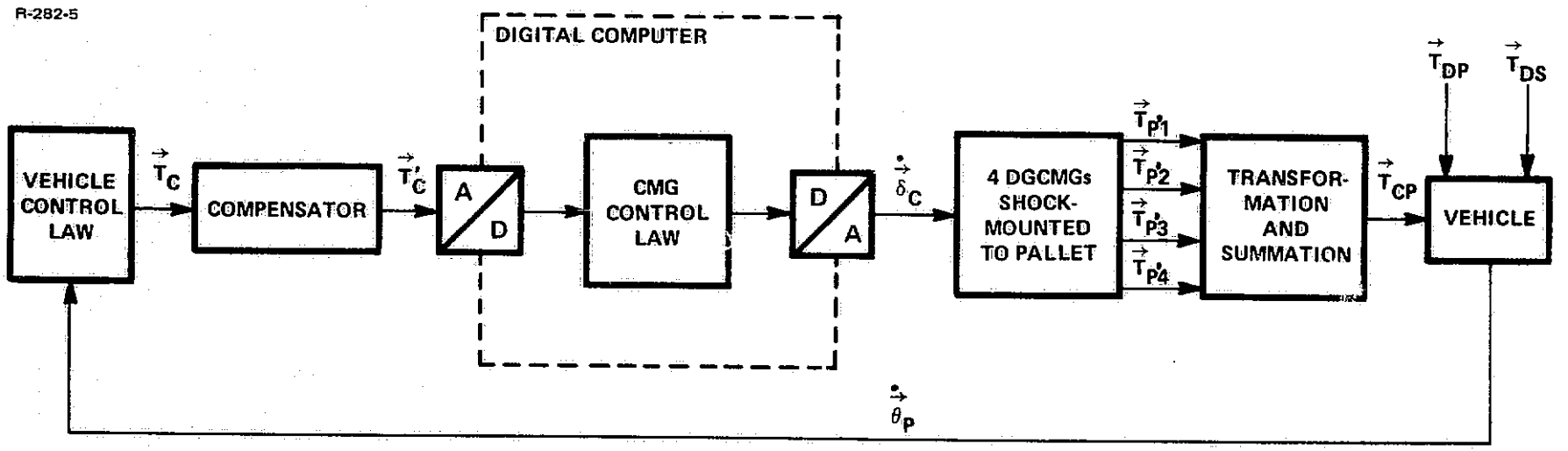

Figure 10-1 - Floated Pallet Pointing Performance Study, Hybrid Computer Model

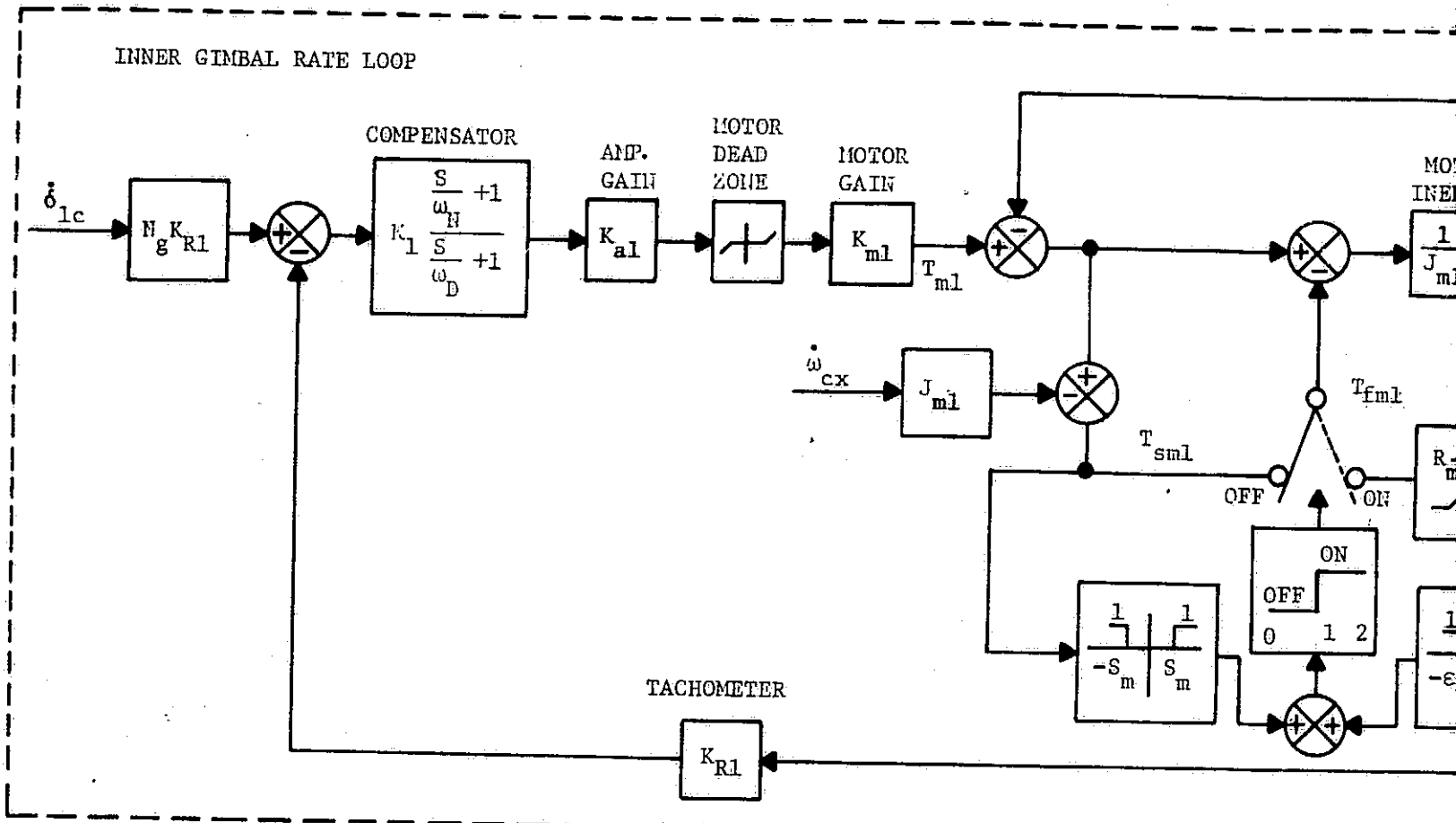
INNER GIMBAL RATE LOOP
COMPENSATOR
AMP. GAIN
MOTOR DEAD ZONE
MOTOR GAIN
$\dot{\delta}_{1c}$
$N_g K_{R1}$
$K_1 \frac{\frac{S}{\omega_N}+1}{\frac{S}{\omega_D}+1}$
K_{a1}
K_{m1}
T_{m1}
$\dot{\omega}_{cx}$
J_{m1}
T_{sm1}
T_{fm1}
OFF
ON
$-S_m$
S_m
TACHOMETER
K_{R1}

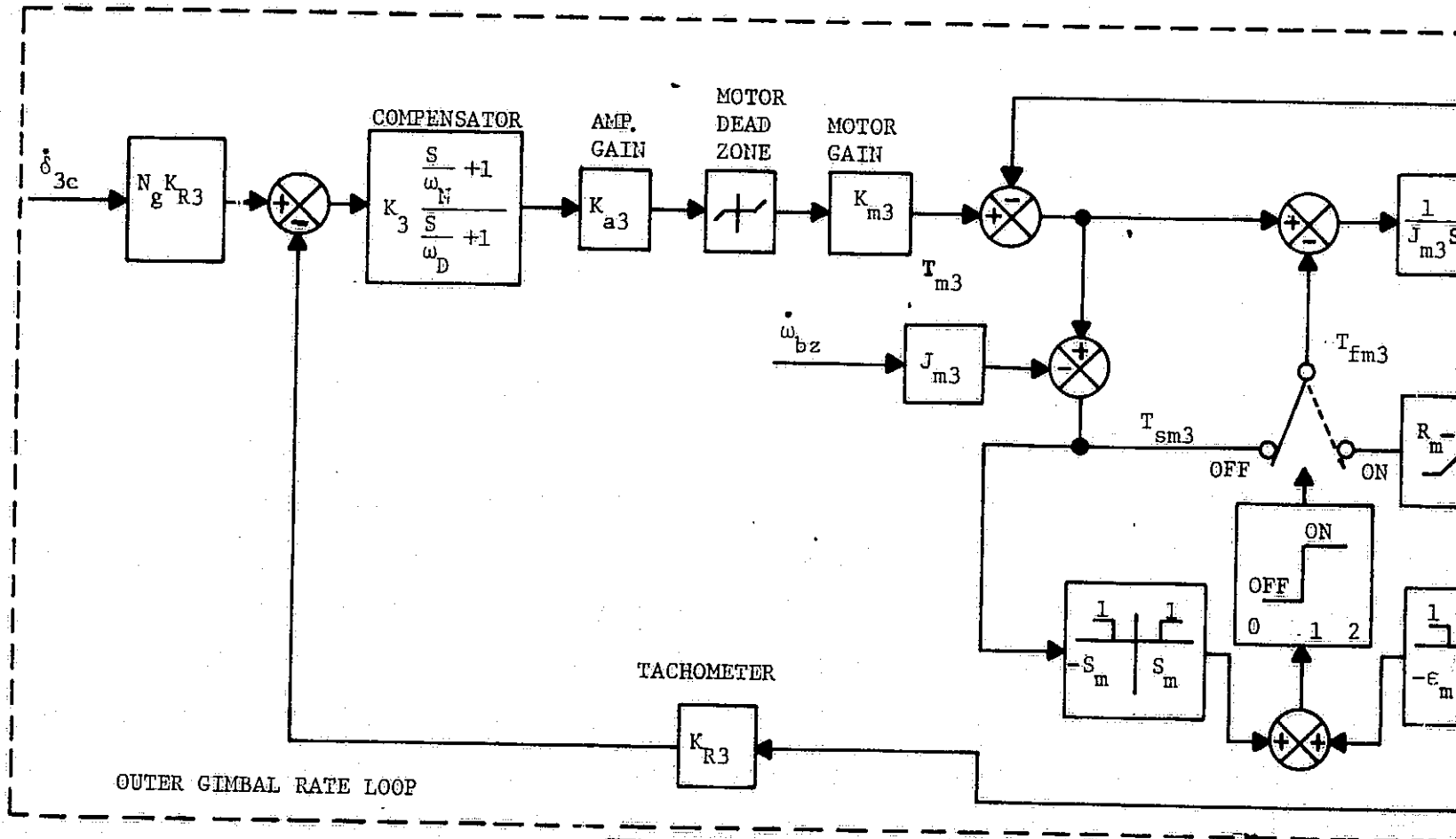
COMPENSATOR
AMP. GAIN
MOTOR DEAD ZONE
MOTOR GAIN
$\dot{\delta}_{3c}$
$N_g K_{R3}$
$K_3 \frac{\frac{S}{\omega_N}+1}{\frac{S}{\omega_D}+1}$
K_{a3}
K_{m3}
T_{m3}
$\dot{\omega}_{bz}$
J_{m3}
T_{sm3}
T_{fm3}
OFF
ON
$-S_m$
S_m
TACHOMETER
K_{R3}
OUTER GIMBAL RATE LOOP

F-1

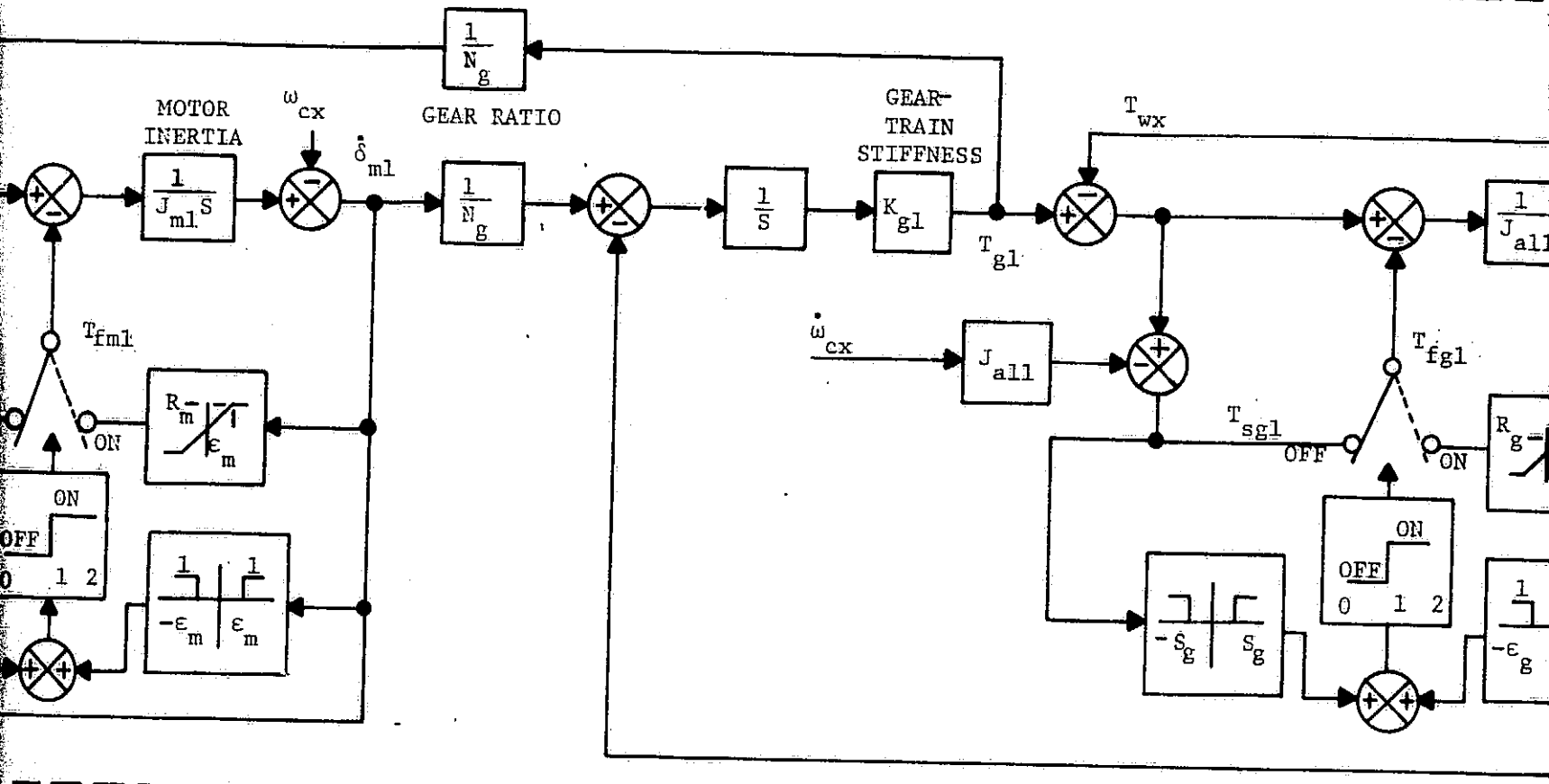

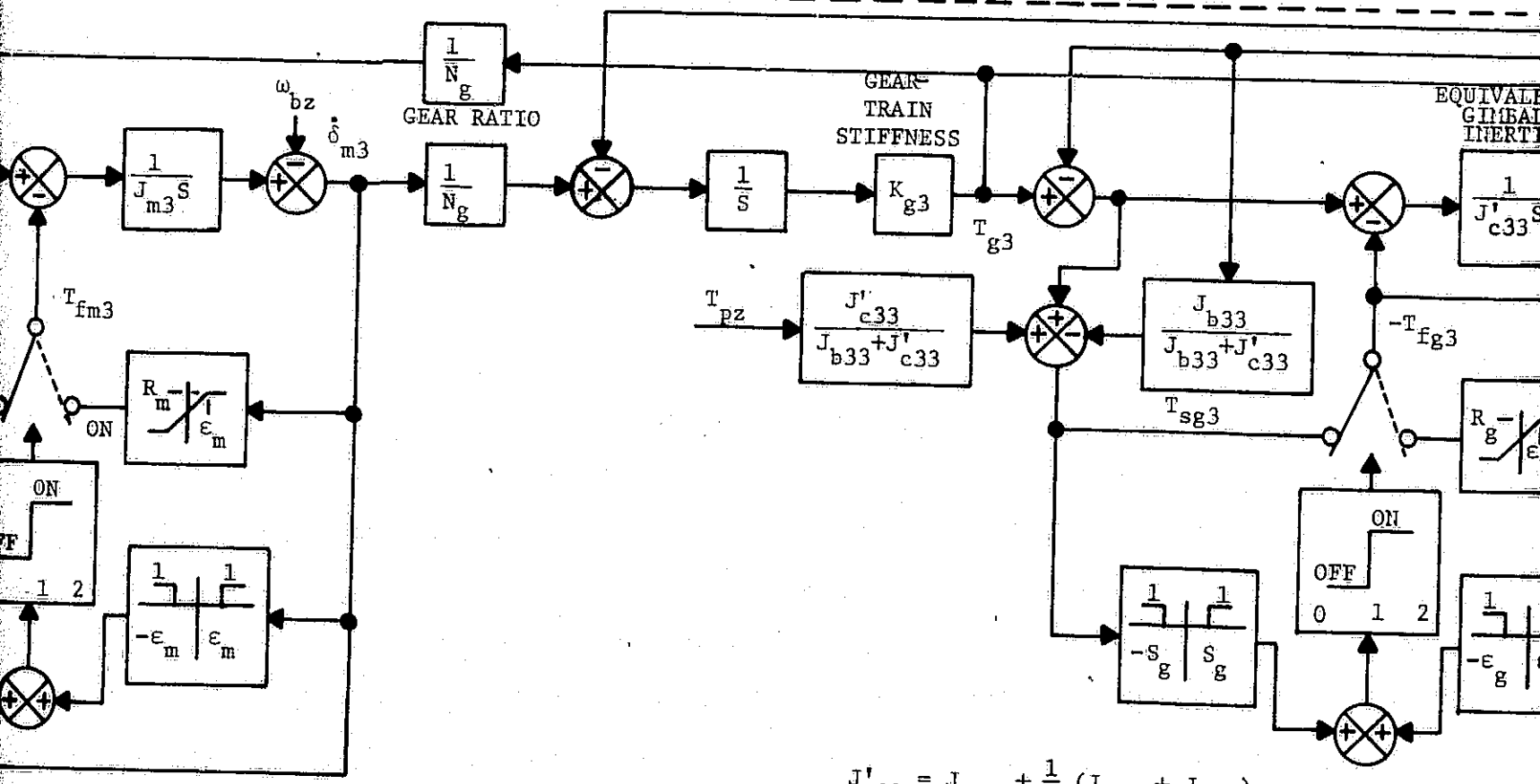

$$J'_{c33} = J_{c33} + \frac{1}{2}\left(J_{a22} + J_{a33}\right)$$

F-2

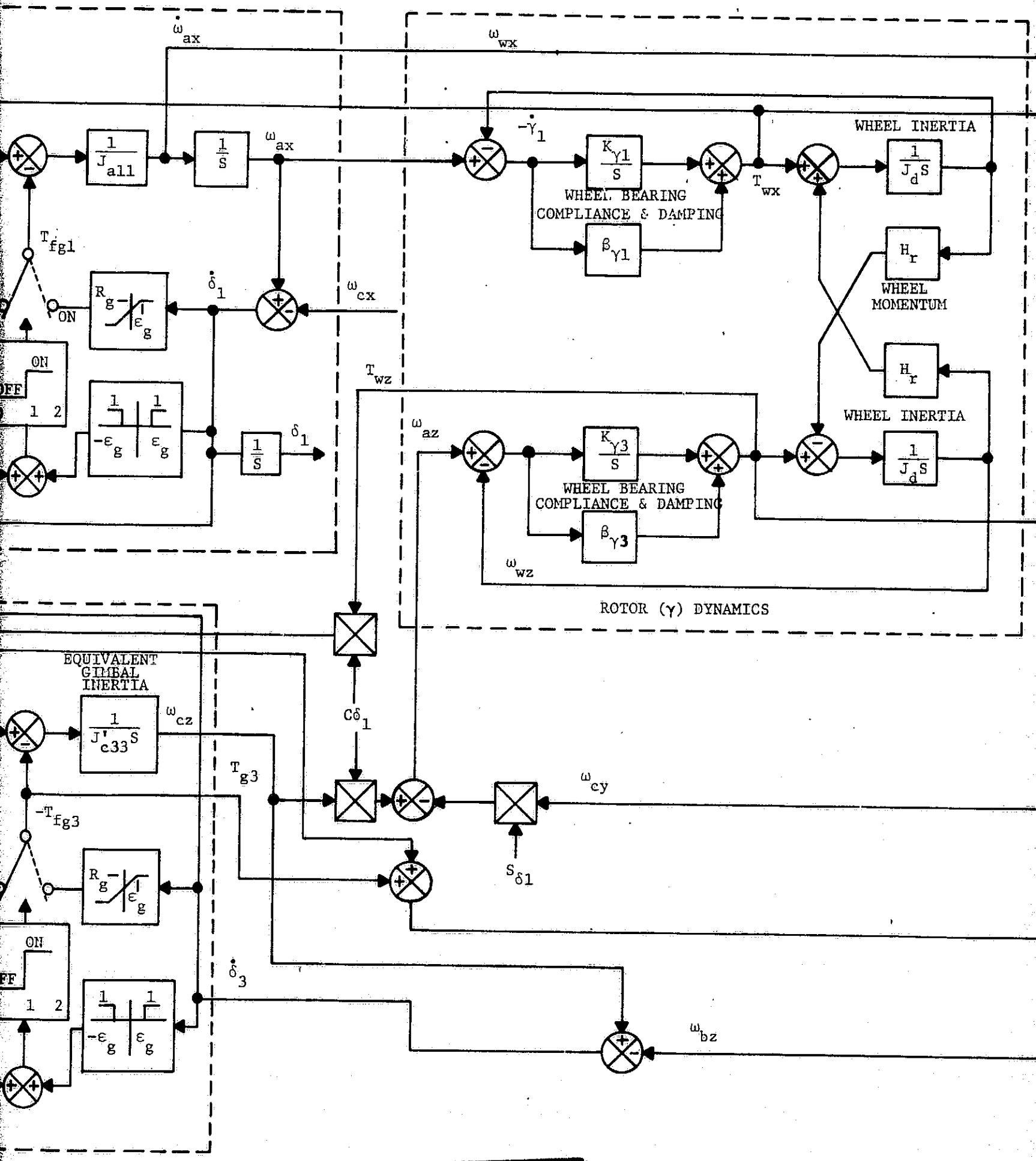
$\dot{\omega}_{ax}$
ω_{wx}
$\frac{1}{J_{all}}$
$\frac{1}{s}$
ω_{ax}
$-\dot{\gamma}_1$
$\frac{K_{\gamma 1}}{s}$
WHEEL BEARING
COMPLIANCE & DAMPING
$\beta_{\gamma 1}$
T_{wx}
WHEEL INERTIA
$\frac{1}{J_d s}$
H_r
WHEEL
MOMENTUM
H_r
WHEEL INERTIA
$\frac{1}{J_d s}$
T_{fg1}
ON
R_g
ε_g
$\dot{\delta}_1$
ω_{cx}
ON
OFF
1 2
1
1
$-\varepsilon_g$
ε_g
$\frac{1}{s}$
δ_1
T_{wz}
ω_{az}
$\frac{K_{\gamma 3}}{s}$
WHEEL BEARING
COMPLIANCE & DAMPING
$\beta_{\gamma 3}$
ω_{wz}
ROTOR (γ) DYNAMICS
EQUIVALENT
GIMBAL
INERTIA
$\frac{1}{J'_{c33} s}$
ω_{cz}
$C\delta_1$
T_{g3}
ω_{cy}
$-T_{fg3}$
$S_{\delta 1}$
R_g
ε_g
ON
OFF
1 2
$\dot{\delta}_3$
1
1
$-\varepsilon_g$
ε_g
ω_{bz}

F 3

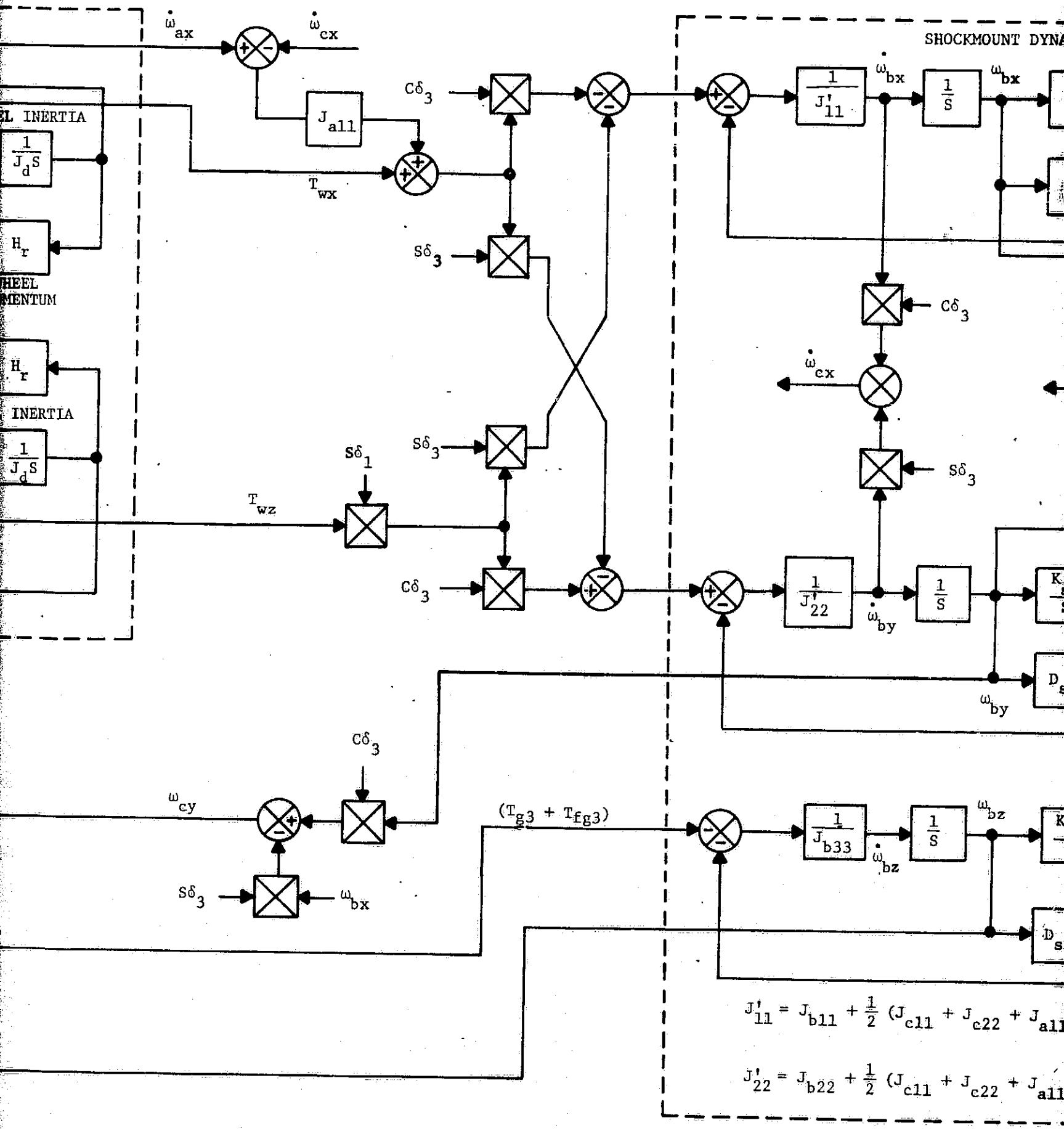

Figure 10-2. Shock Mounted Six-Ma

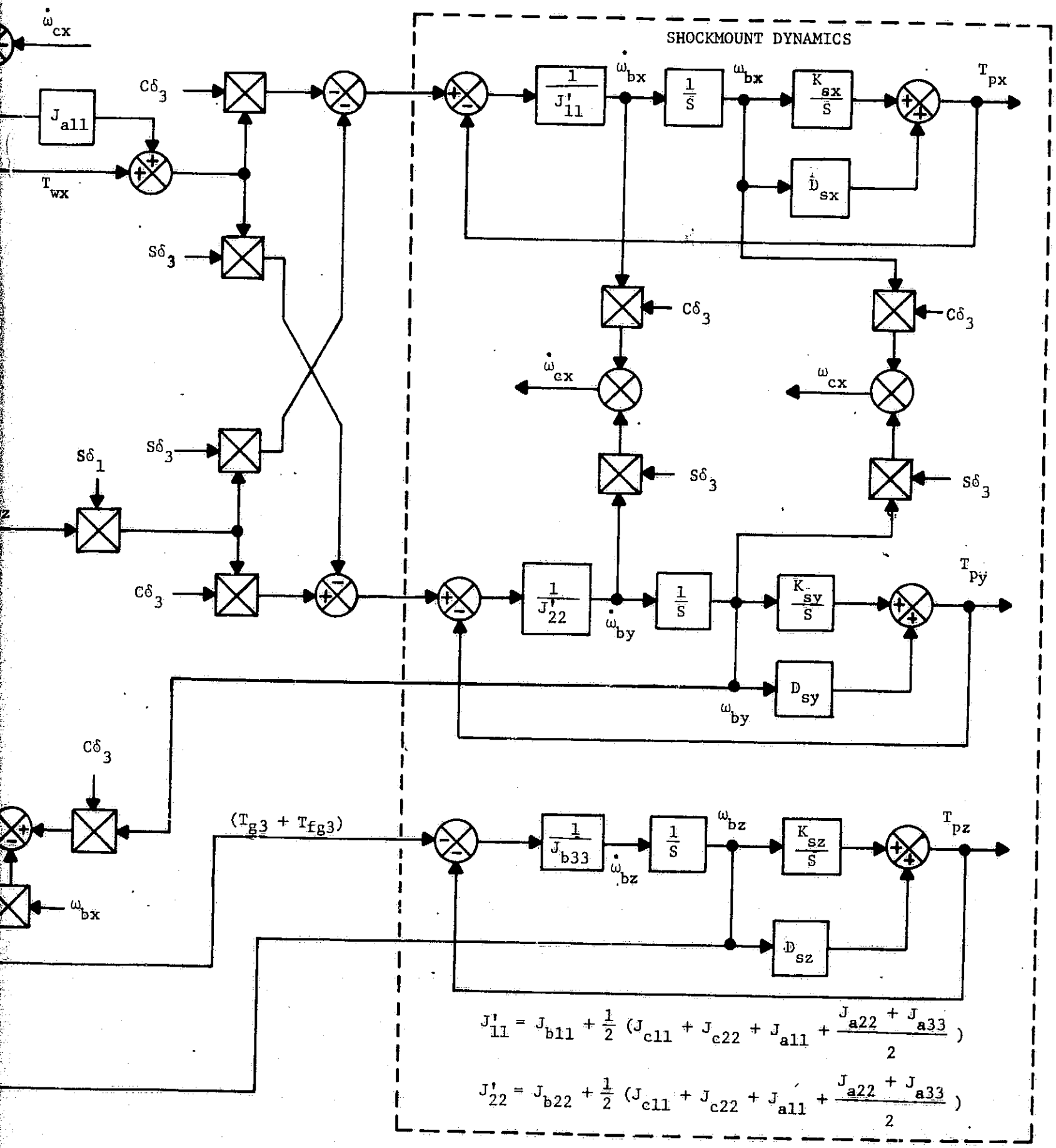

Figure 10-2. Shock Mounted Six-Mass CMG Dynamic Model

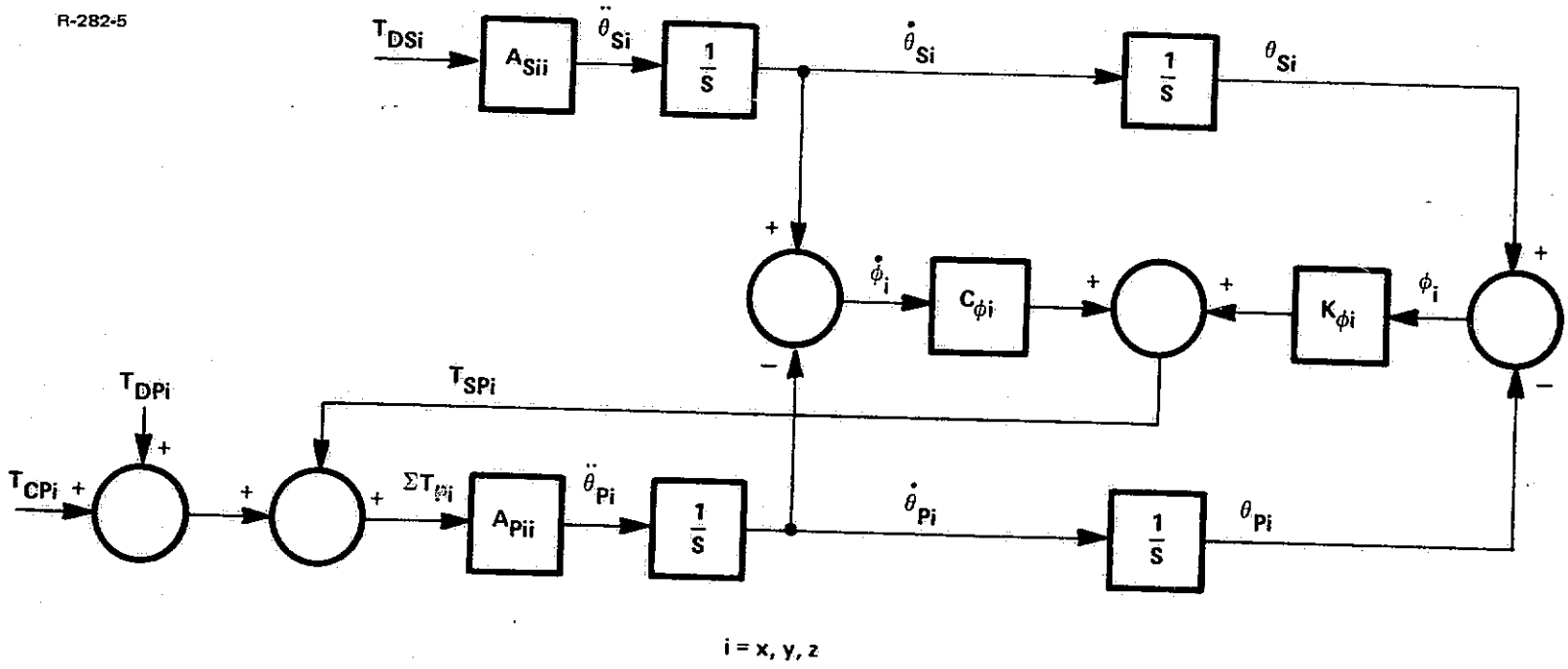

Figure 10-3 - Floated Pallet Pointing Performance Study, Vehicle Dynamics

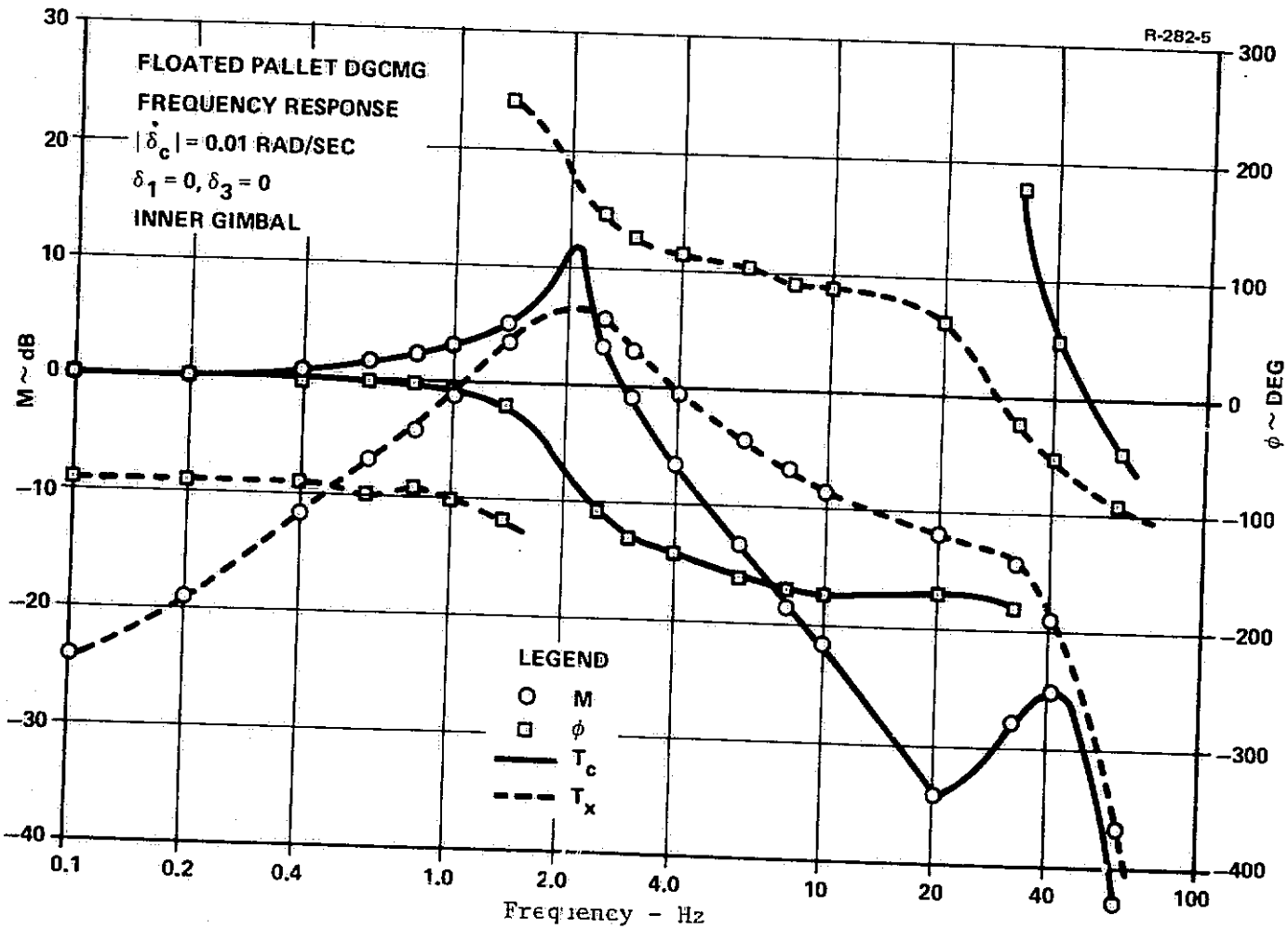

Figure 10-4. Floated Pallet CMG Frequency Response to Inner Gimbal Rate Command

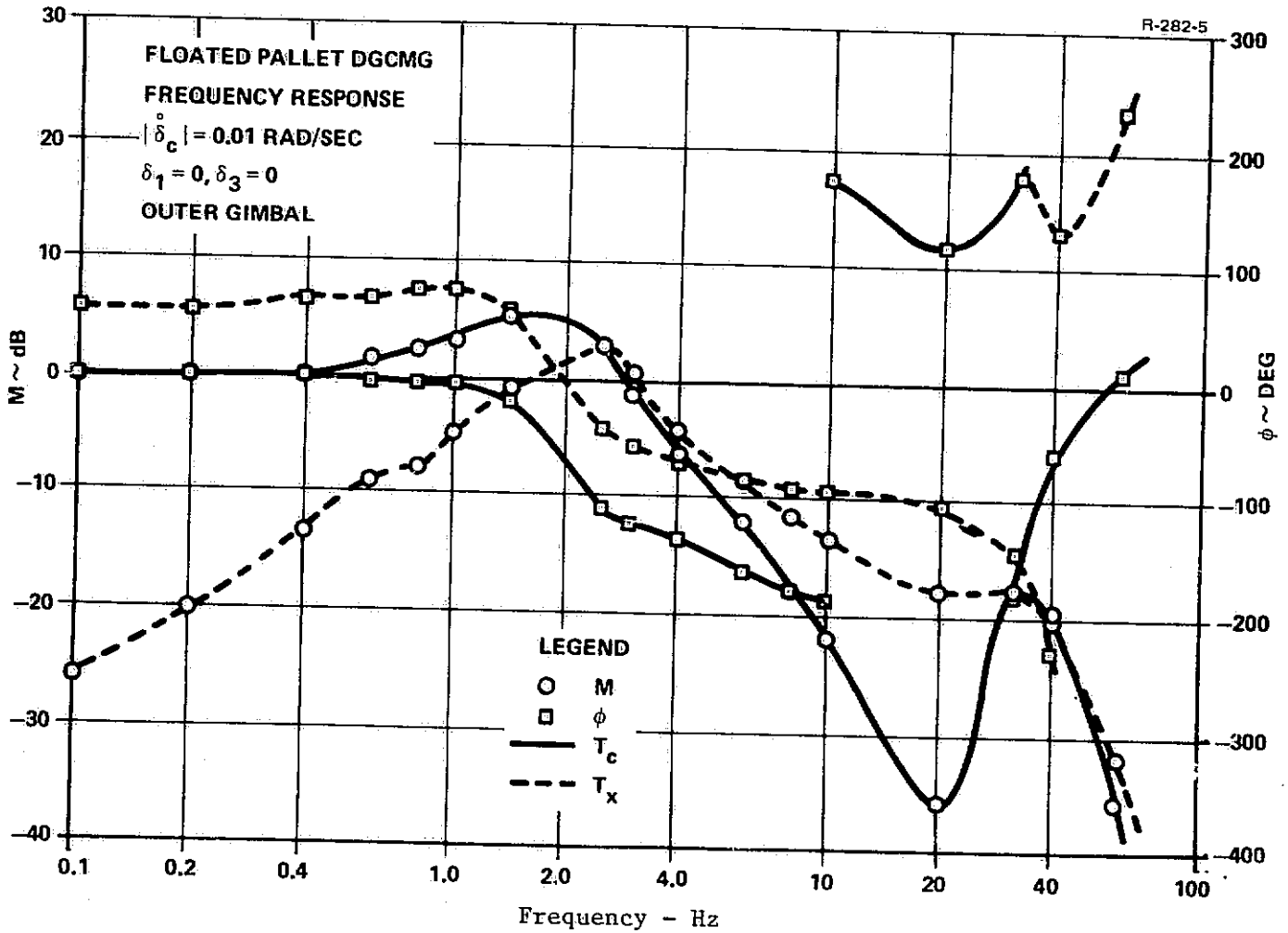

Figure 10-5. Floated Pallet CMG Frequency Response to Outer Gimbal Rate Command

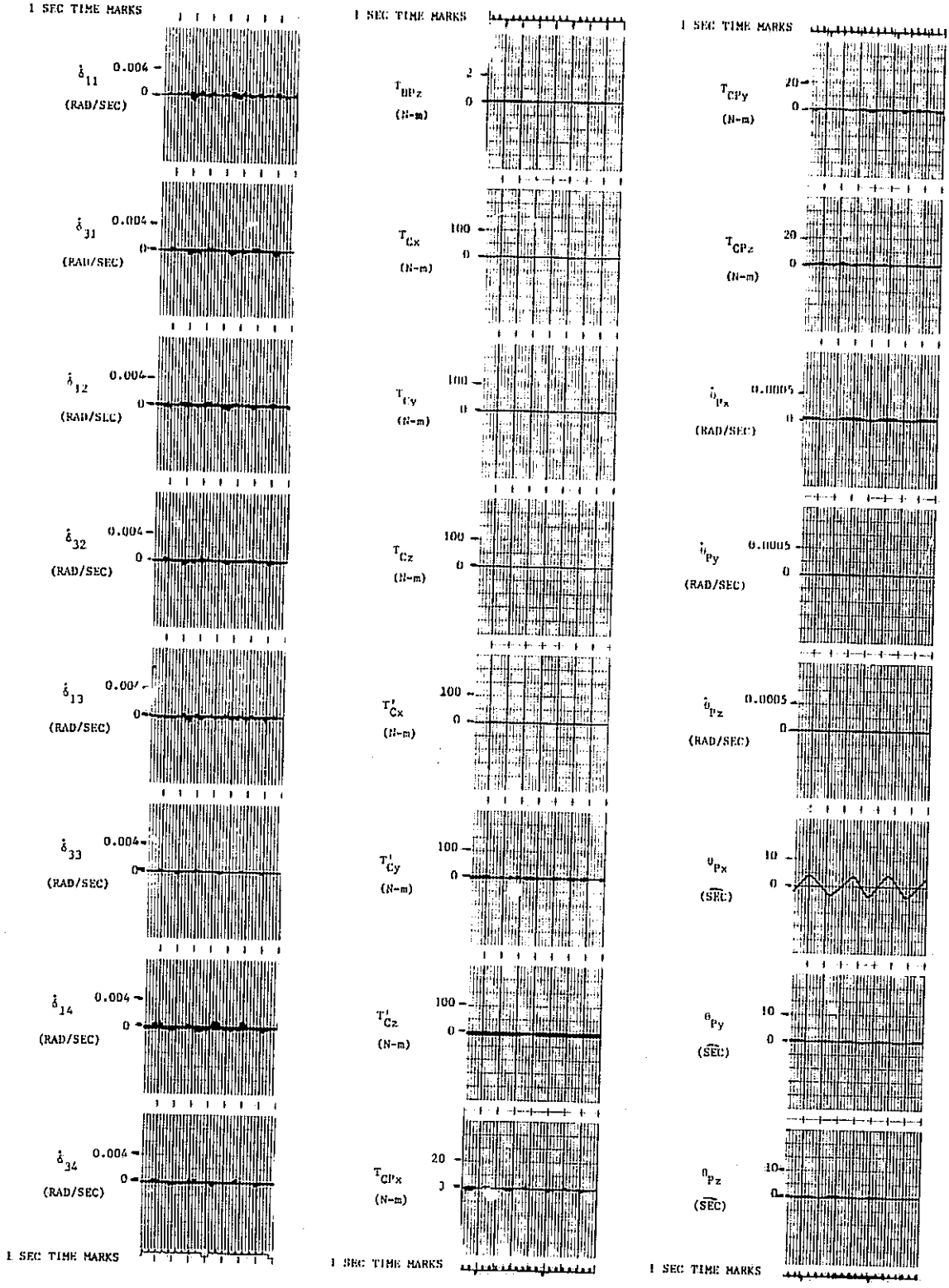

Figure 10-6. No Torque Disturbance, 1/2 Hz System, Zero Gimbal Angles

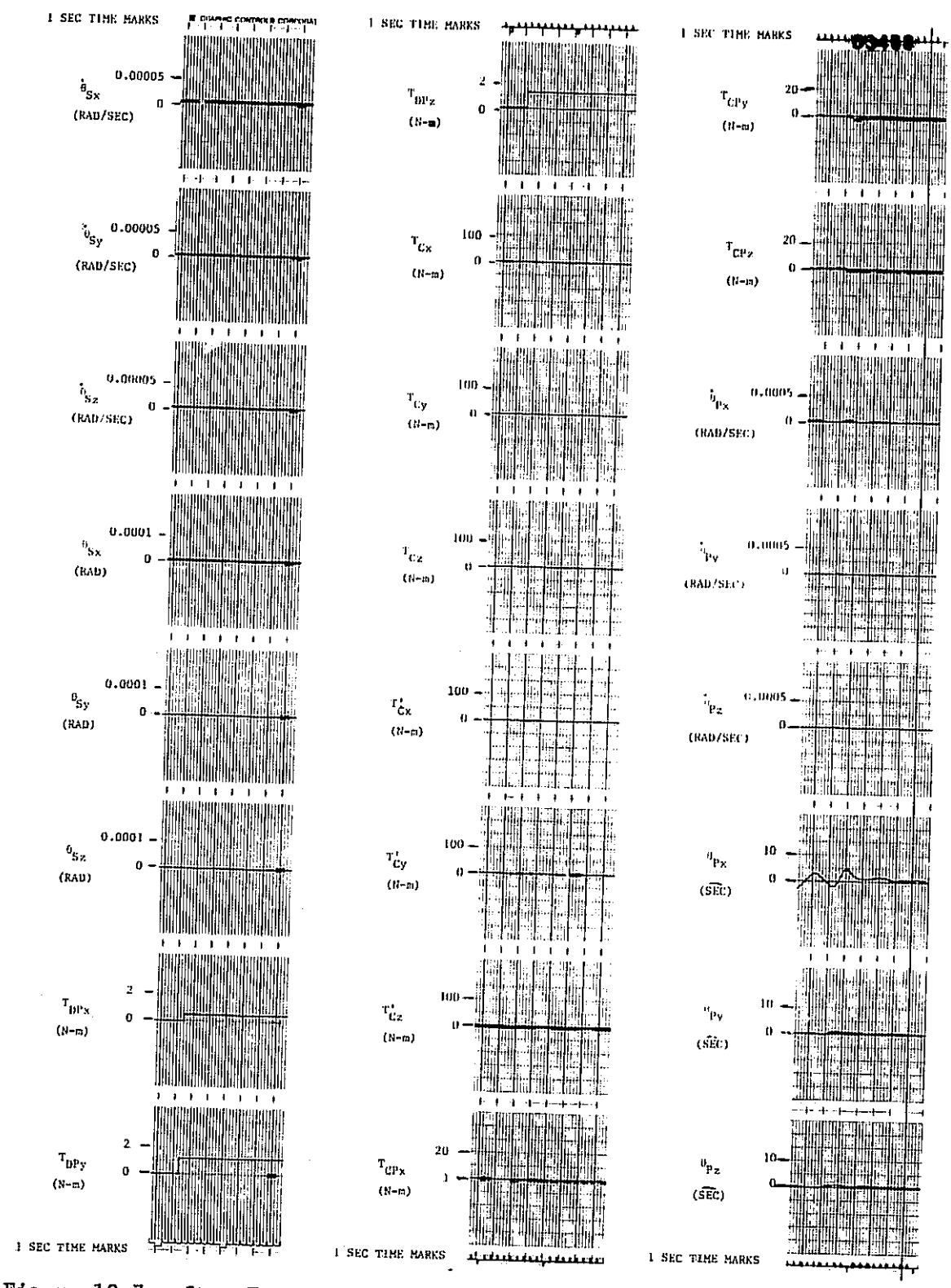

Figure 10-7. Step Torque Disturbance, 1/2 Hz System, Zero Gimbal Angles

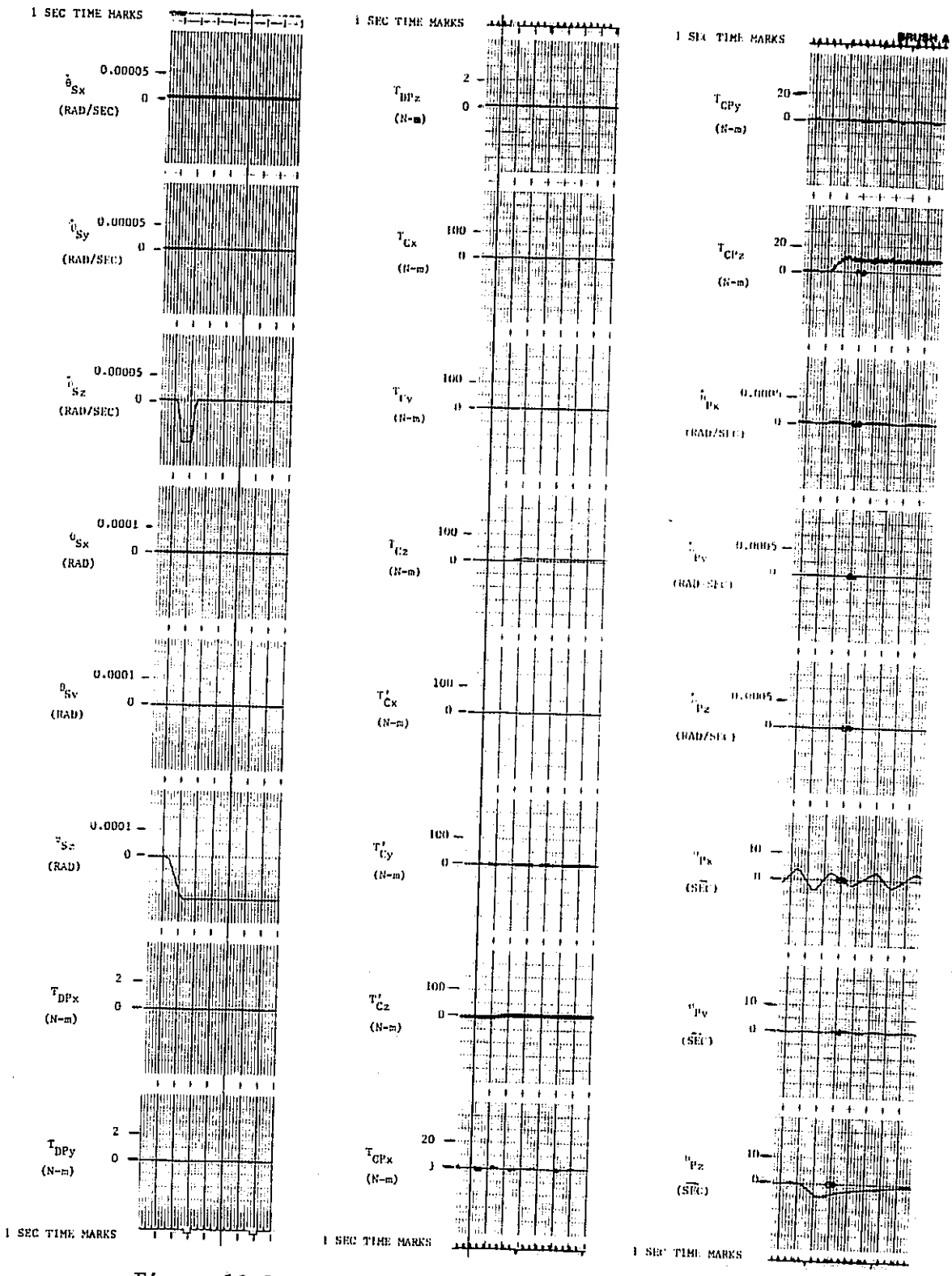

Figure 10-8. Crew Motion Torque Disturbance Case I, 1/2 Hz System, Zero Gimbal Angles

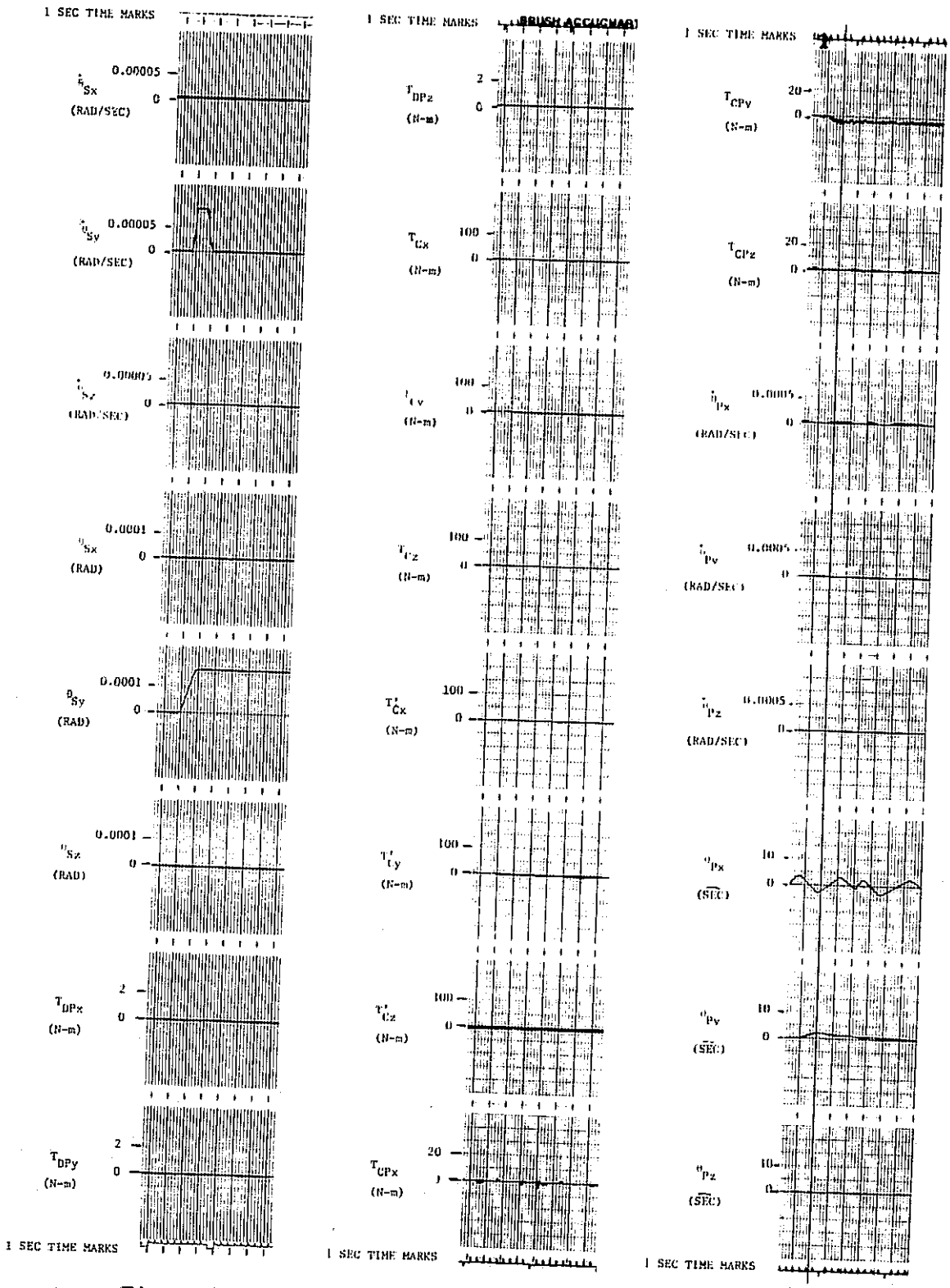

Figure 10-9, Crew Motion Torque Disturbance Case II, 1/2 Hz System, Zero Gimbal Angles

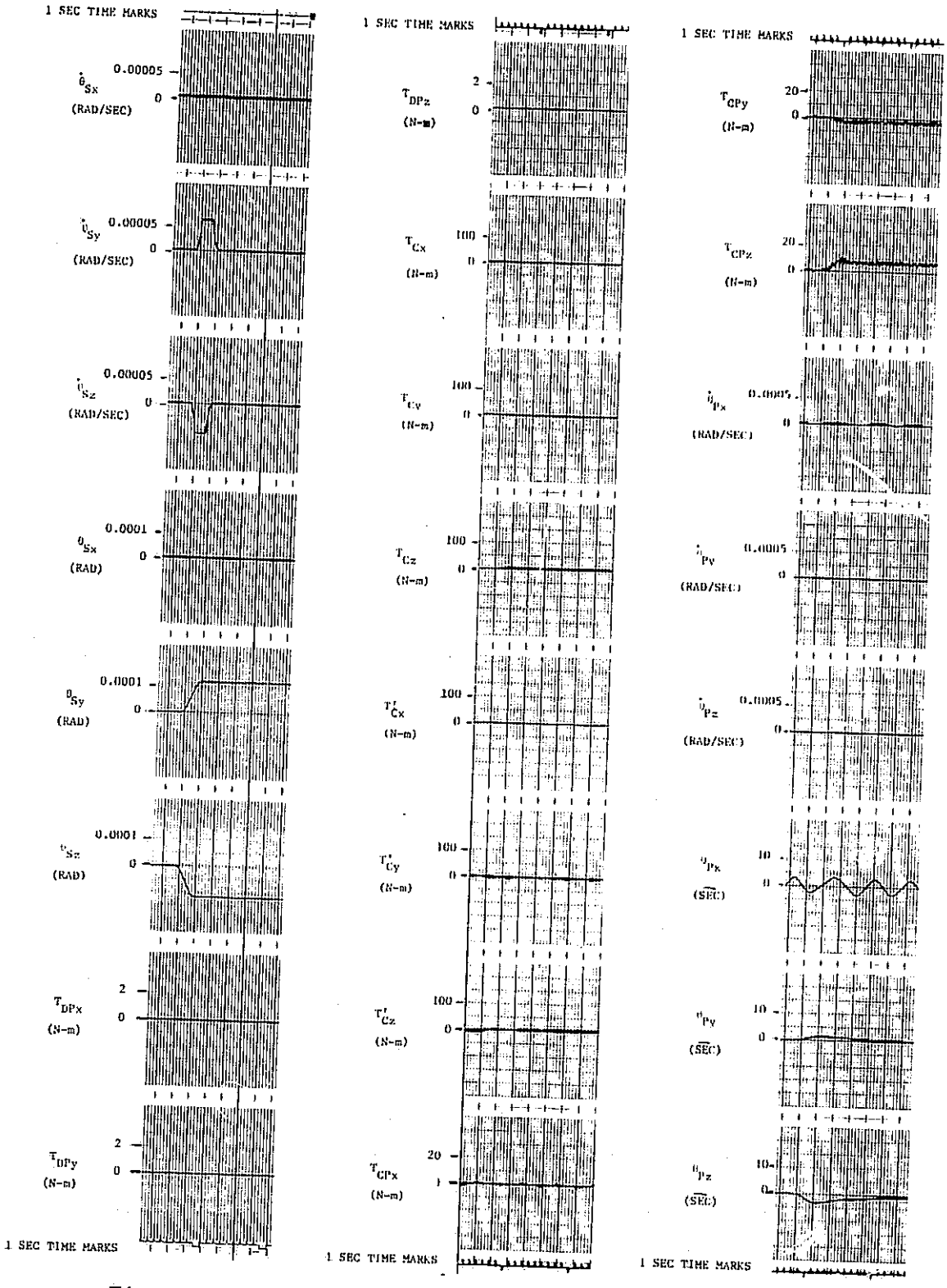

Figure 10-10. Crew Motion Torque Disturbance Case III, 1/2 Hz System, Zero Gimbal Angles

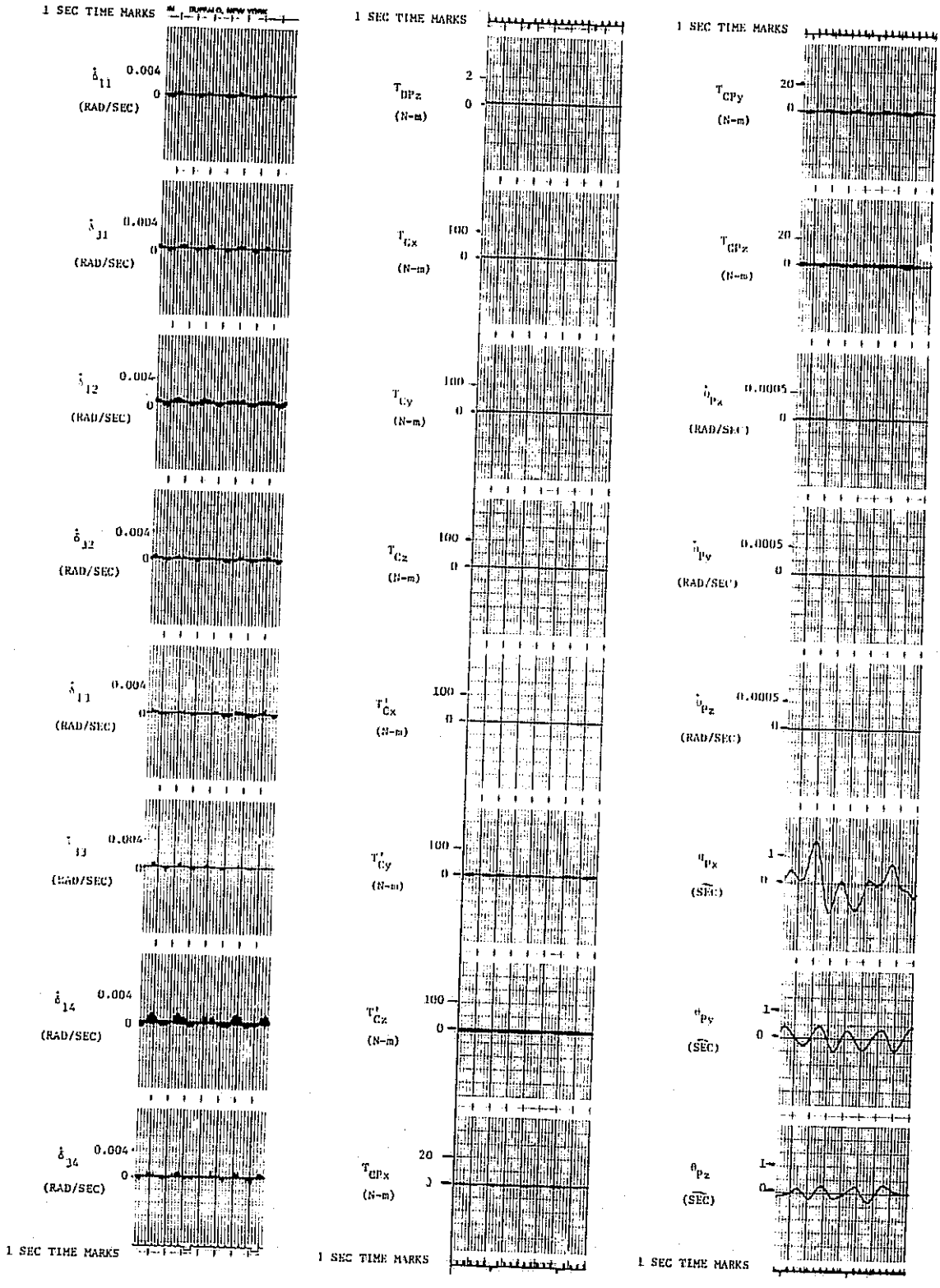

Figure 10-11. No Torque Disturbance, 1/2 Hz System, 45 deg Gimbal Angles

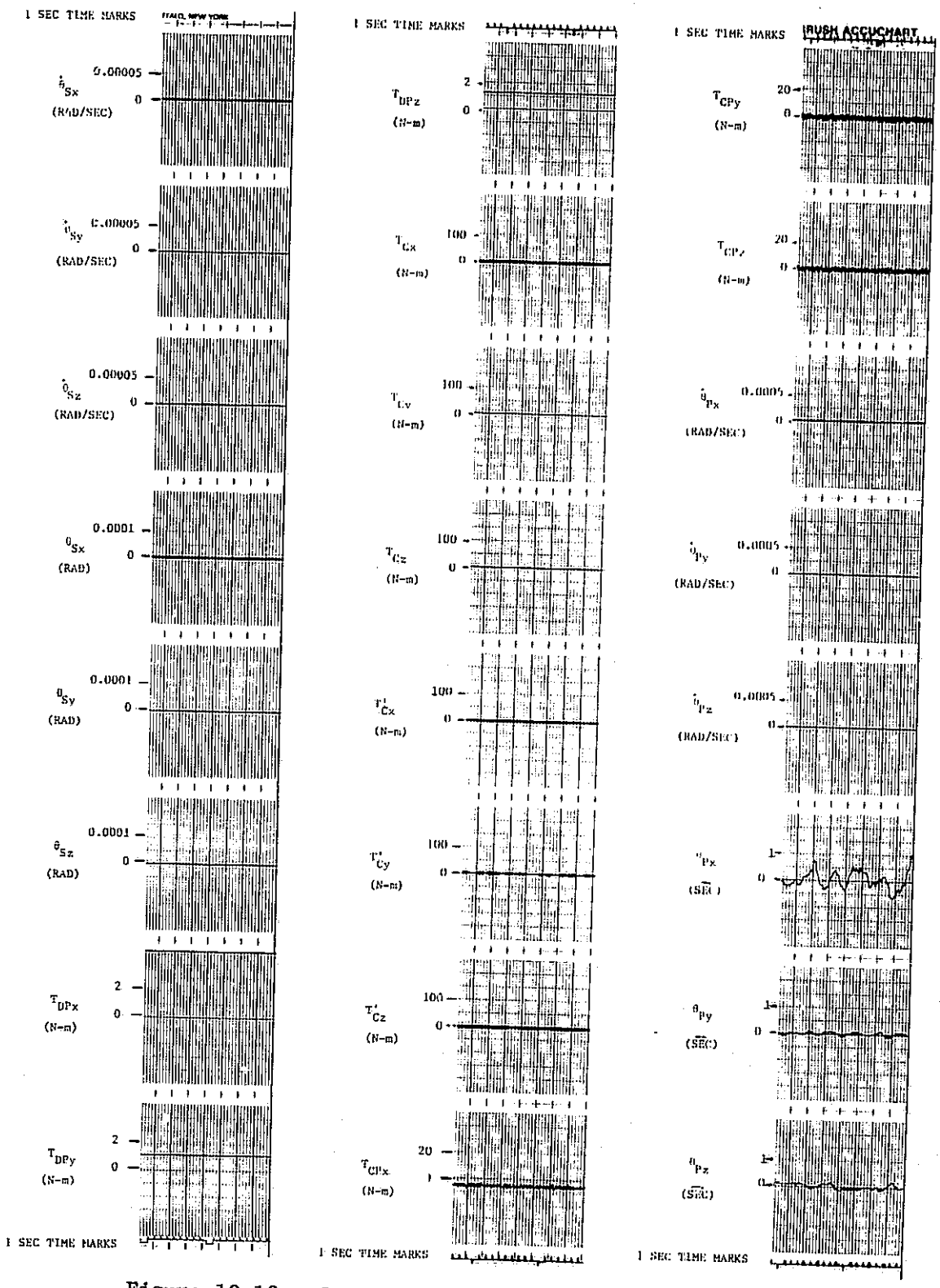

Figure 10-12. Step Torque Disturbance, 1/2 Hz System, 45 deg Gimbal Angles

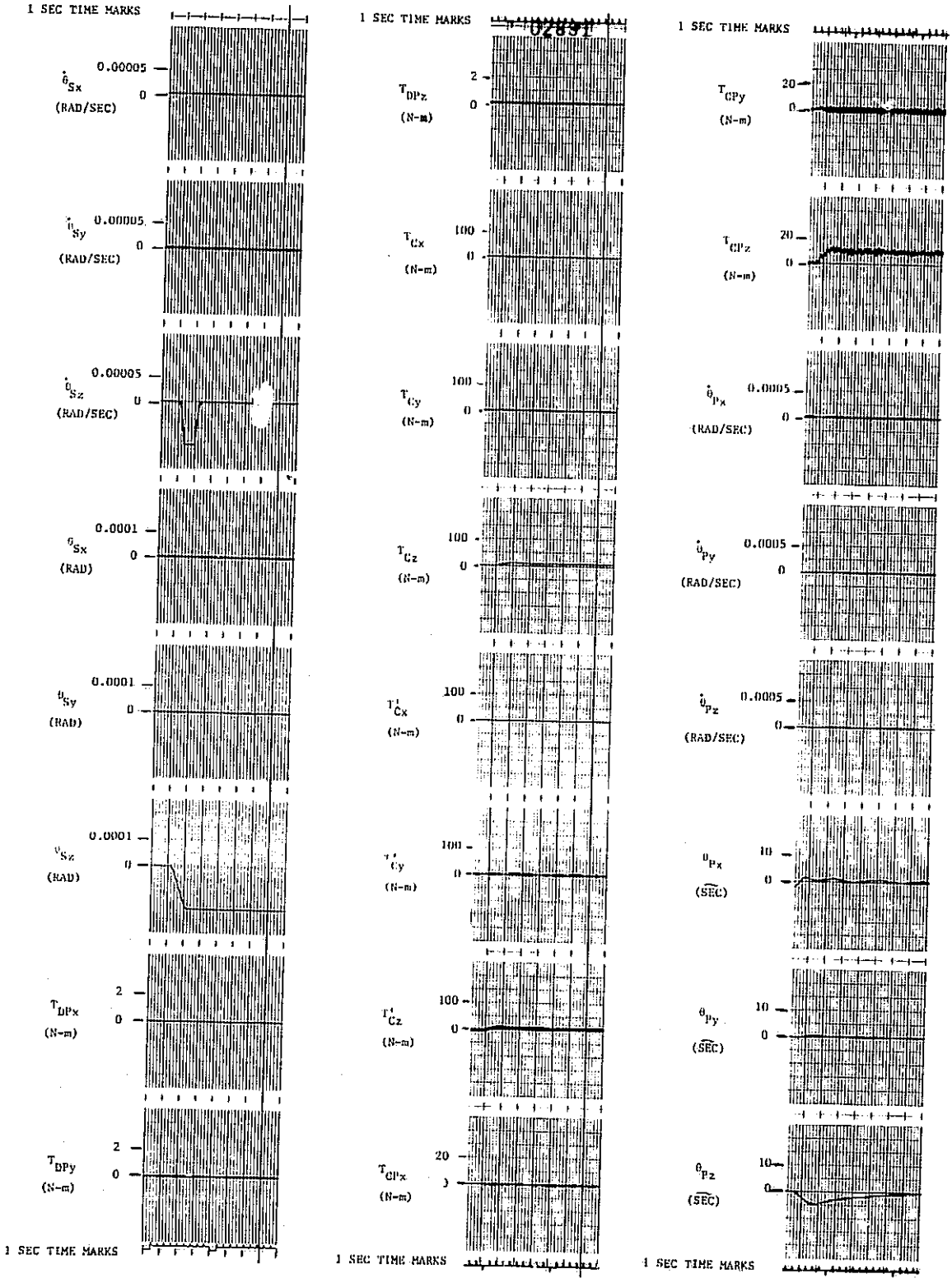

Figure 10-13. Crew Motion Torque Disturbance Case I, 1/2 Hz System, 45 deg Gimbal Angles

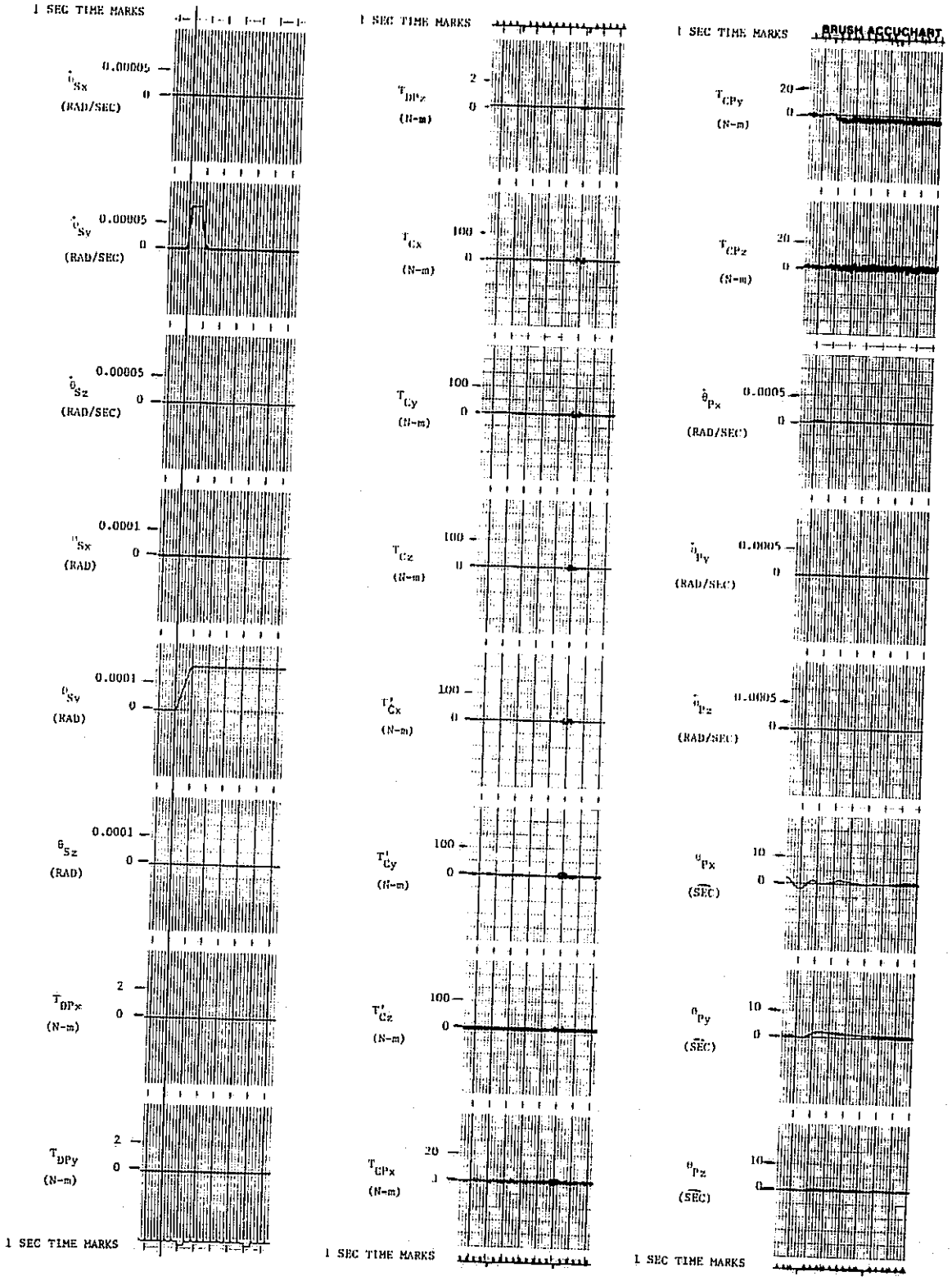

Figure 10-14. Crew Motion Torque Disturbance Case II, 1/2 Hz System, 45 deg Gimbal Angles

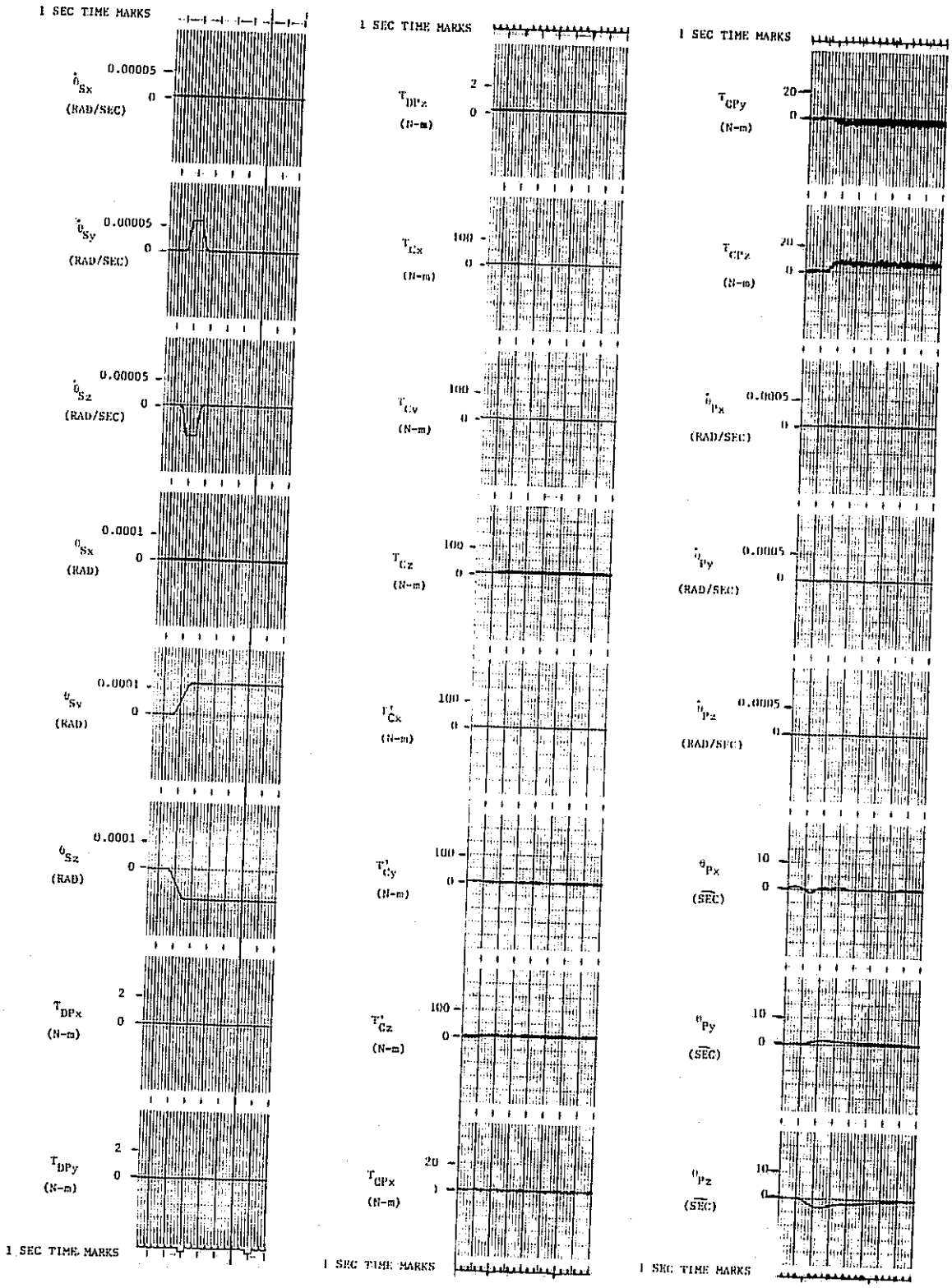

Figure 10-15. Crew Motion Torque Disturbance Case III, 1/2 Hz System, 45 deg Gimbal Angles

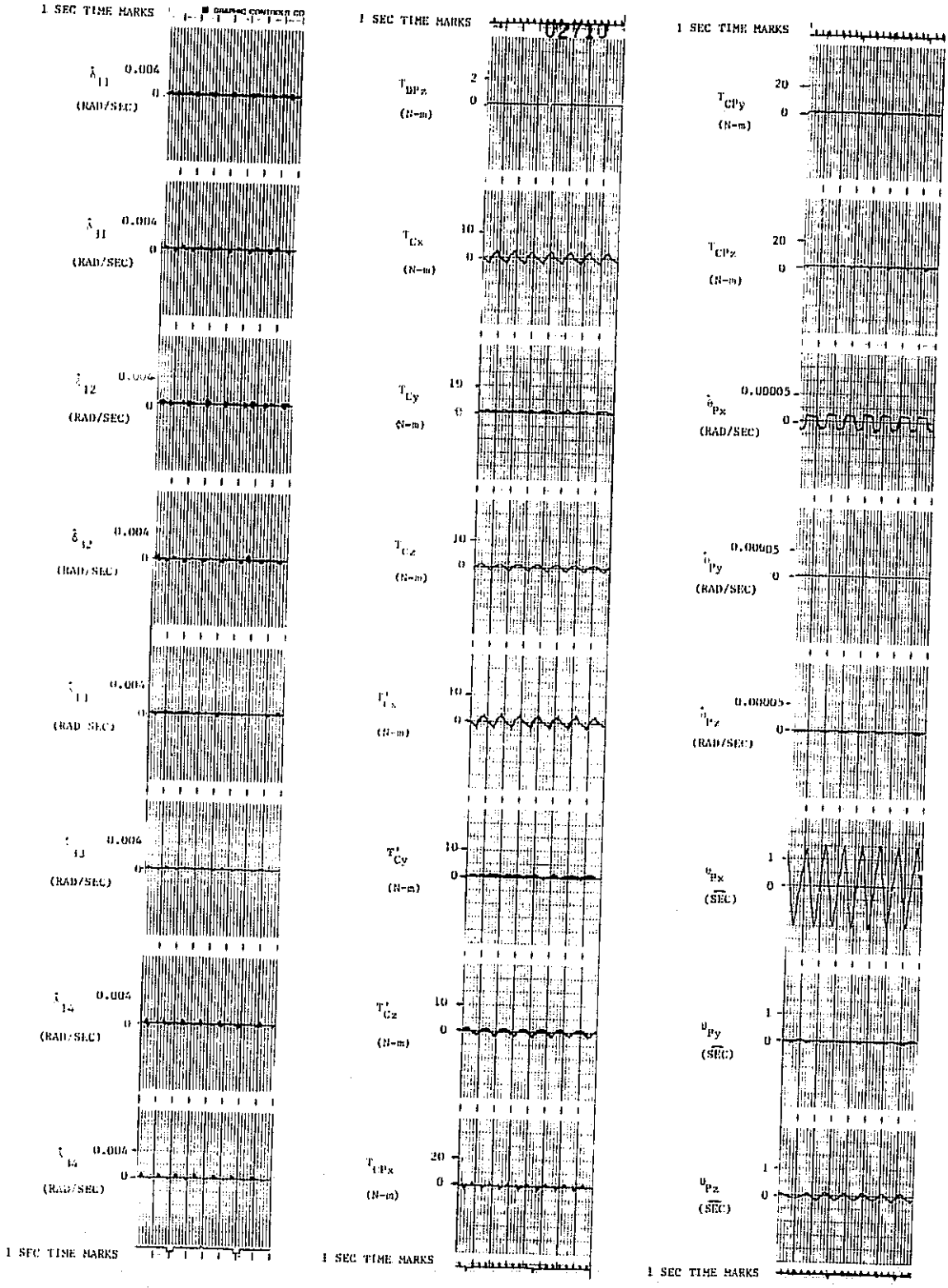

Figure 10-16. No Torque Disturbance, 1 Hz System, Zero Gimbal Angles

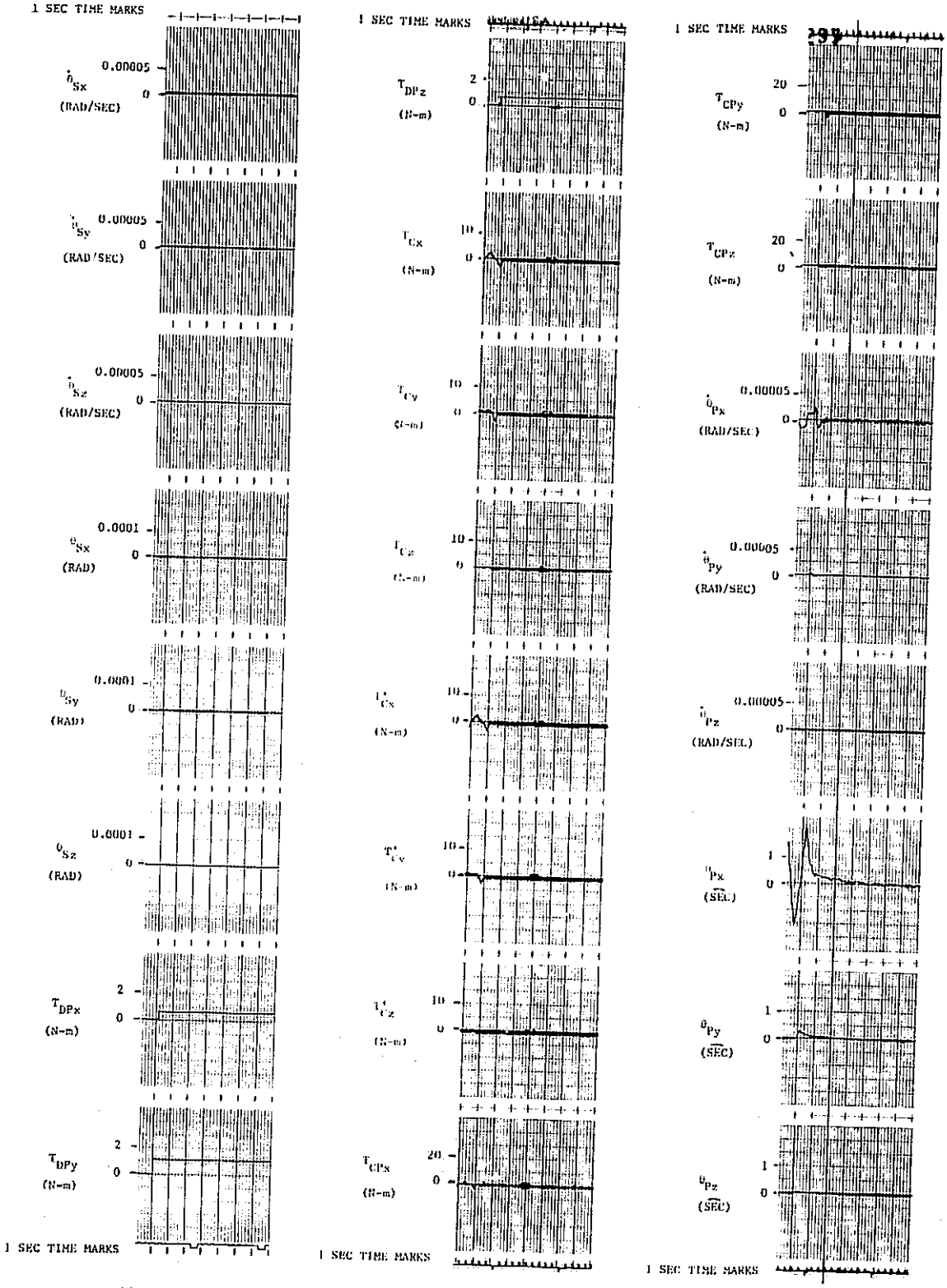

Figure 10-17. Step Torque Disturbance, 1 Hz System, Zero Gimbal Angles

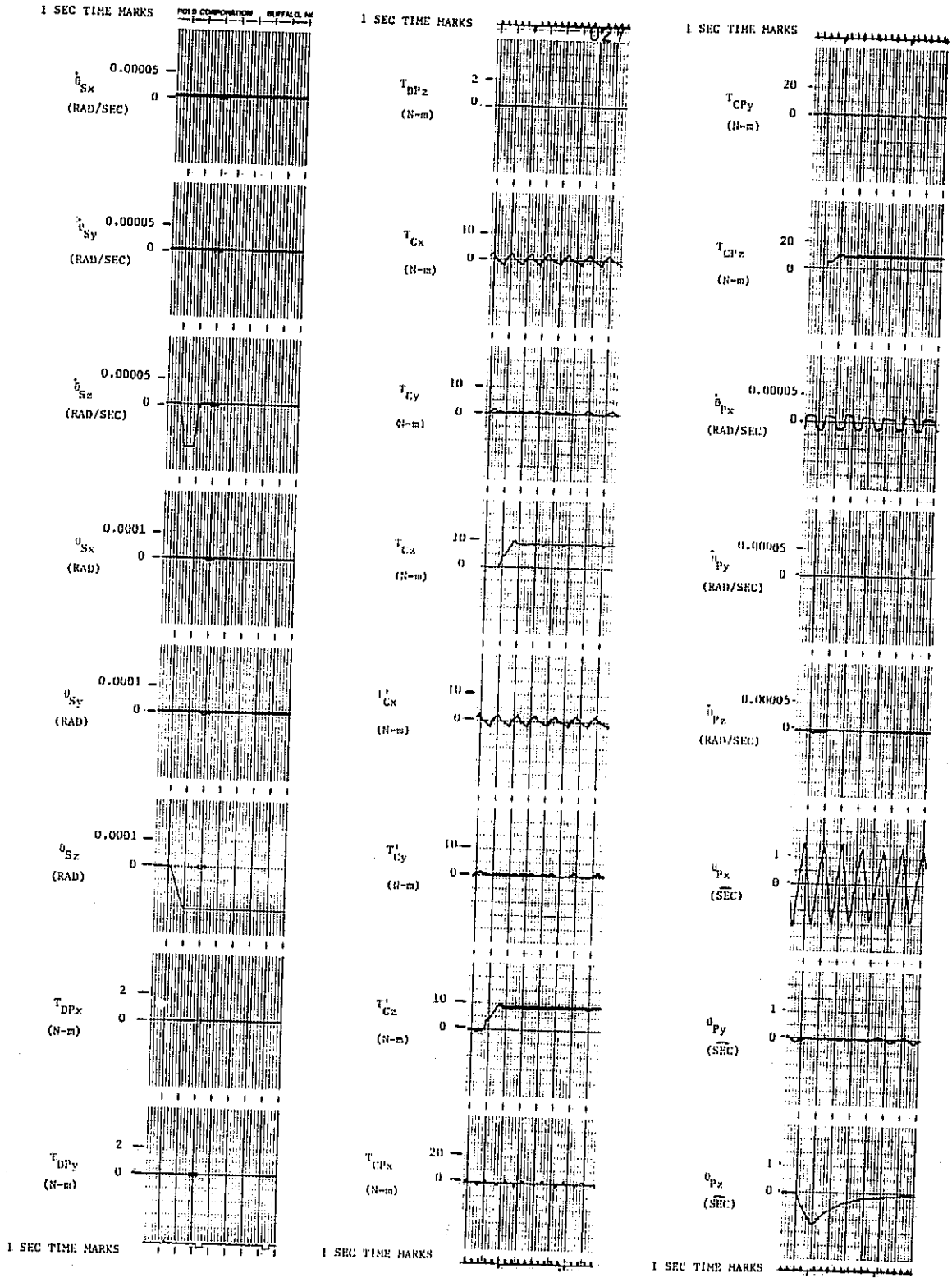

Figure 10-18. Crew Motion Torque Disturbance Case I, 1 Hz System, Zero Gimbal Angles

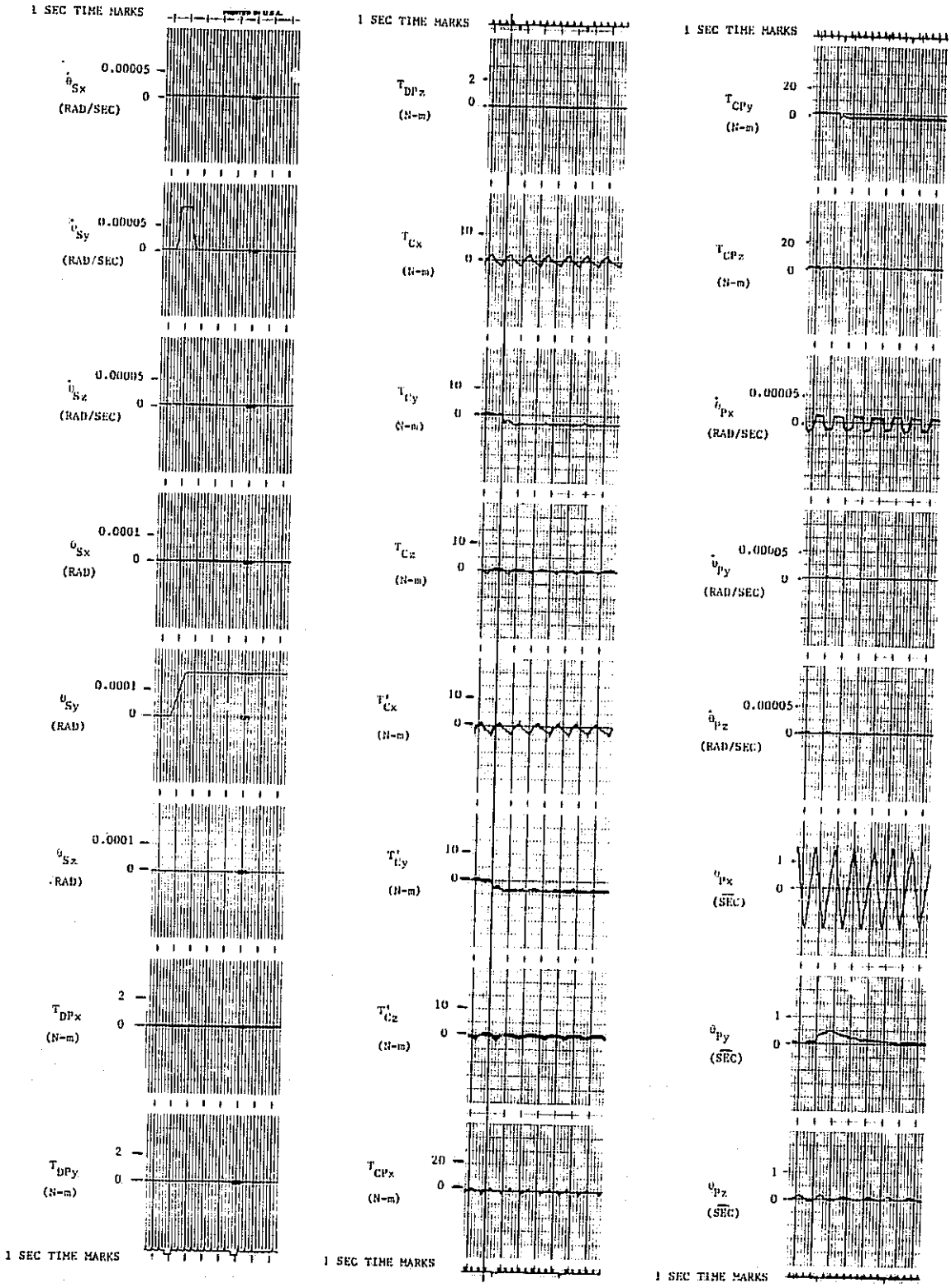

Figure 10-19. Crew Motion Torque Disturbance Case II, 1 Hz System, Zero Gimbal Angles

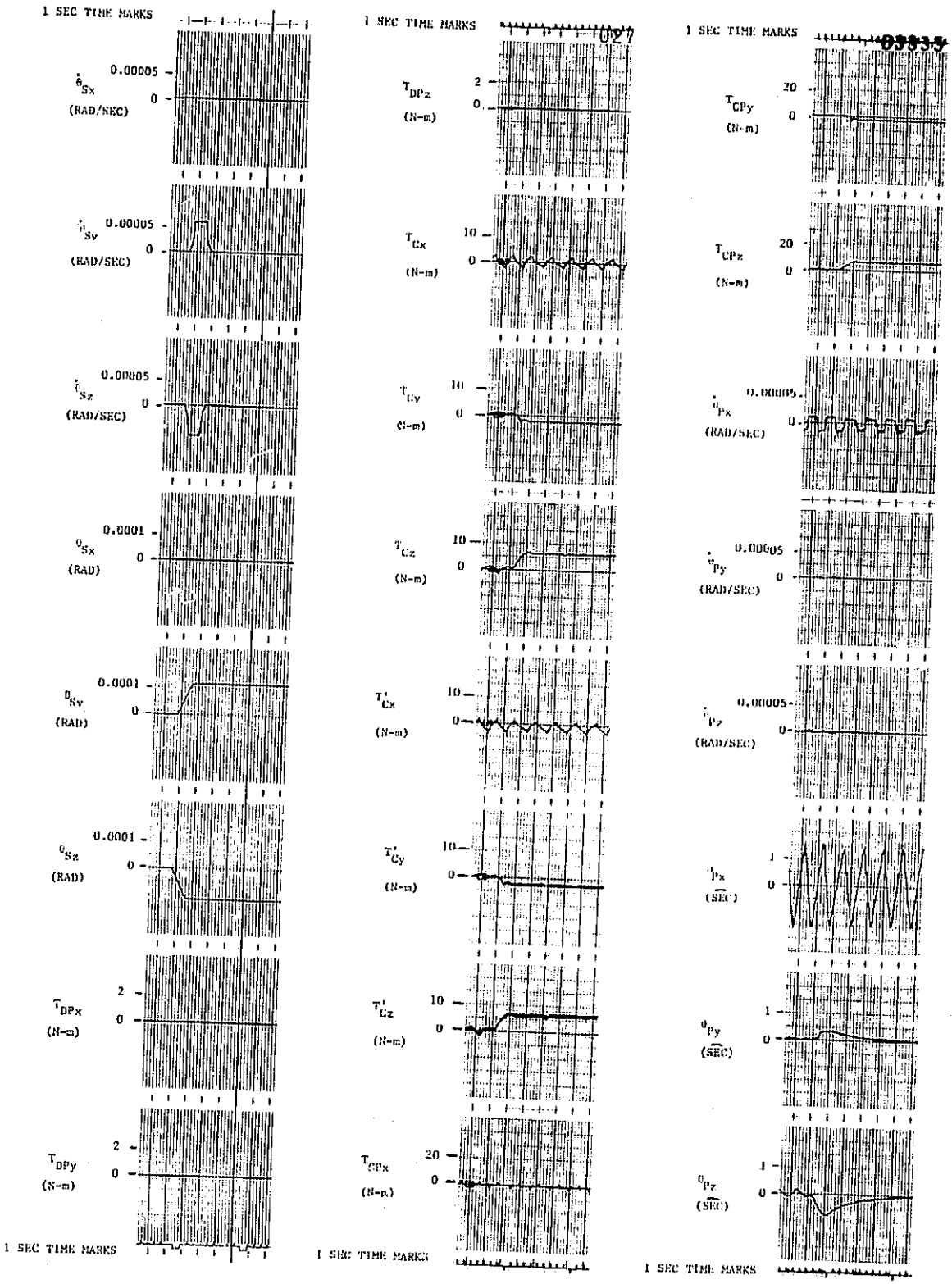

Figure 10-20. Crew Motion Torque Disturbance Case III, 1 Hz System, Zero Gimbal Angles

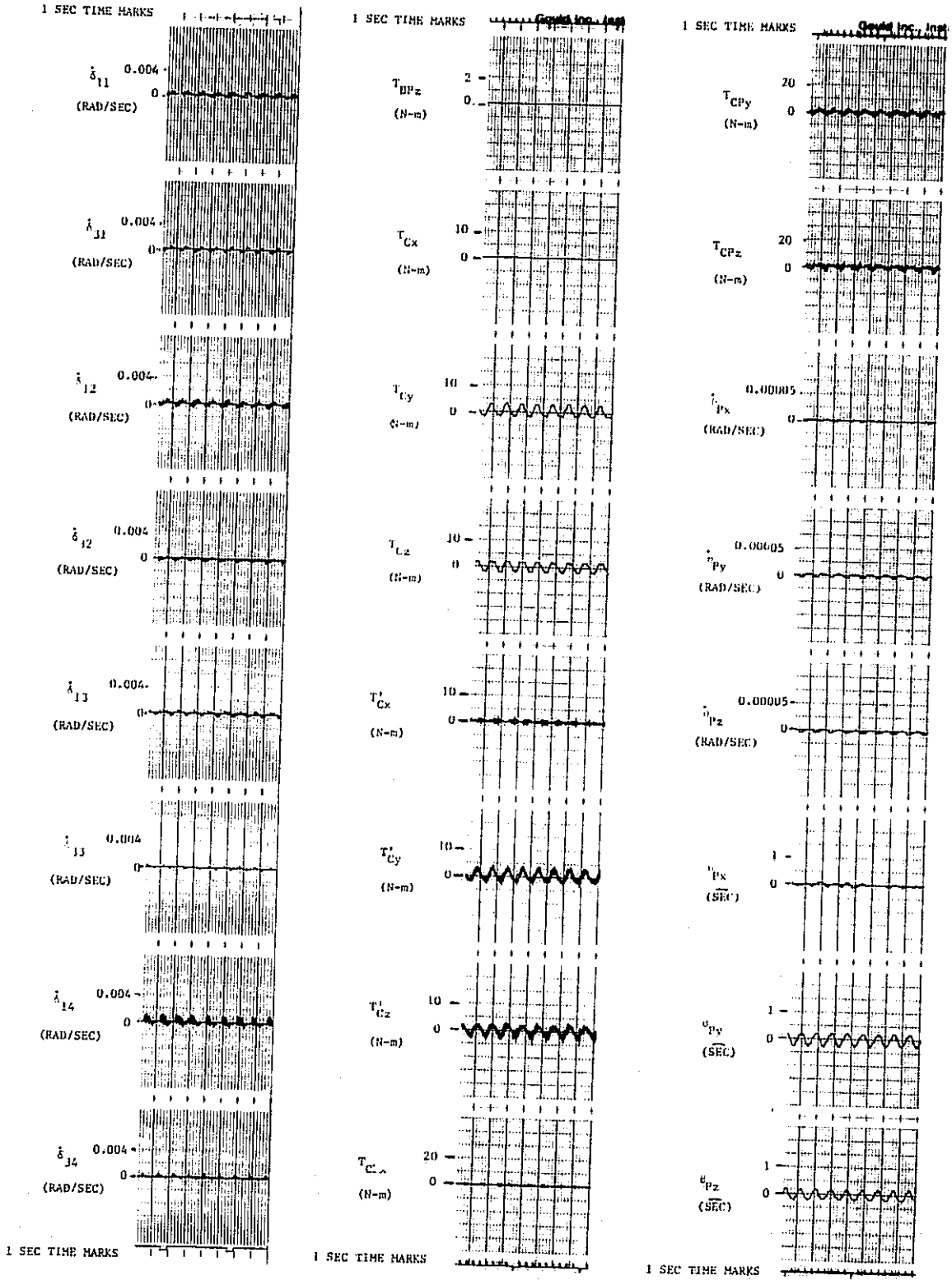

Figure 10-21. No Torque Disturbance, 1 Hz System, 45 deg Gimbal Angles

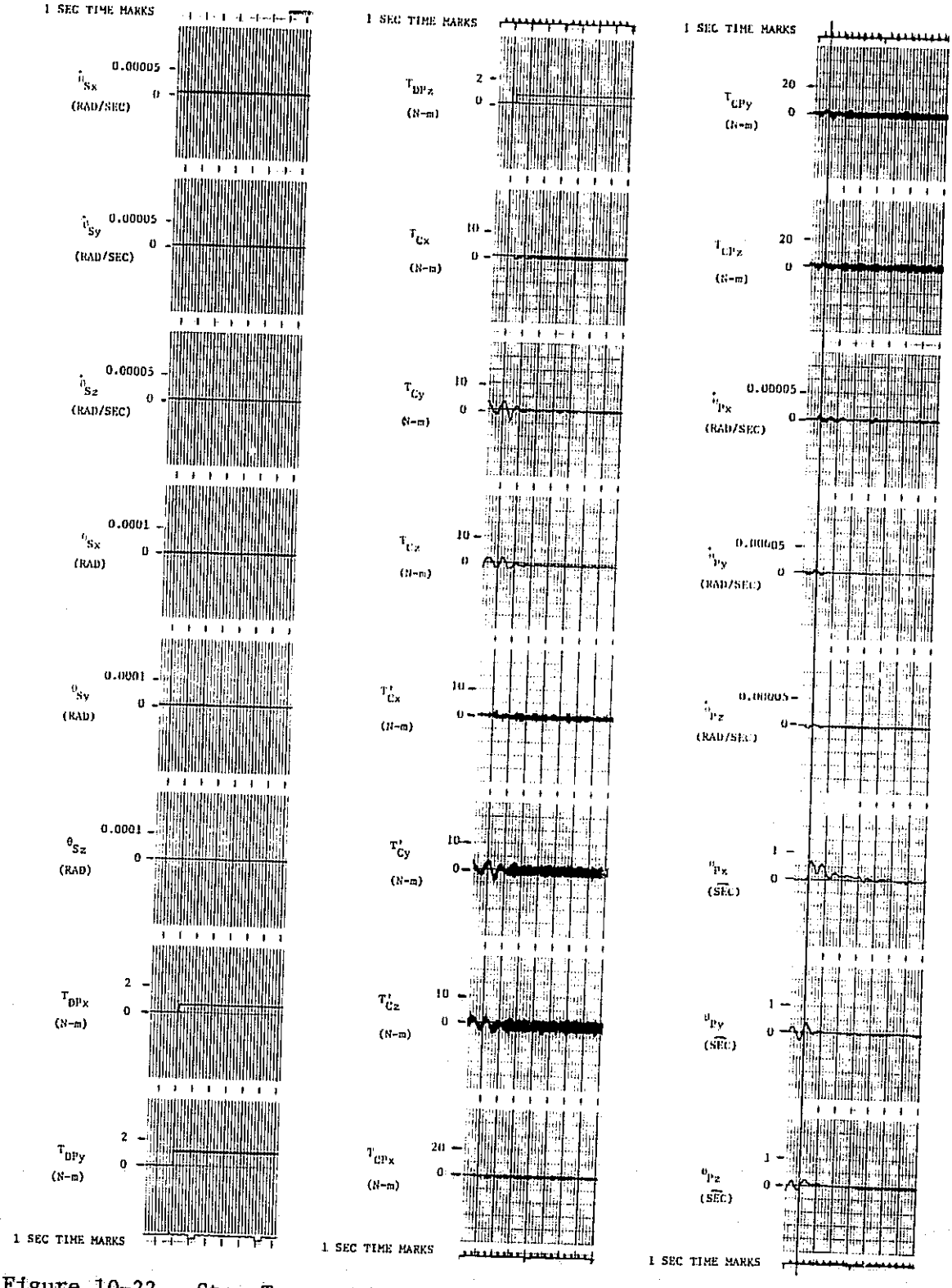

Figure 10-22. Step Torque Disturbance, 1 Hz System, 45 deg Gimbal Angles

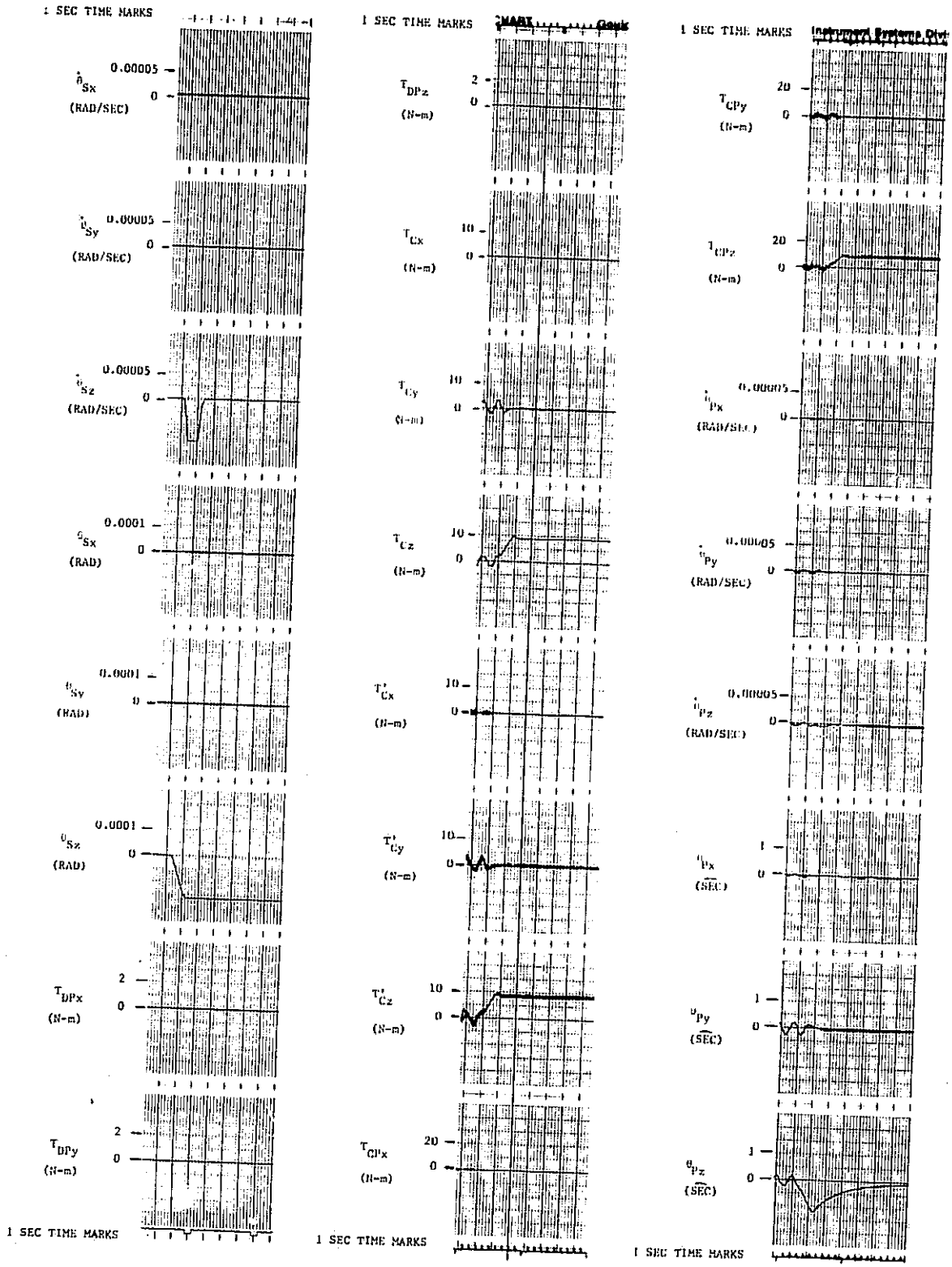

Figure 10-23. Crew Motion Torque Disturbance Case I, 1 Hz System, 45 deg Gimbal Angles

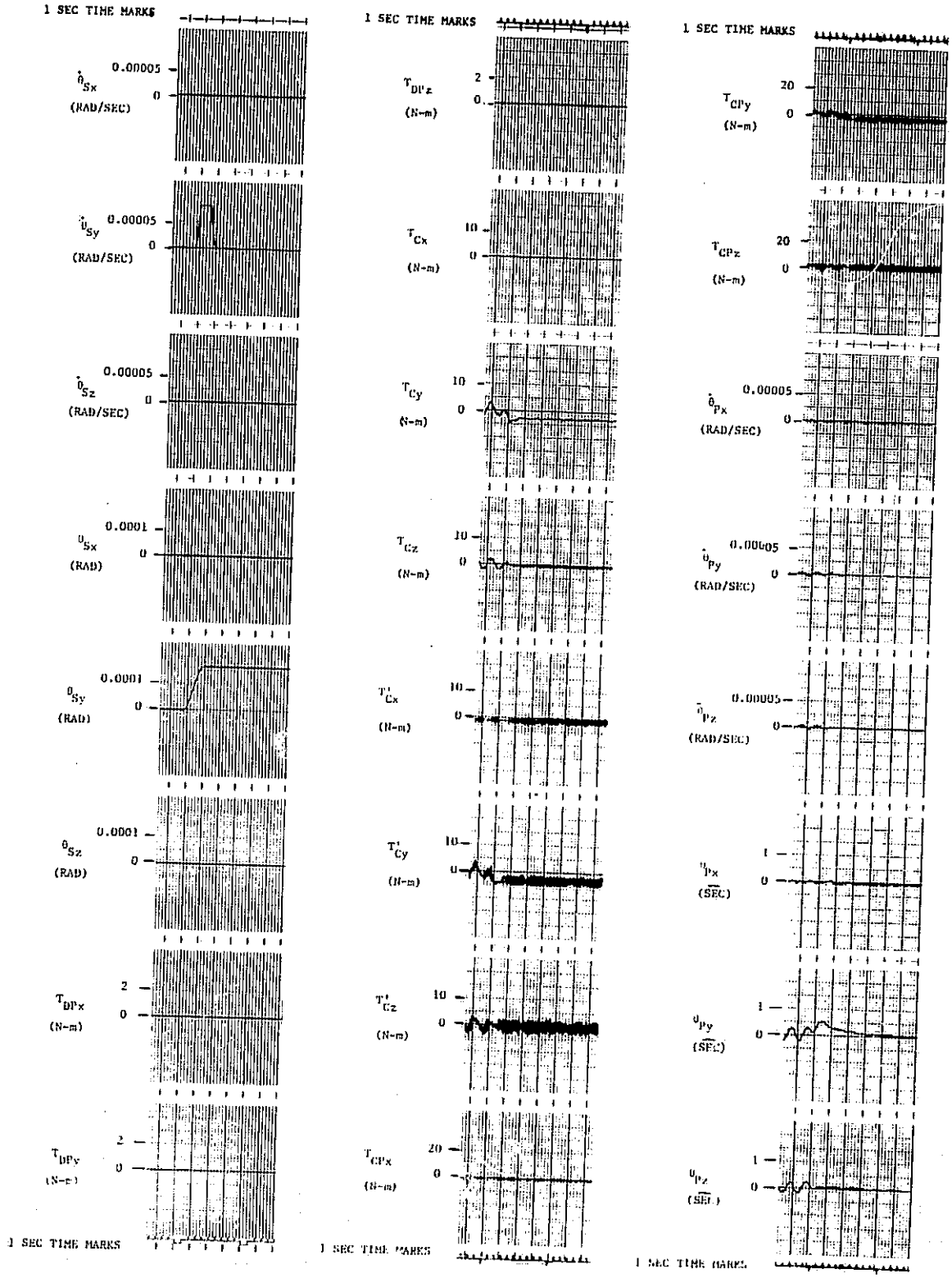

Figure 10-24. Crew Motion Torque Disturbance Case II, 1 Hz System, 45 deg Gimbal Angles

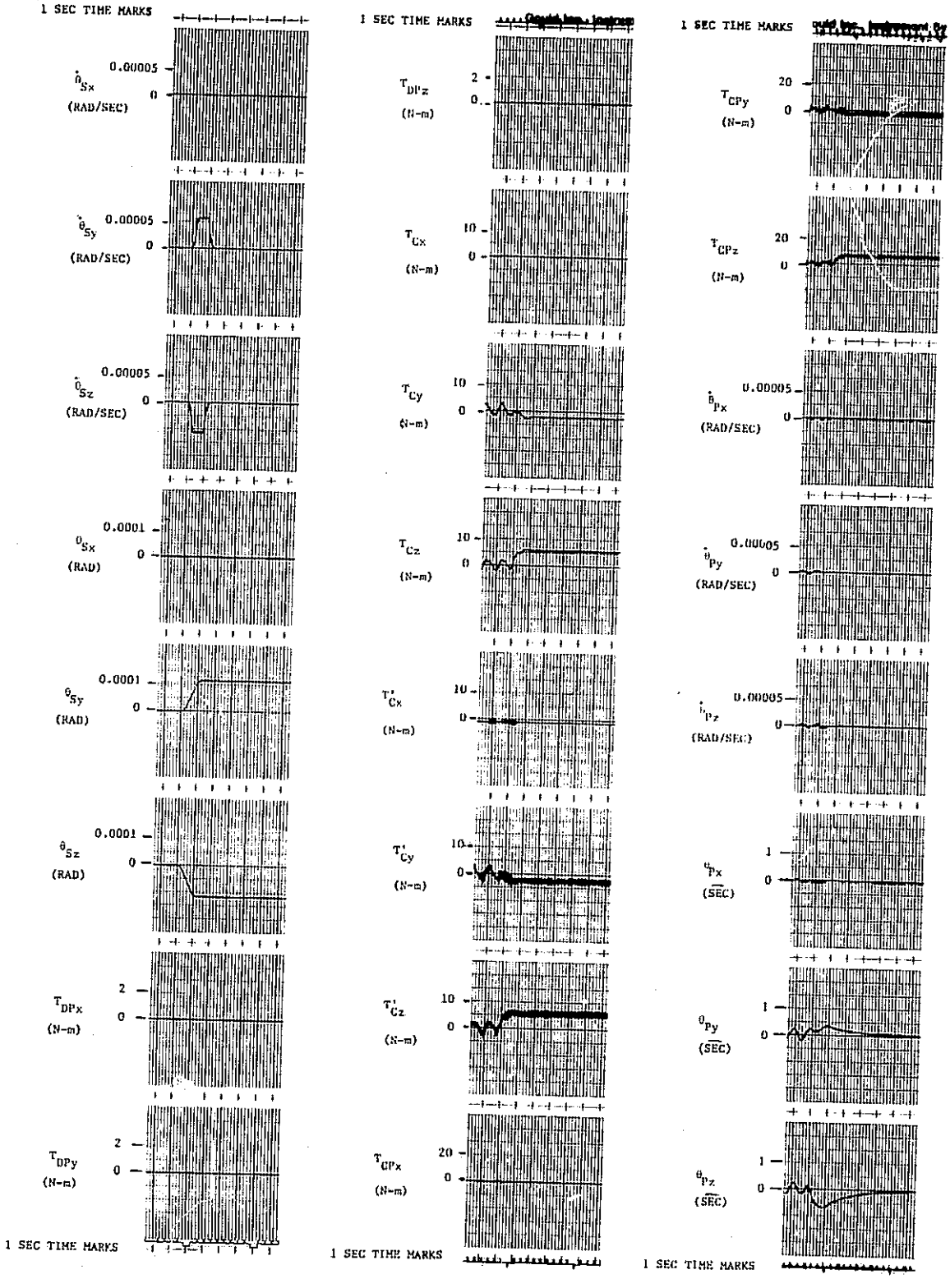

Figure 10-25. Crew Motion Torque Disturbance Case III, 1 Hz System, 45 deg Gimbal Angles

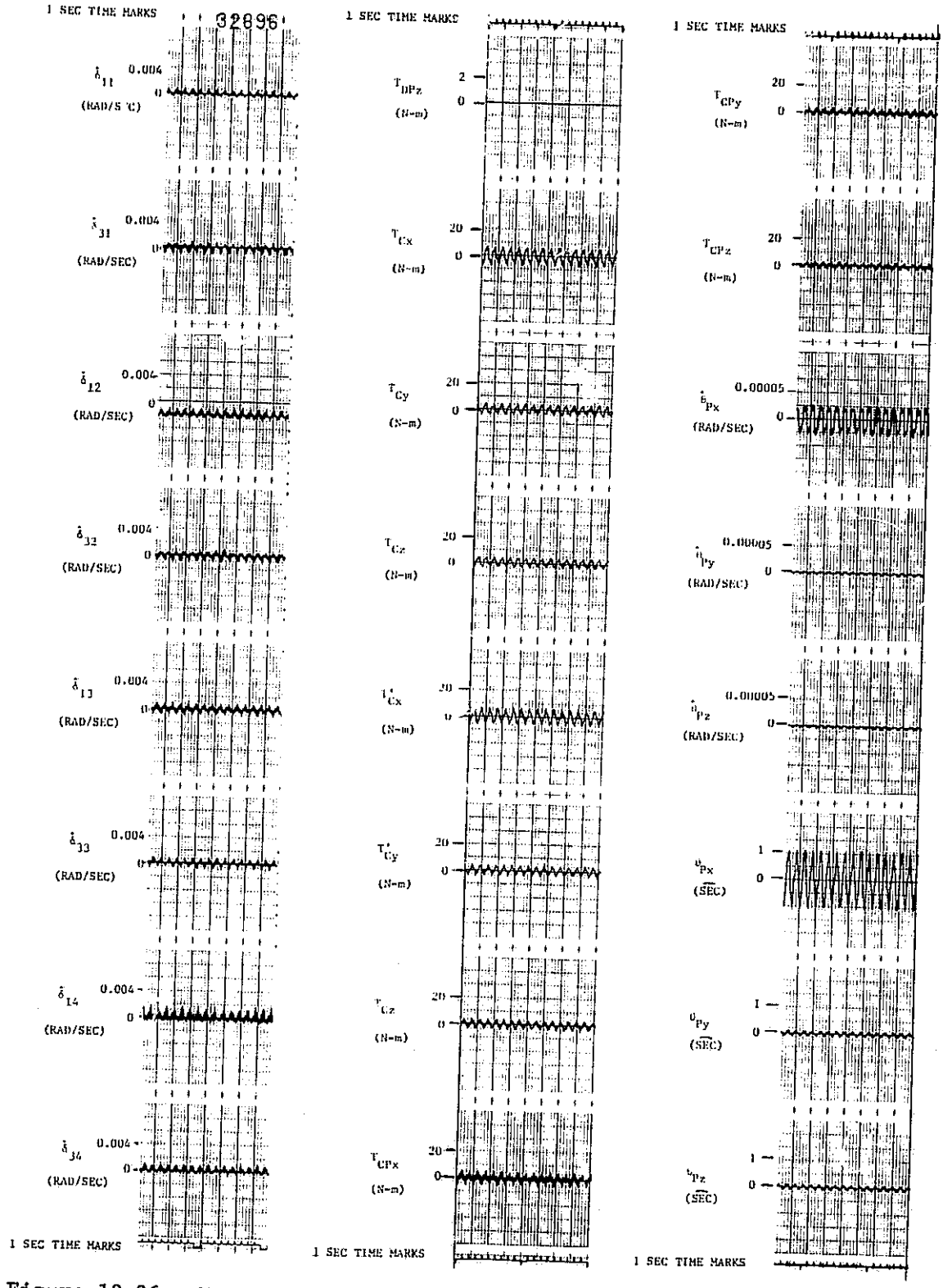

Figure 10-26. No Torque Disturbance, 2 Hz System, Zero Gimbal Angles

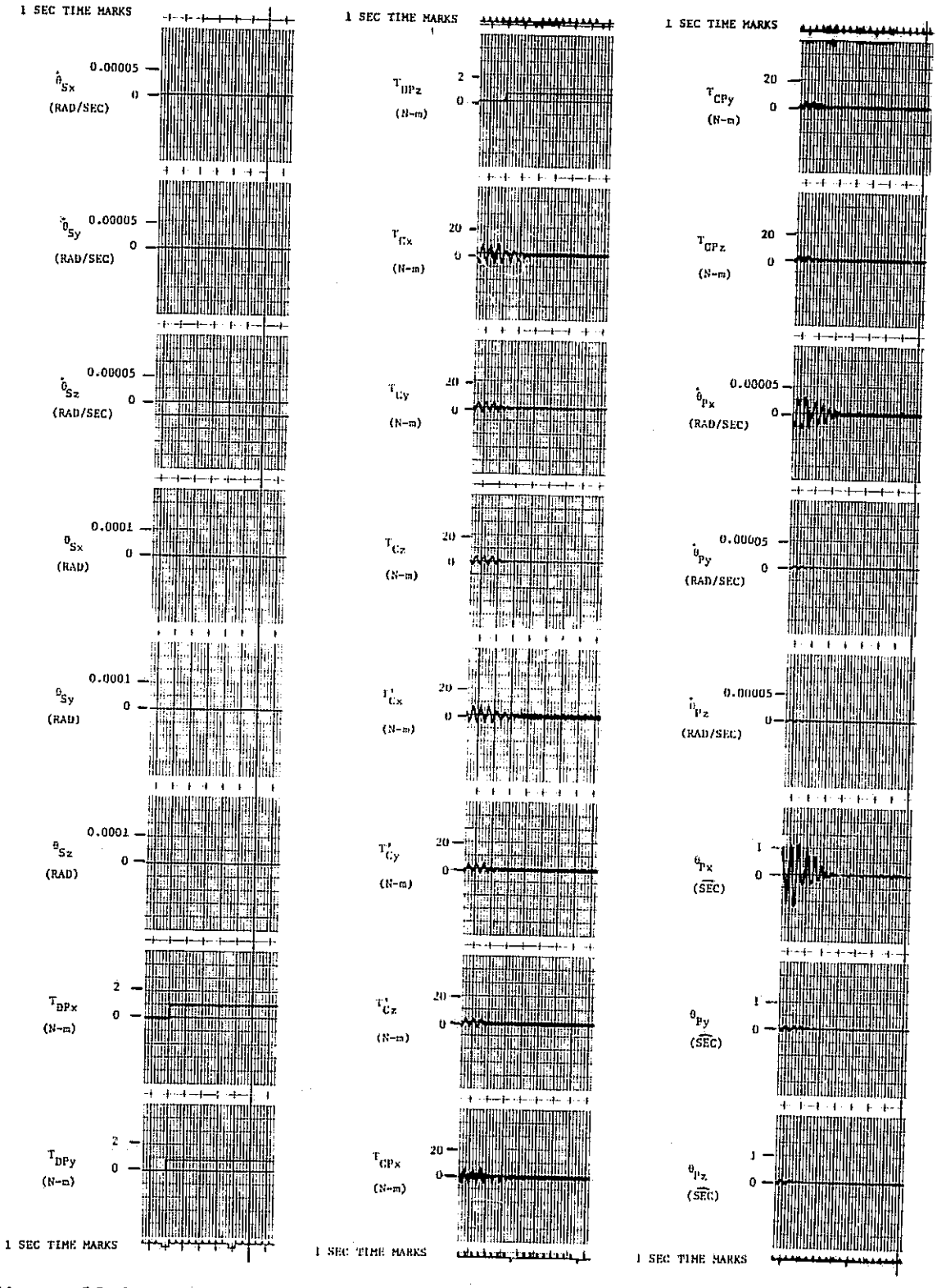

Figure 10-27. Step Torque Disturbance, 2 Hz System, Zero Gimbal Angles

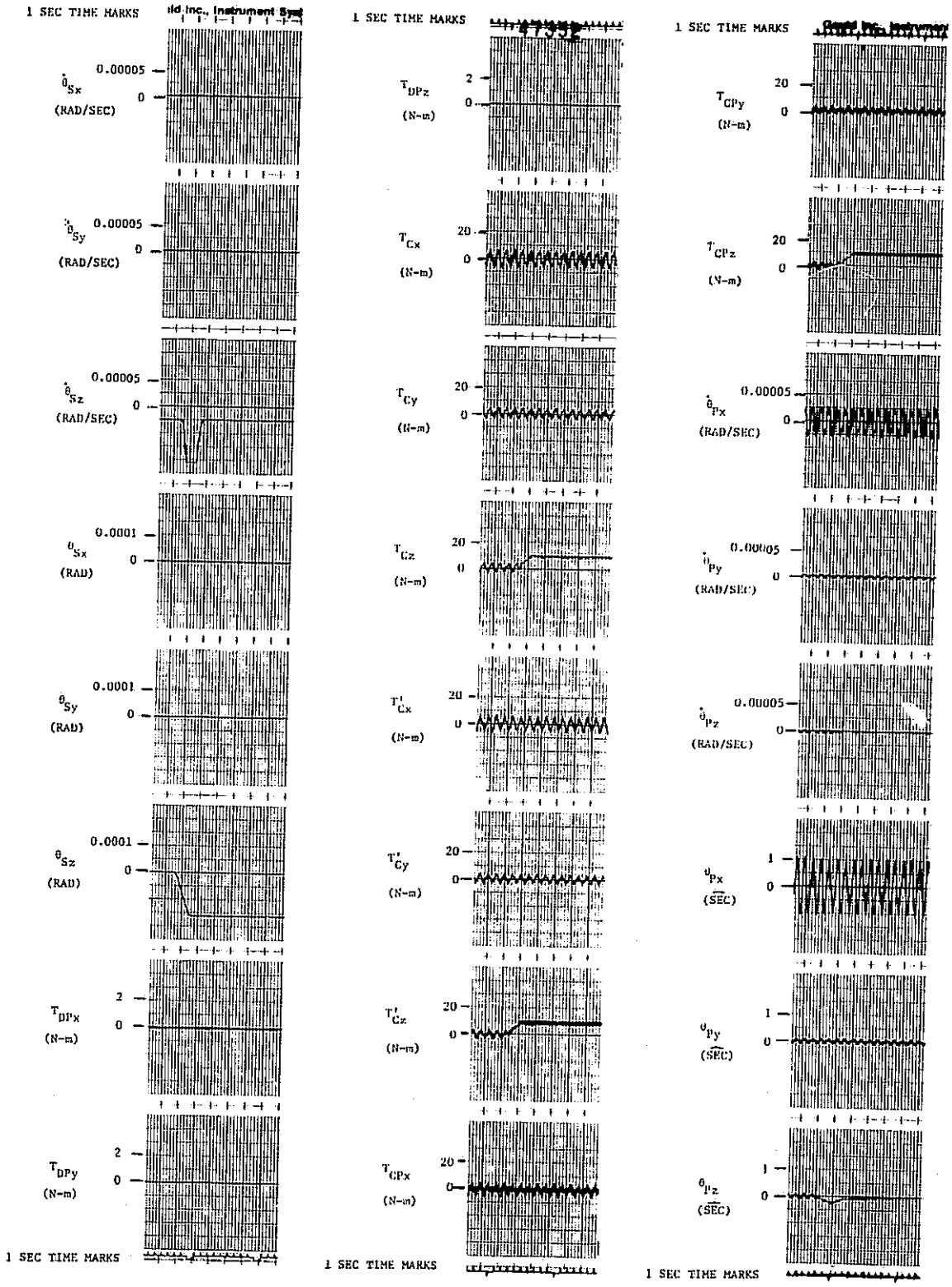

Figure 10-28. Crew Motion Torque Disturbance Case I, 2 Hz System, Zero Gimbal Angles

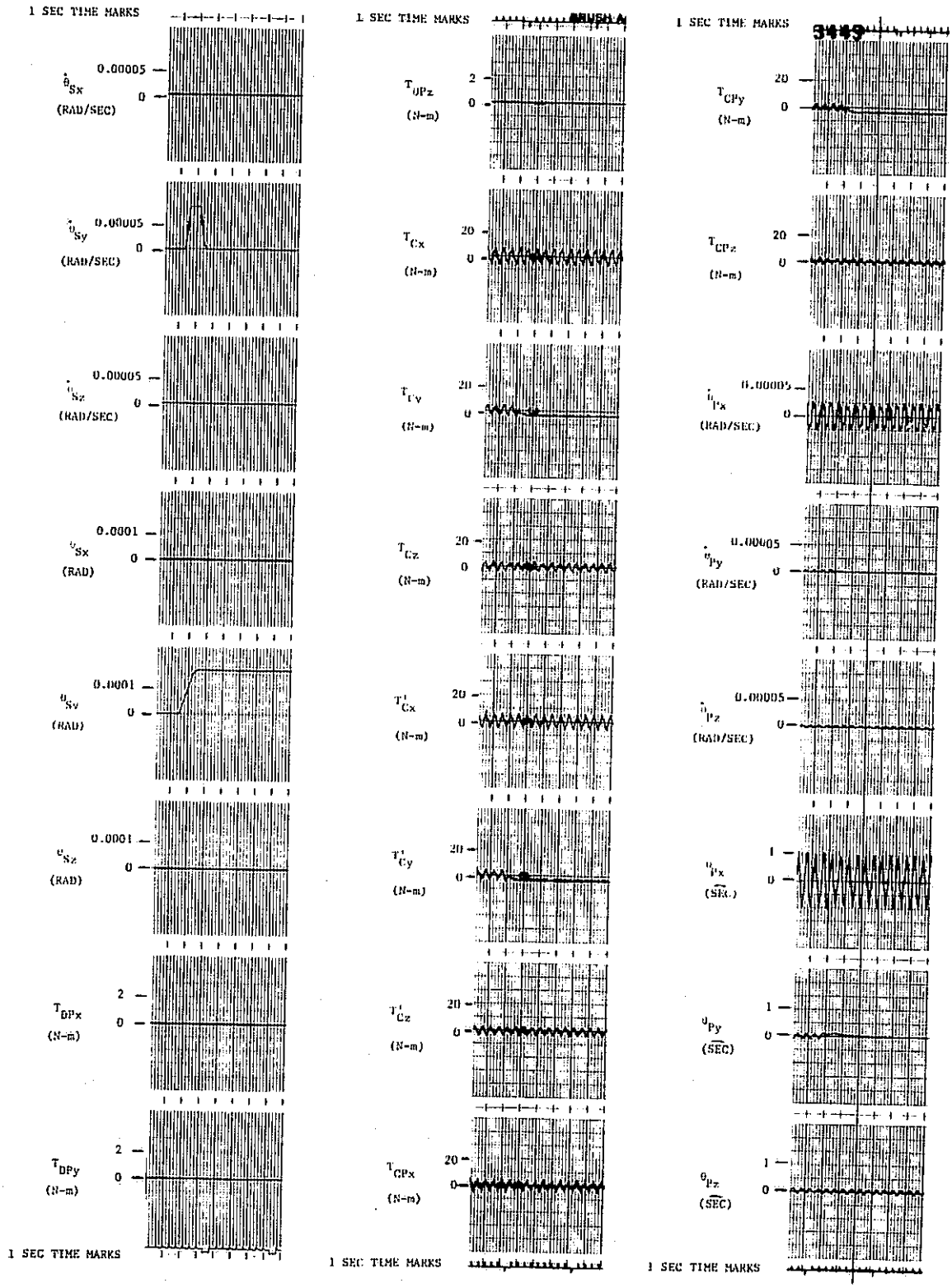

Figure 10-29. Crew Motion Torque Disturbance Case II, 2 Hz System, Zero Gimbal Angles

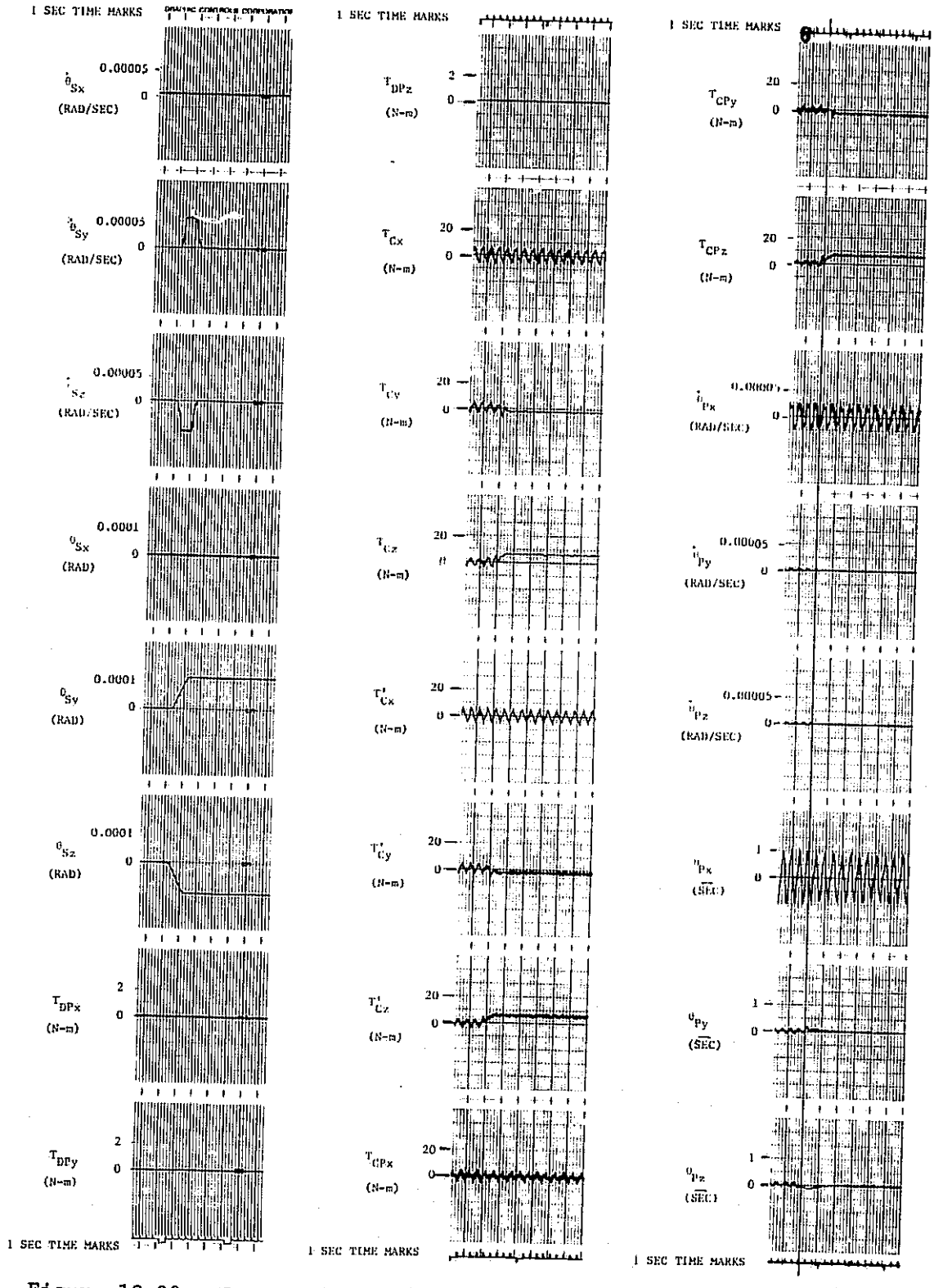

Figure 10-30. Crew Motion Torque Disturbance Case III, 2 Hz System, Zero Gimbal Angles

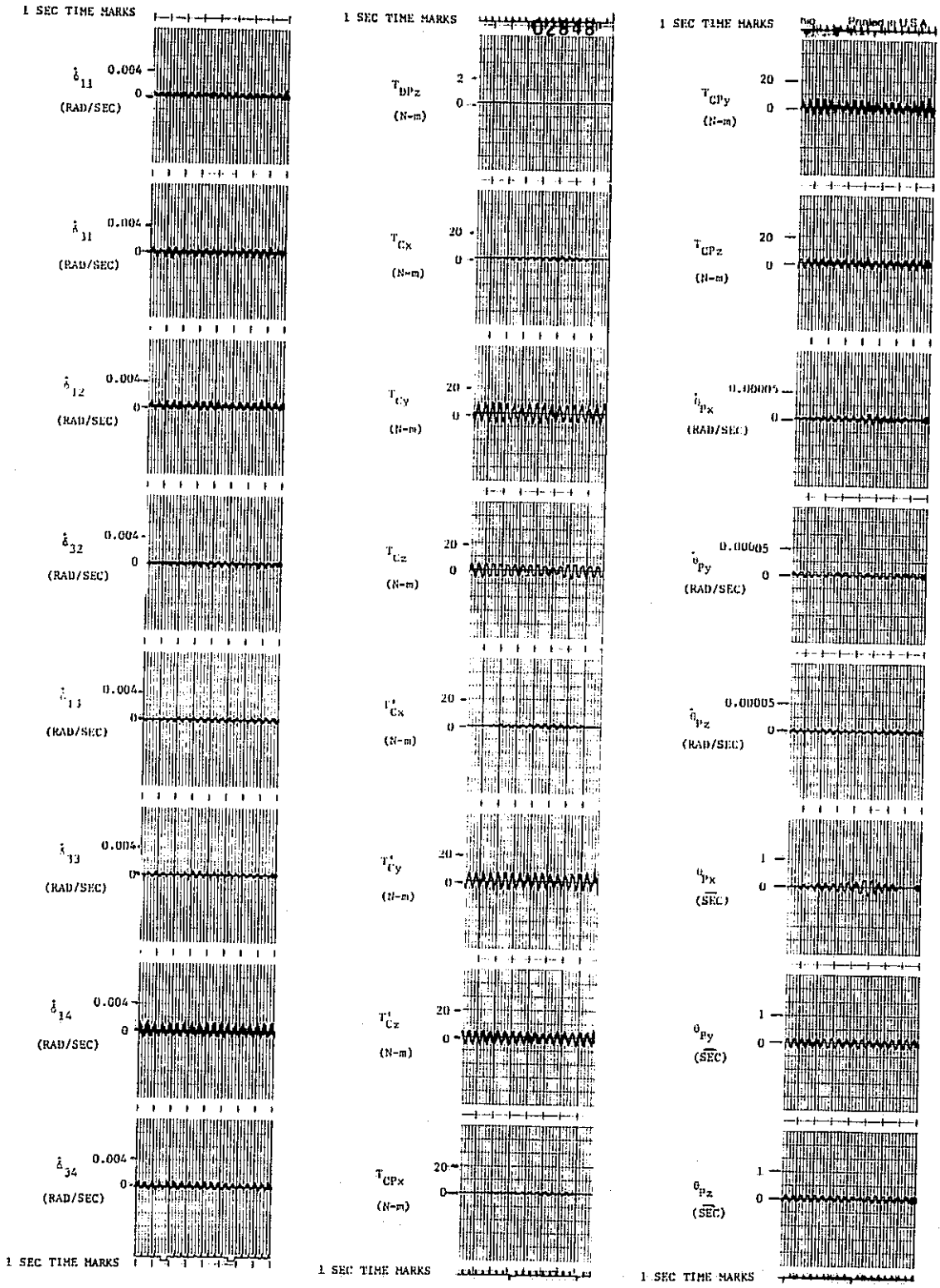

Figure 10-31. No Torque Disturbance, 2 Hz System, Zero Inner Gimbal Angles and 45 deg Outer Gimbal Angles

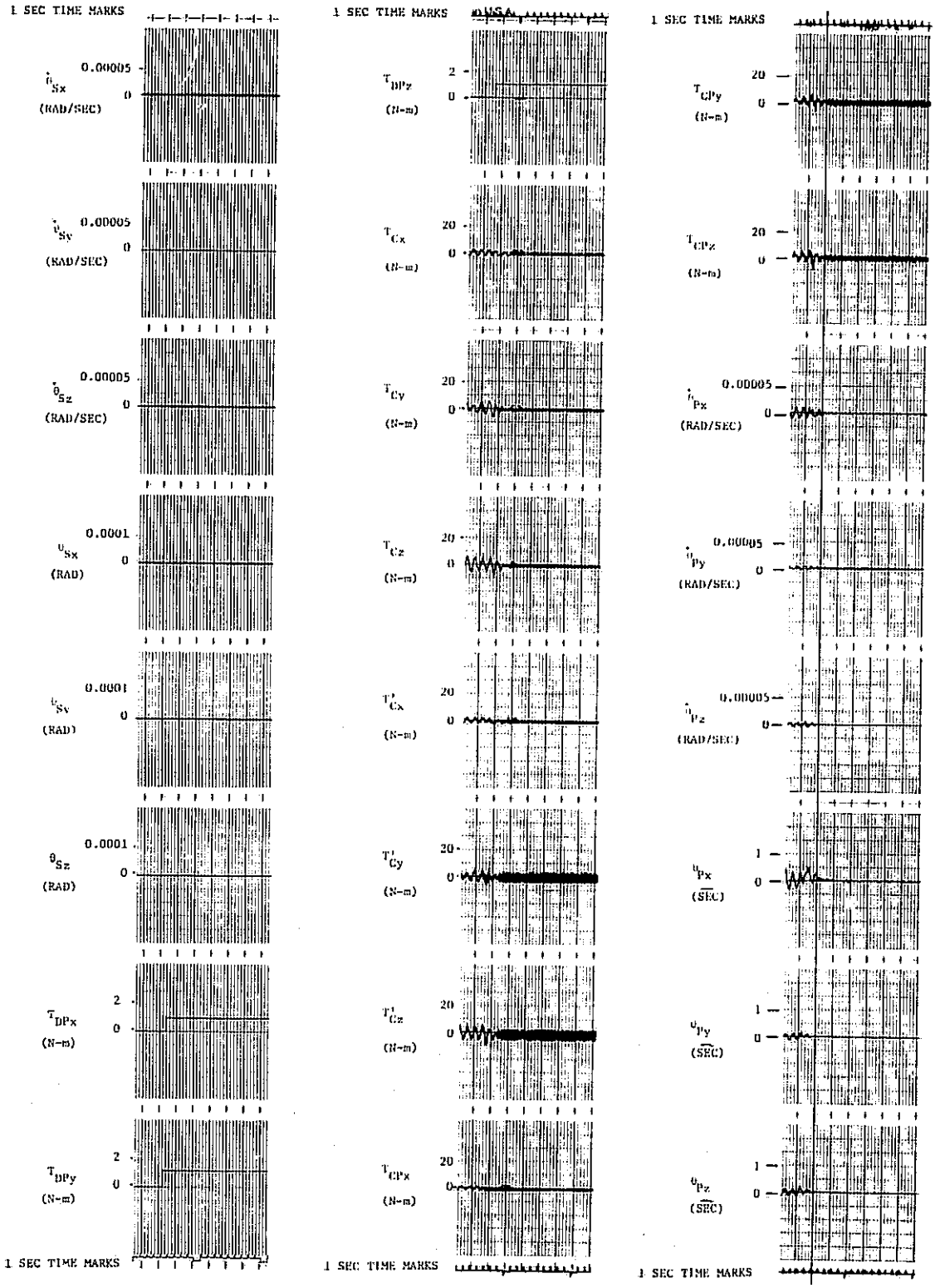

Figure 10-32. Step Torque Disturbance, 2 Hz System, Zero Inner Gimbal Angles and 45 deg Outer Gimbal Angles

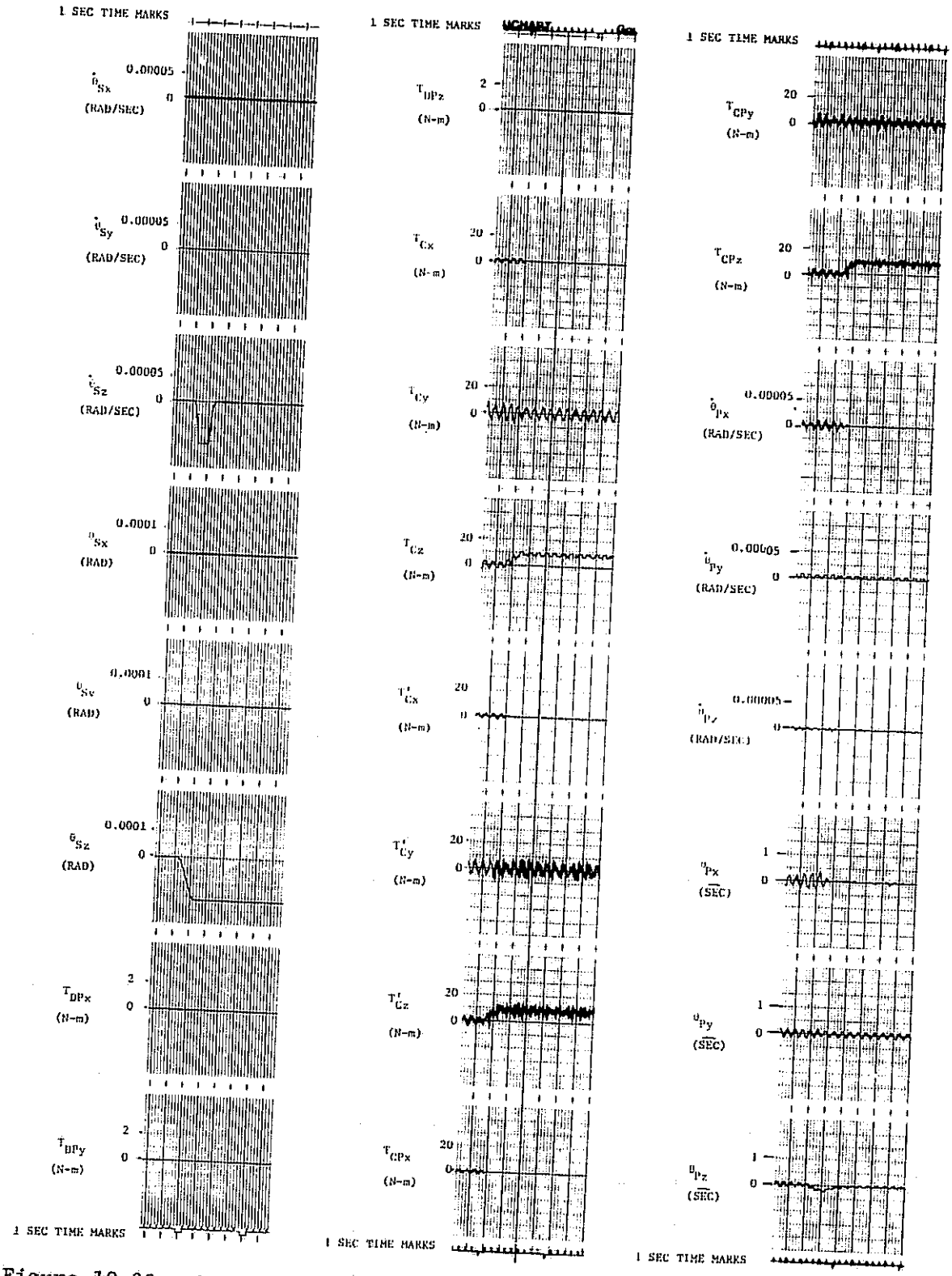

Figure 10-33. Crew Motion Torque Disturbance Case I, 2 Hz System, Zero Inner Gimbal Angles and 45 deg Outer Gimbal Angles

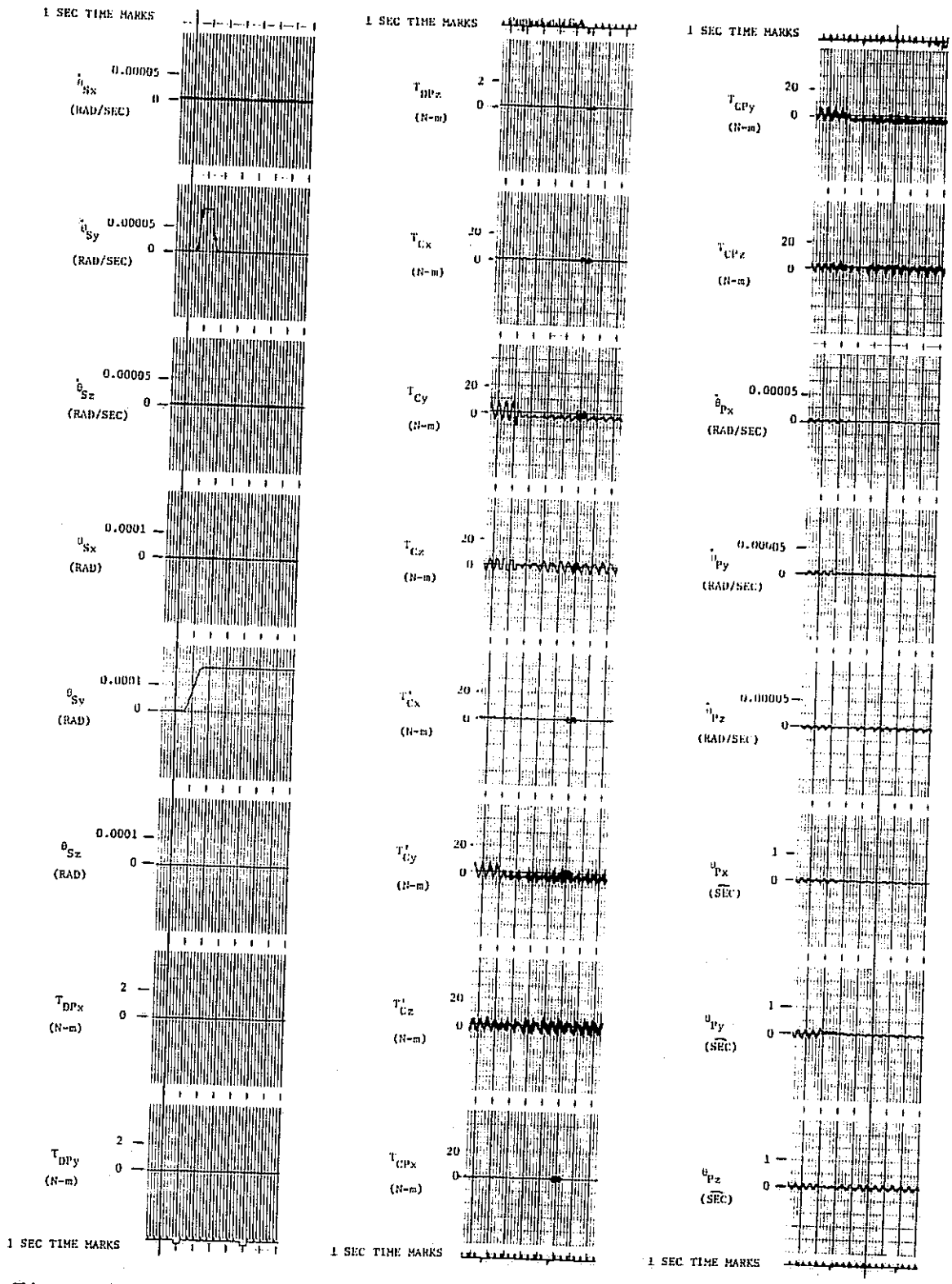

Figure 10-34. Crew Motion Torque Disturbance Case II, 2 Hz System, Zero Inner Gimbal Angles and 45 deg Outer Gimbal Angles

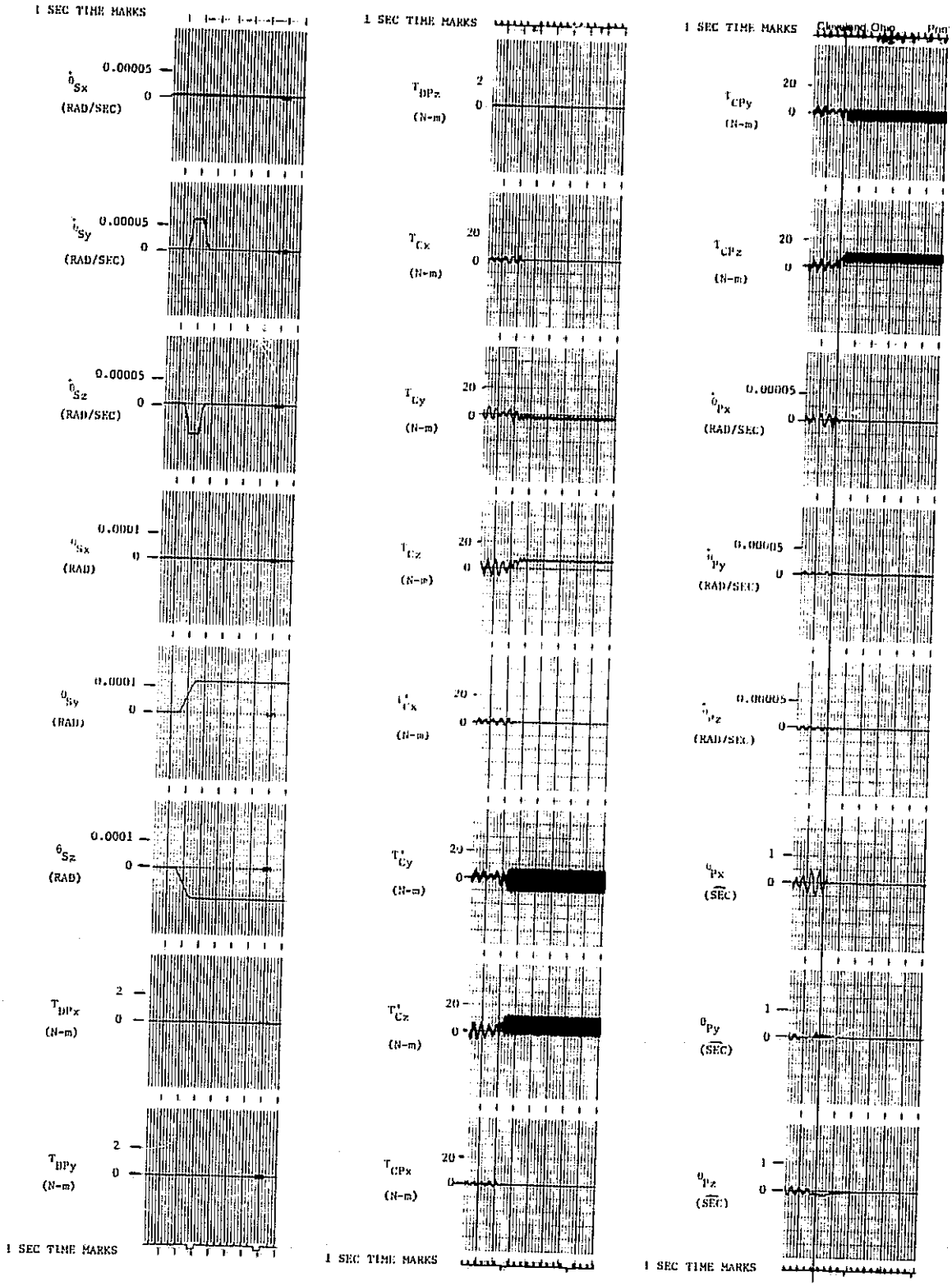

Figure 10-35. Crew Motion Torque Disturbance Case III, 2 Hz System, Zero Inner Gimbal Angles and 45 deg Outer Gimbal Angles

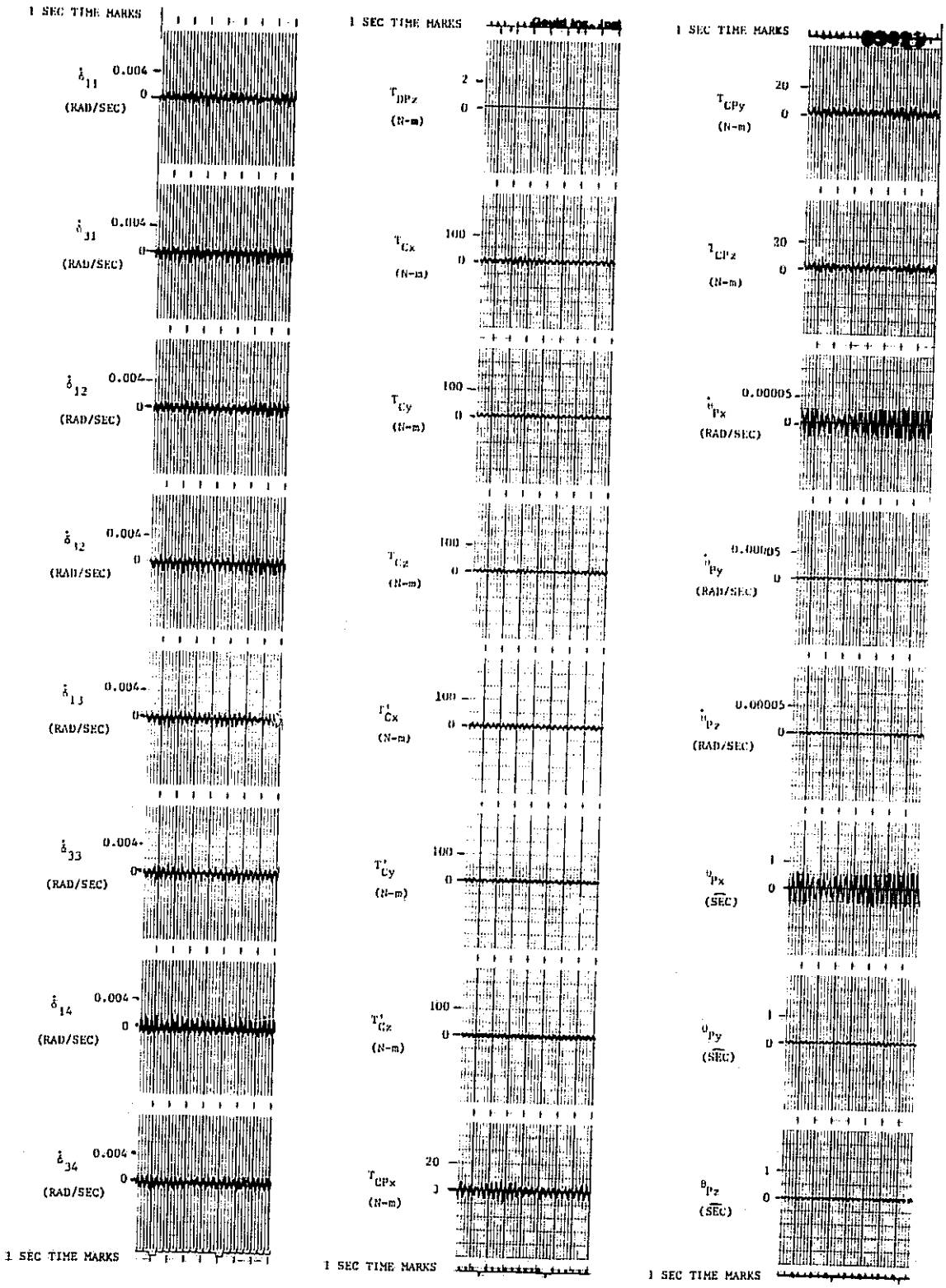

Figure 10-36. No Torque Disturbance, 4 Hz System, Zero Gimbal Angles

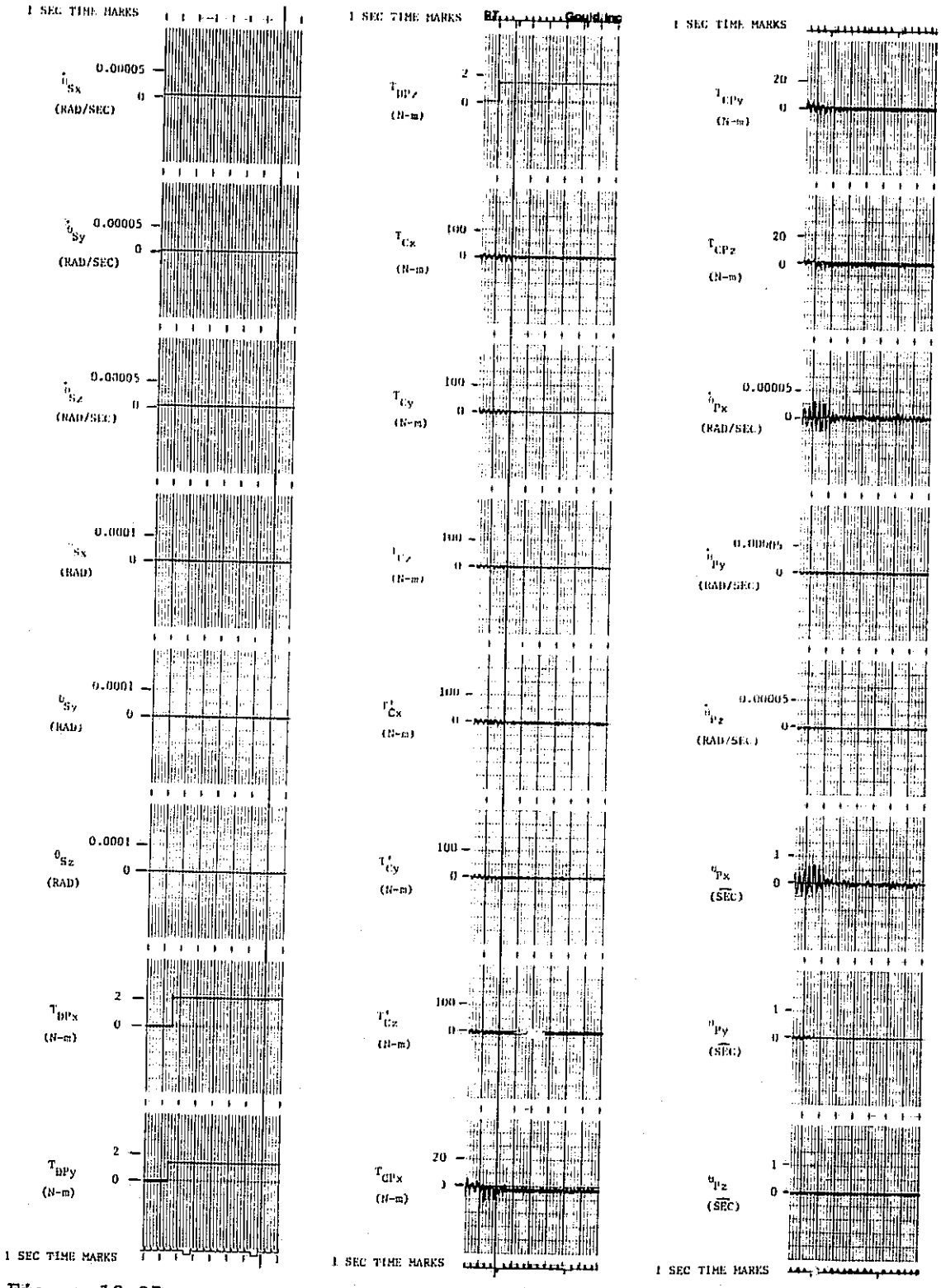

Figure 10-37. Step Torque Disturbance, 4 Hz System, Zero Gimbal Angles

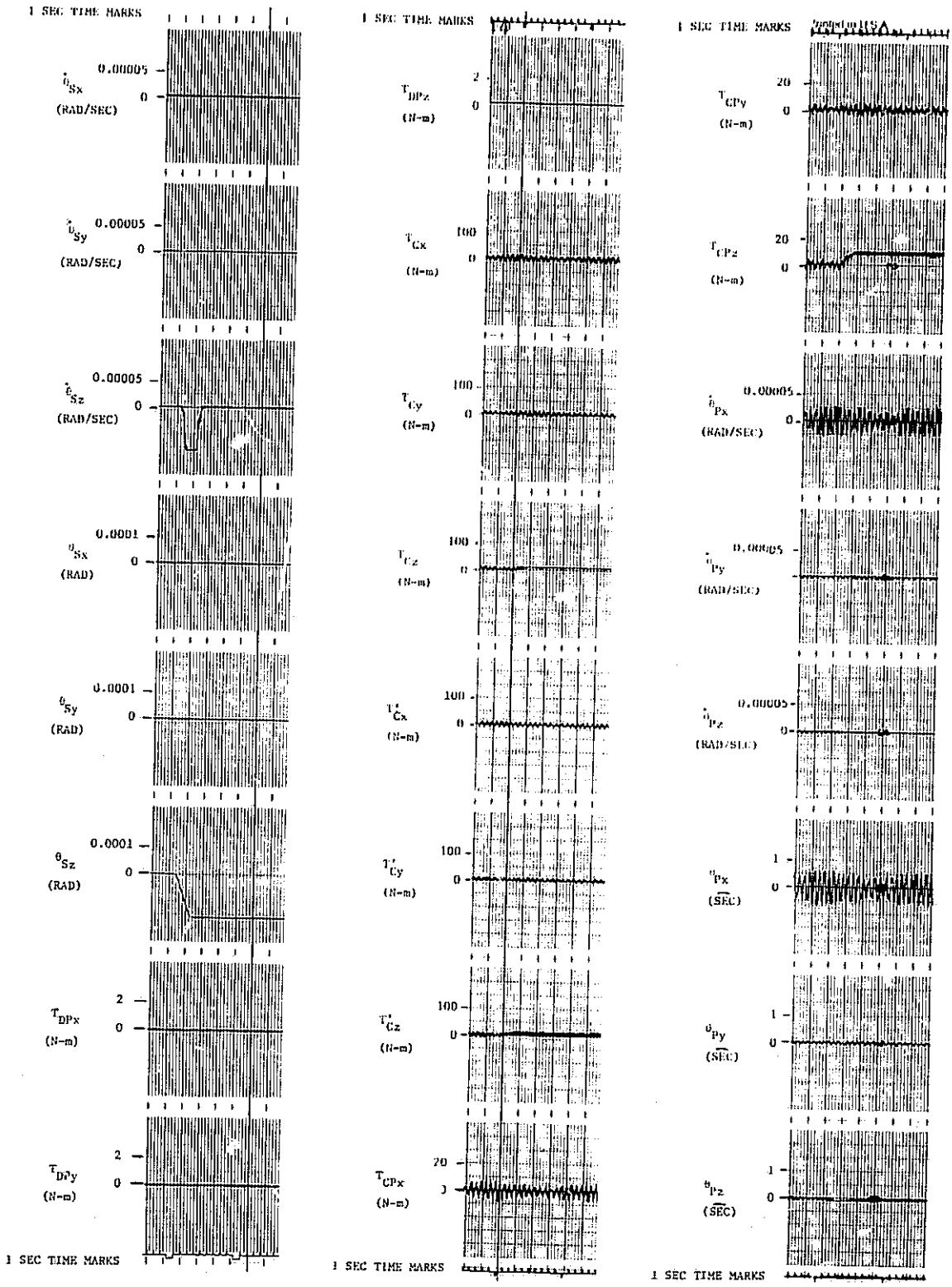

Figure 10-38. Crew Motion Torque Disturbance Case I, 4 Hz System, Zero Gimbal Angles

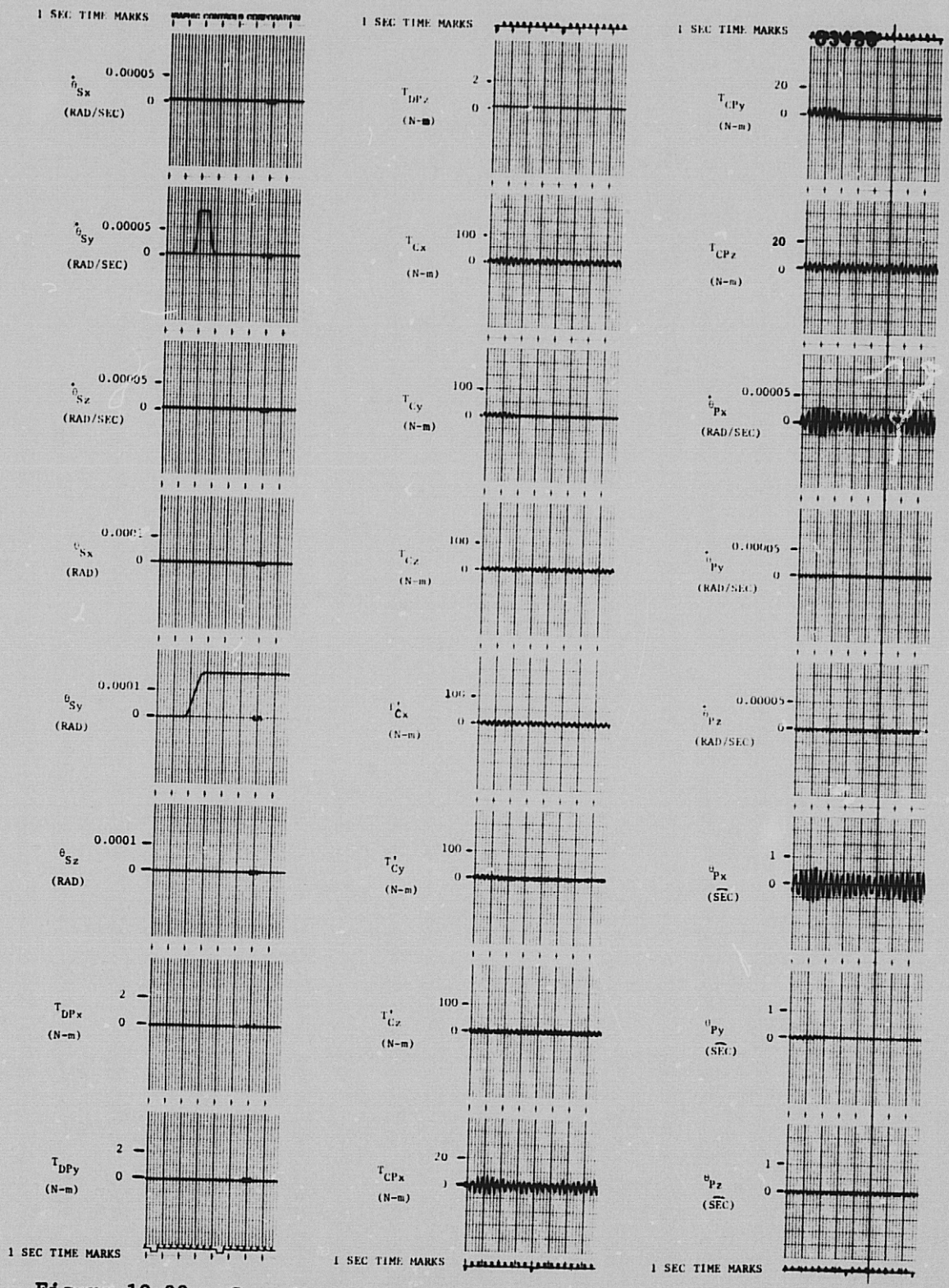

Figure 10-39. Crew Motion Torque Disturbance Case II, 4 Hz System, Zero Gimbal Angles

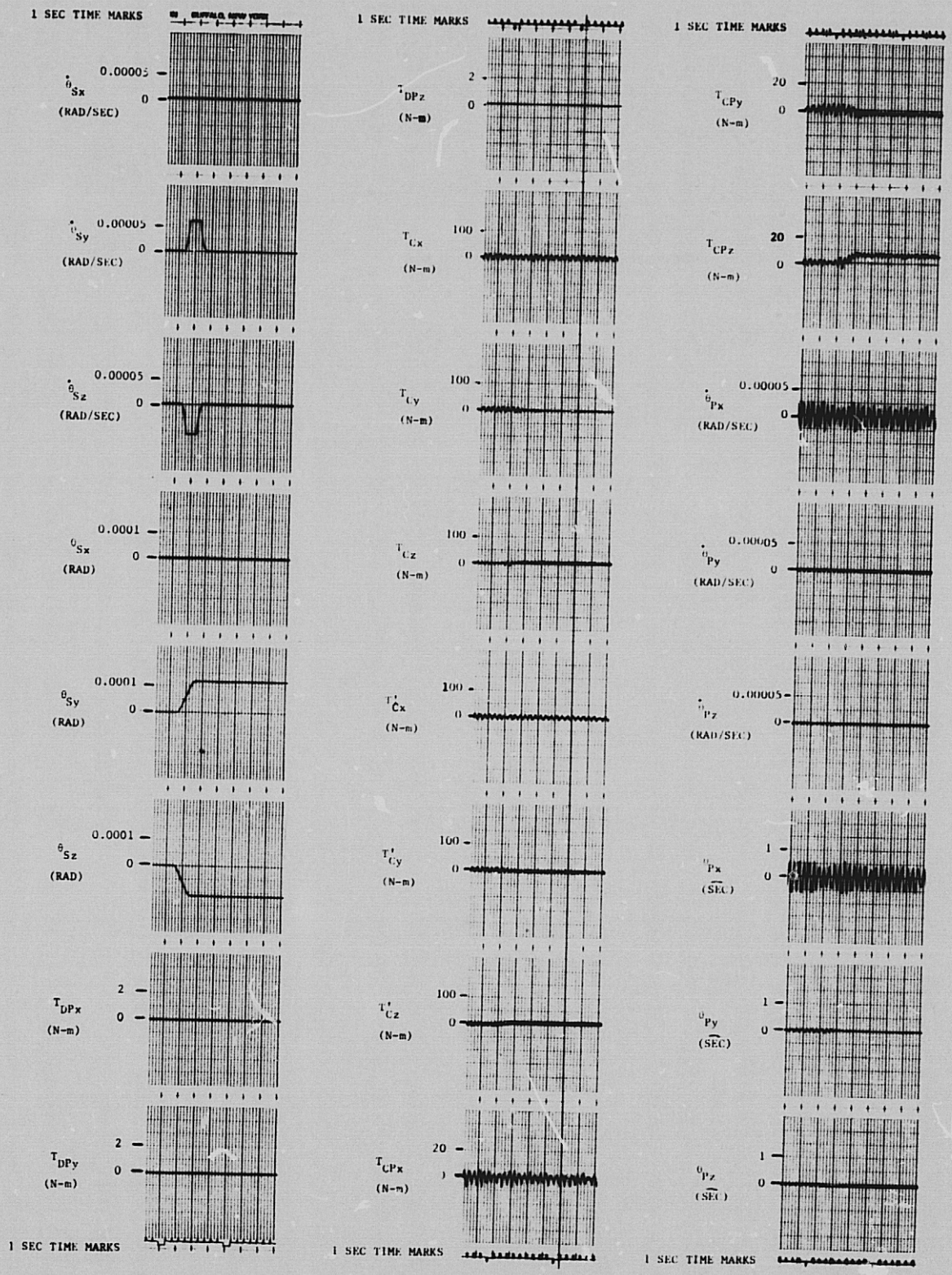

Figure 10-40. Crew Motion Torque Disturbance Case III, 4 Hz System, Zero Gimbal Angles

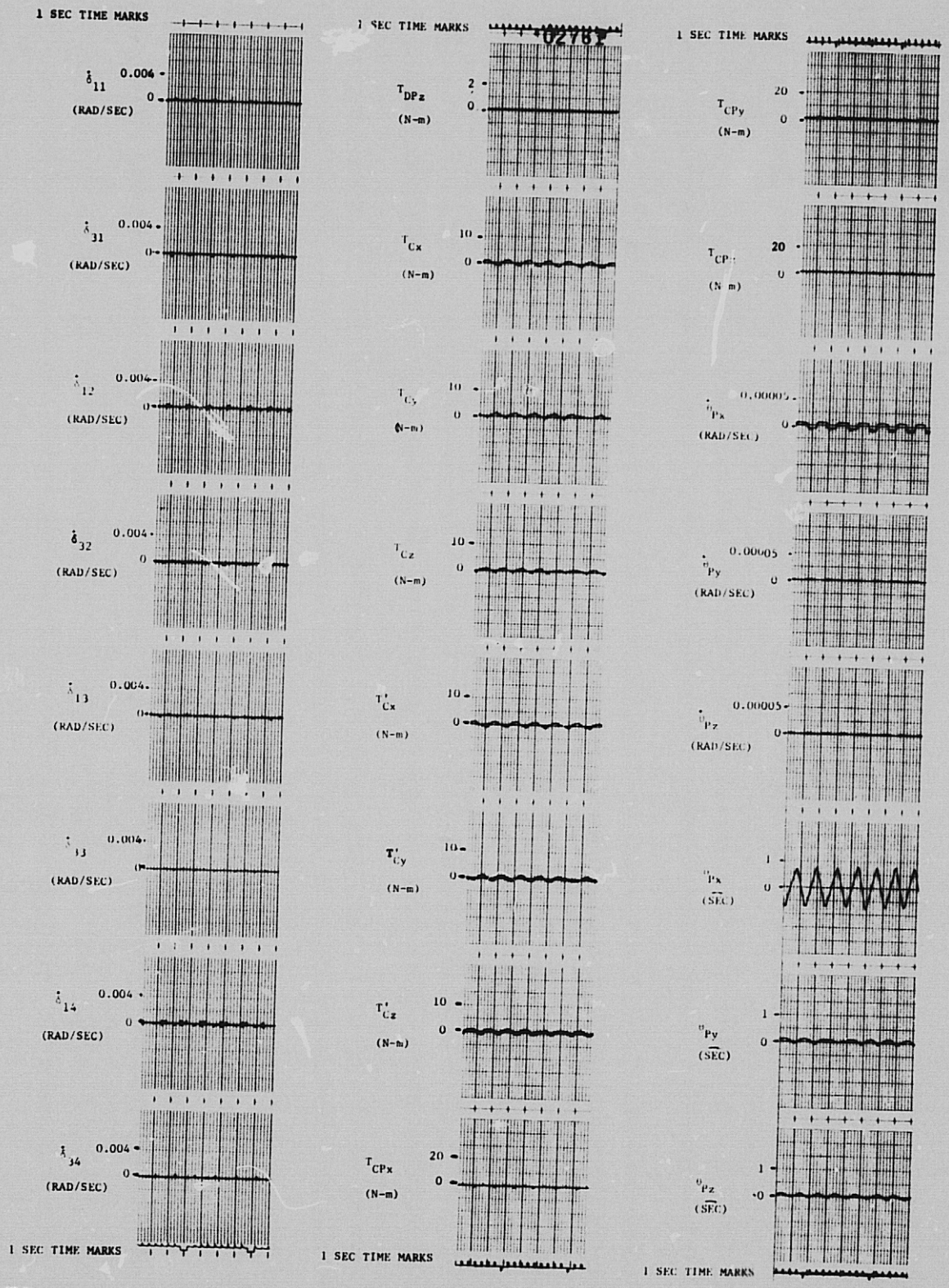

Figure 10-41. No Torque Disturbance, 1 Hz System, Zero Gimbal Angles, Half CMG Friction

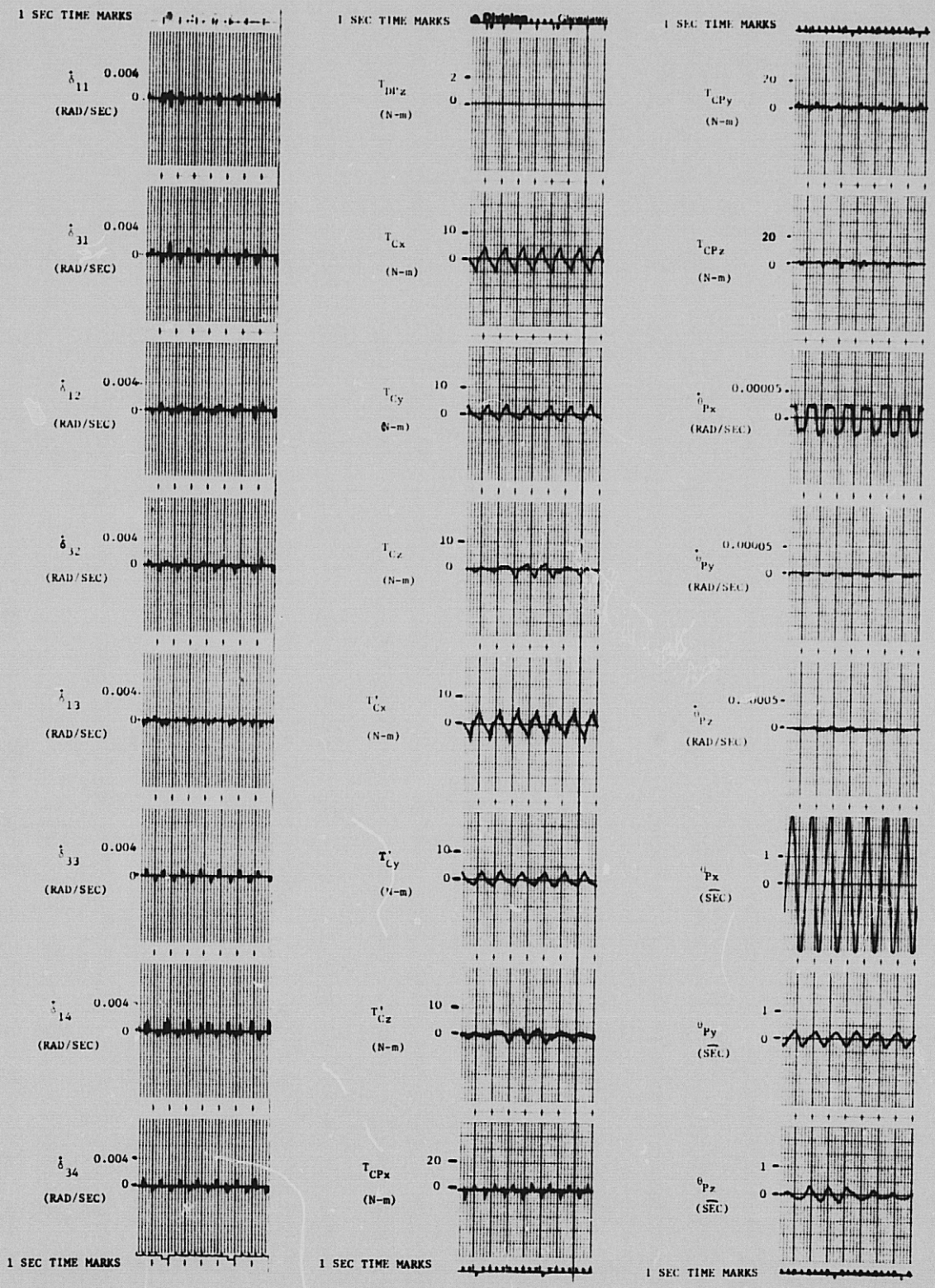

Figure 10-42. No Torque Disturbance, 1 Hz System, Zero Gimbal Angles, Double CMG Friction

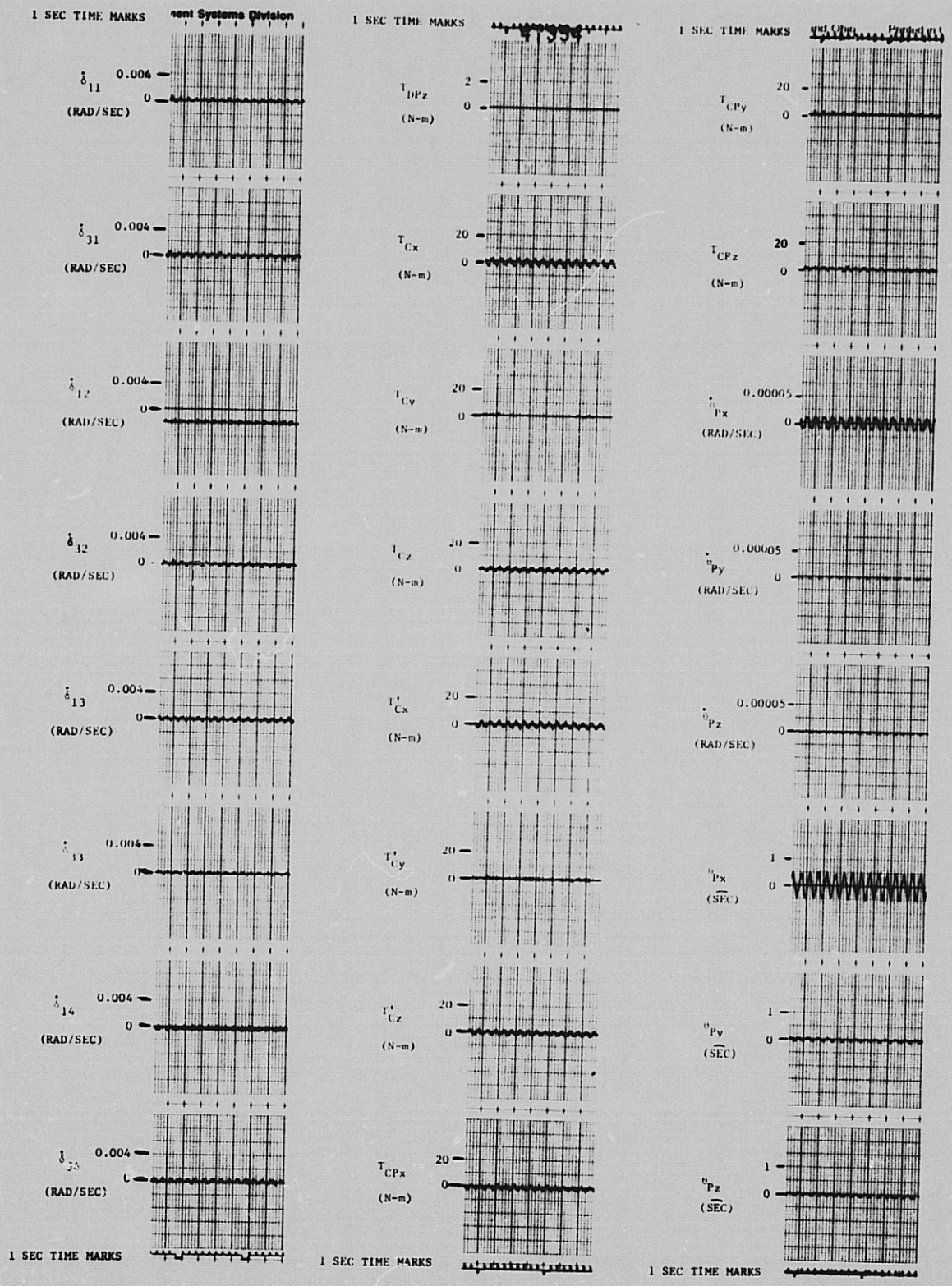

Figure 10-43. No Torque Disturbance, 2 Hz System, Zero Gimbal Angles, Half CMG Friction

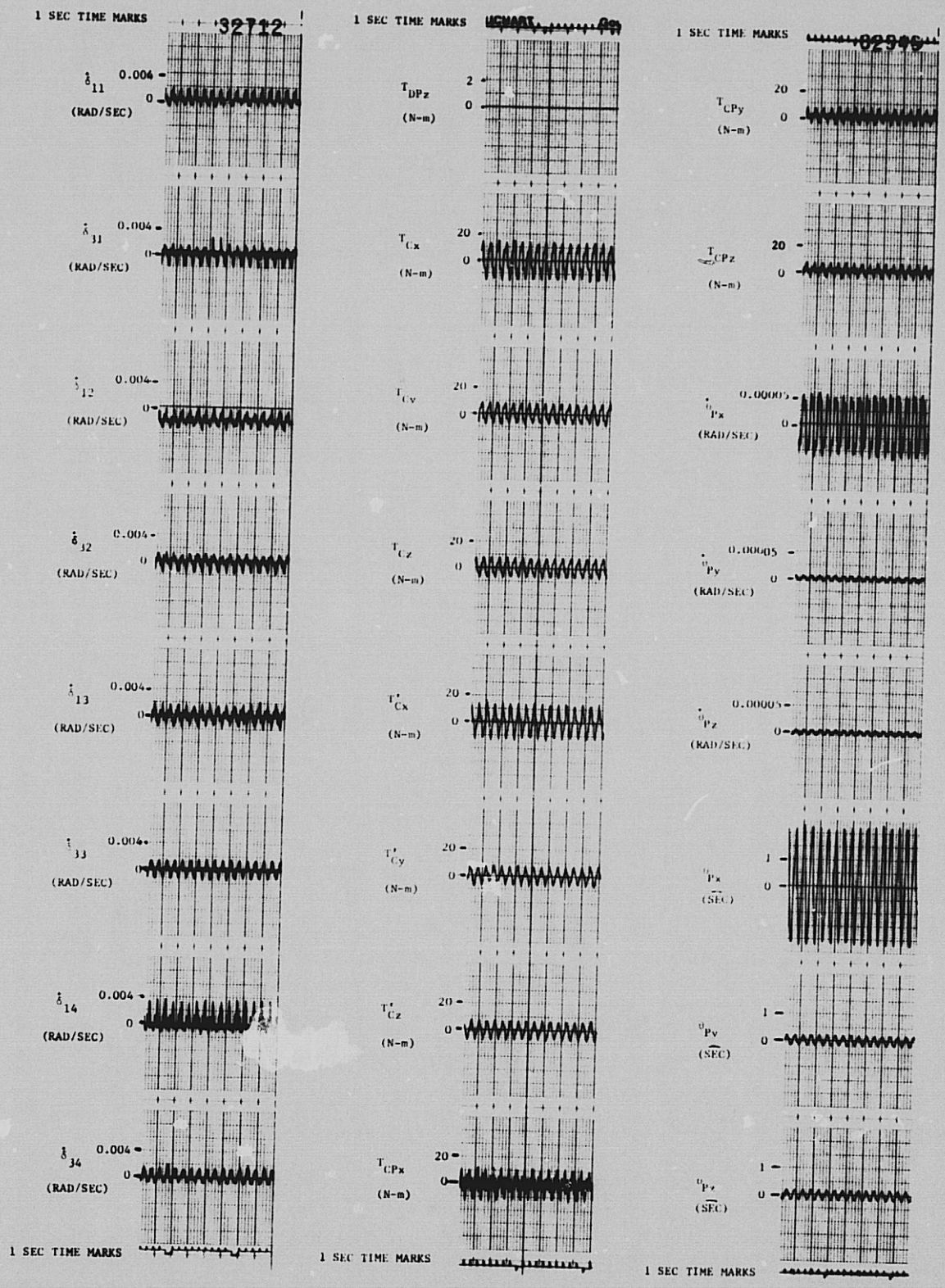

Figure 10-44. No Torque Disturbance, 2 Hz System, Zero Gimbal Angles, Double CMG Friction

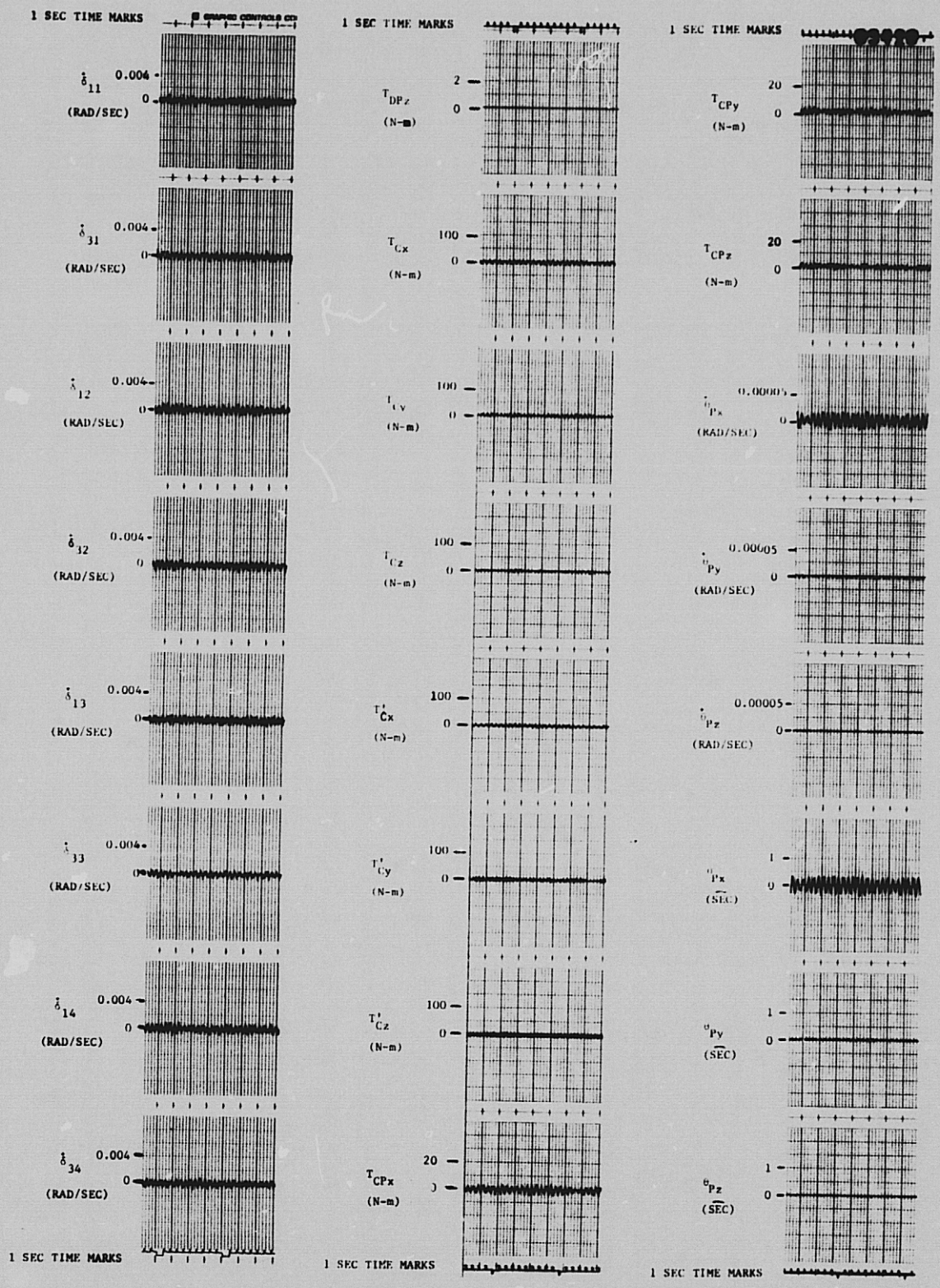

Figure 10-45. No Torque Disturbance, 4 Hz System, Zero Gimbal Angles, Half CMG Friction

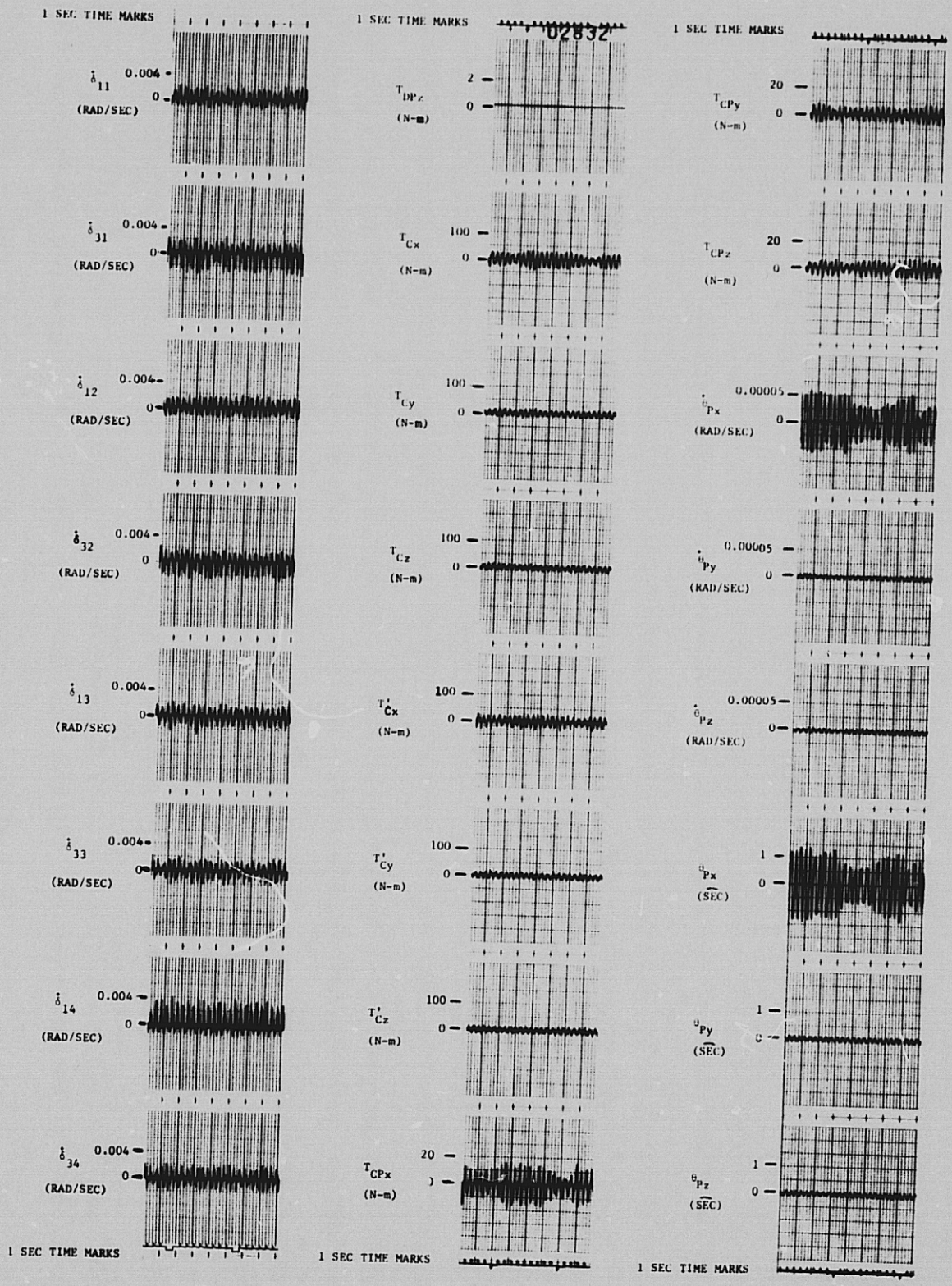

Figure 10-46. No Torque Disturbance, 4 Hz System, Zero Gimbal Angles, Double CMG Friction

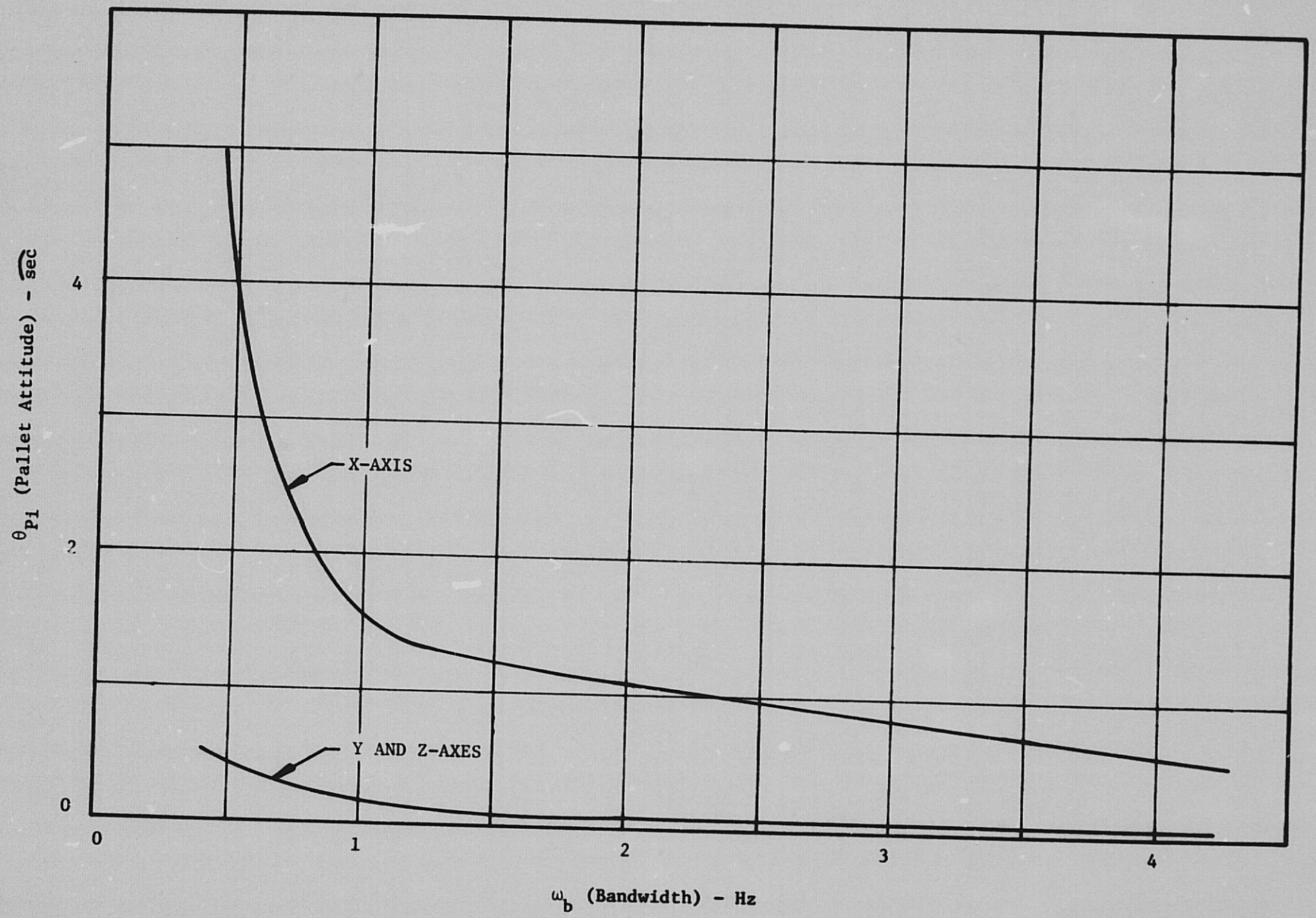

Figure 10-47. Unloaded Limit Cycle Peak Value Versus System Bandwidth (Zero Gimbal Angles)

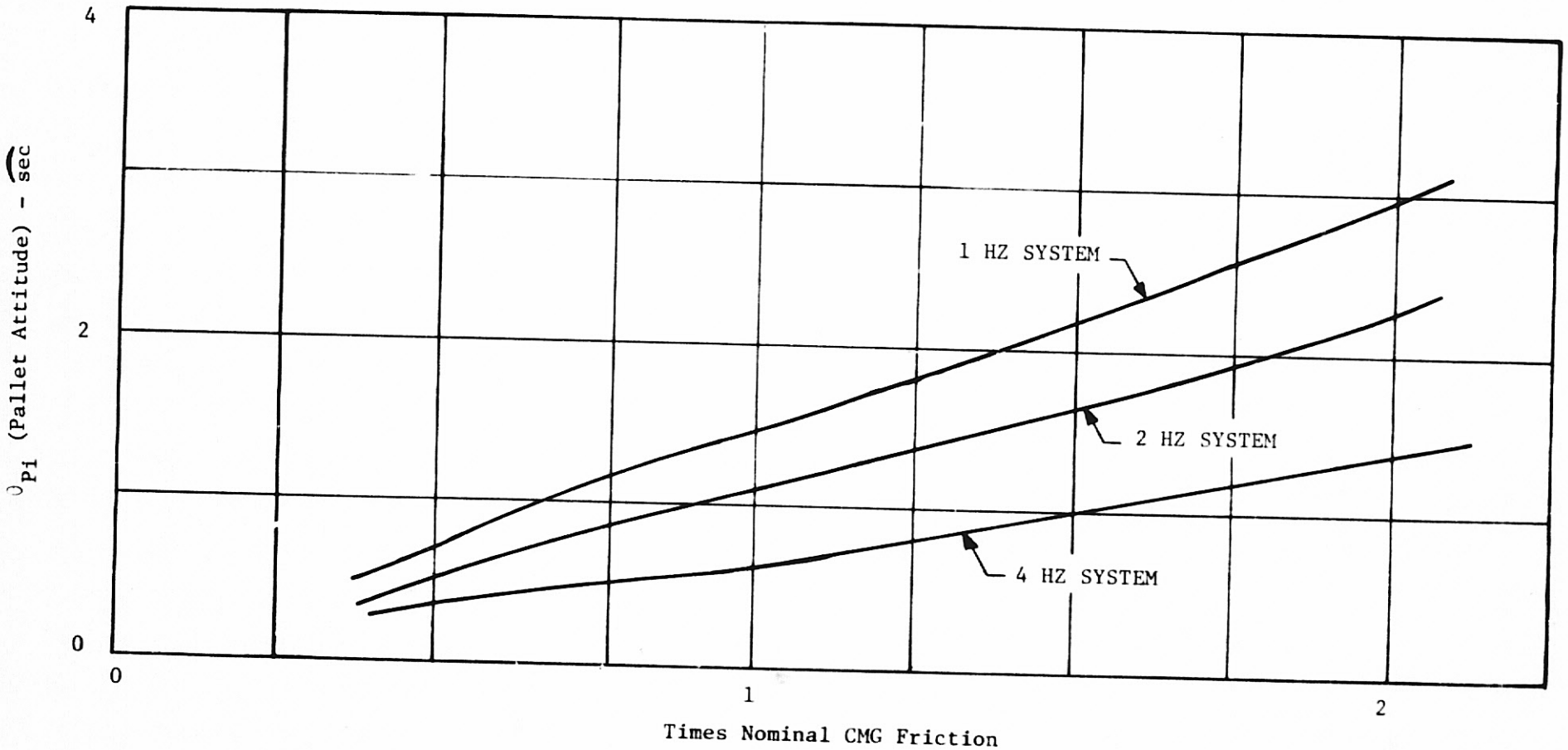

Figure 10-48. Unloaded Limit Cycle X-Axis Peak Value Versus CMG Friction Level (Zero Gimbal Angles)

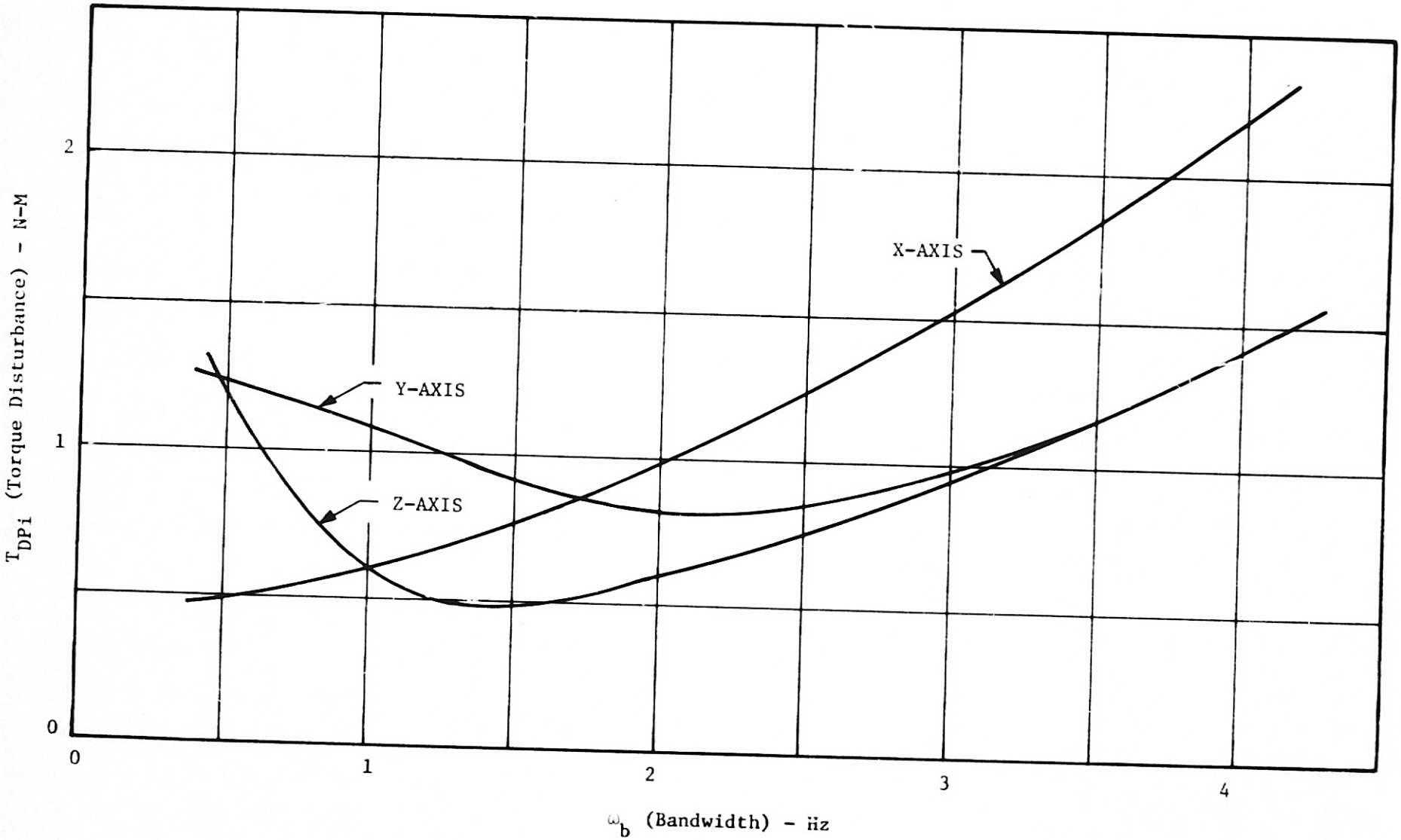

Figure 10-49. Torque Disturbance Required to Eliminate Limit Cycle Versus System Bandwidth (Zero Gimbal Angles)

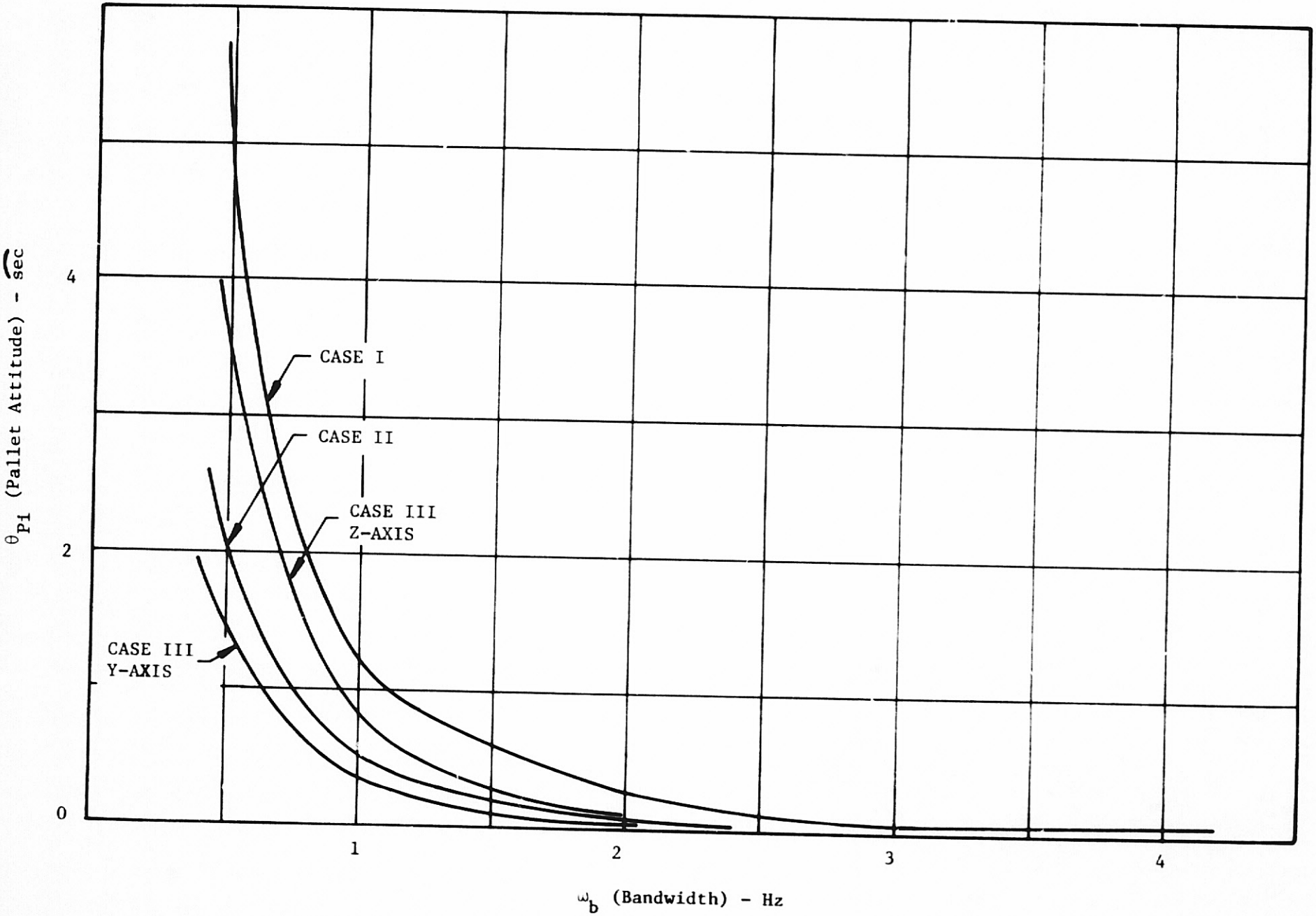

Figure 10-50. Crew Motion Disturbance Peak Value Versus System Bandwidth (Zero Gimbal Angles)

11. CONCLUSIONS

The following are the major conclusions of this study:

a. Two shuttle pointing orientations (X-IOP and X-POP) were studied to determine actuator torque and momentum storage requirements. The X-IOP attitude has the advantage of allowing instrument pointing anywhere in the celestial sphere without the need for gimballed payloads, however, momentum accumulation due to gravity gradient torques is larger than when operating in the X-POP attitude. It was decided that the momentum exchange system would be sized for X-IOP in order to allow all sky viewing without the requirement of additional gimbals when considering single payload operation.

b. A CMG cluster having a momentum storage capability of 12,200 n-m-sec and a minimum torque capability of 200 n-m can meet the requirements of the orbiter/pallet vehicle for gravity gradient stabilization during observation in an X-IOP orientation, and for momentum desaturation maneuvers.

c. Of the three candidate double gimbal CMG actuators (Bendix MA-2300, Bendix MA-2000, Sperry 4500) the modified Bendix MA-2300, a version of the Skylab ATM CMG was chosen primarily on the basis of being space qualified and its off-the-shelf availability. This choice dictated a CMG cluster of four Skylab ATM CMGs of 3,115 n-m-sec momentum capability each in order to meet vehicle momentum requirements.

d. A 20 Hz isolator was placed between each CMG and the pallet. High frequency disturbances generated by the CMG, which could not be eliminated by a second level of Experiment Control (e.g., Image Motion Compensation) due to its high frequency nature, are prevented from reaching the pallet.

An unwanted effect of the isolator is to lower the frequency response of the actuator (CMG/isolator combination) to approximately 2 Hz. Design of a compensator was required to insure stability when operating at a system bandwidth of 2 Hz.

e. Computer studies were parameterized as a function of CMG friction level, CMG gimbal angle, system bandwidth, and crew motion disturbance. Major conclusions obtained from the computer runs were: 1) with no torque present, there exists a pallet attitude limit cycle (1.1 arc-second maximum for 2 Hz system) which decreases in amplitude with an increase in system bandwidth, 2) limit cycle amplitude varied proportionately with friction level, 3) a torque disturbance (approximately 1 n-m for a 2 Hz system) causes the limit cycle to disappear, the torque level being a function of system bandwidth, and 4) pointing error due to crew motion disturbance (0.25 arc-second for a 2 Hz system) decreases as system bandwidth increases.

f. The 2 Hz system could easily meet the 1 arc-second pointing requirement considering the fact that an orbital vehicle almost always has disturbance torques acting upon it which would virtually eliminate limit cycle behavior.

g. Redesign of the CMG rate loops, to better compensate for the effects of the CMG shockmounts and friction at zero gimbal rate commands, will allow the use of lower vehicle loop bandwidths (i.e, approximately 1 Hz) while still meeting the 1 arc-second pointing stability performance desired for all system states.

12. NOTES

12.1 References

1. Report on Disturbance Profile Identifications, Skylab SWS/OA APCS Postflight Performance Evaluation, NASA MSFC 80M19008 (Revision A), June 30, 1974.

2. Study to Define Logic Associated With CMGs to Maneuver and Stabilize an Orbiting Spacecraft, Final Report for Contract NAS9-13085, The Bendix Corporation, Guidance Systems Division, Denver Operations, September 4, 1973.

3. Low Cost Systems, Stabilization and Control, Hardware and Software Inventory, NASA-MSFC, May 1974.

4. Powell, B. K., Binroth, W., Attitude and Pointing Control System Mathematical Model, 3635-1323-7a14, The Bendix Corporation, Research Laboratories, Southfield, Michigan, August 14, 1970.

5. Binroth, W., CMG Control Subsystem Model Description, 7613-72-49, The Bendix Corporation, Research Laboratories, Southfield, Michigan, December 5, 1972.

12.2 Abbreviations

A/D	Analog to Digital
APCS	Attitude Pointing Control System
ASM	Astronomy Sortie Mission
ATM	Apollo Telescope Mount
CM	Center-of-Mass
C&D	Control and Display
CMG	Control Moment Gyro
D/A	Digital to Analog
DCMG	Double Gimbal Control Moment Gyro
GG	Gravity Gradient
kg	Kilogram
$kg\text{-}m^2$	Kilogram-(Meters)^2
km	Kilometer
n-m	Newton-Meter
n•mi	Nautical Mile
OMS	Orbital Maneuvering Subsystem
RAM	Research and Applications Module
RCS	Reaction Control System

rpm	Revolutions Per Minute
SCMG	Single Gimbal Control Moment Gyro
SRB	Solid Rocket Booster
wrt	With Respect To

12.3 Symbols

a_i	Components of unit vector along the local vertical (i=x,y,z)
A-space	CMG inner gimbal coordinate frame
B-space	CMG base coordinate frame
C-space	CMG outer gimbal coordinate frame
$[C_i]$	Pallet isolator spring damping matrix
C(s)	CMG/shockmount transfer function
D_{si}	Shockmount spring damping
$\vec{F}_f$	Total friction force on orbiter from suspension system
$\vec{f}_i$	Friction of the ith pallet suspension point
$\vec{F}_{Pi}$	Force on the pallet due to the ith suspension point
F(s)	Lapace of any time function f(t)
$\vec{F}_{Si}$	Force on the orbiter due to ith suspension point
$\vec{F}_{SP}$	Sum of the suspension forces acting on the pallet
$\vec{F}_{SS}$	Sum of the suspension forces acting on the orbiter
$G_1(s)$	Vehicle control law
$G_c(s)$	Compensation network
$\vec{H}_a$	Angular momentum of the inner gimbal written in A-space
$\vec{H}_{Aj}$	Wheel momentum of the jth CMG (i=1,2,3,4)
$\vec{H}_c$	Angular momentum of the outer gimbal written in C-space
$\vec{H}_d$	Accumulated momentum for one orbit
$\vec{H}_{gg}$	Momentum accumulation due to gravity gradient
$\vec{H}_{ggm}$	Upper bound on momentum due to gravity gradient torque
$\vec{H}_P$	Peak momentum due to gravity gradient torque

$\vec{H}_r$	Angular momentum of the CMG rotor
$\vec{H}_w$	CMG wheel momentum vector
J	Inertia about axis of rotation
J_{all}	Inertia of inner gimbal and motor rotor about gimbal X axis
J_{b33}	CMG base inertia about the Z axis
J_c	Outer gimbal inertia
J'_c	Equivalent outer gimbal inertia
J'_{c33}	Equivalent outer gimbal inertia about the outer gimbal Z axis
J_d	Moment of inertia of the CMG rotor about the diameter (X or Z axis)
$[J_p]$	Inertia tensor of the pallet
J_r	Moment of inertia of the CMG rotor about the spin (Y) axis
$[J_s]$	Inertia tensor of the orbiter
$[J_v]$	Inertia tensor in vehicle coordinates
K_1	Root locus gain
K_m	Gain margin
$[K_i]$	Pallet isolator spring constant matrix
K_P	Control law position gain
K_{PI}	Control law position integral gain
K_R	Control law rate gain
K_{Si}	Shockmount spring stiffness
L	Lagrangian adjoint
m_P	Mass of the pallet
m_S	Mass of the orbiter
P	Performance index
P'_j	CMG output coordinate system (j=1,2,3,4)
$\hat{r}_o$	Components of the local vertical unit vector resolved in vehicle coordinates
$\vec{R}_o$	Vector locating pallet CM to orbiter CM
S	Laplace operator
S_g	Friction level at which switching from static to running friction occurs
T	Torque output from the CMG

t_a	Time to accelerate to maximum vehicle rate for GG maneuver
$\vec{T}_a$	Torque exerted on the inner gimbal by the outer gimbal
t_b	Maneuver time during constant rate period during GG maneuver
$\vec{T}_b$	Torque exerted on CMG base by shockmount expressed in B-space
$\vec{T}_c$	CMG command torque
$\vec{T}_C$	Torque exerted on the outer gimbal by the CMG base
$\vec{T}'_C$	Commanded torque
$\vec{T}_{CP}$	Total control torque exerted on the pallet by the CMG cluster
T_D	Disturbance torque
$\vec{T}_D$	Output torque of DCMG
$\vec{T}_{DS}$	Disturbance torque acting on the orbiter
T_ε	Error torque command
$\vec{T}_{ext}$	External torques acting on the inner gimbal
$\vec{T}_f$	Friction torque on orbiter
T_{fg}	Friction torque
T_g	CMG gear train torque output
$\vec{T}_{gg}$	Gravity gradient torque
$\vec{T}_{ggm}$	Upper bound on gravity gradient torque
$\vec{T}_{Gs}$	Gravity Gradient torque acting on the orbiter
t_m	Total maneuver time
T_{ms}	Torque about rotor Y axis
T_P	Torque exerted on the pallet by the shockmount
$\vec{T}_{P'_j}$	Torque for the jth CMG expressed in P' coordinates
T_{Rg}	Running level of bearing friction
$\vec{T}_s$	Output torque of SCMG

T_{sg}	Static level of bearing friction
$\vec{T}_{SP}$	Sum of the suspension torques acting on the pallet
$\vec{T}_{SS}$	Sum of the suspension torques acting on the orbiter
$\vec{T}_{w}$	Torque exerted on the w-frame written in w-space
T_{wx}	Wheel reaction torque about inner gimbal X axis
w-space	CMG rotor (wheel) coordinate frame
X_I, Y_I, Z_I	Inertial coordinates
X_P, Y_P, Z_P	Pallet coordinates
X_S, Y_S, Z_S	Orbiter coordinates
XIOP	X vehicle principle axis in the orbit plane
XPOP	X vehicle principle axis perpendicular to the orbit plane
$\vec{\alpha}_i$	Locates pallet end of the ith isolator
$\vec{\beta}_i$	Locates orbiter end of the ith isolator
γ_i	Small angle rotation of CMG rotor wrt A-space (i=1,3)
δ_i	CMG gimbal angle (i=1, inner; i=3, outer)
$\dot{\delta}_i$	CMG gimbal rate (i=1, inner; i=3, outer)
$\vec{\dot{\delta}}_{ij}$	CMG gimbal rate vector (i=1, inner; i=3, outer) (j=1,2,3,4 for four CMGs)
$\vec{\dot{\delta}}_{1C}$	Inner gimbal rate command
$\vec{\dot{\delta}}_{3C}$	Outer gimbal rate command
$\dot{\delta}_{mi}$	Rate of CMG motor rotor (i=1,3)
ΔI	Difference in inertia terms
$\Delta(s)$	Control loop characteristic equation
$\vec{\varepsilon}$	Pointing offset
$\vec{\varepsilon}_C$	Mass offset of the pallet wrt to the pallet initial position expressed in I coordinates
ε_g	Threshold level at which friction model switches from running to stiction state
$\vec{\varepsilon}_P$	Small angle rotation about the vehicle axes
ζ_i	Damping factor (i=1,2,n)

θ	Sensed vehicle position
θ_D	Desired vehicle position
θ_P	Pallet position
θ_S	Orbiter position
θ_{si}	Small angle rotation of CMG base wrt the pallet
$\vec{\lambda}$	Lagrange multiplier
$\vec{\rho}$	Location of pallet CM wrt orbiter CM
ρ_{Po}	Initial card on $\vec{\rho}_P$, i.e., value of $\vec{\rho}_P$ when suspension is relaxed
$\vec{\rho}_P$	Relates pallet coordinate system to origin of I coordinate system
$\vec{\rho}_{So}$	Initial condition on $\vec{\rho}_S$, i.e., value of $\vec{\rho}_S$ when suspension is relaxed
$\vec{\rho}_S$	Relates orbiter coordinate system to the origin of the I coordinate system
ϕ_m	Phase margin
ψ	Maneuver angle for desaturation maneuvers
$\vec{\omega}$	Sensed vehicle rate
$\dot{\vec{\omega}}$	Acceleration of the ith coordinate frame
$\vec{\omega}_a$	Inertial rate of the CMG inner gimbal
$\vec{\omega}_b$	Inertial rate of the CMG base
$\vec{\omega}_B$	System bandwidth
$\vec{\omega}_C$	Inertial rate of the CMG outer gimbal
$\vec{\omega}_D$	Desired vehicle rate
$\vec{\omega}_g$	CMG gimbal rate
$\vec{\omega}_i$	Compensator undamped natural frequency (i=1,2)
$\vec{\omega}_o$	Orbital rate
$\vec{\omega}_s$	Spin rate of the CMG rotor
$\vec{\omega}_w$	Inertial rate of the CMG w-frame
$\cdot$	Vector dot (inner) product

X	Vector cross product
sec	Arc second of rotation

12.4 Transformations

$[{}_aT_c]$	Transformation from C-space to A-space
$[{}_{Aj}T_{Cj}]$	Transformation from outer gimbal to inner gimbal coordinates
$[{}_bT_{p'}]$	Transformation from p'-space to B-space
$[{}_cT_b]$	Transformation from B-space to C-space
$[{}_{Cj}T_{p'_j}]$	Transformation from p' to CMG outer gimbal coordinates
$[{}_IT_P]$	Transformation from pallet to inertial coordinates
$[{}_IT_S]$	Transformation from orbiter to inertial coordinates
$[{}_PT_V]$	Transformation from vehicle to principle axis coordinates
$[{}_PT_{p'_j}]$	Transformation from the p' to the p coordinate system
$[{}_wT_a]$	Transformation from A-space to w-space